National Technical University of Athens
School of Civil Engineering
Department of Geotechnical Engineering

MONUMENTIC ARCHED STRUCTURES:

Stability, Seismic Response, Soil-Structure Interaction

This thesis is submitted for the Degree of Doctor of Philosophy

Aikaterini Leontari

Civil Engineer, MSc.

Supervisor:
George Gazetas, Emeritus Professor NTUA

Athens, September 2023

Εθνικό Μετσόβιο Πολυτεχνείο
Σχολή Πολιτικών Μηχανικών
Τομέας Γεωτεχνικής

ΜΝΗΜΕΙΑΚΕΣ ΤΟΞΩΤΕΣ ΚΑΤΑΣΚΕΥΕΣ:

Ευστάθεια, Σεισμική Απόκριση, Αλληλεπίδραση Εδάφους-Κατασκευής

Διδακτορική Διατριβή

της

Αικατερίνης Λεοντάρη

Διπλωματούχου Πολιτικού Μηχανικού, MSc.

Επιβλέπων:
Γεώργιος Γκαζέτας, Ομότιμος Καθηγητής Ε.Μ.Π

Αθήνα, Σεπτέμβριος 2023

NATIONAL TECHNICAL UNIVERSITY OF ATHENS
SCHOOL OF CIVIL ENGINEERING
DEPARTMENT OF GEOTECHNICAL ENGINEERING

MONUMENTIC ARCHED STRUCTURES:

Stability, Seismic Response, Soil-Structure Interaction

DOCTORAL THESIS

Aikaterini Leontari

Civil Engineering, M.Sc.

ADVISORY COMMITTEE:

1. G. Gazetas,
   Emeritus Professor N.T.U.A.

2. N. Makris,
   Professor S.M.U.

3. N. Gerolymos,
   Associate Professor N.T.U.A.

EXAMINATION COMMITTEE:

1. G. Gazetas,
   Emeritus Professor N.T.U.A.

2. N. Makris,
   Professor S.M.U.

3. N. Gerolymos,
   Associate Professor N.T.U.A.

4. P. Tsopelas,
   Professor N.T.U.A.

5. Ach. Papadimitriou,
   Associate Professor N.T.U.A.

6. G. Tsiatas,
   Associate Professor N.T.U.A.

7. Y. Chaloulos,
   Assistant Professor A.U.TH.

Athens, September 2023

Στον Ιάσονα, το φως της ζωής μου…..

Στον Μάριο, τον συνοδοιπόρο μου….

Στους γονείς μου, Γιώργο και Λίντα, που δίνουν και την ζωή τους για μένα…

ΕΚΤΕΝΗΣ ΠΕΡΙΛΗΨΗ

I. Περιγραφή του προβλήματος & Σκοπός της Διατριβής

Περιγραφή του προβλήματος.- Ένα μεγάλο μέρος της πολιτιστικής κληρονομιάς του Ελλαδικού χώρου καλύπτει το σύνολο του δομικού πλούτου που μπορεί να χαρακτηρισθεί με τον όρο μνημειακές κατασκευές. Λαμβάνοντας υπόψη ωστόσο, ότι απειλείται όλο και περισσότερο με φθορά, απώλεια ακεραιότητας ή ακόμη χειρότερα με πλήρη αστοχία, η επιστημονική έρευνα επικεντρώνεται στην ανάπτυξη μεθόδων παρέμβασης ειδικά προσανατολισμένων για κάθε περίπτωση μνημειακών κατασκευών με σκοπό την εξουδετέρωση αυτών των μακροπρόθεσμων επιπτώσεων. Η σταθερότητα των μνημειακών κατασκευών επηρεάζεται από πολλούς παράγοντες που πρέπει όλοι να ληφθούν υπόψη όταν πρόκειται να διεξαχθούν διαδικασίες συντήρησης, αποκατάστασης ή και ενίσχυσης. Προκειμένου να αντιμετωπιστεί αυτό το ζήτημα, πρέπει πρώτα να διερευνήσουμε διεξοδικά ένα από τα θεμελιώδη δομικά στοιχεία αυτών των ιστορικών κατασκευών που είναι το *λίθινο τόξο*. Στο **Σχήμα 1** περιλαμβάνονται μερικά αντιπροσωπευτικά παραδείγματα τέτοιων κατασκευών όπου το τόξο είναι το κυρίαρχο δομικό στοιχείο.

Το λίθινο τόξο είναι μια αρθρωτή κατασκευή, που αποτελείται από σφηνοειδείς πέτρες, τους θολίτες (‘voussoirs’). Αυτές οι πέτρες είναι διατεταγμένες σε μια καμπύλη γραμμή διατηρώντας την θέση τους με αμοιβαίες πιέσεις επαφής σε κάθε διεπιφάνεια. Η στήριξη που παρέχει η κάθε πέτρα στη γειτονική της, περιστασιακά ενισχύεται και με κονίαμα στις αρθρώσεις. Το ίδιο βάρος του τόξου μαζί με τα υπόλοιπα φορτία του τόξου, μεταφέρονται μέσω των θολιτών κατά μήκος των αρθρώσεων, από το υπερκείμενο στο υποκείμενο στοιχείο. Μόλις το ‘‘κλειδί’’ (κεντρικός θολίτης) τοποθετηθεί στην κορυφή του τόξου, οι θολίτες “κλειδώνουν”

στην θέση τους μεταφέροντας τις πλευρικές και κατακόρυφες τάσεις, εξασφαλίζοντας έτσι την ισορροπία του τόξου.

Σχήμα 1 Μερικά αντιπροσωπευτικά παραδείγματα ιστορικών μνημείων γύρω από την Μεσόγειο Θάλασσα: λίθινα τόξα στηριζόμενα σε αψιδοστάτες και κυλινδρικοί θόλοι ενσωματωμένοι στο έδαφος.

Τα βασικά μέρη ενός λίθινου τόξου που στηρίζεται σε αψιδοστάτες απεικονίζονται στο **Σχήμα 2**. Το λεγόμενο εξωρράχιο και εσωρράχιο του τόξου, δηλαδή η κυρτή και η κοίλη πλευρά αντίστοιχα, επισημαίνονται με συνεχή έντονη μαύρη γραμμή και διακεκομμένες αντίστοιχα.

Η συμπεριφορά της λιθοδομής περιγράφεται κυρίως με την αισθητά χαμηλότερη αντοχή στον εφελκυσμό παρά στην θλίψη. Στην πλειονότητα των επιστημονικών μελετών ως βασική προσέγγιση για την ανάλυση της λιθοδομής χρησιμοποιείται το μοντέλο του Heyman (1966) που προσομοιώνει το εξιδανικευμένο άκαμπτο σε θλίψη υλικό χωρίς εφελκυσμό. Υπό δεδομένες συνθήκες φόρτισης, οι λιθόκτιστες κατασκευές μπορεί να υποστούν ρωγμές ή αποσυνδέσεις δημιουργώντας πεδία μετατόπισης που ονομάζονται μηχανισμοί, οι οποίοι αναπτύσσονται απουσία οποιασδήποτε αστοχίας υλικού. Η ανθεκτικότητα του τόξου στον χρόνο ανάγεται σε πρόβλημα ευστάθειας καθώς υπό την επίδραση διαδοχικών αποκλίσεων από την αρχική τους θέση (διαταραχών), η ισορροπία του δύναται να καταστεί ασταθής και να οδηγήσει σε κατάρρευση. Κατά συνέπεια είναι πολύ σημαντικό, η ανάπτυξη

σωρευτικών μετακινήσεων στις αρθρώσεις υπό στατικές συνθήκες να είναι η ελάχιστη δυνατή. Παρομοίως, ο σχηματισμός αρθρώσεων λόγω σεισμικής φόρτισης επιδιώκεται να είναι αναστρέψιμος μετά το πέρας της διέγερσης.

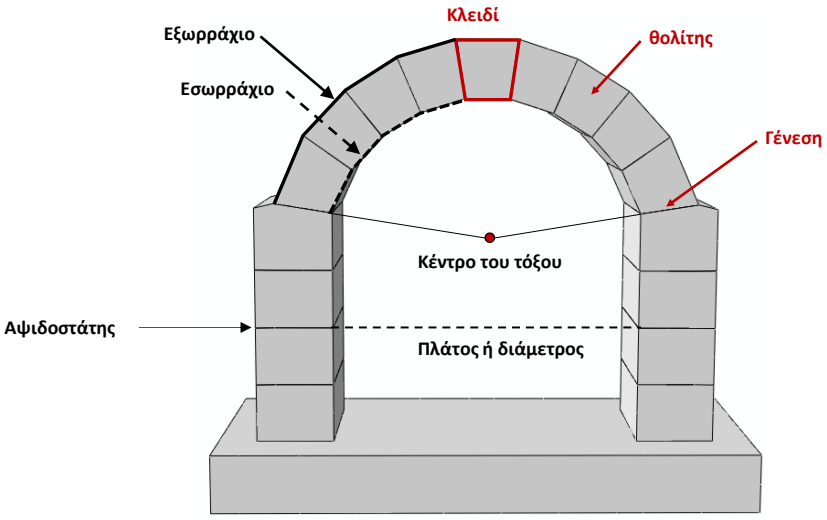

Σχήμα 2 Η γεωμετρία ενός λίθινου τόξου που στηρίζεται σε αψιδοστάτες.

Στην διατριβή αυτή εξετάζεται η σεισμική απόκριση των λιθόκτιστων τόξων με αναλυτικές και αριθμητικές μεθόδους. Έμφαση δίνεται στην ανάπτυξη απλουστευμένων διαδικασιών για την εκτίμηση της απόκρισης τόξου σε σεισμογενείς περιοχές. Με τον σχηματισμό αρθρώσεων η δυναμική απόκριση του τόξου αναγάγεται σε λικνιστική ταλάντωση στερεών σωμάτων εν επαφή μεταξύ τους.

Το έδαφος θεμελίωσης διαδραματίζει κυρίαρχο ρόλο στην δομική ακεραιότητα των μνημείων τα οποία με βάση την αλληλεπίδρασή τους με αυτό δύνανται να διαχωριστούν σε: (α) υπέργειες κατασκευές (πχ. αρχαίοι ναοί, γέφυρες) όπου το έδαφος λειτουργεί αποκλειστικά ως υποστηρίζον μέσο και, (β) γεω-κατασκευές (π.χ. θολωτοί τάφοι, θολωτές είσοδοι σε αρχαία στάδια, θέατρα, ορύγματα) όπου το έδαφος εκτός από υποστηρίζον λειτουργεί ενίοτε και ως αντιστηριζόμενο μέσο ή και ως φορτίζον μέσο. Οι δυσμενείς εδαφικές συνθήκες μπορούν να επιδράσουν καταστρεπτικώς τόσο στην θεμελίωση όσο και στην υπέργεια μνημειακή κατασκευή.

Επομένως, η αναγνώριση του εδαφικού προφίλ καθώς και η διερεύνηση του συστήματος εδάφους-θεμελίωσης πρέπει να αποτελούν αναπόσπαστο κομμάτι της μελέτης αναστήλωσης και αποκατάστασης των μνημείων. Όλα τα είδη μνημειακών κατασκευών προορίζονται να αντέχουν μέσω μιας σειράς μακροπρόθεσμων επιπτώσεων που προκαλούνται από το έδαφος. Αυτές οι σωρευτικές επιδράσεις είναι πιο έντονες στις γεωδομές καθώς οι δυσμενείς εδαφικές συνθήκες μπορούν να προκαλέσουν μεγάλες ζημιές όχι μόνο στην θεμελίωση αλλά και στην δομή του μνημείου. Οι δυσμενείς εδαφικές συνθήκες είναι γενικά συνέπεια μιας συνεχιζόμενης διαδικασίας, τα αποτελέσματα της οποίας γίνονται εμφανή με την πάροδο των χρόνων. Επιπλέον, η υψηλή σεισμική δραστηριότητα που συναντάται στην ελληνική επικράτεια, εκτός από τις ίδιες τις κατασκευές, μπορεί να επιδεινώσει μακροπρόθεσμα τις συνθήκες του εδάφους. Τέλος, οι ανθρωπογενείς δραστηριότητες όπως οι εκσκαφές, η κατασκευή νέων κτιρίων, οι σήραγγες ή ακόμη και οι αλλαγές στον υδροφόρο ορίζοντα δύνανται επίσης να επηρεάσουν τις εδαφικές συνθήκες κοντά σε γεωδομές.

Σκοπός της Διδακτορικής διατριβής.- Με βάση τα ανωτέρω, η παρούσα Διδακτορική Διατριβή αποσκοπεί να εμπλουτίσει τις ήδη υπάρχουσες γνώσεις σχετικά με την απόκριση υπό στατική, ψευδο-στατική και δυναμική φόρτιση των λίθινων τοξωτών κατασκευών είτε αυτές είναι υπέργειες ή χαρακτηρίζονται ως γεω-κατασκευές.

Ειδικότερα, διερευνώνται περαιτέρω οι μηχανισμοί αστοχίας τέτοιων κατασκευών και με έμφαση στην ανάδειξη της σημασίας της αλληλεπίδρασης εδάφους-κατασκευής των μνημειακών λίθινων θολωτών κατασκευών είτε αυτές φορτίζονται στατικά (κάτω από το ίδιο βάρος και το υπερκείμενο έδαφος) ή διεγείρονται δυναμικά από εξιδανικευμένους παλμούς και πραγματικές σεισμικές καταγραφές. Η κύρια ιδέα είναι η ενσωμάτωση των αναπτυγμένων μεθόδων στις μελέτες αποκατάστασης.

Οι πρωταρχικοί στόχοι της διατριβής μπορούν να συνοψιστούν ως εξής:

α) η συμβολή στην λικνιστική απόκριση της απλούστερης μορφής του τοξωτού δομικού στοιχείου: του κυκλικού τόξου

β) η επέκταση αναλυτικών και κλειστών αναλυτικών λύσεων σε τόξα με γεωμετρία πιο σύνθετη από την ομοιόμορφη κυκλική

γ) η αξιολόγηση και η ανάπτυξη μεθόδων βασιζόμενων στην ανάλυση οριακής ισορροπίας προκειμένου να αναγνωρισθούν οι μηχανισμοί αστοχίας ενός τόξου φερόμενου επί αψιδοστατών, καθώς και να εξετασθεί η λικνιστική απόκριση όταν αυτό υποβάλλεται σε εξιδανικευμένους παλμούς

δ) η διερεύνηση της αλληλεπίδρασης εδάφους-κατασκευής

Προς τον σκοπό αυτό τρεις βασικές τοξωτές κατασκευές θα διερευνηθούν διεξοδικά:

- Το τόξο στην απλούστερη μορφή του που εδράζεται ελεύθερα σε άκαμπτη και επιταχυνόμενη βάση. Λαμβάνονται υπόψη δύο διαφορετικά γεωμετρικά προφίλ, το *κυκλικό* και το *υβριδικό ελλειπτικό-κυκλικό* που από εδώ και στο εξής θα αναφέρεται ως "*μερικώς ελλειπτικό*" (Σχήμα **3α**).
- Ο λίθινος κυλινδρικός θόλος που χάριν απλότητας προσομοιώνεται με επίπεδο τόξο (Σχήμα **3β**).
- Ο τυπικός κυλινδρικός θόλος με ομοιόμορφη κυκλική διατομή στηριζόμενο σε αψιδοστάτες που περιβάλλεται από έδαφος (Σχήμα **3γ**).

Προς επίτευξη των σκοπών της μελέτης, οι ακόλουθες μέθοδοι ανάλυσης θα εφαρμοσθούν:

- Αναλυτικές μέθοδοι που ενσωματώνουν την Ανάλυση Οριακής Ισορροπίας (Limit Equilibrium Analysis). Αρχικά, η *ανάλυση οριακής ισορροπίας* βασιζόταν στον προσδιορισμό της οριακής γραμμής ώθησης (line of thrust) δηλαδή στον γεωμετρικό τόπο των σημείων από τα οποία διέρχεται η συνισταμένη των εσωτερικών δυνάμεων για δεδομένη φόρτιση και απεικονίζει ουσιαστικά την πορεία των φορτίων μέχρι τις στηρίξεις. Η γεωμετρική αυτή μέθοδος χρησιμοποιείτο ευρέως στις μελέτες ισορροπίας τόξου αλλά η περίπλοκη φύση της την καθιστούσε χρονοβόρα. Προσφάτως, ερευνητές ανέπτυξαν μια ενεργειακή προσέγγιση του προβλήματος της ευστάθειας ενός τόξου χρησιμοποιώντας την αρχή της στάσιμης δυναμικής ενέργειας (principle of stationary potential energy) (Αλεξάκης και Μακρής 2013, 2014, 2015, 2017, 2018). Άλλες αναλυτικές μέθοδοι περιλαμβάνουν: α) την κατά Lagrange κατάστρωση των εξισώσεων κινήσεως, ένα βολικό εργαλείο για την

ανάλυση του δυναμικού συστήματος, β) ένα λογισμικό γενικής χρήσης για μαθηματικές εφαρμογές (Mathematica) που χρησιμοποιείται περιστασιακά και γ) μια αρχετυπική εξίσωση της μη-γραμμικής θεωρίας κραδασμών (γραμμική συνήθης διαφορική εξίσωση δευτέρας τάξεως που ονομάζεται συνάρτηση Mathieu).

- Η αριθμητική ανάλυση ευοδούται με την αριθμητική μέθοδο των πεπερασμένων στοιχείων (Abaqus). Δισδιάστατα και τρισδιάστατα μοντέλα καταστρώνονται στο περιβάλλον Abaqus, ενώ οι αλγόριθμοι άρρητης και έμμεσης ολοκλήρωσης αντίστοιχα, χρησιμοποιούνται για τον υπολογισμό της γραμμικής, της μη γραμμικής στατικής και της δυναμικής απόκρισης του συστήματος.

a) Το τόξο σε άκαμπτη βάση

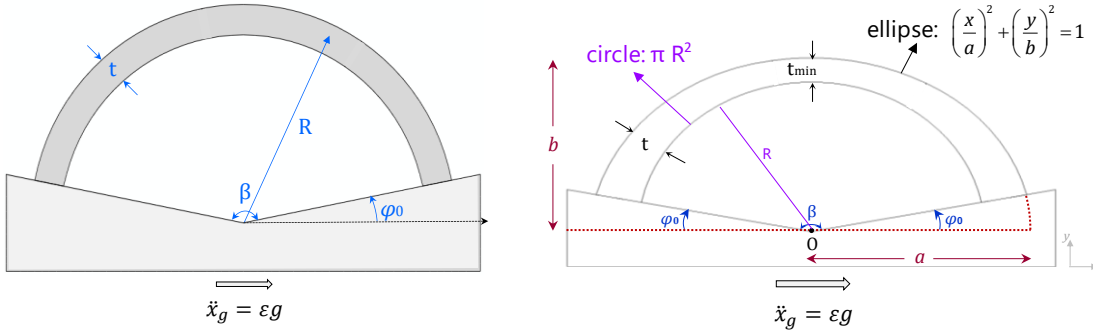

(i) *"μερικώς κυκλικό"* τόξο **(ii) *"μερικώς ελλειπτικό"* τόξο**

β) Τόξο επί αψιδοστατών

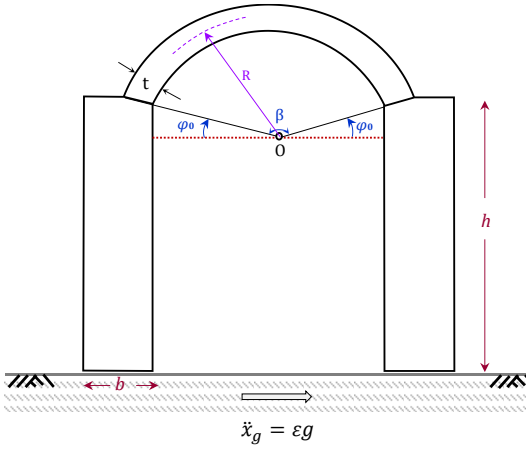

γ) Το εγκιβωτισμένο τόξο επί αψιδοστατών

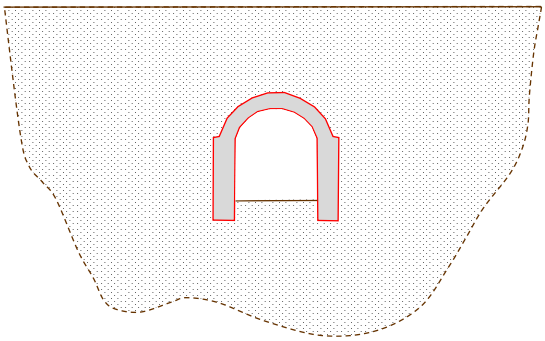

Σχήμα 3 Οι κύριες τοξωτές κατασκευές που μελετώνται σε αυτήν την διατριβή: (α) ένα τόξο κυκλικής και μερικώς ελλειπτικής γεωμετρίας που εδράζεται σε άκαμπτη βάση, (β) το τόξο επί αψιδοστατών εδραζόμενο σε άκαμπτη βάση, (γ) το εγκιβωτισμένο τόξο επί αψιδοστατών.

II. ΒΙΒΛΙΟΓΡΑΦΙΚΗ ΑΝΑΔΡΟΜΗ

Ο πατέρας Vicente Tosca, αρχιτέκτων, φιλόσοφος, μαθηματικός και αστρονόμος με σοφία είχε δηλώσει ότι: «Το λεπτότερο και πιο εξαίσιο μέρος της Αρχιτεκτονικής... είναι ο σχηματισμός κάθε είδους τόξων και θόλων» (μέρος της Compedio mathematico, 1707-1715) . Η τοξωτή λειτουργία ως μηχανισμός μεταφοράς φορτίου είναι εγγενής σε συστήματα συνεχούς ροής όπως δομικά (π.χ. τοίχος τοιχοποιίας με ανοίγματα) ή ακόμα και φυσικά (π.χ. εδαφικό μέσο). Οι 'πρωτο-μάστορες' της αρχαιότητας εξαρχής αντιλήφθηκαν αυτόν τον μηχανισμό και αναγνώρισαν τα πλεονεκτήματά του στην σχεδίαση ευρύτερων αλλά ταυτόχρονα υπερφορτωμένων ανοιγμάτων. Κάτω από αυτή την προοπτική, επινόησαν δομικές μορφές είτε μονοδιάστατες, αξονικού τύπου (τόξα), είτε δισδιάστατες, τύπου κελύφους (θόλοι, τρούλοι), στις οποίες η τοξωτή λειτουργία είναι ο κυρίαρχος μηχανισμός μεταφοράς φορτίου.

Δύο αρχέτυπα *κάλυψης ενός ανοίγματος* με εκτροπή της διαδρομής κατακόρυφου φορτίου είναι: (α) δοκός επί στύλων (the post and lintel system), και (β) το εκφορικό (ή ψευδές) τόξο (corbel arch). Οι λίθινες κατασκευές που απεικονίζονται στο **Σχήμα 4** είναι εμφανή παραδείγματα αυτών των δομικών μορφών που έθεσαν την βάση για την εξέλιξη της κάλυψης ενός ανοίγματος. Το τελευταίο μπορεί να θεωρηθεί ως πρωτοπόρος του αρχιτεκτονικού λίθινου τόξου με ακτινωτούς αρμούς.

Σχήμα 4 Παραδείγματα ενός συστήματος δοκός επί στυλών (α'- η Πύλη των Λεόντων στις Μυκήνες) και ενός εκφορικού τόξου (β'- το ιερό του Ηρακλή στην Δήλο).

Η εμφάνιση της Αρχιτεκτονικής των Καμπυλών χρονολογείται πίσω στα προϊστορικά χρόνια. Λίθινα τόξα ανεγέρθηκαν στην Βαβυλώνα πριν από περίπου 6000 χρόνια. Εξαιρετικά παραδείγματα θολωτών τάφων είναι οι βασιλικοί θολωτοί τάφοι στην Μεσοποταμία που χρονολογούνται στο 3000 π.Χ. και στην Ελλάδα που χρονολογούνται το 1250 π.Χ. (τάφος του Αγαμέμνονα). Θολωτές κατασκευές στην Ελλάδα χρησίμευαν ως είσοδοι σε αρχαία στάδια ή θέατρα (θολωτή δίοδος ή κρυπτή είσοδος του σταδίου της αρχαίας Νεμέας, η θολωτή σήραγγα του σταδίου της αρχαίας Ολυμπίας και η θολωτή δίοδος στο θέατρο της αρχαίας Σικυώνας).

Η πρώτη προσέγγιση της μηχανικής συμπεριφοράς του τόξου αποδόθηκε στον Leonardo da Vinci (1451-1519). Στο βιβλίο του ο Marcolongo αποδίδει στον da Vinci την εξής φράση: «...το τόξο δεν είναι παρά μια δύναμη που δημιουργείται από δύο αδυναμίες...". Το πείραμα που διεξήχθη σε ένα τόξο από όπου προέκυψε το κριτήριο ασφάλειας και ο κανόνας αστοχίας. Το 1675, ο Robert Hooke έδωσε μια διορατική ερμηνεία της ισορροπίας του λίθινου τόξου: «...όπως κρέμεται ένα εύκαμπτο καλώδιο, έτσι, αλλά ανεστραμμένο, θα σταθεί το τόξο». Από τις πρώτες κιόλας επιστημονικές μελέτες διατυπώθηκε η ευστάθεια των τοξωτών κατασκευών ως *γεωμετρικό πρόβλημα* και όχι ως πρόβλημα αντοχής των υλικών. Ο De la Hire (1695) για να εκτιμήσει την ευστάθεια του τόξου επινόησε το σχοινοπολύγωνο δυνάμεων (funicular polygon). Ο Couplet (1729) διαπίστωσε πως η ισορροπία επιτυγχάνεται όταν η γραμμή ώθησης βρίσκεται μέσα στο τόξο, ενώ η κατάρρευση επέρχεται μόλις η γραμμή ώθησης τμήσει τις εξωτερικές καμπύλες. Η θεωρία του Coulomb (1773) όμως επισημαίνει ότι πρέπει να εξεταστούν γειτονικοί αποδεκτοί μηχανισμοί και ότι η αστοχία του τόξου συμβαίνει μόνο με τον σχηματισμό αρθρώσεων στους αρμούς των θολιτών. Αρκετά χρόνια αργότερα ο Milankovitch (1907), επανεξέτασε την θεωρία της γραμμής ώθησης και εξήγαγε μια κλειστή τύπου εξίσωση. Επίσης, υπολόγισε ορθώς το ελάχιστο επιτρεπτό πάχος του τόξου (t / R = 0.1075). Μια πολύ σημαντική διαπίστωση έγινε από τους Pippard and Baker (1943) που κατέληξαν πως για να μετατραπεί το τόξο σε μηχανισμό πρέπει να σχηματιστούν τέσσερις αρθρώσεις. Ο Kooharian (1952) οδήγησε την έρευνα στην χρήση μεθόδων οριακής ισορροπίας στα πρότυπα της πλαστικής ανάλυσης των μεταλλικών κατασκευών η

οποία θα μπορούσε να εφαρμοστεί και σε άλλες κατασκευές. Ο Heyman (1969) εφάρμοσε αυτήν την θεωρία στους λίθινους θολίτες και έθεσε επίσης τρεις θεμελιώδεις παραδοχές σχετικά με τις ιδιότητες των υλικών των λίθων: (α) άπειρη αντοχή σε συμπίεση, (β) μηδενική αντοχή εφελκυσμού, και (γ) μεγάλος συντελεστής τριβής στην διεπιφάνεια για την αποφυγή της ολίσθησης. Οι Αλεξάκης και Μακρής (2013, 2014, 2017, 2018) διερεύνησαν διεξοδικά την σταθερότητα ενός μονολιθικού τόξου διαφορετικών γεωμετριών με μη προκαθορισμένες θέσεις των αρθρώσεων. Για τον υπολογισμό των θέσεων καθώς και του ελάχιστου επιτρεπτού πάχους, εισήγαγαν τον λογισμό των μεταβολών (variational formulation) στην αρχή της στάσιμης δυναμικής ενέργειας. Ένα αυξανόμενο ενδιαφέρον για την θεωρία της οριακής ανάλυσης στην ευστάθεια των τόξων έχει παρατηρηθεί προσφάτως στην βιβλιογραφία (Dimitri, 2015; Cavalagli, 2017; Di Carlo, 2018; Zampieri, 2017; Stockdale, 2019, 2020).

Ο Oppenheim (1992) στην αξιοσημείωτη και πρωτοπόρα εργασία του μελέτησε την δυναμική συμπεριφορά του λίθινου τόξου που μετατρέπεται σε μηχανισμό τεσσάρων αρθρώσεων όταν στην βάση ασκείται η κρίσιμη εδαφική επιτάχυνση. Ο επικρατών μηχανισμός αστοχίας περιγράφεται από την εξίσωση κίνησης η οποία εξάγεται από την εξίσωση Lagrange. Συνεχιστές υπήρξαν αρκετοί μελετητές όπως ο Clemente (1998), Ochsendorf (2002), De Lorenzis, 2007; Dimitrakopoulos, 2013; De Santis, 2014; Gaetani, 2017; Leontari, 2018; Kollar, 2019)

III. Γραμμική Απόκριση Τοξωτών Κατασκευών υποκείμενες σε παλμικές διεγέρσεις

Αρχικώς μελετάται το λίθινο τόξο, με όψη που περιγράφεται από ομόκεντρα κυκλικά τμήματα. Χάριν απλότητας, εφεξής θα περιγράφεται ως *κυκλικό τόξο*. Η άκαμπτη αυτή κατασκευή, υπό οριζόντια επιτάχυνση στην βάση της μετατρέπεται σε έναν λικνιστικό μηχανισμό τεσσάρων αρθρώσεων. Κρούσεις μπορεί να συμβούν μόνο στα τέσσερα σημεία περιστροφής (Α, Β', Γ', Δ) όπου σχηματίζονται αρθρώσεις σε προκαθορισμένες θέσεις. Ο επικρατών μηχανισμός σύμφωνα με τον Oppenheim (1992) σκιαγραφείται στο **Σχήμα 5** και είναι αυτός που αποδίδει την χαμηλότερη

δυνατή οριζόντια εδαφική επιτάχυνση που απαιτείται για να τεθεί το τόξο σε ταλάντωση. Τα γεωμετρικά χαρακτηριστικά του προσομοιώματος είναι τα εξής: α) η γωνίας περισφίξεως $\beta = 157.5°$, β) η μέση ακτίνα R = 10m, και γ) η αναλογία t / R = 0.15. Για τις μηχανικές ιδιότητες του υλικού μιας λίθινης τοξωτής κατασκευής υιοθετούνται οι παραδοχές του Heyman, 1966: έχει άπειρη αντοχή σε θλίψη, μηδενική αντοχή σε εφελκυσμό και μεγάλο συντελεστή τριβής ώστε να αποφευχθεί η ολίσθηση κατά την ταλάντωση. Κατά τη δυναμική κίνηση, ένα σημείο άρθρωσης μπορεί να κινείται κατά μήκος του άξονα του τόξου, επομένως αναπτύσσονται διαφορετικοί στιγμιαίοι κινηματικοί μηχανισμοί.

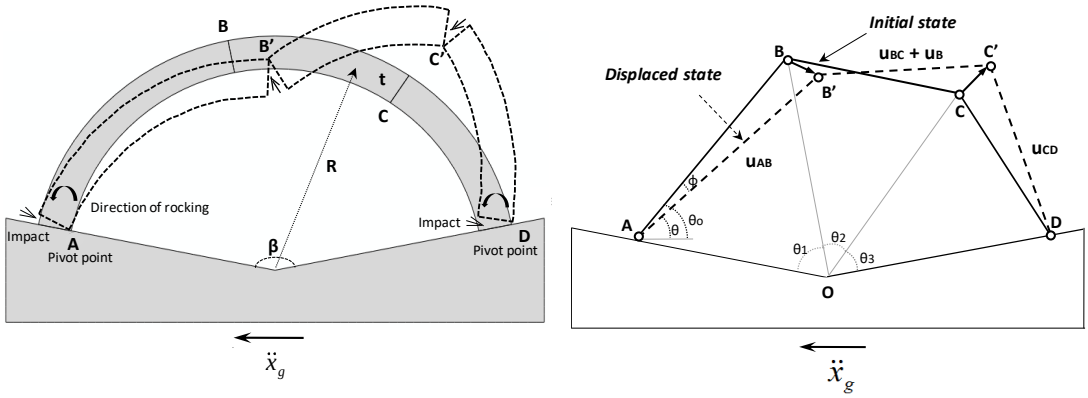

Σχήμα 5 Το λίθινο τόξο σε διεγειρόμενη άκαμπτη βάση ως μηχανισμός τεσσάρων αρθρώσεων που σχηματίζονται στα σημεία A, B', C, D (αριστερή μεριά); τα είδη των κινήσεων που κάνει ο κάθε σύνδεσμος με σημειωμένες τις βασικές παραμέτρους του προβλήματος που είναι οι επιμέρους γωνίες περισφίξεως θ_i (i = 1, 2, 3), η στροφή θ του μετατοπισμένου συνδέσμου AB με την οριζόντιο, η στροφή κατά την αρχική του κατάσταση θ_0, και η στροφή φ ως η διαφορά των δυο καταστάσεων ($\varphi = \theta_0 - \theta$) (αριστερή μεριά).

Η απόκριση ενός τόσο περίπλοκου δυναμικού μη γραμμικού συστήματος διερευνάται χρησιμοποιώντας τις ακόλουθες διαδικασίες ανάλυσης: (α) αναλυτικές ή ημι-αναλυτικές μεθόδους και, (β) αριθμητικές μεθόδους με πεπερασμένα στοιχεία. Αναφορικά με το (α), υιοθετείται η μέθοδος Lagrange για την εξαγωγή της εξίσωσης κίνησης η οποία απλοποιείται στην γραμμικοποιημένη της μορφή. Όποτε μια λύση κλειστής μορφής της εξίσωσης κίνησης δεν είναι εφικτή, ένα λογισμικό για μαθηματικές εφαρμογές ("Mathematica") χρησιμοποιείται για τον υπολογισμό της απόκρισης. Αναφορικά με το (β), επιλέχθηκε ο εξελιγμένος κώδικας πεπερασμένων στοιχείων *''Abaqus''*. Η αριθμητική επίλυση των εξισώσεων πραγματοποιήθηκε με βήμα-προς-βήμα εν-χρόνω ολοκλήρωση, μέσω της μεθόδου άμεσης διατύπωσης

(explicit algorithm). Κατά την ανάλυση οι θέσεις των αρθρώσεων θεωρήθηκαν προκαθορισμένες και τα στοιχεία από τα οποία αποτελείται το μοντέλο, επίπεδης παραμόρφωσης. Οι ιδιότητες του υλικού, όπως το μέτρο ελαστικότητας (*E*) και η πυκνότητα (*ρ*) έχουν τις εξής τιμές. Για τα τμήματα του τόξου, *E* = 10 GPa, *ρ* = 2.2 t/m^3 ενώ για την άκαμπτη βάση, *E* = 30 GPa, *ρ* = 2.5 t / m^3). Η ολίσθηση στις διεπιφάνειες αποφεύγεται με την υψηλή τιμή του συντελεστή τριβής (*μ* = 0.7). Ο βασικός ρόλος της ανάλυσης πεπερασμένων στοιχείων είναι να αξιολογήσει την αποτελεσματικότητα των μεθόδων γραμμικοποίησης για την μη γραμμική απόκριση.

Τεχνικές απλοποίησης της Εξίσωσης Κίνησης. - Για το εξεταζόμενο μονοβάθμιο σύστημα η γωνία $\theta = \theta_{AB} = \theta_0$ επιλέγεται ως η ανεξάρτητη μεταβλητή της εξίσωσης Lagrange. Η γενική μορφή της είναι:

$$M(\theta)\ddot{\theta} + L(\theta)\dot{\theta}^2 + F(\theta)g = P(\theta)\ddot{x}_g \quad (1)$$

όπου οι συντελεστές $M(\theta)$, $L(\theta)$, $F(\theta)$, $P(\theta)$ είναι μη γραμμικές εξισώσεις της θ.

Αναδιατυπώνοντας την (1):

$$\ddot{\theta} + b(\theta)\dot{\theta}^2 = c(\theta)g + d(\theta)\ddot{x}_g \quad (2)$$

όπου $b(\theta) = L(\theta)/M(\theta)$, $c(\theta) = F(\theta)/M(\theta)$ και $d(\theta) = P(\theta)/M(\theta)$.

Η εξίσωση 1 είναι έγκυρη μόνο όταν η $\theta < \theta_0$. Κατά αυτόν τον τρόπο οι υπολογισμοί της γωνίας αυτής περιορίζονται στην κατάσταση πριν την κρούση. Μετά από μια σειρά υπολογισμών και απλοποιήσεων η εξίσωση κίνησης μπορεί να γραφτεί ως μια γραμμική διαφορική εξίσωση 2^{ου} βαθμού:

$$\ddot{u}(t) - b\big(|c|g + d\,\ddot{x}_g\big)u(t) = 0 \quad (3)$$

Η εξίσωση κίνησης ως προς την *φ*.-

$$2\ddot{\varphi} - b\dot{\varphi}^2 - c\varphi - h = 0 \quad (4)$$

Η γενική λύση της εξίσωσης (4) παρουσιάζεται μετά και χαρακτηρίζεται ως μια διαφορική εξίσωση ως προς τις μεταβλητές του χώρου των φάσεων $(\dot{\varphi}, \varphi)$.

$$\dot{\varphi}^2 = \frac{c + bh}{b^2}\left(e^{b\varphi} - 1\right) - \frac{c\varphi}{b} \quad (5)$$

Έναρξη της κίνησης του μηχανισμού. – Το εύρος της εδαφικής επιτάχυνσης που απαιτείται για να μετατραπεί το τόξο σε μηχανισμό τεσσάρων αρθρώσεων εξάγεται από την εξίσωση (1) εφαρμόζοντας το κριτήριο για την έναρξη του λικνισμού: $\ddot{\varphi} = \dot{\varphi} = 0$. Επομένως, για εδαφική επιτάχυνση μεγαλύτερη από $|\ddot{x}_g| = \frac{F(\varphi)}{P(\varphi)} > 0.37g$ οι αναπτυσσόμενες αδρανειακές δυνάμεις λικνίζουν το τόξο. Από αυτό το σημείο και μετά, η ισορροπία είναι ασταθής και η κατάρρευση επίκειται. Ωστόσο, υπάρχει ένα κρίσιμο σημείο που ο Oppenheim το ονόμασε σημείο «μη ανακτήσεως» ($\varphi_{N\text{-}R}$), καθώς καθορίζει εάν η κατασκευή θα επιστρέψει στην αρχική της θέση (περιοχή ανάκτησης όπου $\varphi < \varphi_{N\text{-}R}$) ή τελικά θα καταρρεύσει (περιοχή μη ανάκτησης όπου $\varphi > \varphi_{N\text{-}R}$) (**Σχήμα 6**). Για στροφή λικνισμού μεγαλύτερη από φ = 0.07 rad, η βαρυτική δύναμη αποκτά αποσταθεροποιητικό ρόλο αφού από δύναμη επαναφοράς μετατρέπεται σε δύναμη ανατροπής (αποκτά αρνητικό πρόσημο όταν $\varphi > \varphi_{N\text{-}R}$). Αντίθετα, από τον συντελεστή *P(φ)* προκύπτει ότι η επιτάχυνση του εδάφους αποσταθεροποιεί το σύστημα εξαρχής, έχοντας σχεδόν γραμμική σε σχέση με την στροφή φ.

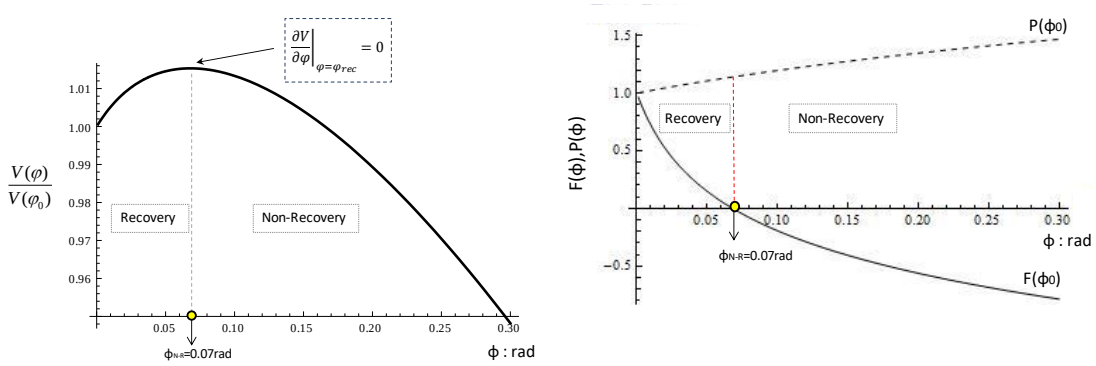

Σχήμα 6 Η δυναμική ενέργεια κανονικοποιημένη ως προς την μέγιστη τιμή της ($V(\varphi)/V(\varphi_0)$), οι δύο περιοχές ισορροπίας (recovery) και ανατροπής (non-recovery) που ορίζονται από το σημείο *''μη-ανακτήσεως της ισορροπίας''* $\varphi_{N\text{-}R}$ =0.07 rad (πάνω σχήμα); ο συντελεστής $F(\theta)$ που αντιπροσωπεύει τις γενικευμένες βαρυτικές δυνάμεις σε κάθε μετατοπισμένη θέση του τόξου και ο συντελεστής $P(\theta)$ που αντιπροσωπεύει τις εξωτερικές δυνάμεις ως προς την στροφή φ (κάτω σχήμα).

Παλμός σταθερής επιτάχυνσης $\ddot{x}_g = -\lambda\, g$. - Η λύση της εξίσωσης (3) είναι:

$$u(t) = c_2\, cos\left(\sqrt{b\tilde{c}}\,(t - c_1)\right) \qquad (6)$$

Η λύση ως προς την γωνία θ(t) δίδεται:

$$\theta(t) = c_2 + \frac{\log(\cos(\sqrt{b\tilde{c}}\,(t - c_1))}{b} \qquad (7)$$

Από την οποία προκύπτει το διάγραμμα του **Σχήματος 7** εξάγοντας το συμπέρασμα πως όσο πιο δυνατή η ώθηση τόσο πιο γρήγορα οδηγείται το τόξο στην ανατροπή.

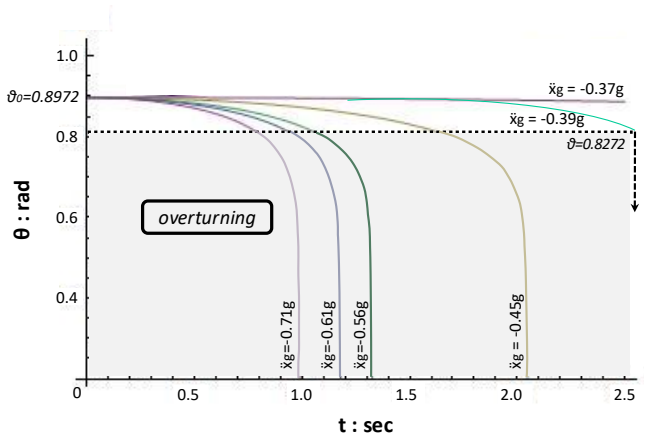

Figure 7 Χρονοϊστορία της γωνίας θ_{AB} για διάφορα επίπεδα εδαφικής διέγερσης. Η αρχική γωνία του συνδέσμου AB είναι $\theta_0 = 0.8972\,rad$, και συνεπώς το σημείο εκκίνησης όλων των καμπυλών. Η γωνία στην παραμορφωμένη κατάσταση $\theta_{min} = 0.8272 rad$ με μαύρη διακεκομμένη γραμμή. Καμπύλες που τέμνουν αυτή την γραμμή (π.χ. $|\ddot{x}_g|$ = 0.39 g, 0.45 g, 0.56 g, 0.61 g, 0.71 g) αντιπροσωπεύουν τόξα που καταρρέουν καθώς η γωνία θ λαμβάνει τιμές μικρότερες από την κρίσιμη τιμή. Σε αντίθεση, η καμπύλη 0.37 g αντιπροσωπεύει ένα λικνιζόμενο τόξο σε οριακή ισορροπία.

Παλμός ημιτόνου ενός κύκλου.- Εάν στην εξίσωση (3) θέσουμε την εξίσωση του ημιτονοειδούς παλμού προκύπτει:

$$\ddot{u}(t) - b\big(|c|g - da_p \sin(\omega\, t)\big)u(t) = 0 \qquad \text{όπου} \qquad \omega\, t = 2x + \frac{\pi}{2} \qquad (8)$$

Και από την εξίσωση (7) παράγεται μια γραμμική δευτέρας τάξεως ομοιογενής διαφορική εξίσωση γνωστή από την βιβλιογραφία ως “Mathieu Equation” [Εξ.(8)].

$$\ddot{u}(x) + (A - 2Q\cos(2\,x))u(x) = 0 \qquad (9)$$

Κάνοντας χρήση της εξίσωσης (8) προκύπτει το διάγραμμα του **Σχήματος 8**. Η επιζήμια επίδραση της αυξανόμενης a_p είναι προφανής καθώς υψηλότερες τιμές οδηγούν ταχύτερα το τόξο σε ανατροπή.

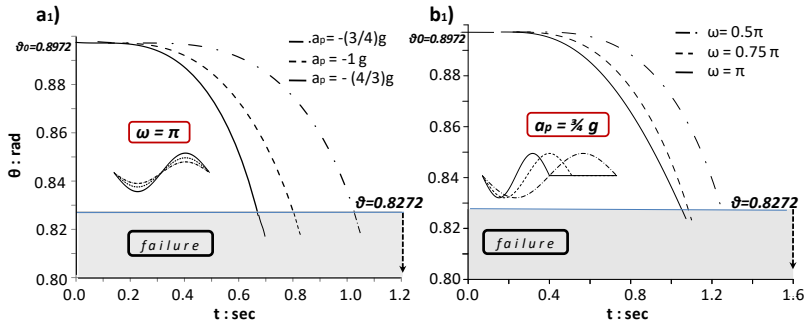

Σχήμα 8 Επίδραση του εύρους της επιτάχυνσης a_p (a_1) και της συχνότητας ω_p (b_1) στην λικνιστική απόκριση. Η περιοχή κατάρρευσης σκιαγραφείται με γκρι χρώμα και διαχωρίζεται από την υπόλοιπη περιοχή του διαγράμματος με μια μπλε γραμμή που αντιστοιχεί στην οριακή τιμή της γωνίας θ = 0.8272 rad.

Οι χρονοϊστορίες της γωνίας θ_{AB} για διάφορες ημιτονοειδείς διεγέρσεις με περίοδο που κυμαίνεται από T_p = 0.75 sec μέχρι 4sec παρουσιάζονται στο **Σχήμα 9**. Η μελέτη της απόκρισης είναι εφικτή μόνο μέχρι την πρώτη κρούση. Τα αποτελέσματα που εξάγονται από την εξίσωση Mathieu συγκρίνονται με αυτά άλλων δύο μεθόδων: α) μίας ημι-αναλυτικής μεθόδου, στην οποία η γραμμική εξίσωση (9) επιλύεται επαναληπτικά μέσω ενός κώδικα αριθμητικής επίλυσης διαθέσιμου στην Mathematica, b) διδιάστατης ανάλυσης πεπερασμένων στοιχείων χρησιμοποιώντας τον κώδικα. Η σύγκριση μεταξύ των τριών μεθόδων αποδεικνύεται αξιοσημείωτα καλή υποδεικνύοντας την εγκυρότητα των μεθόδων γραμμικοποίησης.

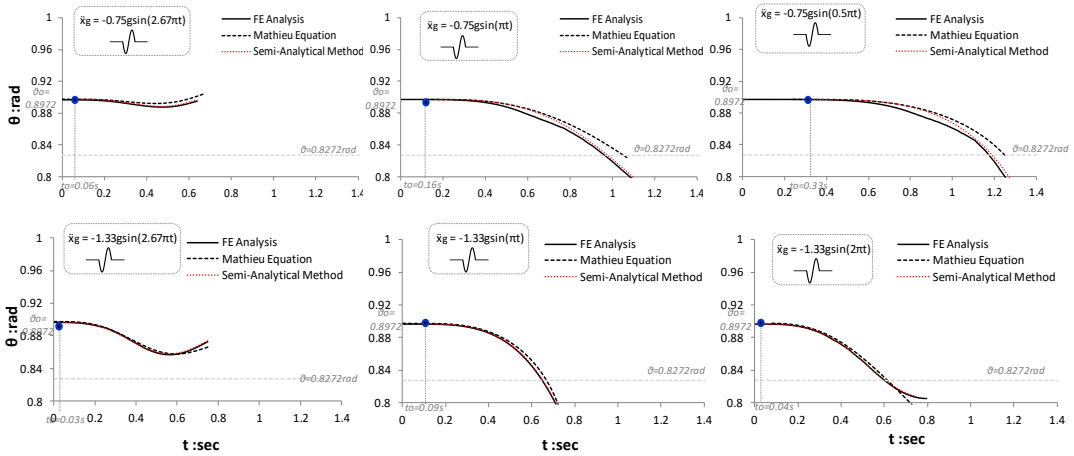

Σχήμα 9 Χρονοϊστορίες της γωνίας θ_{AB} που αντιστοιχούν σε ημιτονοειδείς παλμούς: (γραμμή 1) a_p = -0.75 g, T_p = 0.75, 2, 4 sec; (γραμμή 2) a_p = -1.33 g, T_p = 0.75, 1, 2 sec; σύγκριση μεταξύ ανάλυσης πεπερασμένων στοιχείων και γραμμικοποιημένων αναλυτικών λύσεων (ημι-αναλυτική επίλυση της εξίσωσης (9) και κλειστής-μορφής επίλυση με την εξίσωση Mathieu).

Η απλοποιημένη ανάλυση της λικνιστικής απόκρισης με βάση την εξίσωση Mathieu χρησιμοποιείται στην συνέχεια, για περισσότερες τιμές του λόγου *t / R* (**Σχήμα 10**).

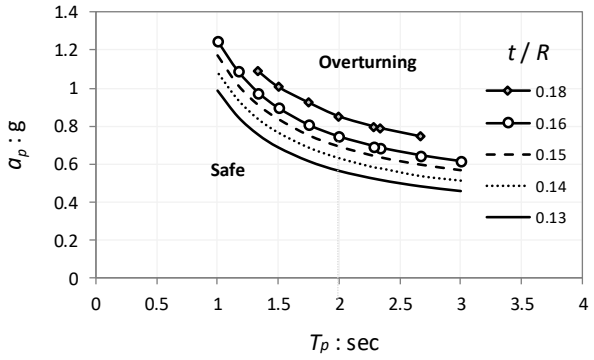

Σχήμα 10 Ασφαλής περιοχή και περιοχή ανατροπής που καθορίζεται όταν ημιτονοειδείς παλμοί διαφόρων ζευγών επιτάχυνσης (α_p)- περιόδου (T_p) διεγείρουν διαφορετικές γεωμετρίες τόξου (*t / R* =0.13-0.18). Η ασφαλής περιοχή αντιστοιχεί μόνο για το χρονικό διάστημα πριν την κρούση.

Ορθογωνικοί Παλμοί.- Τα αποτελέσματα που προέκυψαν με τις παραπάνω μεθόδους μαζί με τα αποτελέσματα που προέκυψαν από τον Oppenheim απεικονίζονται στο **Σχήμα 11**. Επιπλέον, η μέθοδος των πεπερασμένων στοιχείων μέσω του κώδικα Abaqus εφαρμόζεται για την αξιολόγηση αυτών των αναλυτικών λύσεων. Η σύγκρισή τους είναι ικανοποιητική.

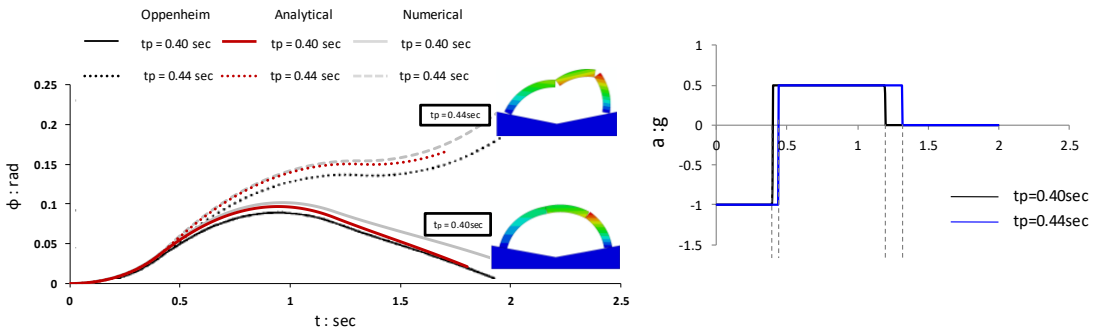

Σχήμα 11 Απόκριση του τόξου σε εξιδανικευμένους ορθογωνικούς παλμούς. Στην περίπτωση που η χρονική διάρκεια του παλμού είναι t_p = 0.40 sec (μαύρη γραμμή στο δεξί διάγραμμα), το τόξο αφού λικνίζεται για λίγο επιστρέφει στην αρχική του θέση (φ = 0). Αντιθέτως, όταν η χρονική διάρκεια του παλμού είναι t_p = 0.44 sec (μπλε γραμμή στο δεξί διάγραμμα) η στροφή φ αυξάνεται σταδιακά και το τόξο ανατρέπεται. Με συνεχείς γραμμές συμβολίζονται οι αποκρίσεις στον παλμό t_p = 0.40 sec ενώ με διακεκομμένες συμβολίζονται οι αποκρίσεις στον παλμό t_p = 0.44 sec. Η καμπύλες που φέρουν το μαύρο χρώμα αντιστοιχούν στα αποτελέσματα του Oppenheim, στο κόκκινο αντιστοιχούν τα αποτελέσματα της αναλυτικής λύσης και στο γκρι της μεθόδου των πεπερασμένων στοιχείων.

IV. Ευστάθεια και Λικνισμός Τοξωτών κατασκευών αναμοιόμορφης όψης: το μερικώς ελλειπτικό τόξο

Σε αυτό το κεφάλαιο η απόκριση ενός τόξου ανομοιόμορφου πάχους που υπόκειται σε λικνιστική ταλάντωση διερευνάται σε σύγκριση με ένα κυκλικό τόξο. Το εν λόγω '*μερικώς ελλειπτικό τόξο*' χαρακτηρίζεται από μια ελλειπτική καμπύλη στο εξωρράχιο και με μια κυκλική στο εσωρράχιο (**Σχήμα 12 αριστερά**). Αυτού του είδους η γεωμετρία απαντάται συχνά σε γέφυρες μεγάλου ανοίγματος. Εν συνεχεία, η ανάλυση ευστάθειας υπό στατικούς όρους διερευνάται μέσω του λογισμού των μεταβολών και της μεθόδου Lagrange (**Σχήμα 12 δεξιά**). Οι εν χρόνω αναλύσεις της απόκρισης διενεργούνται μέσω της αναλυτικής προσέγγισης και της μεθόδου των πεπερασμένων στοιχείων. Ο σκοπός αυτού του κεφαλαίου είναι διττός: από την μία η επίδραση που έχει η κατ' ελάχιστον μεταβολή της γεωμετρίας ενός κυκλικού τόξου καθώς και η αξιοπιστία των προτεινόμενων αναλυτικών μεθόδων με κριτήριο την απόκλιση από την μέθοδο των πεπερασμένων στοιχείων.

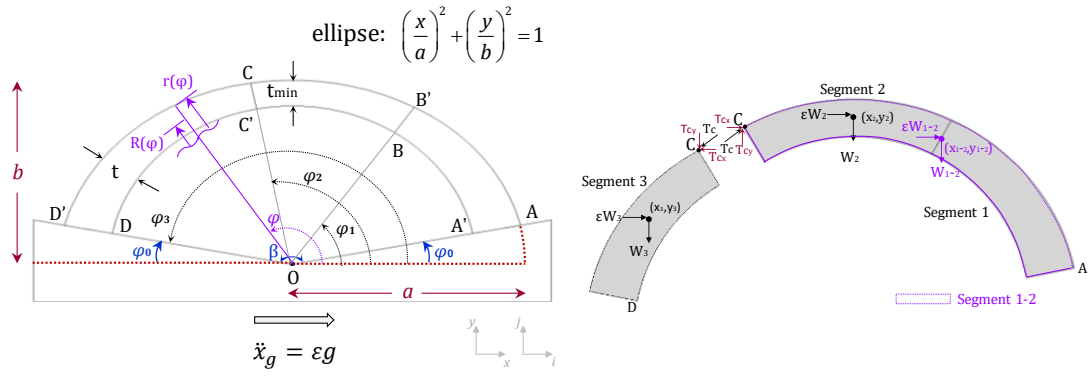

Σχήμα 12 Αριστερά: Σχηματική αναπαράσταση του μερικώς ελλειπτικού τόξου μεταβαλλόμενης ακτίνας $R(\varphi)$, αυξανόμενου πάχους t ξεκινώντας από μια ελάχιστη τιμή t_{min} στην στέψη του και οι γεωμετρικές παράμετροι της έλλειψης $a > b > R(\varphi)$. Η άρθρωση A σχηματίζεται στην εξωτερική μεριά της δεξιάς γένεσης του τόξου, στην θέση $\varphi_o = (\pi-\beta)/2$, η άρθρωση D σχηματίζεται στην εσωτερική μεριά της γένεσης, στην θέση $\varphi_3 = \pi - \varphi_o$. Οι αρθρώσεις B (θέση φ_1) και C (θέση φ_2) κείτονται στην εσωτερική και στην εξωτερική μεριά του τόξου αντίστοιχα. Δεξιά: Το μερικώς ελλειπτικό τόξο υπόκειται σε ανάλυση οριακής ισορροπίας. Το βάρος του κάθε τμήματος Wi (i=1, 2, 1-2), οι συντεταγμένες του K.B του κάθε τμήματος x_{cm}, y_{cm}. Οι καρτεσιανές συντεταγμένες της δύναμης ώθησης στην άρθρωση C, T_c (T_{c_x}, T_{c_y}).

Για δεδομένο λόγο *λ*(=*b* / a), διαπιστώθηκε ότι απαιτούνται υψηλότερες τιμές επιτάχυνσης για να τεθεί ένα μερικώς ελλειπτικό τόξο σε λικνιστική ταλάντωση σε σύγκριση με τις επιταχύνσεις που απαιτούνται για ένα κυκλικό (**Σχήμα 13**).

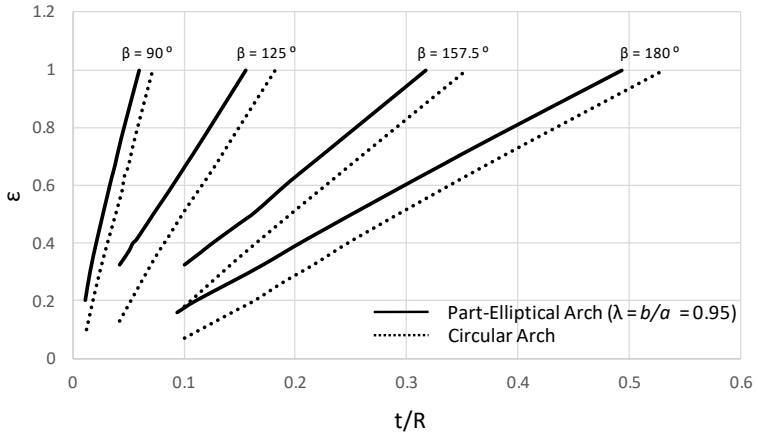

Σχήμα 13 Ο σεισμικός συντελεστής *ε* ενός κυκλικού και ενός μερικώς ελλειπτικού τόξου (λ = *b / a* = 0.95) ως προς την λυγηρότητα *t / R* για δεδομένες τιμές της γωνίας περισφίξεως *β* (90^0, 125^0, 157.5^0, 180^0).

Από το **Σχήμα 14** προκύπτει ότι ο λόγος *λ* (= *b / a*) είναι γραμμικός με την λυγηρότητα *t / R* για διαφορετικά επίπεδα του σεισμικού συντελεστή *ε*. Επιβεβαιώνεται ότι η αύξηση του πάχους του τόξου λειτουργεί ευνοϊκά στην σταθερότητα του συστήματος, μιας και απαιτούνται υψηλότερες τιμές επιτάχυνσης για να λικνιστεί. Επιπλέον, όταν συγκρίνουμε δύο τόξα της ίδιας λυγηρότητας *t / R* αλλά διαφορετικών γωνιών περισφίξεως *β* συμπεραίνεται ότι αυτό με την μεγαλύτερη *β* μετατρέπεται σε μηχανισμό τεσσάρων αρθρώσεων για μικρότερες επιταχύνσεις *ε g*.

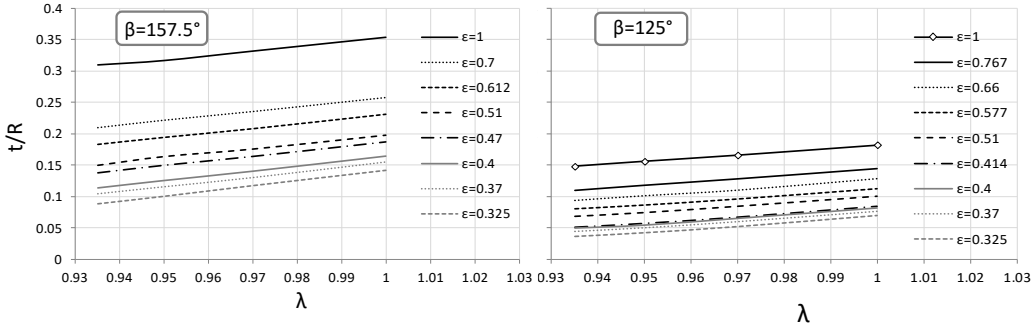

Σχήμα 14 Η ελάχιστη απαιτούμενη λυγηρότητα *t / R* ως συνάρτηση του λόγου λ = *b / a* για διαφορετικά επίπεδα της οριζόντιας επιτάχυνσης ανατροπής $\ddot{x}_g = \varepsilon\, g$. Λαμβάνονται υπόψιν δύο διαφορετικές γωνίες περισφίξεως, *β* = 157.5^0 (αριστερό διάγραμμα) και *β* = 125^0 (αριστερό διάγραμμα).

Αστοχία του τόξου ως μηχανισμού τεσσάρων αρθρώσεων. – Τα υπό εξέταση τόξα (κυκλικό και μερικώς ελλειπτικό) έχουν τα παρακάτω γεωμετρικά χαρακτηριστικά: β = 157.5°, t / R = 0.194, η μέση ακτίνα R (R = 10 m), το πάχος t (t / R = 0.194 => t = 1.94 m), η εσωτερική ακτίνα b (b = R + $t/2$ = 10.971 m) που ταυτίζεται για τα δύο τόξα, και επιπροσθέτως για το μερικώς ελλειπτικό ο λόγος λ (λ = b / a = 0.95) & a (a = b / λ = 10.971/0.95 = 11.5484). Οι κρίσιμες επιταχύνσεις για τις δύο γεωμετρίες προκύπτουν από το Σχήμα 14 (για το κυκλικό: $|\ddot{x}_g|$ = $F(\theta)$ / $P(\theta)$ = 0.51 g; για το μερικώς ελλειπτικό: $|\ddot{x}_g|$ = $F(\theta)$ / $P(\theta)$ = 0.61 g. Συγκρίνοντας τις δύο περιπτώσεις προκύπτει πως το τελευταίο προσφέρει ενισχυμένη αντίσταση στον λικνισμό. Αφ 'ετέρου, πλησιάζει στην αστοχία για μικρότερες στροφές από ότι το κυκλικό για δεδομένο λόγο t / R (ϕ_E = 0.20 rad ϕ_C = 0.20 rad). Όπως πολύ εύστοχα διατύπωσε ο Oppenheim (1992): *"΄΄ένα τόξο προβάλει αξιοσημείωτη αντίσταση στην έναρξη της κίνησης αλλά σχετικώς μικρή αντοχή στην απορρόφηση εξαναγκασμένων μετακινήσεων"*.

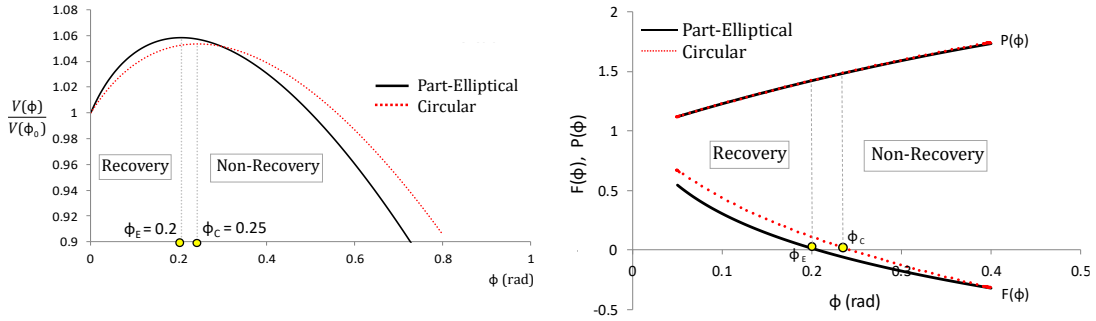

Σχήμα 15 Αριστερό Διάγραμμα: η δυναμική ενέργεια κανονικοποιημένη ως προς την μέγιστη τιμή της ($V(\varphi)$ / $V(\varphi_0)$), οι δύο περιοχές ισορροπίας (recovery) και ανατροπής (non-recovery) που ορίζονται από το σημείο *''μη-ανακτήσεως της ισορροπίας''* (φ_C = 0.25 rad για το κυκλικό τόξο, φ_E=0.20 rad για το μερικώς ελλειπτικό τόξο); Δεξί Διάγραμμα: ο συντελεστής $F(\theta)$ που αντιπροσωπεύει τις γενικευμένες βαρυτικές δυνάμεις σε κάθε μετατοπισμένη θέση του τόξου και ο συντελεστής $P(\theta)$ που αντιπροσωπεύει τις εξωτερικές δυνάμεις ως προς την στροφή φ για τα κυκλικά και μερικώς ελλειπτικά τόξα (κόκκινη διακεκομμένη και μαύρη συνεχής γραμμή αντίστοιχα).

Ανάλυση στο πεδίο του χρόνου: (1) Επίδραση της ανομοιόμορφης διατομής. - Η ανάλυση της δυναμικής απόκρισης πραγματοποιείται στο πεδίο του χρόνου μέσω αναλυτικών (εξίσωση κίνησης Lagrange) και αριθμητικών μεθόδων. Ως διέγερση στην βάση χρησιμοποιήθηκαν εξιδανικευμένοι παλμοί της εδαφικής κίνησης (κυρίως

τριγωνομετρικοί παλμοί ενός κύκλου και παλμοί τύπου Ricker). Από τα διαγράμματα του **Σχήματος 16** συμπεραίνεται ότι τα μερικώς ελλειπτικά τόξα λόγω της ελαφρώς διαφορετικής γεωμετρίας τους είναι πιο σταθερές κατασκευές από τα κυκλικά. Συγκεκριμένα, όσο πιο «ελλειπτική» είναι η επάνω καμπύλη τόσο λιγότερο επιρρεπές είναι το τόξο στην ανατροπή. Η ευστάθειά τους μειώνεται καθώς ο γεωμετρικός λόγος *λ* αυξάνεται έως την τιμή 1 όπου το τόξο γίνεται κυκλικό.

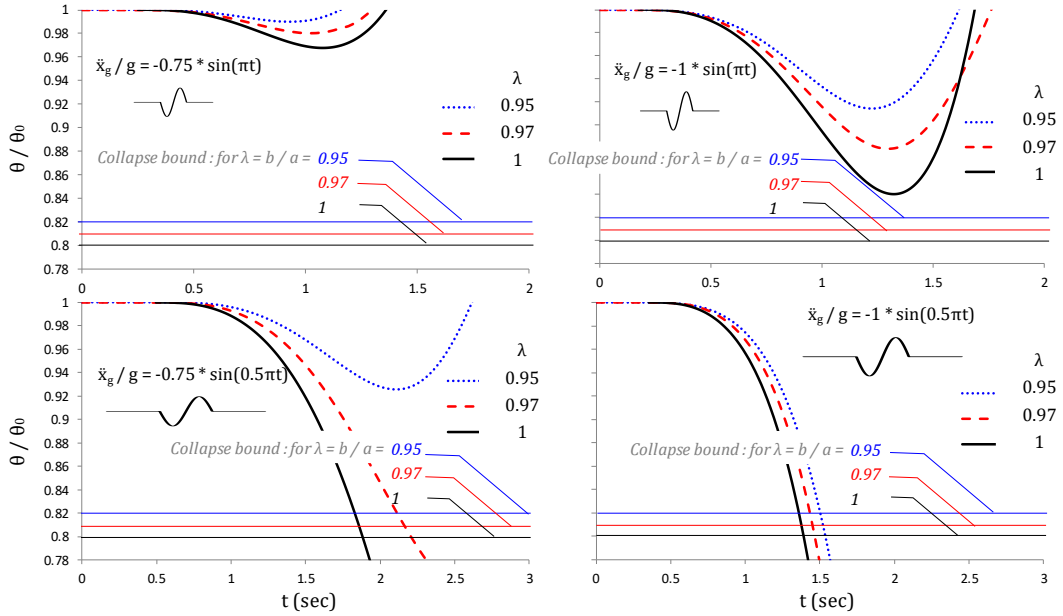

Σχήμα 16 Η επίδραση του γεωμετρικού λόγου, *λ* στην χρονοϊστορία της κανονικοποιημένης γωνίας *θ* όταν το τόξο υποβάλλεται σε διάφορους ημιτονοειδείς παλμούς. Τρεις διαφορετικές περιπτώσεις διερευνώνται: (α) για *λ* = 0.95 (μερικώς ελλειπτικό τόξο), (β) *λ* = 0.97 (μερικώς ελλειπτικό τόξο), και (γ) *λ* = 1 (κυκλικό τόξο). Τα όρια ανατροπής: με μπλε γραμμή για την περίπτωση (α), με κόκκινη γραμμή για την περίπτωση (β), και με μαύρη γραμμή για την περίπτωση (γ).

(2) Σύγκριση μεταξύ αναλυτικής και αριθμητικής λύσης. –Εκτός από την αναλυτική επίλυση του συστήματος, διενεργείται επίσης διδιάστατη αριθμητική ανάλυση με πεπερασμένα στοιχεία. Τα αποτελέσματα παρουσιάζονται συγκριτικά με αυτά της αναλυτικής μεθόδου για παλμούς μεγάλης διάρκειας. Και οι δύο μέθοδοι παρέχουν χρονοϊστορίες της δυναμικής απόκρισης, οι οποίες σε γενικές γραμμές βρίσκονται σε αξιοσημείωτη συμφωνία, γεγονός που υπογραμμίζει την αξιοπιστία και των δύο προσεγγίσεων. Αυτό είναι πολύ σημαντικό λαμβάνοντας υπόψη τις

ουσιαστικά διαφορετικές υποθέσεις που υιοθετούνται σε δύο προσεγγίσεις: Η αναλυτική μέθοδος θεωρεί ένα άκαμπτο, μονολιθικό τόξο μηδενικής εφελκυστικής αντοχής στο οποίο αποτρέπεται η ολίσθηση στις αρθρώσεις. Αντιθέτως, το αριθμητικό μοντέλο προσομοιώνει μια δύσκαμπτη κατασκευή αλλά όχι μια ιδεατά άκαμπτη, με προκαθορισμένο μηχανισμό αρθρώσεων, όπου οι διεπιφάνειες δεν είναι αρκετά τραχιές ώστε να αποτρέψουν την ολίσθηση.

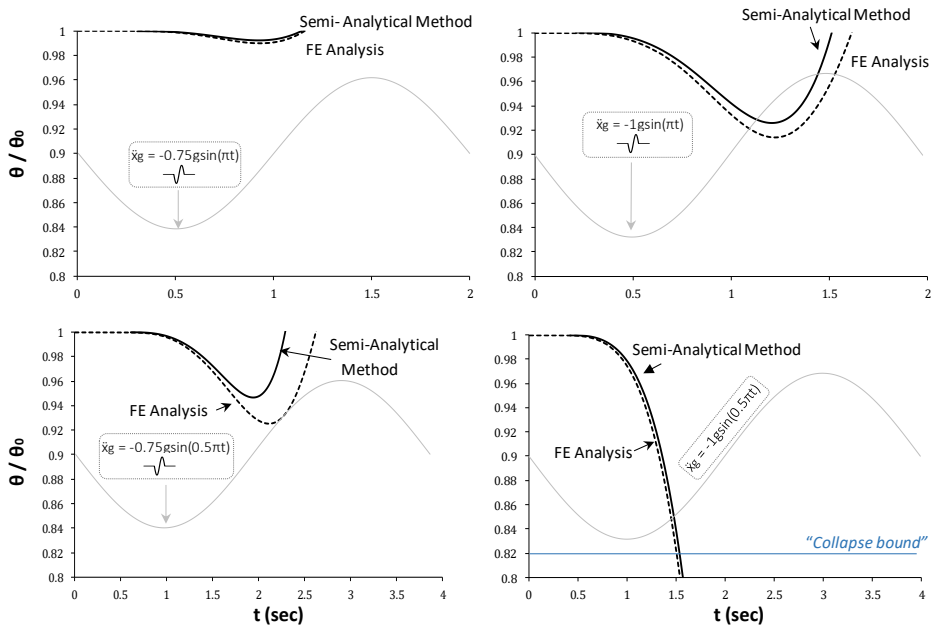

Σχήμα 17 Χρονοϊστορίες της κανονικοποιημένης γωνίας *θ* ενός μερικώς ελλειπτικού τόξου (*λ* = 0.95) που διεγείρεται από ημιτονικούς παλμούς στην βάση του (γκρι γραμμή). Σύγκριση μεταξύ της μεθόδου πεπερασμένων στοιχείων (διακεκομμένη γραμμή) και της ημι-αναλυτικής επίλυσης (συνεχής γραμμής). Το όριο ανατροπής σκιαγραφείται με μπλε γραμμή.

V. Λίθινα Τόξα επί αψιδοστατών

Ένα από τα θεμελιώδη στοιχεία πολλών μνημείων παγκοσμίως όπως οι λίθινες γέφυρες, τα υδραγωγεία, οι γοτθικοί καθεδρικοί ναοί, οι βυζαντινές εκκλησίες, και οι στοές μεταξύ άλλων είναι το λίθινο τόξο επί αψιδοστατών. Οι κεκλιμένες δυνάμεις ώθησης που ασκούν τα τόξα στις στηρίξεις τους μεταφέρονται στους αψιδοστάτες οι οποίοι συμβάλλουν ευνοϊκά στη σταθερότητα της κατασκευής καθώς μεταφέρουν αυτή την ώθηση στο έδαφος θεμελίωσης. Για την ακρίβεια της ανάλυσης της

ευστάθειας μέσω της κινηματικής θεωρίας απαιτείται η αναγνώριση των αρθρωτών μηχανισμών.

Ανάλογα με την γεωμετρία και συγκεκριμένα με την σχετική αναλογία τόξου-αψιδοστάτη, διακρίνονται οι ακόλουθοι μηχανισμοί αρθρώσεων στο **Σχήμα 18**, όπως αρχικά προτάθηκε από τον De Luca (2004): (i) Μηχανισμός I (Τοπικός ή αρθρωτός μηχανισμός) συνήθως απαντάται στην περίπτωση λεπτών τόξων που στηρίζονται σε παχύς αψιδοστάτες όπου όλες οι αρθρώσεις σχηματίζονται στο πιο ευάλωτο τμήμα, το τόξο, και καμία στους αψιδοστάτες, (ii) Μηχανισμός II (ημι-καθολικός ή υβριδικός Μηχανισμός) απαντάται όταν εκτός από το τόξο, στον αρθρωτό μηχανισμό συμμετέχει και ένας αψιδοστάτης. Συγκεκριμένα, η μία άρθρωση ανοίγει στην κάτω γωνία του αψιδοστάτη ενώ οι άλλοι τρεις κατά μήκος του τόξου, και (iii) Μηχανισμός III (καθολικός Μηχανισμός) απαντάται όταν αναπτύσσονται δύο αρθρώσεις στο τόξο και οι άλλες δύο σε κάθε αψιδοστάτη. Οι δύο τελευταίοι μηχανισμοί διαμορφώνονται συνήθως για παχιά τόξα και υψίκορμους αψιδοστάτες (ειδικότερα ο τελευταίος για ακόμη πιο υψίκορμους αψιδοστάτες και άρα πιο τρωτούς). Εάν η άρθρωση B ή D υπερβαίνει την γένεση του τόξου και σχηματίζεται εντός του αψιδοστάτη, τότε ενεργοποιείται ο Μηχανισμός IV (παραλλαγή του Μηχανισμού II). Σε αυτήν την περίπτωση όμως για την αποφυγή του εφαρμόζονται κατάλληλες οριακές συνθήκες. Αντιπροσωπευτικά παραδείγματα των άνωθεν κινηματικών μηχανισμών απεικονίζονται στο **Σχήμα 19** (Brandonisio 2017).

Οι Alexakis & Makris (2017, 2018) στις πρωτοποριακές τους εργασίες για τους κυλινδρικούς θόλους, τους οποίους κατά την ανάλυση της Οριακής Ισορροπίας θεώρησαν μονολιθικούς, υπολόγισαν με την εφαρμογή της αρχής της στάσιμης δυναμικής ενέργειας την ελάχιστη οριζόντια επιτάχυνση ανασηκώματος και τις θέσεις των τεσσάρων αρθρώσεων μηδενίζοντας τις μερικές παραγώγους της δυναμικής ενέργειας.

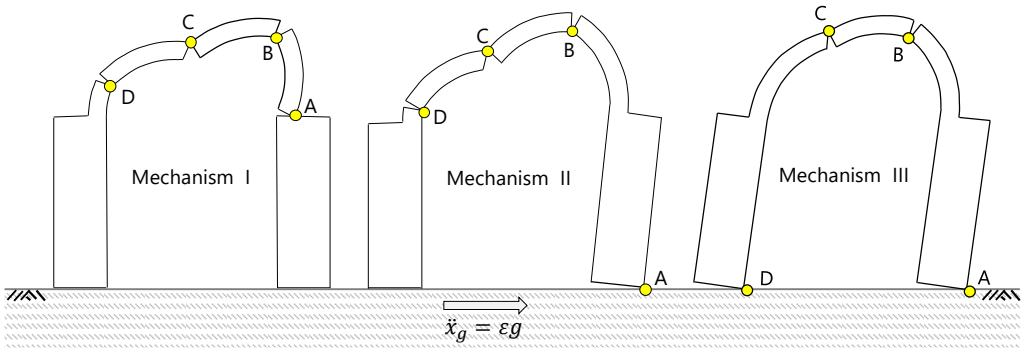

Σχήμα 18 Τρεις διαφορετικοί κινηματικοί μηχανισμοί (I, II, III) που είναι πιθανόν να ενεργοποιηθούν όταν μια εδαφική επιτάχυνση $\ddot{x}_g$ ασκείται την βάση τους από αριστερά προς τα δεξιά.

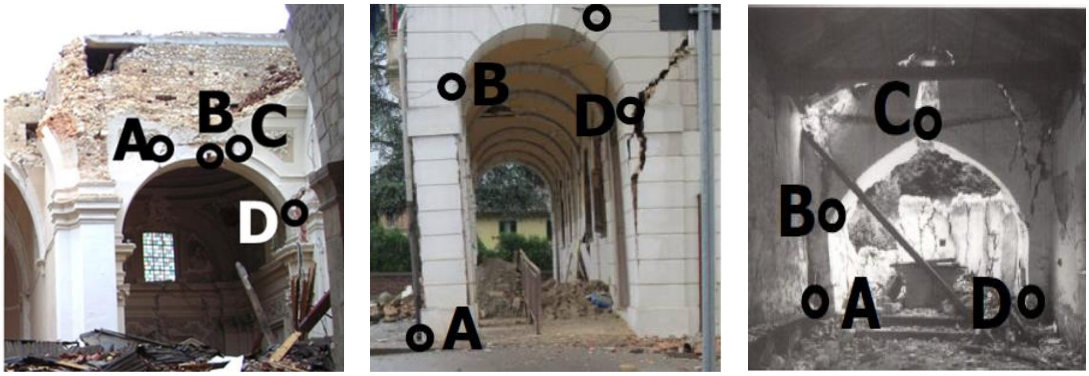

Σχήμα 19 Αντιπροσωπευτικά παραδείγματα των άνωθεν κινηματικών μηχανισμών: Η εκκλησία της Αγίας Μαρίας του Collemaggio στην L'Aquila (Ιταλία) κατά την διάρκεια του σεισμού L'Aquila (2009), το δημαρχείο στο San Agostino (Ιταλία) στον σεισμό του 2012 στην Emilia Romagna, η εκκλησία της Αγίας Αικατερίνης στην Venzone (Ιταλία) το 1976 στον σεισμό Friuli (Brandonisio 2017).

Στις ψευδοστατικές αναλύσεις που ακολουθούν θα εξεταστεί η ικανότητα των υψίκορμων αψιδοστατών που στηρίζουν ένα παχύ κυκλικό τόξο να αντιστέκονται στην λικνιστική ταλάντωση (**Σχήμα 20-αριστερά**). Σύμφωνα με τα προαναφερθέντα, όταν η ελάχιστη κρίσιμη οριζόντια επιτάχυνση ασκηθεί στην άκαμπτη βάση ενεργοποιείται ο Μηχανισμός II (ή μεικτός ή ημι-καθολικός) (**Σχήμα 20-δεξιά**). Η γεωμετρία του αψιδοστάτη (*b*, *h*) παίζει κυρίαρχο ρόλο στη σταθερότητα της δομής σε αντίθεση με τον δευτερεύοντα ρόλο της γεωμετρίας του τόξου. Η συμβολή τους διερευνάται παρακάτω. Τέσσερις διαφορετικές γεωμετρίες λαμβάνονται υπόψιν. Η λυγηρότητα του αψιδοστάτη $s = b / h$ κυμαίνεται από 0.25 σε 0.75. Το εύρος των τιμών των παραμέτρων του τόξου είναι: (i) για την γωνία περισφίξεως β, οι τιμές κυμαίνονται από 90˚ (τμηματικό τόξο) σε 180˚ (ημικυκλικό τόξο), και (ii) για την αναλογία μέσου πάχους t / R, από 0.025 σε 0.275 θεωρώντας αντιστοίχως πολύ λεπτά μέχρι πολύ παχιά τόξα.

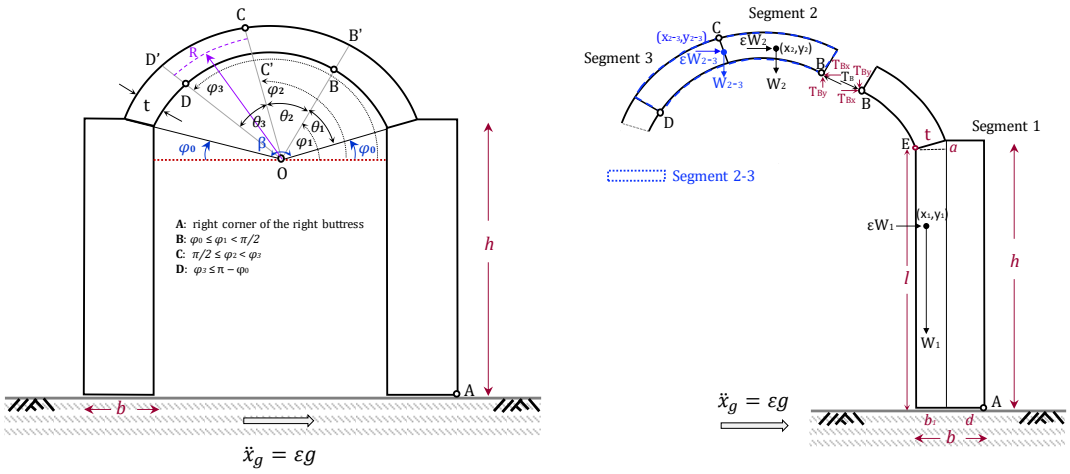

Σχήμα 20 Αριστερά: σχηματική αναπαράσταση ενός παχέος κυκλικού τόξου επί υψίκορμων αψιδοστατών. Όταν η κρίσιμη οριζόντια επιτάχυνση ασκείται στην βάση του από τα αριστερά προς τα δεξιά ενεργοποιείται ο Μηχανισμός II; οι κύριες γεωμετρικές παράμετροι που επηρεάζουν την ευστάθεια του συστήματος. Δεξιά: λεπτομερή αναπαράσταση της Οριακής Ανάλυσης Ισορροπίας. Τα τρία τμήματα του Κινηματικού Μηχανισμού II και το συνδυαστικό τμήμα 2-3 που χρησιμοποιούνται στην ανάλυση; Οι οριζόντιες (εW_i) και οι κατακόρυφες (W_i) δυνάμεις που ασκούνται στο κέντρο της μάζας (x_i, y_i) για κάθε τμήμα καθώς οι καρτεσιανές συνιστώσες της δύναμης ώθησης.

Η αύξηση του πλάτους του αψιδοστάτη εξασφαλίζει μεγαλύτερη σταθερότητα καθώς απαιτούνται υψηλότερες τιμές επιτάχυνσης για να μετατραπεί η κατασκευή

σε μηχανισμό (**Σχήμα 21**). Για παράδειγμα, μια αύξηση του πλάτους κατά 50% οδηγεί σε 50% υψηλότερες τιμές κρίσιμων επιταχύνσεων. Γενικά, όταν η λυγηρότητα *s* αυξάνεται (είτε αυξάνοντας το πλάτος του αψιδοστάτη ή μειώνοντας το ύψος του), η κατασκευή γίνεται πιο σταθερή καθώς η έναρξη του λικνισμού απαιτεί μεγαλύτερες τιμές επιτάχυνσης. Μικρότερες τιμές της γωνίας περισφίξεως β έχουν ευνοϊκή επίδραση στην ευστάθεια. Η περίπτωση ενός σχετικά στιβαρού αψιδοστάτη (b / R =0.75, H / R = 1) είναι μια οριακή κατάσταση όπου για μεγαλύτερα πλάτη το τόξο μετατρέπεται στο ευάλωτο τμήμα της κατασκευής και υπό μια κρίσιμη επιτάχυνση κινητοποιείται ο Μηχανισμός I όπου και οι τέσσερις ρήξεις συμβαίνουν μόνο στο τόξο. Από τα διαγράμματα επιβεβαιώνεται το εύρημα του Housner (1963) ότι ανάμεσα σε δύο εξίσου υψίκορμες κατασκευές διαφορετικού μεγέθους η μεγαλύτερη είναι τόσο πιο σταθερή. Τέλος, μια σημαντική διαπίστωση προκύπτει από το **Σχήμα 22** όπου παρουσιάζονται οι θέσεις των επικείμενων αρθρώσεων φ_1, φ_2, φ_3 των σημείων B, C, D. Η διαμόρφωση του τόξου που μετατρέπεται σε μηχανισμό υπό την κρίσιμη οριζόντια επιτάχυνση περιλαμβάνει έναν μεγαλύτερο σύνδεσμο με άνοιγμα θ_1 που προηγείται πάντα των δύο επικείμενων με ίσα ανοίγματα ($\theta_2 = \theta_3$). Η περιγραφείσα διαμόρφωση συμπίπτει με αυτήν που κατέληξε ο Oppenheim (1992).

Τόξα επί αψιδοστατών ενιαίας και μη-ενιαίας διατομής.-Σε αυτή την ενότητα επικεντρωνόμαστε στην δομική απόκριση των λίθινων τόξων υπό καθεστώς διαρροής όταν διεγείρονται από διακριτούς παλμούς, οι οποίοι υποκαθιστούν επαρκώς τις σεισμικές διεγέρσεις. Η κατασκευή αποτελείται από επιμέρους θολίτες με προκαθορισμένες θέσεις αρθρώσεων. Αναφορικά με τους πεπλατυσμένους αψιδοστάτες η λυγηρότητά τους (b / R) αυξάνεται κατά 25% δηλαδή από b / R = 0.3 σε b'/ R = 0.4 ενώ όλα τα υπόλοιπα γεωμετρικά χαρακτηριστικά (t / R, h / R, β) παραμένουν σταθερά (**Σχήμα 23**). Η αριθμητική επίλυση των εξισώσεων πραγματοποιήθηκε με βήμα-προς-βήμα εν-χρόνω ολοκλήρωση, μέσω της μεθόδου άμεσης διατύπωσης (explicit algorithm). Ως διέγερση στην βάση χρησιμοποιήθηκαν τριγωνομετρικοί παλμοί ενός κύκλου και παλμοί τύπου Ricker. Η ευαισθησία του τρισδιάστατου μοντέλου στα χαρακτηριστικά των παλμών απεικονίζεται στα φάσματα ανατροπής των **Σχημάτων 24**, **25**. Το δομικό σύστημα παρουσιάζει

σημαντική αντίσταση σε υψίσυχνους παλμούς. Για παράδειγμα, ένας παλμός Ricker με περίοδο T_E = 0.2 sec (case A) είναι πρακτικώς αδύνατον να προκαλέσει την ανατροπή της κατασκευής αφού για να επιτευχθεί κάτι τέτοιο πρέπει το εύρος της επιτάχυνσης να φτάσει την τιμή a_p = 3 *g*. Οι μακροπερίοδοι παλμοί Ricker έχουν καταστροφικές συνέπειες στην ευστάθεια της κατασκευής. Στον αντίποδα για αρκετά μεγάλες περιόδους (T_E > 0,9 sec) η ελάχιστη επιτάχυνση προσεγγίζει την ψευδοστατική τιμή.

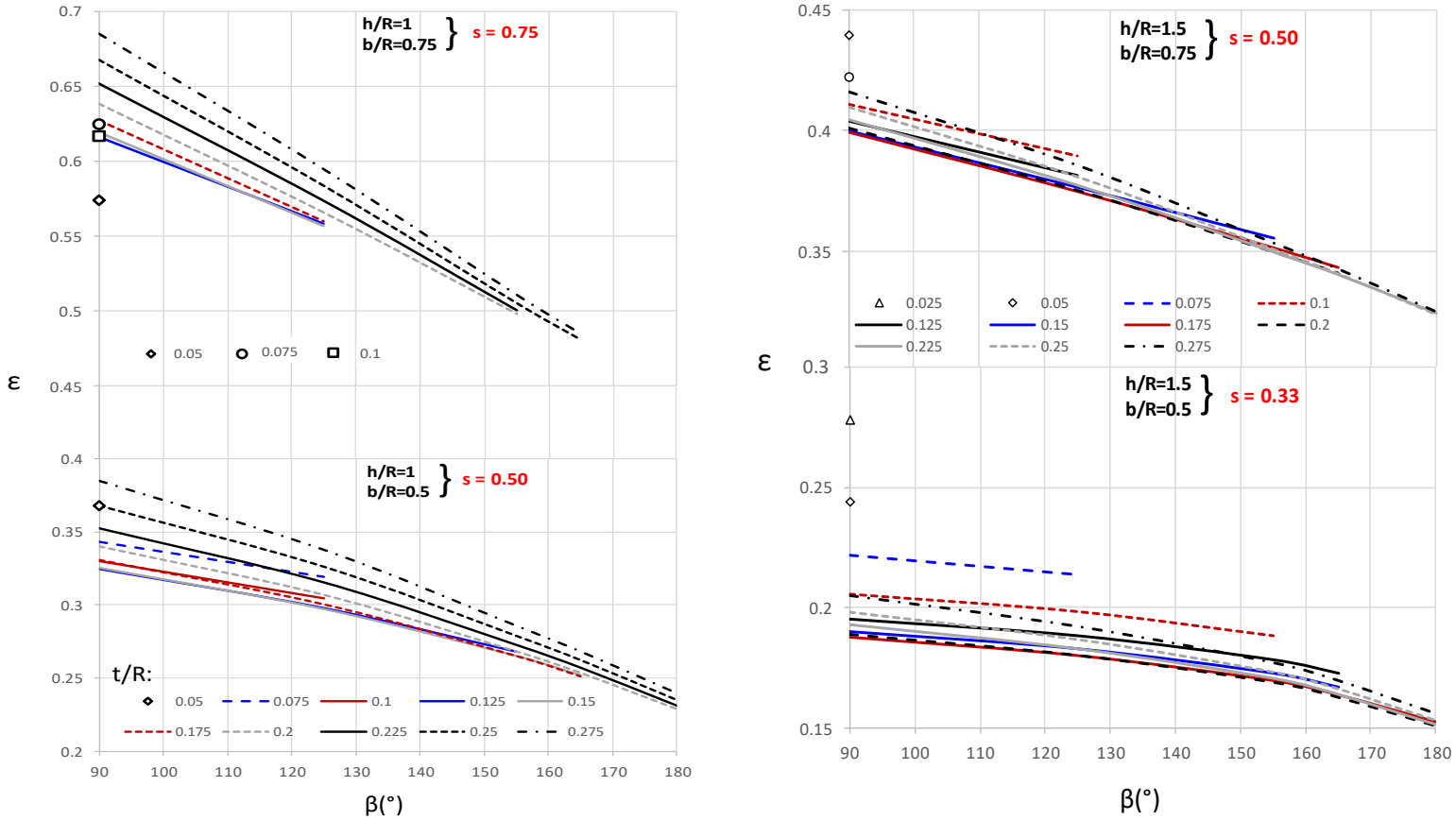

Σχήμα 21 Επίδραση της αύξησης του πλάτους (*b* / *R* = 0.5 - 0.75) ενός αψιδοστάτη με δεδομένο ύψος *h* (*h* / *R* =1 & 1.5) στον σεισμικό συντελεστή *ε* για διαφορετικές γεωμετρίες του τόξου (*t* / *R*, *β*).

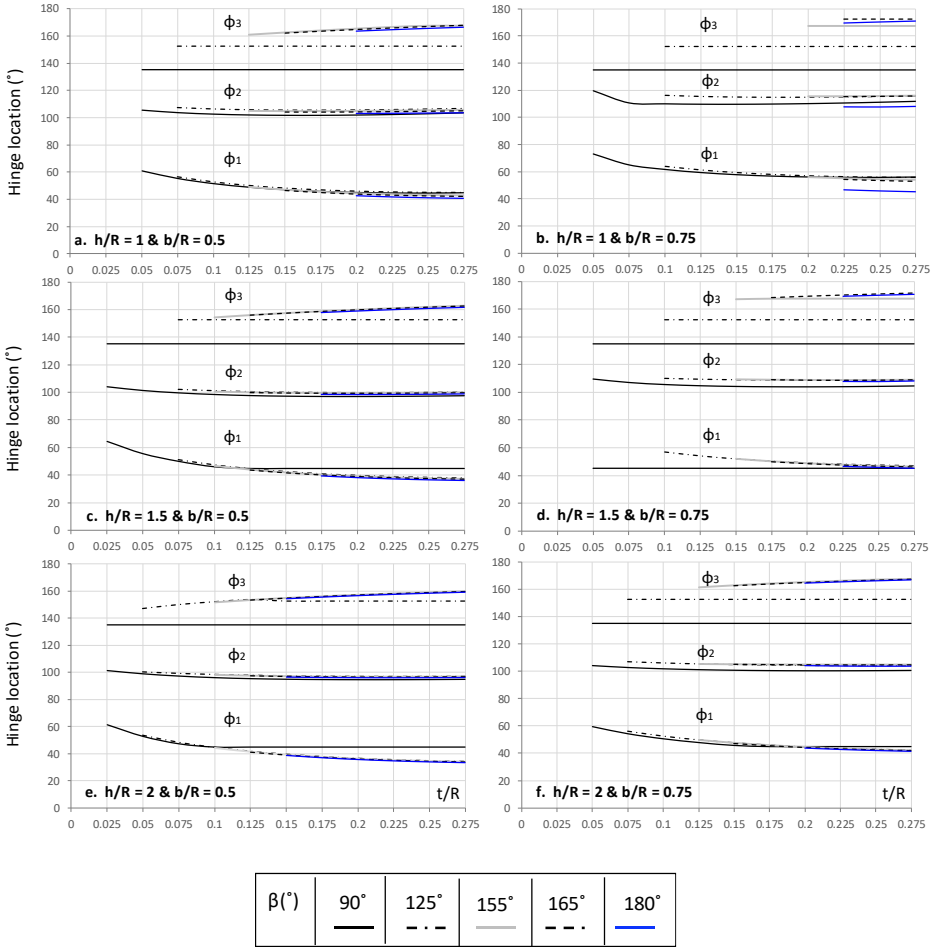

Σχήμα 22 Θέσεις των επικείμενων αρθρώσεων φ_1, φ_2, φ_3 των σημείων B, C, D (Σχήμα 5.2) αντιστοίχως για μία τοξωτή κατασκευή με δεδομένη γεωμετρία αψιδοστατών (b / R, h / R). Οι παράμετρες του τόξου (β και t / R) καλύπτουν ένα ικανοποιητικό εύρος τιμών.

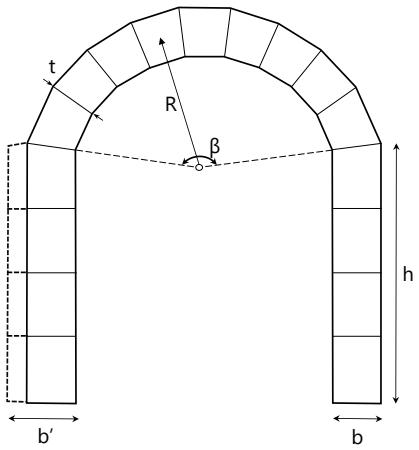

Geometric parameters	
R	1.33 m
t/R	0.3
β	146°
h	1.66 m
b	0.40 m
b′	0.535 m

Σχήμα 23 Γεωμετρικές παράμετροι του τόξου επί αψιδοστατών: η μέση ακτίνα R του τόξου, η λυγηρότητα του τόξου t / R, η γωνία περισφίξεως β, το ύψος και το πλάτος του αψιδοστάτη h, b αντίστοιχα και το πάχος b’ του πεπλατυσμένου αψιδοστάτη.

Αναφορικά με τις επιπτώσεις που ασκεί κάθε παλμός στην κατασκευή διαφαίνεται εναργώς ότι ο ημιτονικός παλμός είναι πιο καταστρεπτικός από τον παλμό Ricker ειδικώς για σεισμούς μικρής διάρκειας (T_E < 0.2 sec). Η λιγότερο καταστρεπτική επίδραση του παλμού Ricker αποδίδεται απλώς στην ευνοϊκή ασυμμετρία που προσφέρει ένα πρόσθετο «δίχτυ ασφαλείας». Για μέτριους και μακροπερίοδους παλμούς ο τύπος του δεν διαδραματίζει σημαντικό ρόλο.

Από τη σύγκριση των διαφορετικών γεωμετριών αποκαλύπτεται ότι ακόμη και μια μικρή αύξηση στο πλάτος του αψιδοστάτη αυξάνει την ευστάθεια της κατασκευής ανεξάρτητα από τον τύπο παλμού. Για τιμές T_E μεγαλύτερες από 0,2 sec, η ελάχιστη PGA για την ανατροπή του ενισχυμένου τόξου μειώνεται γρήγορα.

Στις περισσότερες περιπτώσεις ο επικρατών μηχανισμός είναι ο Μηχανισμός II. Εξαίρεση αποτελεί όταν το σύστημα διεγείρεται από έναν μακροπερίοδο παλμό Ricker (T_E = 1.2 sec) και ενεργοποιείται ο Μηχανισμός III (καθολικός). Ως εκ τούτου, η δυνατότητα ενεργοποίησης ενός μηχανισμού έναντι κάποιου άλλου δεν εξαρτάται μόνο από τη γεωμετρική αναλογία τόξου-αψιδοστάτη αλλά και από τα χαρακτηριστικά της φόρτισης.

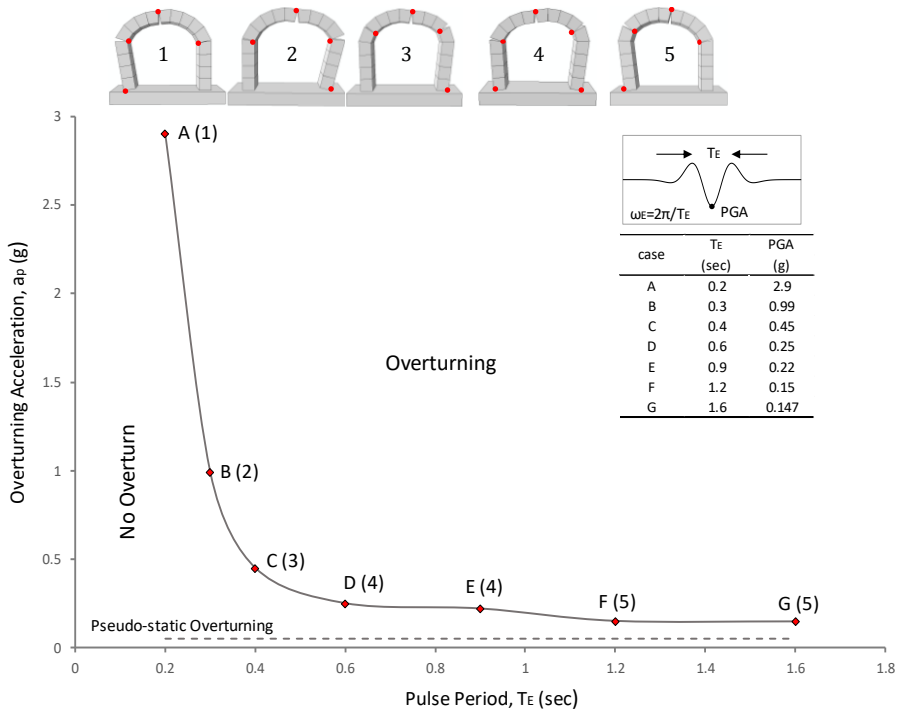

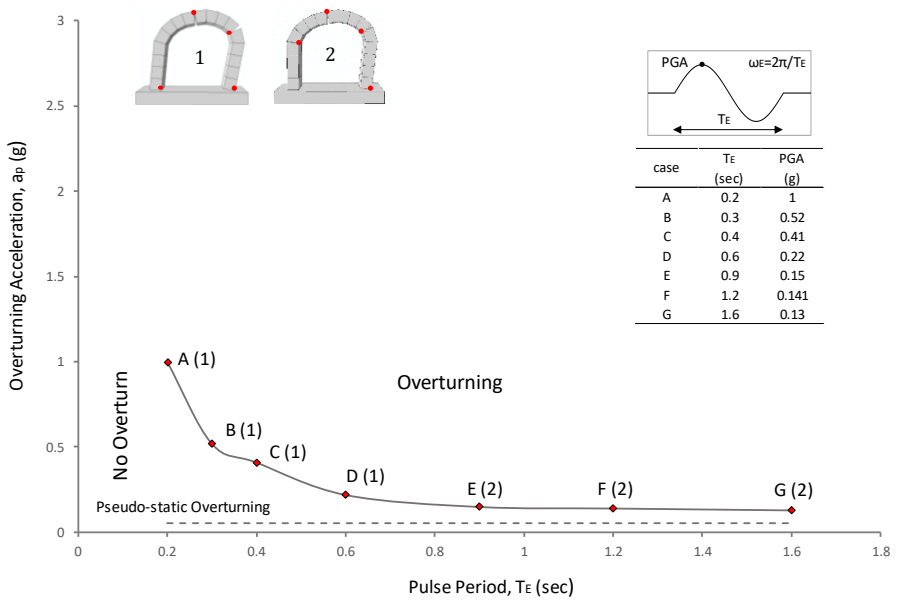

Σχήμα 24 Φάσματα ανατροπής της τοξωτής κατασκευής με ενιαία διατομή που υποβάλλεται σε παλμούς τύπου Ricker (αριστερή μεριά) και σε ημιτονοειδείς παλμούς (δεξιά μεριά). Για κάθε παλμό A-G (περίοδοι T_E: 0.2, 0.3, 0.4, 0.6, 0.9, 1.2, 1.6 sec) απεικονίζεται ο εκάστοτε μηχανισμός των τεσσάρων αρθρώσεων που ενεργοποιείται.

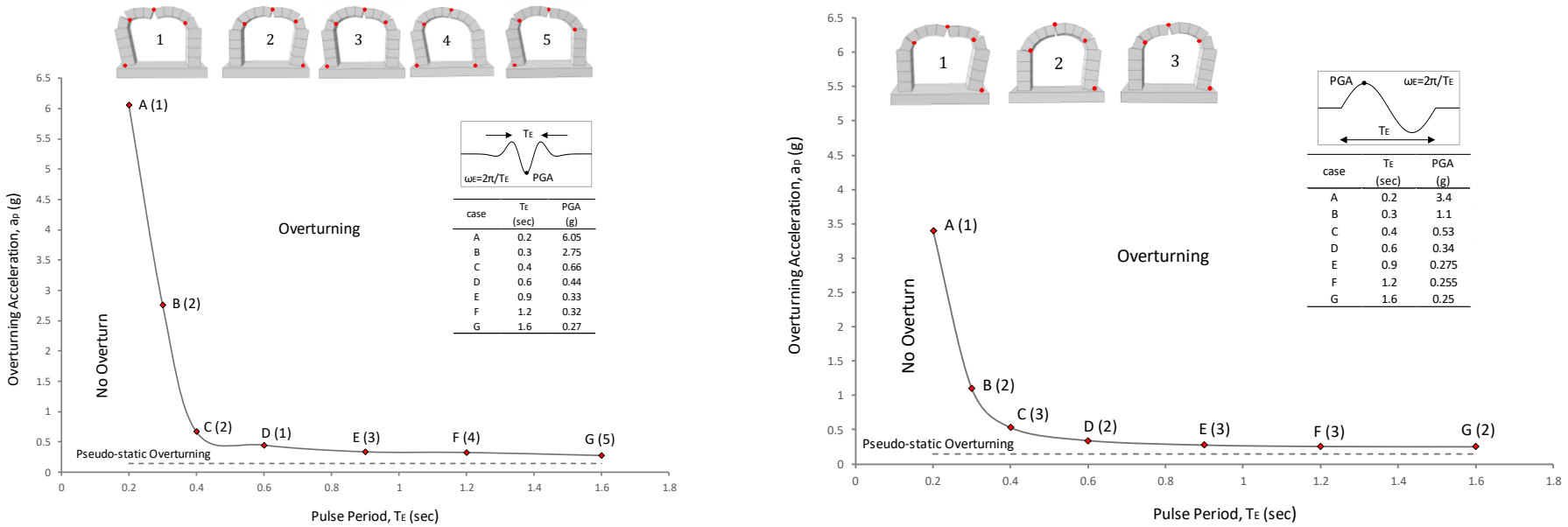

Σχήμα 25 Φάσματα ανατροπής της τοξωτής κατασκευής με μη-ενιαία διατομή που υποβάλλεται σε παλμούς τύπου Ricker (αριστερή μεριά) και σε ημιτονοειδείς παλμούς (δεξιά μεριά). Για κάθε παλμό A-G (περίοδοι T_E: 0.2, 0.3, 0.4, 0.6, 0.9, 1.2, 1.6 sec) απεικονίζεται ο εκάστοτε μηχανισμός των τεσσάρων αρθρώσεων που ενεργοποιείται.

VI. Εγκιβωτισμένες θολωτές κατασκευές: Αλληλεπίδραση Εδάφους-Κατασκευής

Το διάγραμμα ελεύθερου σώματος της εγκιβωτισμένης θολωτής κατασκευής σκιαγραφείται στο **Σχήμα 26**. Όταν η κατασκευή τοποθετείται στην εκσκαφή ("wished in place"), το ίδιο βάρος της (W_{arch} + W_b) ενεργοποιεί δυνάμεις αντίδρασης από το έδαφος θεμελίωσης (N, T_{base}). Η δύναμη αντίδρασης T_{base} είναι εφαπτομένη στην διεπιφάνεια εδάφους-θεμελίωσης με φορά προς το εσωτερικό και εξαρτάται από τον συντελεστή τριβής μ κατά μήκος της διεπιφάνειας. Η ολίσθηση της κατασκευής θα αποφευχθεί εάν αυτή η δύναμη είναι μικρότερη από το γινόμενο του μ*N (όπου N είναι η δύναμη που είναι η κάθετη στην διεπιφάνεια του θολίτη). Με την επίχωση των κενών εκατέρωθεν των τοίχων, οι θολίτες υπόκεινται επιπλέον σε οριζόντιες εδαφικές πιέσεις. Η ζώνη πλήρωσης - πλάτους 30 cm- λειτουργεί υπό θλίψη (δημιουργεί συνθήκες πλευρικής αποφόρτισης) αντισταθμίζοντας την αντίδραση εδάφους - θεμελίωσης. Η τριγωνική κατανομή των οριζόντιων εδαφικών πιέσεων, σύμφωνα με την θεωρία των Rankine και Coulomb, απεικονίζεται στο **Σχήμα 26**. Τελικώς, όταν η κατασκευή επανεπιχωθεί, το βάρος του υπερκείμενου εδάφους θα ληφθεί από την καμπύλη επιφάνεια του τόξου ως κατανεμημένες κατακόρυφες εδαφικές πιέσεις (p_{ver}). Ανάλογα με το ύψος του υπερκείμενου εδάφους καθώς και την ακαμψία της κατασκευής, η φόρτιση του τόξου μπορεί να συνοδεύεται από μια πεπερασμένη μετατόπιση που μπορεί να οδηγήσει ακόμη και σε καθίζηση του εδάφους. Η δυσμενής περίπτωση όπου η κατασκευή και η ζώνη πλήρωσης παραλαμβάνουν όλο το υπερκείμενο φορτίο απεικονίζεται στο **Σχήμα 26α**. Ως αντιστάθμισμα, η διατμητική αντίσταση εντός της ζώνης επαφής των διαρρεουσών και στατικών μαζών μπορεί να αντιτεθεί σε αυτή την κίνηση και να διατηρήσει την αρχική της θέση. Κατά συνέπεια, η πίεση της διαρρέουσας μάζας μειώνεται ενώ η πίεση στην παρακείμενη σταθερή μάζα αυξάνεται. Αυτή η μεταφορά πιέσεων είναι απόρροια της τοξωτής λειτουργίας του εδάφους. Οι διαδρομές των τάσεων παραπέμπουν στη δημιουργία ενός εικονικού τόξου πάνω από την διαρρέουσα ζώνη. Ο μηχανισμός που επιτρέπει αυτή την εκτροπή των τροχιών των τάσεων από την κατακόρυφη κατεύθυνση προέρχεται από την

υπερστατικότητα του διδιάστατου εδαφικού μέσου. Ανάλογοι μηχανισμοί τοξωτής λειτουργίας παρατηρούνται σε φέρουσα τοιχοποιία πάνω από ανοίγματα. Αυτή η κατάσταση, η οποία εξαρτάται από τις μετατοπίσεις της κατασκευής, μπορεί να χαρακτηριστεί ως μια προσωρινή συμπεριφορά της εδαφικής μάζας στην διαρρέουσα ζώνη παρά μια σταθερή. (**Σχήμα 26β**).

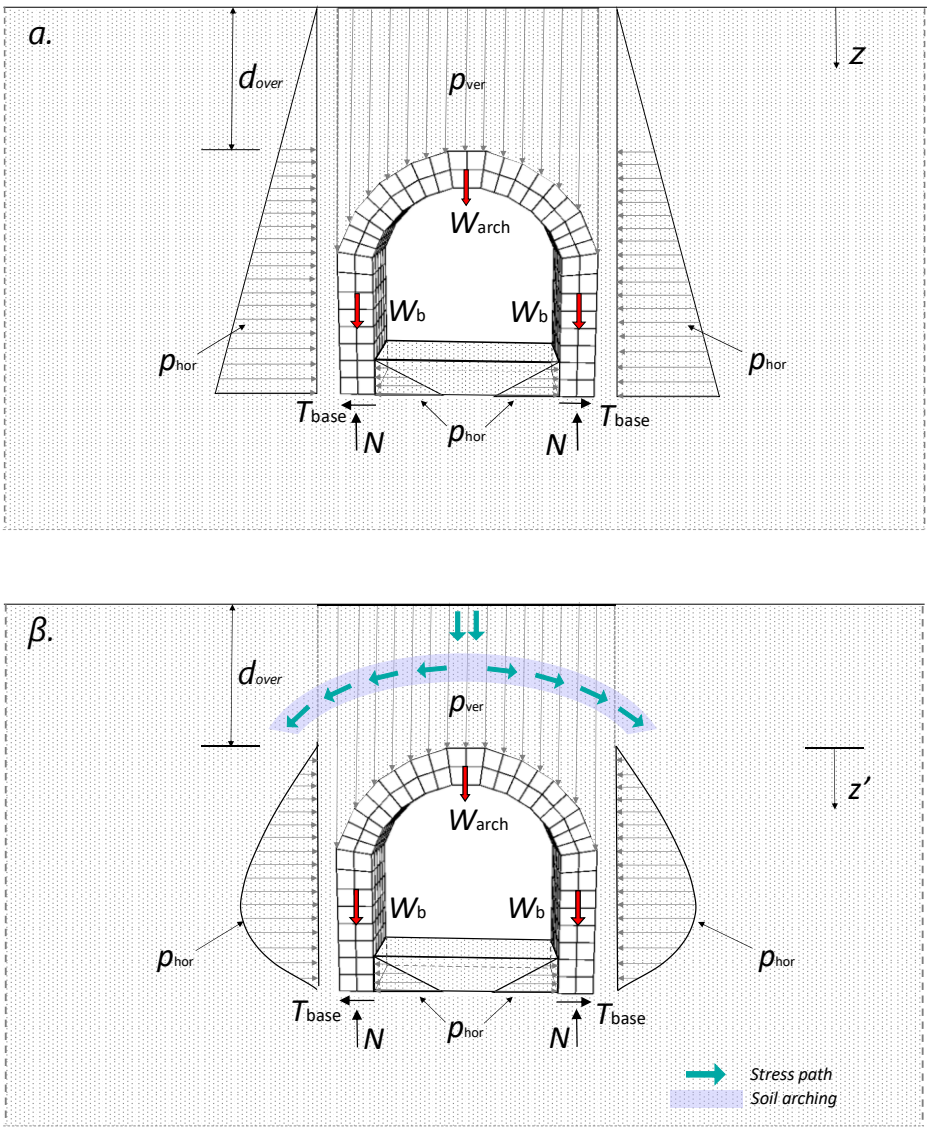

Σχήμα 26 Απεικόνιση του διαγράμματος ελεύθερου σώματος μιας εγκιβωτισμένης θολωτής κατασκευής. α) Η δυσμενής περίπτωση όπου αγνοείται η τοξωτή λειτουργία του εδάφους, β) Συνυπολογίζοντας την τοξωτή λειτουργία η οποία επισημαίνεται μαζί με την διαδρομή τάσεων. Οι οριζόντιες εδαφικές πιέσεις υπολογίζονται από το επίπεδο του κλειδιού.

Η μη γραμμική ανάλυση της στατικής και σεισμικής απόκρισης του συστήματος ευοδούται με την αριθμητική μέθοδο των πεπερασμένων στοιχείων και συγκεκριμένα με τον γενικής χρήσεως κώδικα πεπερασμένων στοιχείων ABAQUS. Το **Σχήμα 27** απεικονίζει την διακριτοποίηση πεπερασμένων στοιχείων του μοντέλου μαζί με μια σχηματική διάταξη των λεπτομερειών μοντελοποίησης. Μια λίθινη θολωτή κατασκευή που αποτελείται από πεπερασμένο αριθμό θολιτών κατασκευάζεται σε κατακόρυφη τάφρο βάθους 5,50 μ. που διανοίχθηκε σε συνεκτικό έδαφος. Η κατασκευή και το περιβάλλον έδαφος αντιπροσωπεύονται με διδιάστατα τετραπλευρικά στοιχεία επίπεδης παραμόρφωσης. Στην άμεση γειτονία της κατασκευής όπου το τασικό πεδίο παρουσιάζει μεγάλο ενδιαφέρον η διακριτοποίηση γίνεται πυκνότερη προκειμένου να διασφαλιστεί η επάρκεια των αποτελεσμάτων. Για την ρεαλιστική προσομοίωση των γεωστατικών συνθηκών, προηγείται οποιασδήποτε στατικής ή δυναμικής ανάλυσης το γεωστατικό “βήμα”, μια διαδικασία ενσωματωμένη στο ABAQUS. Η αριθμητική επίλυση των πεπλεγμένων εξισώσεων ισορροπίας γίνεται με αλγόριθμο άμεσης ολοκλήρωσης (implicit algorithm). Οι πλευρικοί κόμβοι της εκσκαφής συνδέονται μεταξύ τους μέσω κινηματικών περιορισμών, ως προσωρινή μέθοδος αντιστήριξης για την αποφυγή εδαφικών κινήσεων. Κατά τη διαδικασία επίχωσης, αυτοί οι περιορισμοί απενεργοποιούνται σταδιακά για να επιτραπεί η φυσική ανάπτυξη οριζόντιων εδαφικών πιέσεων. Το βραχώδες υπόβαθρο θεωρείται ως ακλόνητο. Για την επίτευξη της αποκόλλησης στις διεπιφάνειες των θολιτών του τόξου μεταξύ τους, του τόξου με τους αψιδοστάτες, του τελευταίου με το έδαφος θεμελίωσης καθώς και στην διεπιφάνεια εδάφους-κατασκευής εφαρμόζεται ένας εξελιγμένος αλγόριθμος επαφής. Ένας αρκετά μεγάλος συντελεστής τριβής (μ = 0,7) επιλέχθηκε ώστε να διασφαλιστεί αμιγώς η λικνιστική ταλάντωση -επικρατούσα στα υψίκορμα συστήματα- και να αποφευχθεί η ολίσθηση.

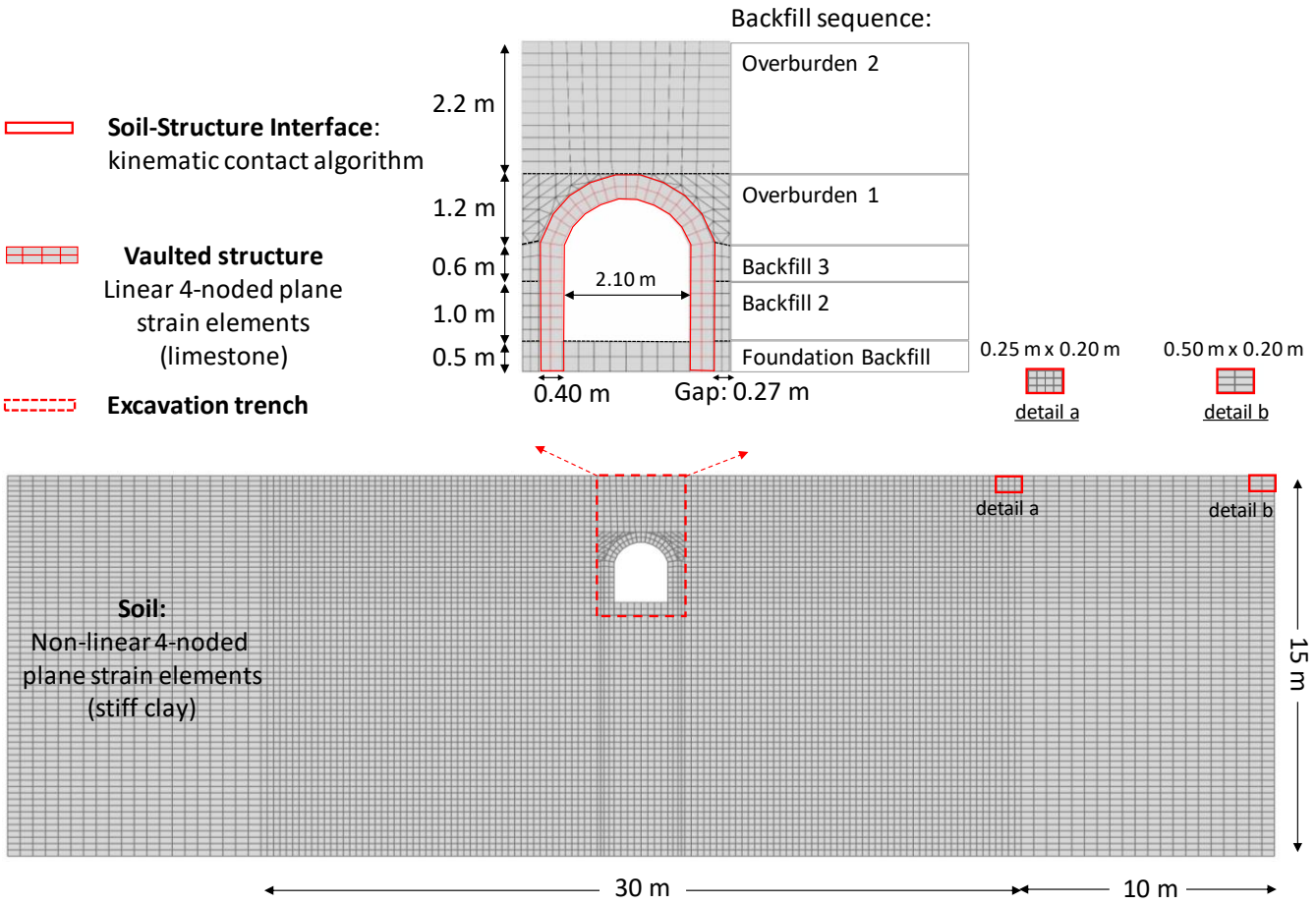

Σχήμα 27 Η εκσκαφή, η λίθινη θολωτή κατασκευή, τα πάχη των επιχώσεων και του υπερκείμενου εδάφους; γεωμετρία και διακριτοποίηση των πεπερασμένων στοιχείων θεωρώντας συνθήκες επίπεδης παραμόρφωσης.

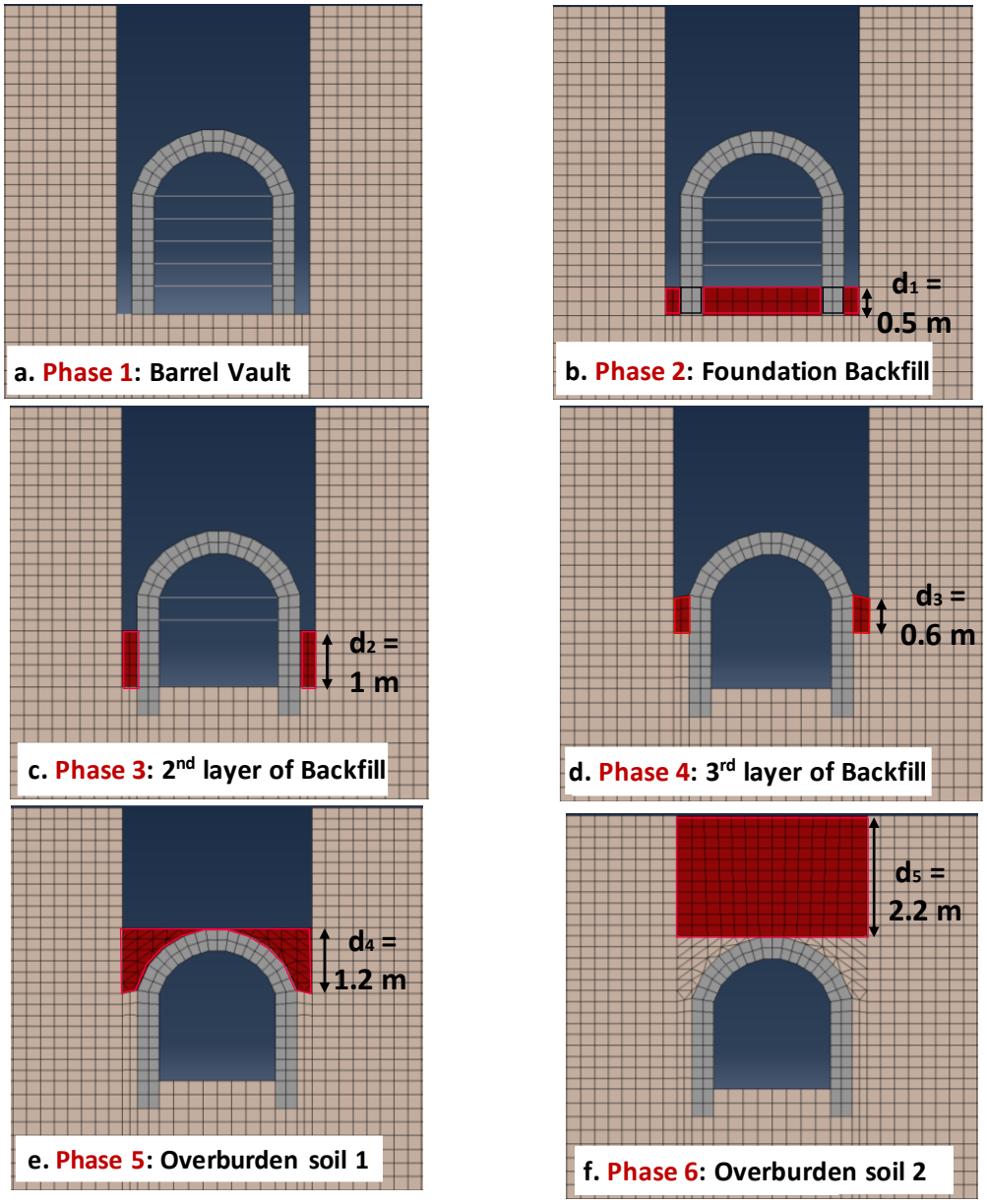

Σχήμα 28 Απεικόνιση της κατασκευαστικής αλληλουχίας με πεπερασμένα στοιχεία: α) Φάση 1: η τοξωτή κατασκευή ''τοποθετείται'' στην εκσκαφή και τα βάθρα υποστηρίζονται προσωρινώς, β) Φάση 2: με μία στρώση επίχωσης d_1 = 0.5 m στις εξωτερικές πλευρές του αψιδοστάτη διαμορφώνεται η θεμελίωση, γ) Φάση 3: το ύψος επίχωσης αυξάνεται κατά d_2 = 1 m (backfill 2), δ) Φάση 4: πλήρως επιχωμένοι αψιδοστάτες (backfill 3, d_3 = 0.60 m), ε) Φάση 5: η πρώτη στρώση υπερκείμενου φορτίου, d_4 = 1.20 m καλύπτει το τόξο μέχρι την στέψη του (overburden 1) και ζ) Φάση 6: μία δεύτερη στρώση υπερκείμενου εδάφους πάχους d_5 = 2.2 m φτάνει στην στέψη της εκσκαφής (overburden 2).

Η σημασία της κατασκευαστικής αλληλουχίας (**Σχήμα 28**) έγκειται στα ακόλουθα: (1) η σταδιακή επίχωση επηρεάζει την ευστάθεια της κατασκευής, (2) απόκτηση λεπτομερών προφίλ των εδαφικών πιέσεων που αναπτύσσονται σε κάθε βήμα, (3)

πιθανή ανάπτυξη του φαινομένου της τοξωτής λειτουργίας του εδάφους κατά την διάρκεια της επίχωσης.

Το εδαφικό προφίλ ενός ομοιογενούς συνεκτικού εδάφους στου οποίου η αστράγγιστη αντοχή και το μέτρο ελαστικότητας αυξάνονται σταδιακά με το βάθος απεικονίζεται στο **Σχήμα 29**. Η ελαστο-πλαστική συμπεριφορά της σκληρής αργίλου υπό αστράγγιστες συνθήκες προσομοιώνεται με το τροποποιημένο κριτήριο αστοχίας Von-Mises με θεώρηση μη-γραμμικής κινηματικής κράτυνσης με συσχετιζόμενο νόμο πλαστικής ροής.

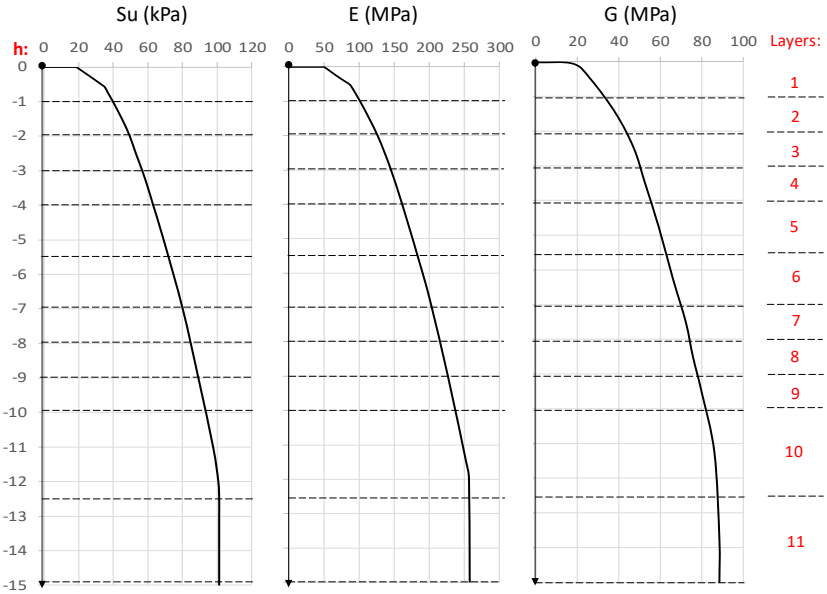

Σχήμα 29 Το εδαφικό προφίλ μιας σκληρής αργίλου. Κατανομή με το βάθος της αστράγγιστης διατμητικής αντοχής S_u (kPa), του μέτρου ελαστικότητας E (MPa), και του μέτρου διάτμησης G (MPa).

Οριζόντιες εδαφικές πιέσεις.- Κατά την προοδευτική επίχωση του ανασκαμμένου ορύγματος και μετά την τοποθέτηση της θολωτής κατασκευής, λαμβάνονται υπόψιν η αλληλεπίδραση εδάφους-κατασκευής ενώ αμφότερες οι αποκρίσεις των αλληλεπιδρώντων τμημάτων εξαρτώνται από τους ακόλουθους παράγοντες:

(1) Την μέθοδο εισαγωγής του εδάφους και του κυλινδρικού θόλου στο αριθμητικό μας μοντέλο που εν τοιαύτη περιπτώσει το πρώτο τοποθετείται σταδιακά και το δεύτερο με την θεώρηση "*wished in place*"

(*ανεπηρέαστη τοποθέτηση* εννοώντας ότι αγνοείται η οποιαδήποτε επίδραση στο τασικό πεδίο του εδάφους).

(2) Τον υψηλό συντελεστή τριβής (μ =0.7) ώστε να αποφευχθεί η ολίσθηση στις διεπιφάνειες.

(3) Την ικανότητα των μετακινήσεων της κατασκευής, που το μέγεθός τους σχετίζεται με την αδράνεια του ασβεστόλιθου, να ενεργοποιούν την διατμητική αντοχή του εδάφους.

Ενδιαφέρον παρουσιάζουν οι θλιπτικές τάσεις που ασκούνται από το έδαφος επίχωσης στην διεπιφάνεια της κατασκευής (**Σχήμα 30**). Οι εδαφικές πιέσεις επαφής μπορούν να ανακατανεμηθούν κατά μήκος της διεπιφάνειας με τέτοιο τρόπο ώστε οι αναπτυγμένες διακυμάνσεις του γραμμικού προφίλ να παρέχουν ροπές σταθεροποίησης του αψιδοστάτη σε κατακόρυφη θέση. Κατόπιν πλήρωσης του υπερκείμενου εδάφους, η απαίτηση του τόξου για μετακίνηση προς τα έξω στην βάση στήριξής του ενεργοποιεί σημαντικές εδαφικές δυνάμεις για να διασφαλιστεί η δομική ακεραιότητα του τόξου. Αυτό το ζεύγος συμμετρικών οριζόντιων δυνάμεων επιδεικνύεται με τοπικό μέγιστο στο προφίλ των δυνάμεων επαφής του εδάφους, γύρω από τα στηρίγματα του τόξου. Το ανωτέρω φαινόμενο είναι αυτό της *δομικής τοξωτής λειτουργίας* χάριν στο οποίο επιτυγχάνεται η στατική ισορροπία της κατασκευής με ελάχιστες μετατοπίσεις.

Για να διευκρινιστεί περαιτέρω ο ευνοϊκός ρόλος του εδάφους επίχωσης, η ανάπτυξη οριζόντιων πιέσεων εδάφους στο τμήμα εκσκαφής παρουσιάζεται στο **Σχήμα 31**. Η επιβολή κινηματικών περιορισμών μεταξύ των κατακόρυφων ορίων της εκσκαφής έχει ως αποτέλεσμα πρόσθετες οριζόντιες εδαφικές πιέσεις. Η συγκέντρωση αυτών των πιέσεων παρατηρείται σε θέσεις όπου θα εμφανιζόταν παραμορφώσεις εάν δεν επιβάλλονταν αυτοί οι περιορισμοί.

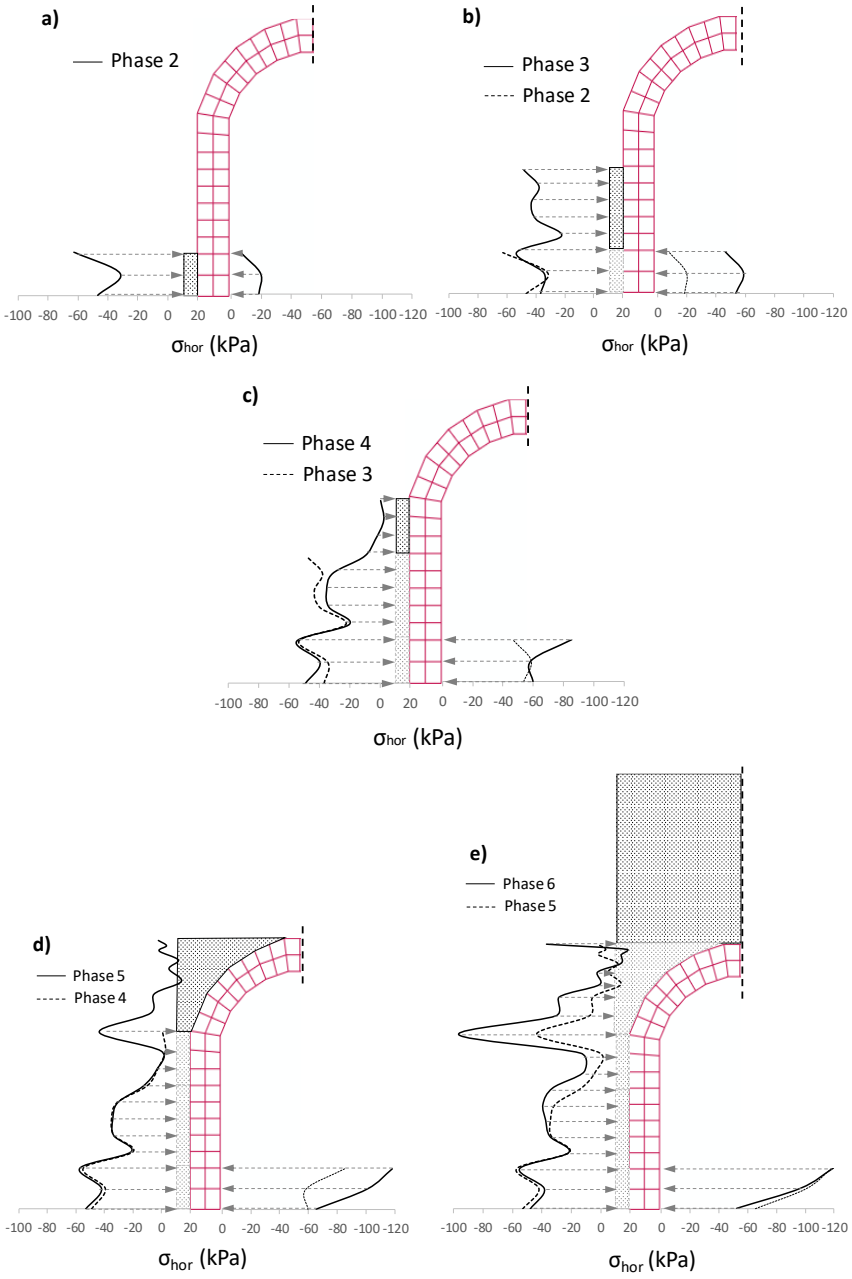

Σχήμα 30 Η κατανομή των οριζόντιων εδαφικών πιέσεων που ασκούνται στην διεπιφάνεια επίχωσης-αψιδοστάτη για κάθε βήμα της κατασκευαστικής λειτουργίας.

Κατά τη διαδικασία επίχωσης (φάσεις 3-6) παρατηρείται ανακούφιση των εδαφικών πιέσεων στο επίπεδο των αψιδοστατών. Καθώς το ύψος επίχωσης αυξάνεται, μεγαλύτερη ποσότητα εδάφους συμβάλλει στην ανακατανομή της τάσης. Στην τελευταία φάση της κατασκευαστικής ακολουθίας (φάση 6), οι τάσεις στο επίπεδο του 1^{ου} υπερκείμενου φορτίου (overburden 1) είναι αρκετά μεγαλύτερες από τις γεωστατικές λόγω της δομικής τοξωτής λειτουργίας ενώ

στο επίπεδο του 2ου υπερκείμενου (overburden 2) είναι ελαφρώς μεγαλύτερες λόγω της τοξωτής λειτουργίας του εδάφους. Συμπερασματικά, το έδαφος επίχωσης συμβάλλει με δύο τρόπους: (1) κατά την φόρτιση του τόξου από το υπερκείμενο έδαφος που έχει ως συνέπεια την ανάπτυξη της δομικής τοξωτής λειτουργίας, προσφέρει την οριζόντια αντίδραση στην βάση του τόξου για να περιορίσει την πλάτυνση του, (2) παραλαμβάνει ένα μέρος του φορτίου του υπερκείμενου εδάφους και γενικώς συμπεριφέρεται ως «*μηχανισμός μαξιλαριού*» (cushion mechanism).

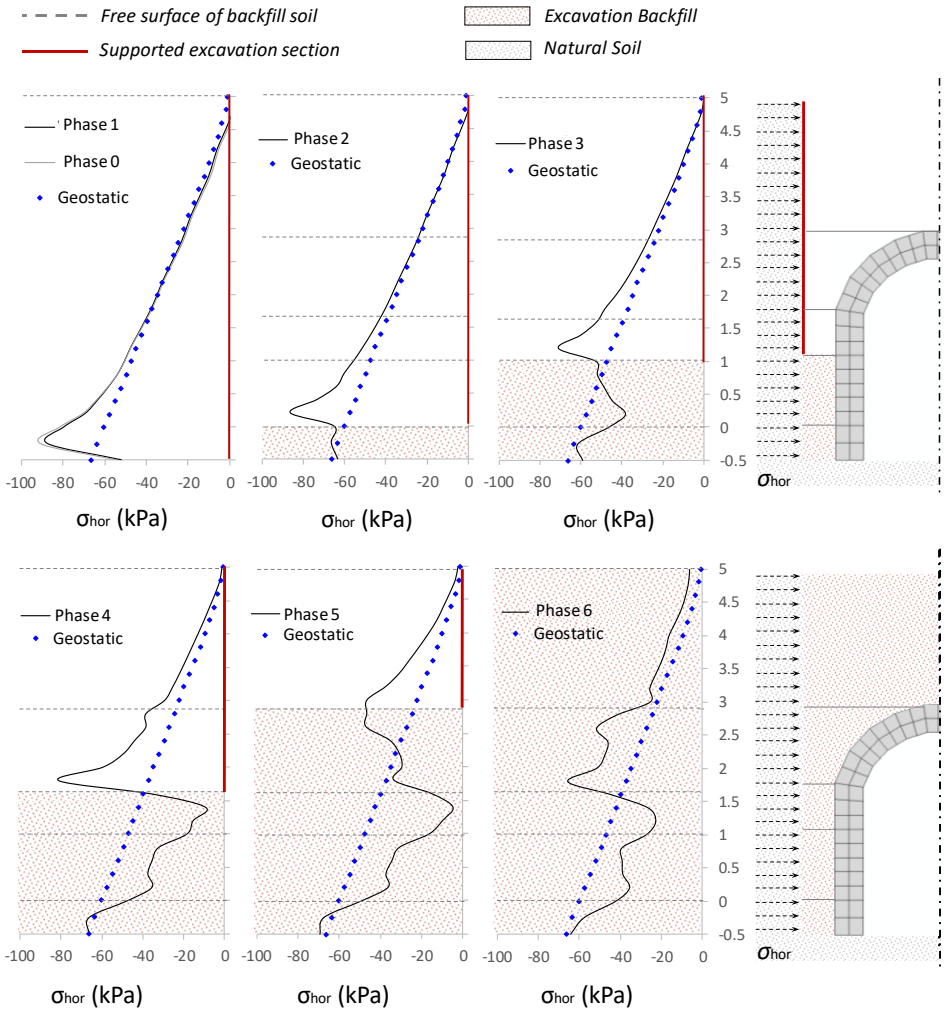

Σχήμα 31 Οριζόντιες εδαφικές πιέσεις κατά μήκος της εκσκαφής με παράθεση την τριγωνική κατανομή πιέσεων ως μέτρο σύγκρισης για την αξιολόγηση της επίδρασης της κατασκευαστικής λειτουργίας.

Οριζόντιες και κατακόρυφες μετατοπίσεις.- Αξιοσημείωτα συμπεράσματα διεξάγονται και από τις καμπύλες μετατόπισης. Στο **Σχήμα 32** απεικονίζονται οι ισοϋψείς των μετακινήσεων της κατασκευής στον οριζόντιο και κατακόρυφο άξονα που προκαλούνται από την διαδοχική επίχωση της κατασκευής. Η απόκριση της κατασκευής διέπεται κυρίως από την απόκριση του εδάφους που γειτνιάζει με την κατασκευή. Οι μεταβαλλόμενες δυνάμεις από το έδαφος επίχωσης ή από το υπερκείμενο που ασκούνται στην θολωτή κατασκευή ενεργοποιούν διαφορετικούς καννάβους παραμόρφωσης. Το μέγεθος αυτών των μετατοπίσεων εξαρτάται από: α) την γεωμετρία της κατασκευής, β) την δυσκαμψία της λιθοδομής, γ) την δυσκαμψία του εδάφους, και δ) την κατασκευαστική αλληλουχία. Διακρίνονται τρεις βασικές φάσεις της επιχώσης της κατασκευής: (i) οι αψιδοστάτες είναι πλήρως επιχωματωμένοι (το έδαφος υψώνεται σε h_3 = 2,16 m από τη βάση θεμελίωσης), (ii) το τόξο καλύπτεται μέχρι το ύψος του κλειδιού (h_4 =3,30 m), και (iii) η τοποθέτηση του υπερκείμενου εδάφους πάνω από το τόξο σχηματίζει την τελική εδαφική επιφάνεια σε ύψος h_5 =5 m από τη βάση θεμελίωσης.

Με την ολοκλήρωση της επίχωσης, η ενδοσιμότητα του αψιδοστάτη ενεργοποιείται πλήρως όπως φαίνεται στο **Σχήμα 32i**. Αυτές οι μεταφορικές και περιστροφικές μετατοπίσεις κάθε αψιδοστάτη (οριζόντια μετατόπιση 0,4 mm) περιορίζονται από το τόξο καθώς έντονες δυνάμεις τριβής αναπτύσσονται στις διεπιφάνειες βάσης-τόξου. Η στατική ισορροπία στο τέλος αυτής της φάσης επιτυγχάνεται με την μείωση των δυνάμεων επαφής στους αψιδοστάτες (πλευρική αποφόρτιση) και την αύξηση (πλευρική φόρτιση) κατά μήκος του τόξου (τάση για ενεργητική και παθητική κατάσταση αντίστοιχα). Καθώς το ύψος της επίχωσης αυξάνεται και το τόξο εγκιβωτίζεται μέχρι την στέψη του (**Σχήμα 32ii**), οι εδαφικές δυνάμεις επαφής επιβάλλουν κάμψη του τόξου συνοδευόμενη από οριζόντιες μετατοπίσεις των αψιδοστατών προς τα μέσα καθώς και άνωθεν κίνηση των κεντρικών θολιτών του (1,8 mm περίπου). Τελικά, όταν η εκσκαφή καλυφθεί πλήρως με έδαφος, η στέψη συμπιέζεται σταδιακά και οι υπερκείμενες πιέσεις αποκαθιστούν την παραμορφωμένη γεωμετρία. Εν κατακλείδι, η στατική ισορροπία καθιδρύεται καθώς το υπερκείμενο φορτίο παραλαμβάνεται μέσω δύο τοξωτών μηχανισμών: (i) από την δομική τοξωτή λειτουργία καθώς οι θολίτες φορτίζονται κυρίως με αξονική

θλίψη και αναπτύσσονται δριμείς οριζόντιες δυνάμεις στις γενέσεις του τόξου ώστε να εξασφαλιστεί το προαναφερθέν φαινόμενο. Αυτές οι δυνάμεις μεταδίδονται στο μέσο του εδάφους γύρω από αυτά τα στηρίγματα που φαίνονται ως συγκέντρωση των πιέσεων επαφής στο προφίλ του **Σχήματος 30e**, (ii) με την τοξωτή λειτουργία του εδάφους. Αυτός ο μηχανισμός αναπτύσσεται στο πίσω μέρος των αψιδοστατών και πάνω από το τόξο και επιτρέπει μέσω των διαδρομών πιέσεων την εκτροπή του δομικού τόξου μεταδίδοντας ένα μέρος του υπερκείμενου φορτίου απευθείας στο εδαφικό μέσο.

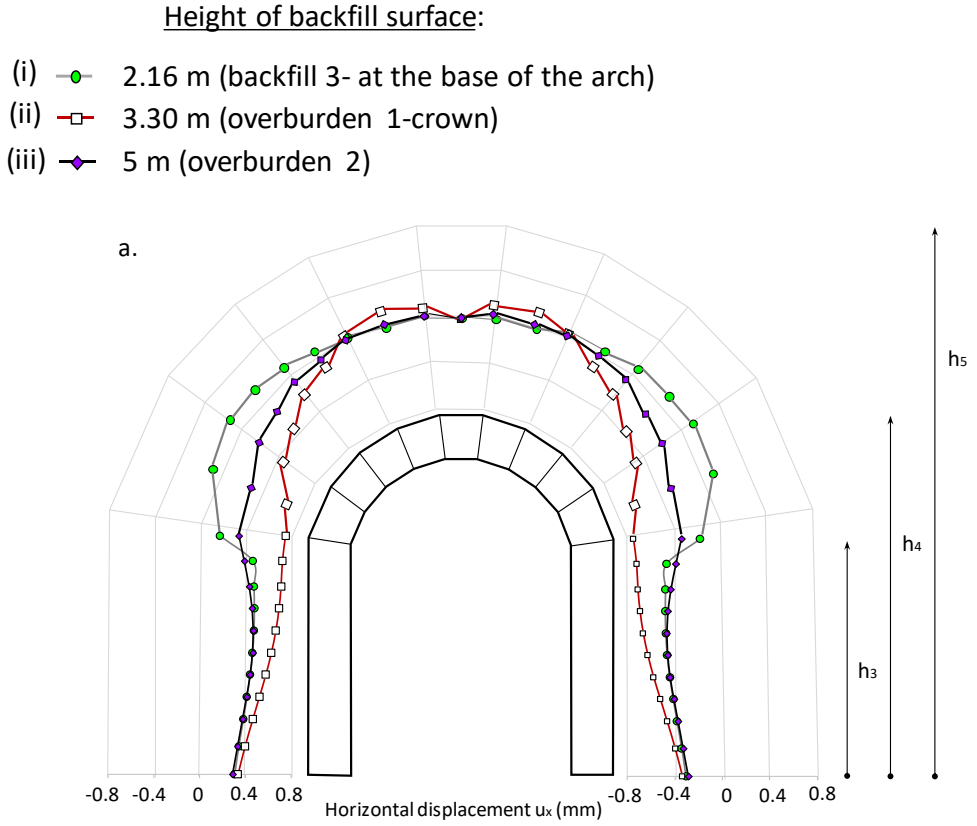

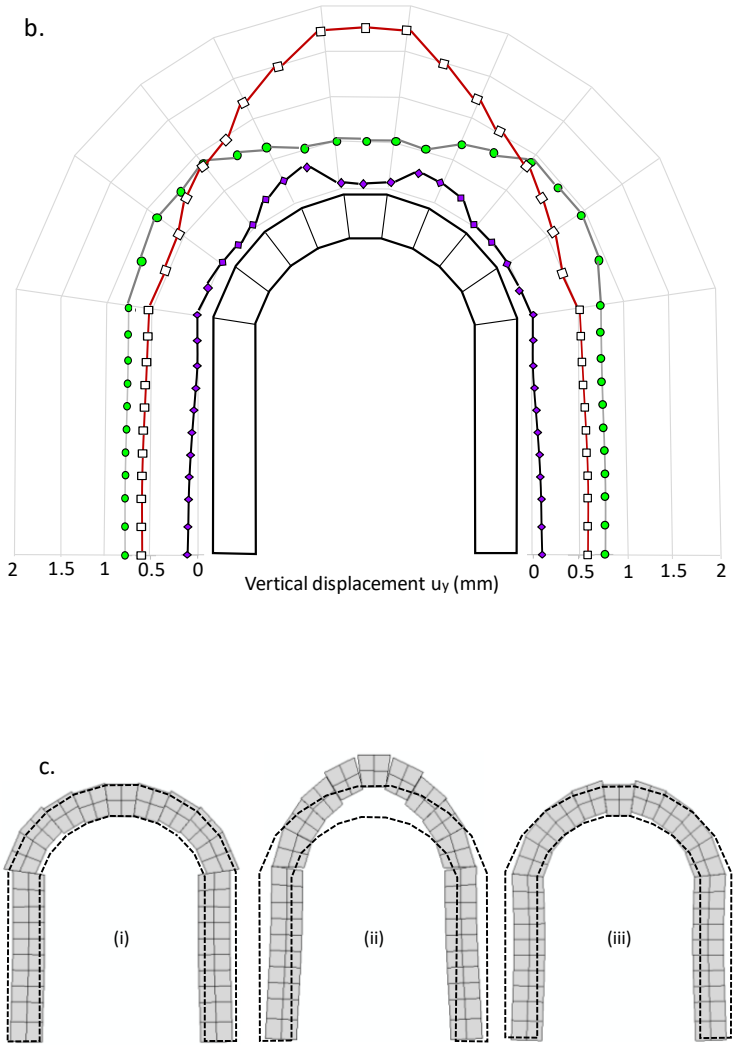

Σχήμα 32 Ισοϋψείς των (α) οριζόντιων u_x και (β) κατακόρυφων μετατοπίσεων u_y, (γ) παραμορφωμένος κάνναβος της κατασκευής (επικλιμάκια αναγωγή 200%) για τρεις διακεκριμένες περιπτώσεις: (i) οι αψιδοστάτες είναι πλήρως επιχωμένοι μέχρι το ύψος h_3 =2.16 m, 2) η επίχωση φτάνει μέχρι την στέψη, h_4 =3.30 m and 3) το υπερκείμενο φορτίο τοποθετείται πάνω από το τόξο, σε ύψος h_5 =5 m από την βάση εκσκαφής.

Επίδραση του πεπλατυσμένου αψιδοστάτη.- Θα διερευνηθεί η επίδραση των πεπλατυσμένων αψιδοστατών στην ευστάθεια μιας εγκιβωτισμένης κατασκευής και στην αλληλεπίδρασή της με το έδαφος. Λαμβάνεται υπόψη η γεωμετρία του κυλινδρικού θόλου που απεικονίζεται στο **Σχήμα 23**, όπου η λυγηρότητα του αυξάνεται μόνο κατά 25% (από b / R =0,3 σε b'/R = 0,4). Είναι ενδιαφέρον ότι μέρος του υπερκείμενου φορτίου παραλαμβάνεται απευθείας από τους δύο αψιδοστάτες όπως υπαγορεύει η διδιάστατη διαμόρφωση. Τα φορτία δεν κατανέμονται σε κάθετη διεύθυνση αλλά κατευθύνονται λοξά προς τα έξω. Αυτή

η προς τα έξω μεταφερόμενη ώθηση παραλαμβάνεται από το πρόσθετο τμήμα. Τα αποτελέσματα των αναλύσεων για κυλινδρικούς θόλους μη ομοιόμορφης διατομής παρατίθενται εν συγκρίσει με αυτά για θόλους ομοιόμορφης διατομής. Το υπό εξέταση μοντέλο σκιαγραφείται στο **Σχήμα 33**. Λεπτομέρειες των δυνάμεων που ασκούνται στην αριστερή γένεση του τόξου απεικονίζονται επίσης στο **Σχήμα 33 (ii)**.

Η συνισταμένη των θλιπτικών δυνάμεων που επιφέρει ο θολίτης (ώθηση T) αντιτίθεται από την παθητική αντίσταση του εδάφους (*P*), την αντίσταση τριβής στην γένεση του θολίτη (F) και το υπερκείμενο βάρος, *W* που ασκείται στο τμήμα του αψιδόλιθου που προεξέχει. Όταν η οριζόντια συνιστώσα της ώθησης υπερνικήσει την αντίσταση τριβής στην διεπιφάνεια (T_x > F), απαιτείται κινητοποίηση παθητικών πιέσεων συγκράτησης από το περιβάλλον έδαφος.

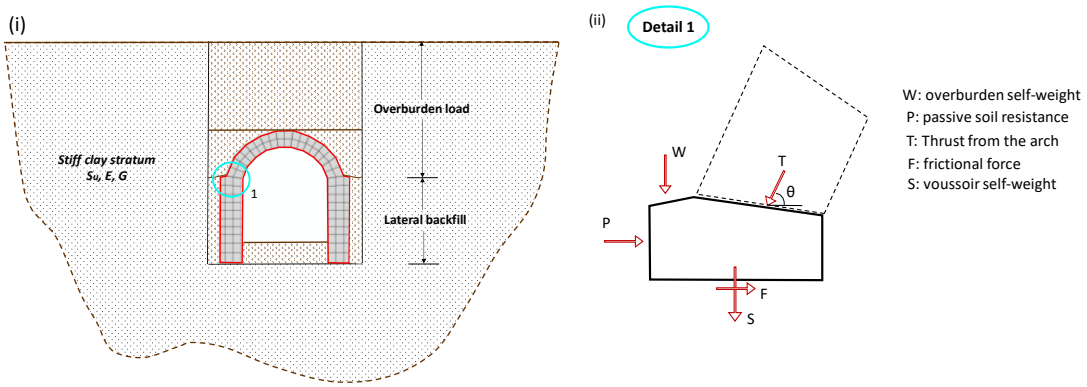

Σχήμα 33 (i) Απεικόνιση της εγκιβωτισμένης θολωτής κατασκευής με διευρυμένους αψιδοστάτες (Σχήμα 6.5) σε σκληρό στρώμα αργίλου. Τα στρώματα επίχωσης διαχωρίζονται με συνεχείς γκρίζες γραμμές, (ii) διάγραμμα δυνάμεων ελεύθερου σώματος ενός θολίτη του αψιδοστάτη.

Συγκρίνοντας τις κατανομές των εδαφικών πιέσεων των απλών και των ενισχυμένων αψιδοστατών (**Σχήμα 34**) είναι εμφανής η ευνοϊκή επίδραση των τελευταίων. Συγκεκριμένα παρατηρείται αισθητή υποχώρηση της συγκέντρωσής των εδαφικών τάσεων γύρω από τη βάση του τόξου, στην περίπτωση του ενισχυμένων αψιδοστατών. Το ψαλίδισμα αυτών των τάσεων οφείλεται στην μείωση της απαιτούμενης οριζόντιας αντίδρασης στη βάση του τόξου χάρις στην ταυτόχρονη ανάπτυξη τέμνουσας δύναμης από τον ενισχυμένο αψιδοστάτη.

Ευνοϊκή είναι και η επίδραση των υπερκειμένων γαιών όπως προκύπτει από τους παραμορφωμένους καννάβους του **Σχήματος 35**. Η σταδιακή επανεπίχωση της εκσκαφής πίσω από τους αψιδοστάτες προκαλεί στροφές και παραμορφώσεις στην τοξωτή κατασκευή. Μακροσκοπικά αυτές οι μετακινήσεις δείχνουν συμπίεση της διατομής η οποία γίνεται όλο και πιο αισθητή με την προοδευτική άνοδο της στάθμης της επανεπίχωσης. Ωστόσο το φαινόμενο αυτό τείνει να αντιστραφεί με την συνέχιση της πλήρωσης της εκσκαφής αφότου έχει επιχωθεί πλήρως η κατασκευή. Συγκεκριμένα, οι πιέσεις των υπερκειμένων γαιών παραμορφώνουν το τόξο και κατά συνέπεια και το σύνολο της κατασκευής προς την αντίθετη κατεύθυνση εν συγκρίσει με τις πλευρικές πιέσεις. Αυτό έχει ως αποτέλεσμα η διατομή να τείνει να επανέλθει στην αρχική της κατάσταση και να αναιρεθεί η δυσμενής επίδραση της μερικής πλήρωσης της εκσκαφής.

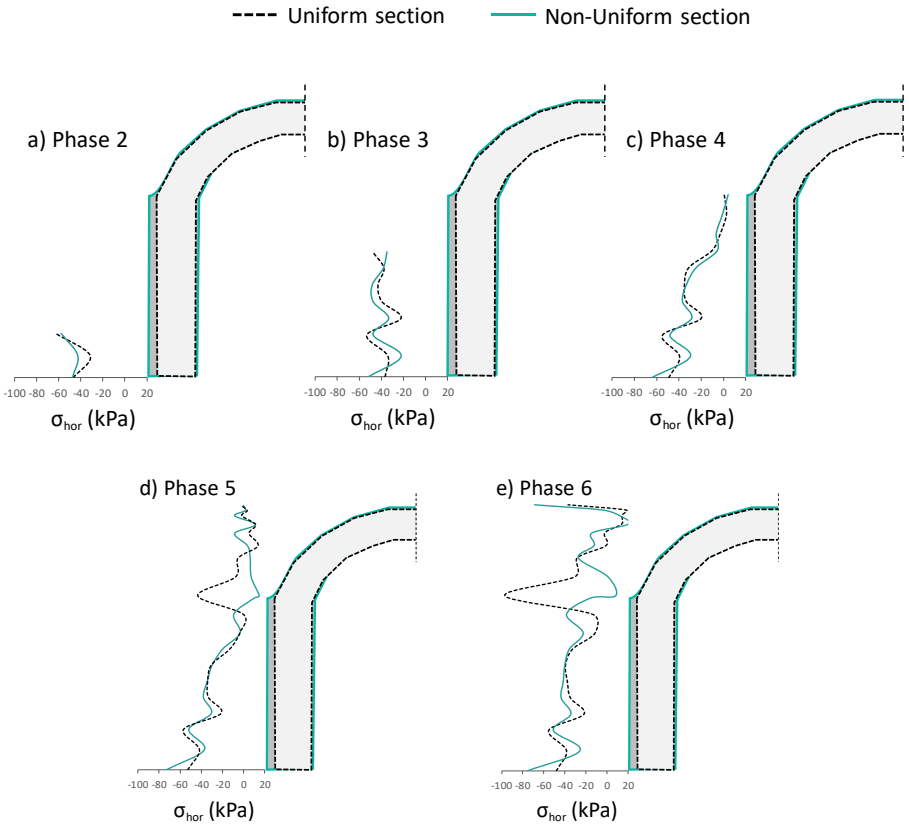

Σχήμα 34 Σύγκριση των καθ' ύψος κατανομών των πλευρικών εδαφικών τάσεων που ασκούνται στην επιφάνεια του αψιδοστάτη σε κάθε βήμα της διαδικασίας επίχωσης μιας θολωτής κατασκευής με ομοιόμορφη (μαύρη διακεκομμένη γραμμή) και μιας με ανομοιόμορφη (πράσινη γραμμή) διατομή.

Κατά τη φάση 5 (**Εικόνα 35(ii)**), το ύψος της επανεπίχωσης συνεπάγεται άσκηση εδαφικών πιέσεων σε όλη την περίμετρο της κατασκευής. Σε σύγκριση με τον αντίστοιχο κάνναβο παραμόρφωσης του **Σχήματος 32**, η ανοδική κίνηση του τόξου είναι φαινομενικά μικρότερη, αλλά η λικνισμός μεταξύ των θολιτών στην περιοχή του θεμελιώδους λίθου είναι εντονότερη. Εν κατακλείδι, η τοποθέτηση του υπερκείμενου εδάφους επαναφέρει μεν τους αψιδοστάτες στην αρχική τους θέση, αλλά έχει ως επακόλουθο μεγαλύτερες μόνιμες τοπικές μετατοπίσεις των άνω θολιτών σε σύγκριση με την προηγούμενη γεωμετρία.

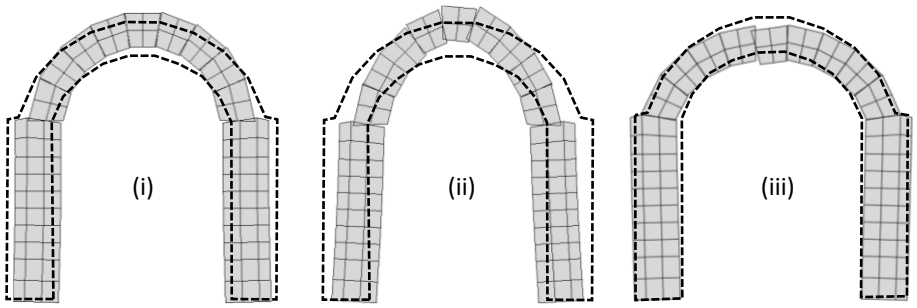

Σχήμα 35 Παραμορφωμένος κάνναβος της κατασκευής (με επικλιμάκια αναγωγή 200%) για τρεις διακεκριμένες περιπτώσεις: (i) οι αψιδοστάτες είναι πλήρως εγκιβωτισμένοι μέχρι το ύψος h_3 =2.16 m, 2) η επίχωση φτάνει μέχρι την στέψη, h_4 =3.30 m, και 3) το υπερκείμενο φορτίο τοποθετείται πάνω από το τόξο, σε ύψος h_5 =5 m από την βάση εκσκαφής.

Σεισμική Απόκριση.- Η σεισμική απόκριση των εγκιβωτισμένων κατασκευών είναι ένα σύνθετο πρόβλημα αλληλεπίδρασης εδάφους-κατασκευής. Οι μετατοπίσεις της κατασκευής και οι δυναμικές εδαφικές πιέσεις εξαρτώνται από την απόκριση του εδάφους θεμελίωσης, την απόκριση του εδάφους επανεπίχωσης, τις αδρανειακές και καμπτικές αποκρίσεις των αψιδοστατών και τις σεισμικές επιταχύνσεις. Η θολωτή κατασκευή διεγείρεται δυναμικά από εξιδανικευμένους παλμούς της εδαφικής κίνησης, παλμοί τύπου Ricker (**Σχήμα 36 (i) ~ (iv)**) και πραγματικές καταγραφές σεισμικών επεισοδίων (**Σχήμα 36 (v) ~ (vi)**).

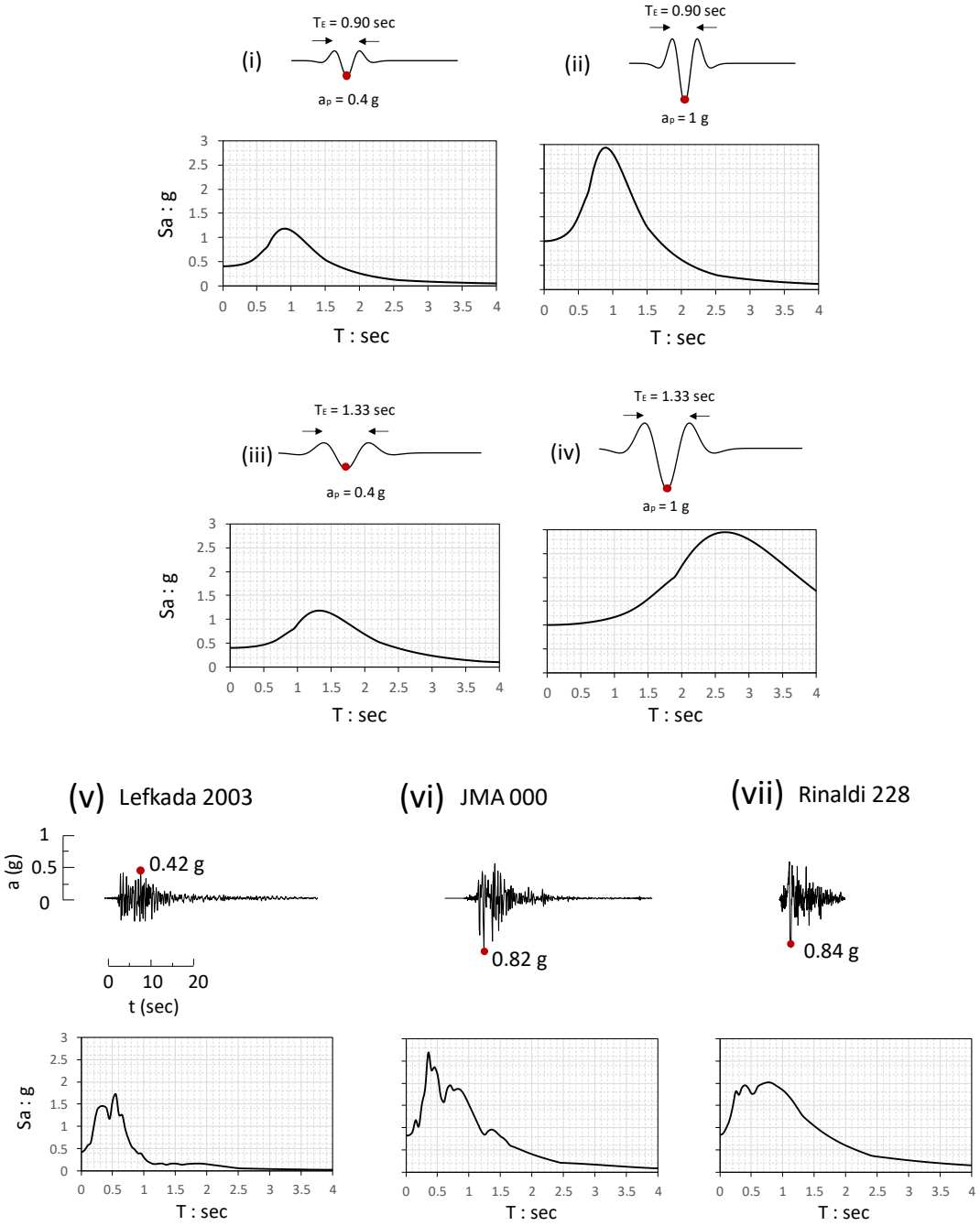

Σχήμα 36 Παλμοί Ricker (i), (ii), (iii), (iv), και τρεις πραγματικές καταγραφές σεισμικές επεισοδίων (v), (vi), (vii) που χρησιμοποιήθηκαν ως διέγερση στην βάση με τα αντίστοιχα φάσματα επιτάχυνσης.

Για κάθε περίπτωση φόρτισης με παλμούς Ricker περιόδου T_E = 0.90 *sec* και αυξανόμενου εύρους επιτάχυνσης a_p (PGA: 0.2 *g*, 0.6 *g*, 1 *g*) υπολογίζονται οι μέγιστες και ελάχιστες δυναμικές εδαφικές πιέσεις στην διεπιφάνεια αψιδοστάτη –

επιχώματος (**Σχήμα 37**). Παρατηρούνται έντονες εδαφικές αντιδράσεις στην διεπιφάνεια τόξου-αψιδοστάτη, υποδηλώνοντας την απαίτηση του τόξου να πεπλατυνθεί. Στην συνέχεια, εξετάζεται ο ανακουφιστικός ρόλος της επίχωσης στο περιβάλλον έδαφος. Η επικρατούσα περίοδος των παλμών Ricker δεν φαίνεται να επηρεάζει τις οριζόντιες εδαφικές πιέσεις που αναπτύσσονται πέρα από το έδαφος επίχωσης. Η κατανομή των εδαφικών πιέσεων στο επίπεδο του υπερκείμενου εδάφους (h=2.8 m - 5 m) είναι γραμμική ανεξάρτητα από τα χαρακτηριστικά του παλμού (a_p, T_E). Ο μηχανισμός του τόξου επηρεάζει το περιβάλλον έδαφος αυξάνοντας τις πιέσεις τοπικά, στο h = 1.66 m. Υπάρχει μια αξιοσημείωτη αύξηση στις πλευρικές εδαφικές πιέσεις όταν εφαρμόζονται μεγαλύτερα πλάτη επιτάχυνσης. Η μορφή της κατανομής δεν παρουσιάζει μεγάλες μεταβολές και είναι ανεξάρτητο από την επιβληθείσα διέγερση και κατά συνέπεια από τα χαρακτηριστικά του παλμού. Έχουν δευτερεύοντα ρόλο στη διαμόρφωση του σχήματος της κατανομής που καθορίζεται από τη στατική απόκριση.

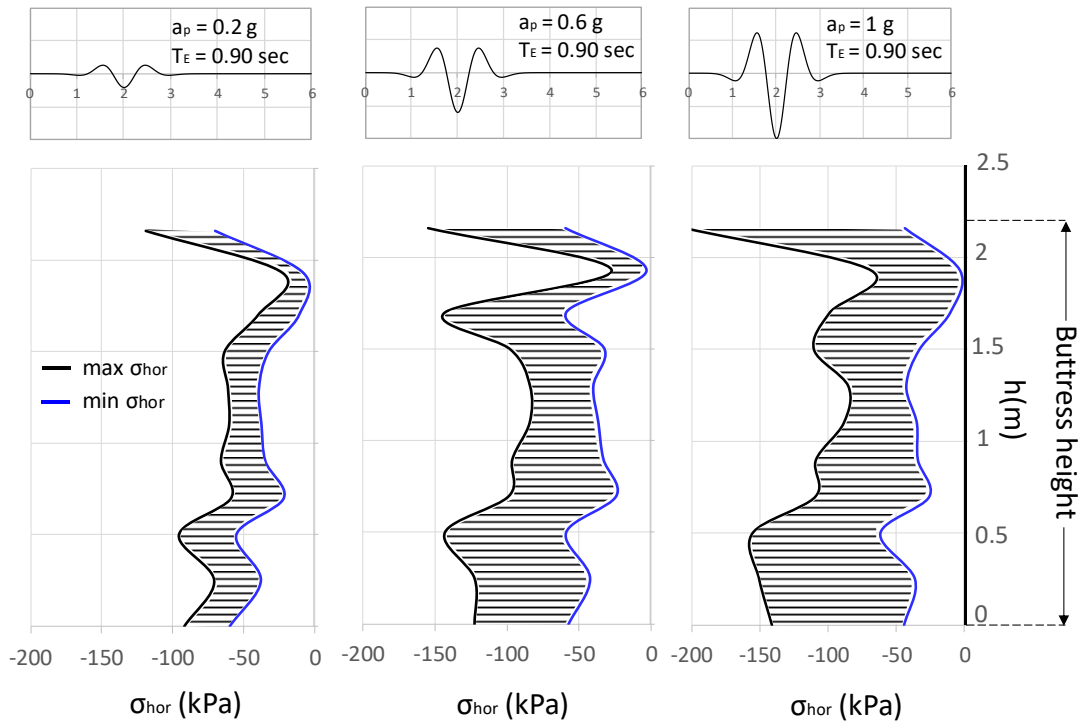

Σχήμα 37 Απεικόνιση των μεγίστων & ελαχίστων δυναμικών εδαφικών πιέσεων στην διεπιφάνεια αψιδοστάτη-επιχώματος όταν η βάση υποβάλλεται σε παλμούς Ricker περιόδου T_E = 0.90 sec και εύρους επιτάχυνσης a_p = 0.2 g, 0.6 g, 1 g.

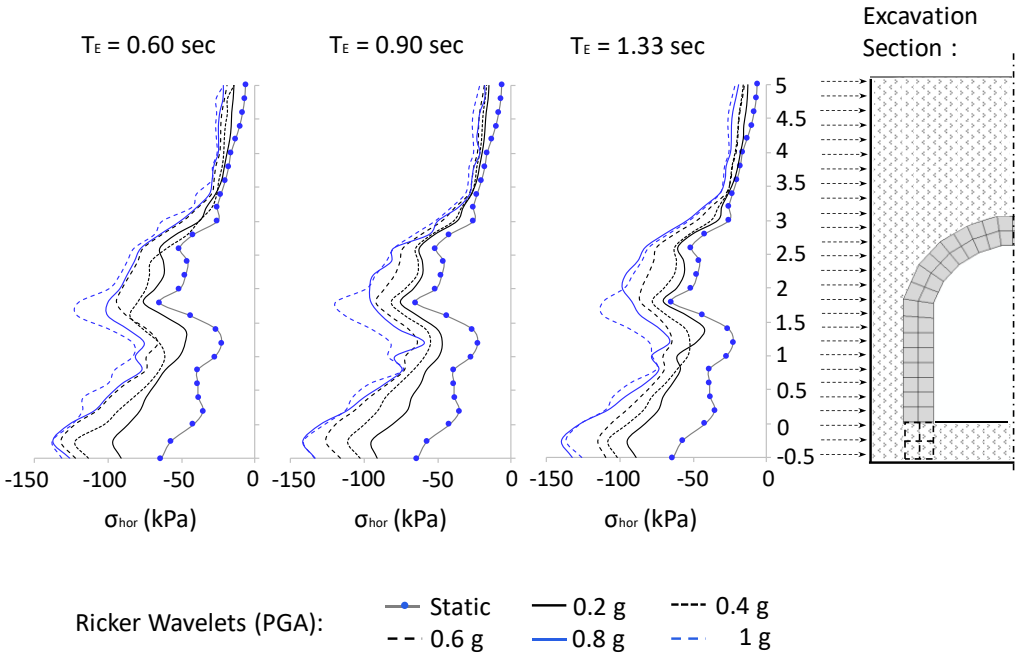

Σχήμα 38 Εξέλιξη των πλευρικών τάσεων που αναπτύσσονται κατά μήκος του αριστερού ορίου εκσκαφής όταν παλμοί Ricker με τρεις διαφορετικές περιόδους (T_E = 0.6 sec, 0.90 sec & 1.33 sec) διεγείρουν την βάση. Για κάθε περίοδο η κατασκευή υπόκειται σε ένα ευρύ φάσμα επιταχύνσεων a_p από χαμηλές τιμές (0.2 *g*) σε μέτριες (0.4 *g*, 0.6 *g*) και πολύ δυνατές (1 *g*). Απεικονίζεται επίσης η κατανομή των πλευρικών τάσεων υπό στατικές συνθήκες.

TABLE OF CONTENTS

CHAPTER 1:

Introduction

1.1 Problem description

Historic building and structural environment of Greece is a valuable asset of the Hellenic Cultural Heritage. Considering though, that it is increasingly threatened with deterioration, loss of integrity or even worse with total failure, scientific research is focused at developing case-oriented intervention methods to counteract these long-term effects. Stability of monumental structures is affected by many factors which should all be taken into consideration when preservation, restoration, rehabilitation or strengthening procedures are about to be conducted. In order to address this issue, we should first explore thoroughly one of the principal components of those heritage structures which is the *masonry arch*. Figure 1.1 summarises some representative examples of historical monuments where the arch is the fundamental structural element.

A masonry arch is an articulated structure, composed of wedge-shaped stones (voussoirs). These stones are arranged on a curved line retaining their position by mutual pressure. Occasionally, they are also reinforced with mortar at joints. The self-weight of the arch along with any other load the arch sustains, are transferred through the voussoirs across the joints, from the overlying to the underlying element. Once the keystone (central voussoir) is placed at the apex of the arch, the voussoirs are locked into position bearing the lateral and vertical stresses and binding the structure of the arch together.

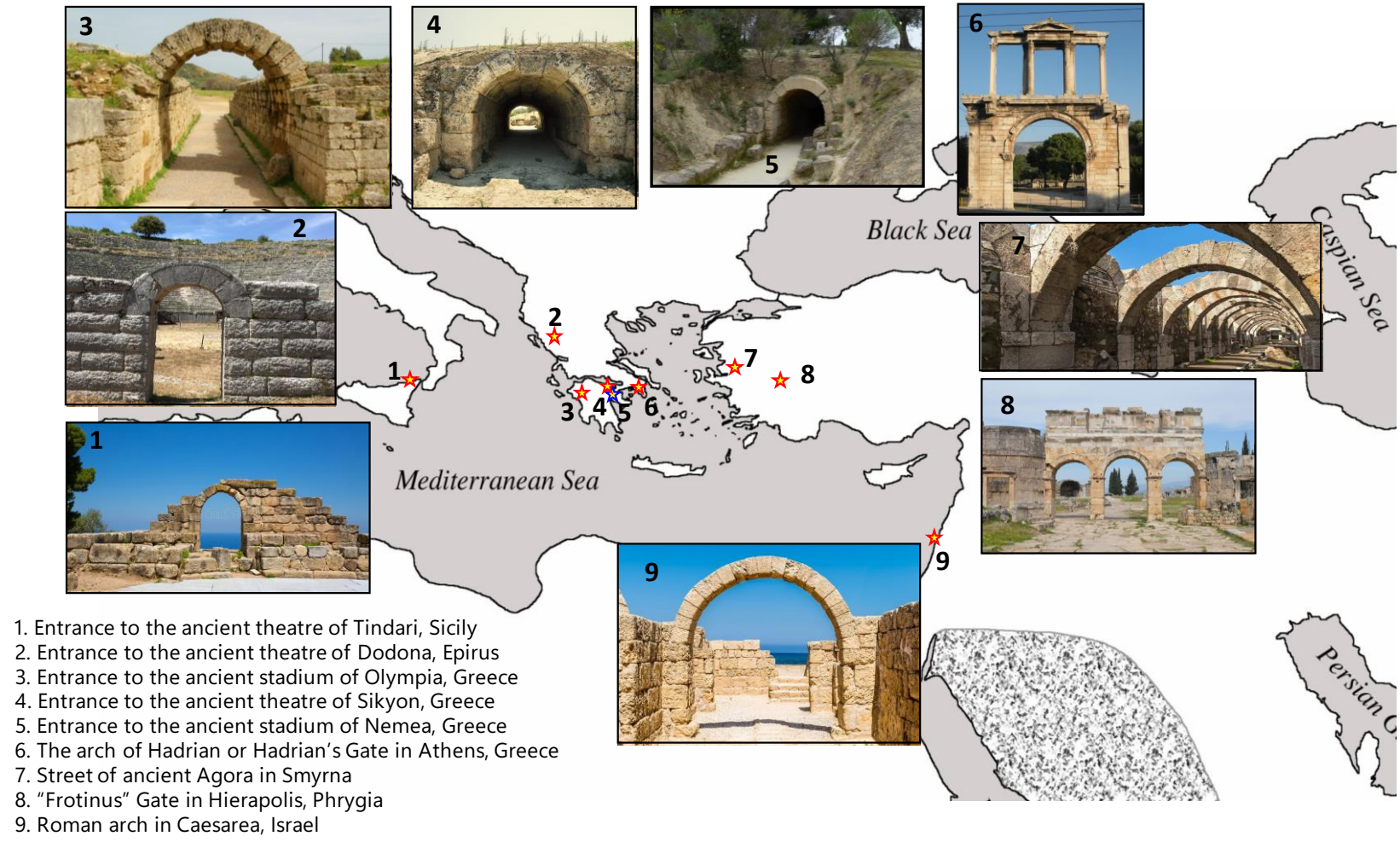

Figure 1.1 Some representative examples of historical monuments around the Mediterranean Sea: masonry buttressed arches-arcades and barrel vaults embedded in soil.

The basic parts of a masonry arch supported on buttresses are depicted in Figure 1.2. The so-called extrados and the intrados lines of the arch, namely the convex and the concave side respectively, are highlighted with continuous bold black line and dotted respectively. The highest point of the extrados is called the crown.

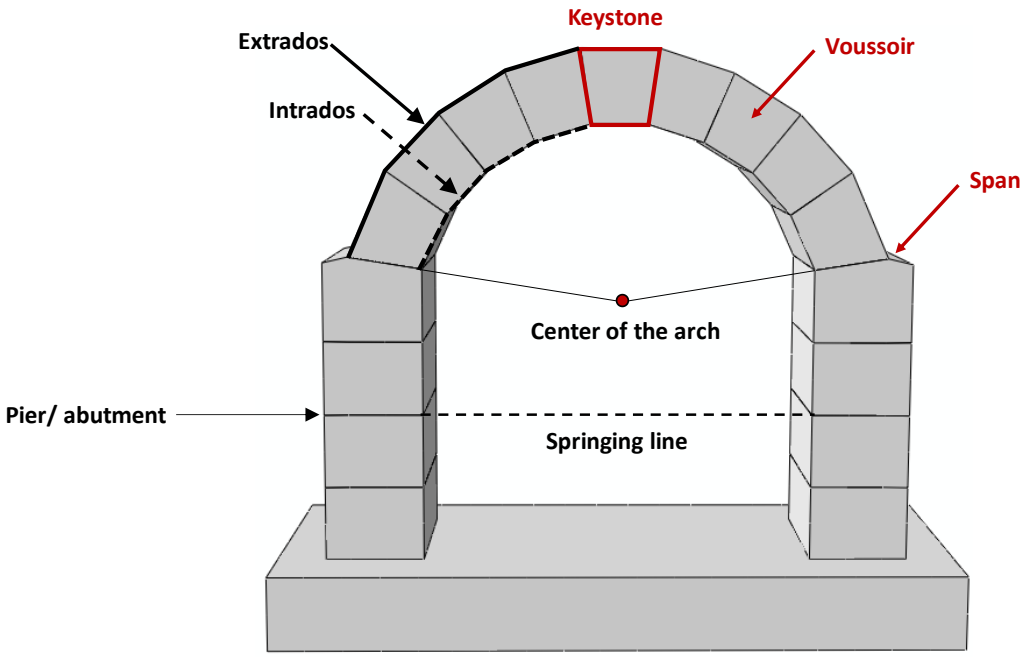

Figure 1.2 Geometry of a masonry arch supported on abutments

Masonry behaviour is mainly described with the lower strength in tension than in compression. In the majority of the scientific studies, the Heyman masonry model (19, the idealised rigid in compression tensionless material is used as the basic approach for the masonry analysis. Under a given loading path, masonry structures can suffer cracks or detachments generating displacement fields called mechanisms, which develop in the absence of any material failure. Collapse may occur solely due to loss of equilibrium even in masonry with infinite compressive strength. Specifically, failure of the arch may occur through the formation of four hinges that turn the arch into a mechanism.

Despite the wealth of results that have been published over the years on the static performance of arches, it is still considered a subject not fully explored and difficult to assess accurately. Most of previous studies are focused on the circular uniform profile and pseudo-static limited equilibrium analyses.

In this work, seismic response of masonry arches is examined by means of analytical and numerical methods. It is of great importance to develop simplified procedures for estimating the levels of low-amplitude arch response in earthquake prone regions. Once rocking occurs, the rigid body mechanism is mobilised. The dynamic response under base excitation turns into a geometrical problem and depends on initial conditions.

With reference to the interplay between structure and soil, monuments of the Hellenic territory can be grouped in two major categories: (i) *Structural systems* rising above the ground such as historical buildings, ancient temples, arches, entrance gateways, bridges etc. In this type of structures, soil performs exclusively as a supporting medium, as superstructural loads are transmitted to it through foundation (either shallow or deep). On the other hand, as an example of deep foundation, piles have been used embedded in the soil stratum of the Amphipolis bridge. Some representative examples of the above described foundation systems are portrayed in Figure 1.3; (ii) *Geo-structures*, namely structural systems lying on or below ground level. In this case, soil is not only a supporting medium but it may also exert loads to the structure through its self-weight or even be retained by it. Some examples are: *Cut and cover* structures such as tumulus tombs (Kasta Tomb in Amphipolis, tholos tomb in Acharnes) or vaulted tunnels (entrance at ancient stadium of Nemea, entrances at the Sikyon theatre). *Bored tunnels* such as the Eupalinian aqueduct. *Retaining structures* such as bastions which are elements of monumental fortifications, as part either of a castle (Corfu, Mytilene etc.) or of a town's acropolis (Acropolis in Athens). Ancient theatres can also be included in this category (ancient theatre of Dodona, Epidaurus, Sikyon). Their geotechnical behaviour is twofold. They can be considered a foundation system as much as a retaining system.

All kinds of monumental structures are meant to withstand through a series of soil-induced long-term effects. These cumulative effects are more pronounced on geo-structures as unfavorable soil conditions can cause major damages not only to the foundation alone but also to the structure of the monument. Poor soil conditions are generally a consequence of an ongoing process the effects of which become evident through the years. In addition, high seismic activity encountered in Greek territory, apart from the structures themselves, may deteriorate soil conditions in the long run. Finally, man-induced activities such as excavations, construction of new buildings, tunneling or even changes in the water table may also affect soil conditions in the vicinity of geo-structures.

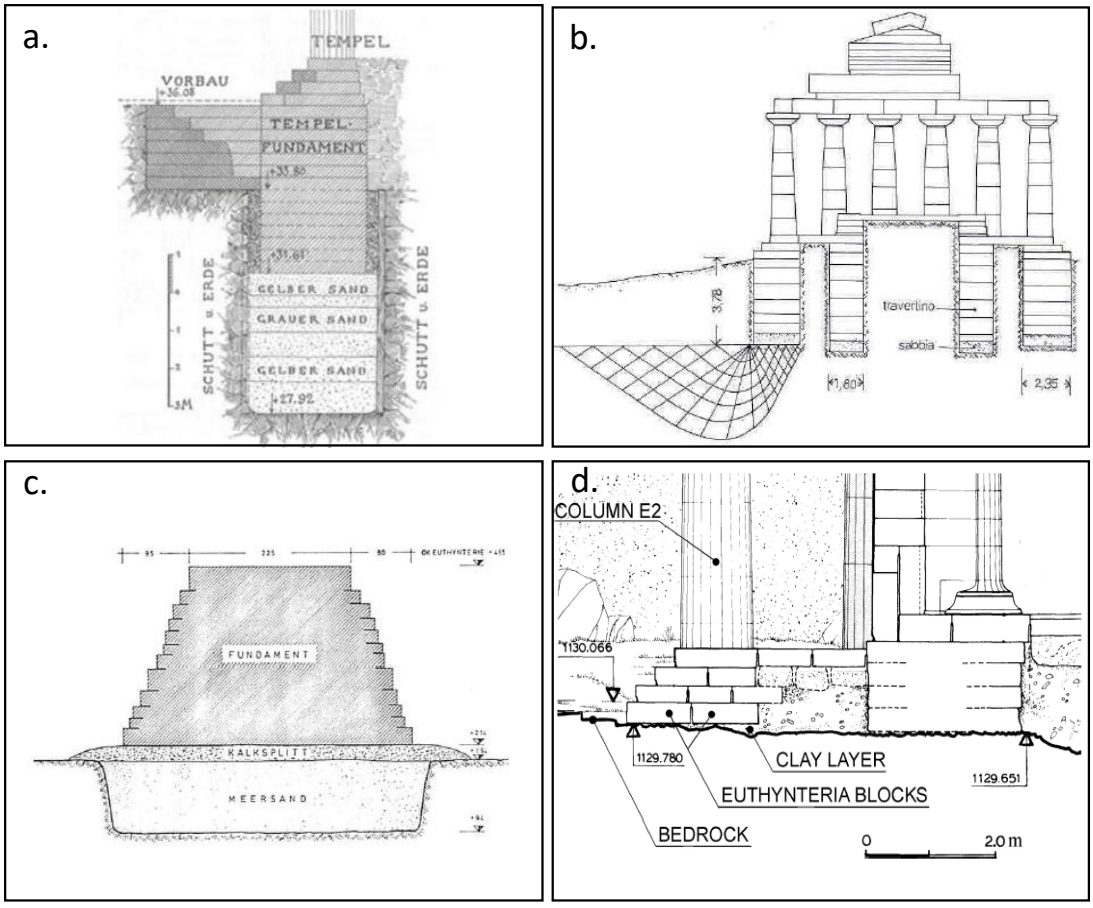

Figure 1.3 Foundation systems of iconic monuments of antiquity: a) temple of Athena in Ilion, b) Athenaion of Paestum, Italy, c) Heraion in Samos, and d) temple of Apollo Epikourios, Peloponnese.

1.2 Primary objectives of the study

The research aim of this thesis is to offer new knowledge on the response under static, pseudo-static, and dynamic loading of masonry arched structures whether they are above or below the ground surface.

In particular, the aim is to extend previous works on the rocking failure mechanisms of such structures and to prompt the interest of the scientific community on the soil-structure interaction of heritage masonry barrel vaults, loaded statically (under their self-weight and overburden soil) or excited dynamically by idealised pulses, and real accelerograms.

The main idea therefore is to integrate the developed methods with the restoration studies of the historic buildings.

Within this framework the primary objectives of the study can be summarised as follows:

a) to contribute to the rocking response of the simplest form of an arch structural element: the circular arch
b) to extend analytical and closed-form solutions to more complicated geometrical forms of the arch
c) to evaluate and develop methods based on limit equilibrium analysis in order to identify the failure mechanisms when the arch structure is supported on buttresses, as well as to examine the rocking response when subjected to idealised pulses
d) to incorporate the role of soil to the structural response of barrel vaults

Three fundamental arch structures are thoroughly investigated in this thesis:

- The arch structure in its simplest form on a rigid base. Two different profiles are taken into consideration, the *circular* and the hybrid elliptical-circular called from now on *"part-elliptical"* (Figure 1.4a).
- A masonry barrel vault (which behave as a series of side-by side arches) supported by lateral walls. Assumed for simplicity for the static and dynamic

analyses, the masonry vault is thus reduced to that of a masonry vault with equal profile and thickness (Figure 1.4b).

- A common barrel vault with part-circular uniform profile supported at its ends by transverse walls, and surrounded by soil. Soil-structure interaction is taken into account (Figure 1.4c).

The following analysis procedures will be undertaken in order to attain these objectives:

- Analytical methods incorporating Limit Equilibrium Analysis. Although the traditional limit equilibrium analysis based on geometric formulation (identification of a limiting thrust line) has gained widespread use among arch equilibrium studies, its complicated nature renders it time consuming. Many researchers have overcome this drawback by developing an energy approach utilising the principle of stationary potential energy (Alexakis and Makris 2013, 2014, 2015, 2017, 2018). Other analytical treatments include: (a) the Lagrangian method, a convenient tool for the analysis of the dynamic system, (b) a general-purpose software for mathematical applications (Mathematica) which is occasionally used, and (c) an archetypical equation of non-linear vibration theory (linear second-order ordinary differential equation called Mathieu function)
- Numerical analysis is accomplished by using the comprehensive finite element code (Abaqus). Two and three dimensional models are designed in the Abaqus environment while implicit and explicit integration algorithms respectively, are utilised to compute the linear, the non-linear static, and the dynamic response of the system.

a) The arch structure on a rigid base

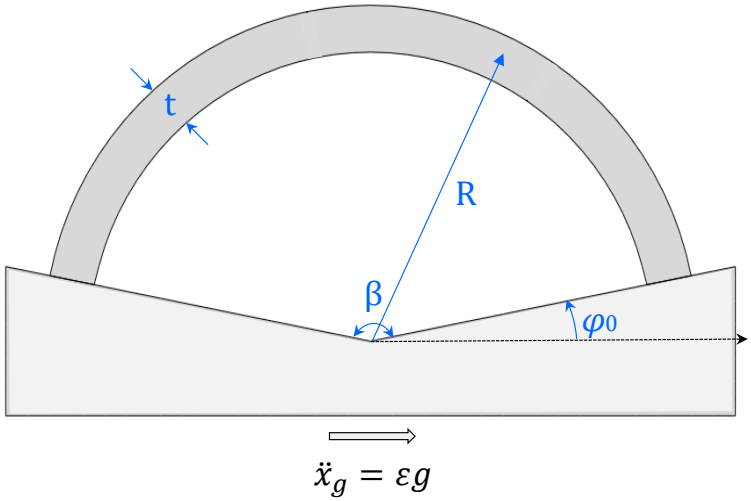

(i) "*part-circular*" profile

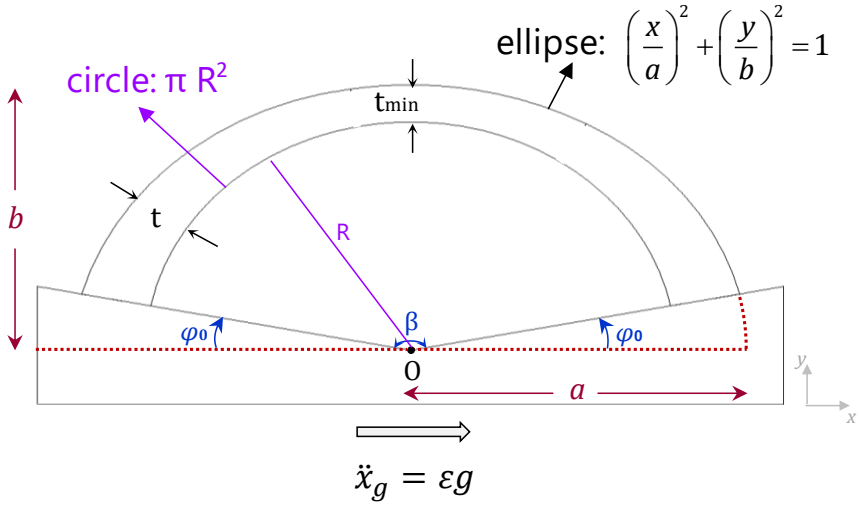

(ii) "*part-elliptical*" profile

b) The buttressed arch

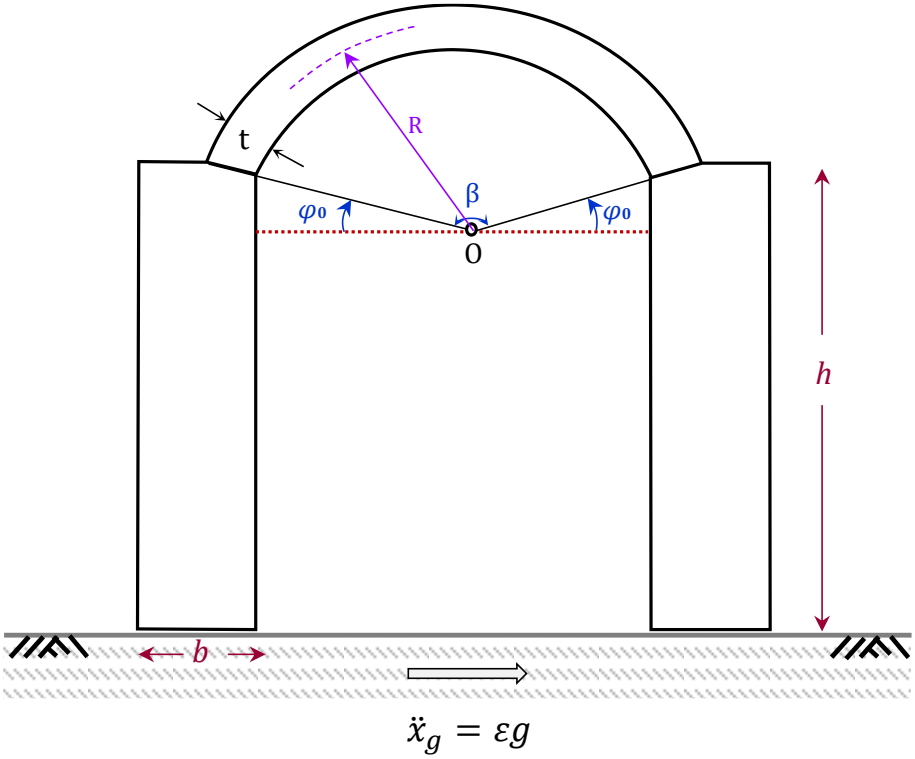

c) The embedded buttressed arch

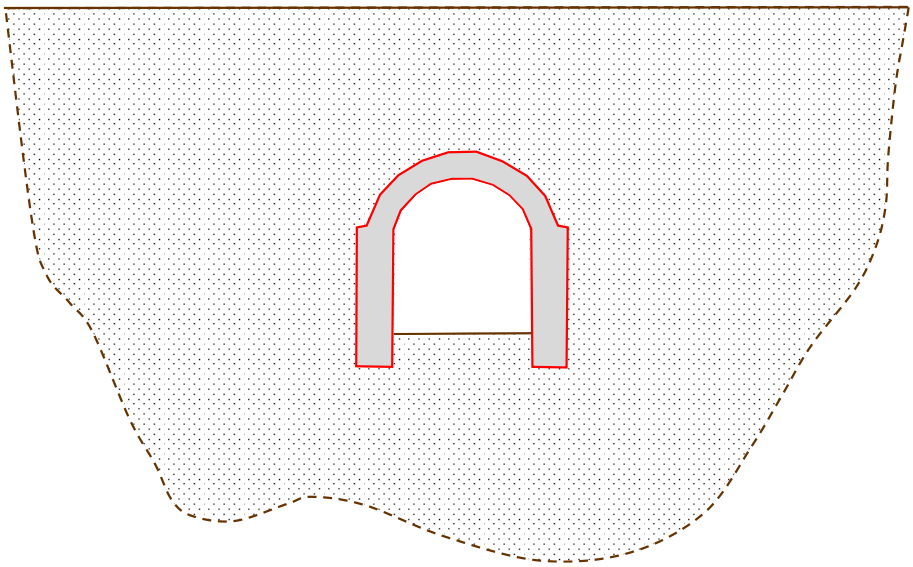

Figure 1.4 The fundamental arched structures investigated in this thesis: a) the arch structure (circular & part-elliptical profile) on a rigid base, b) the buttressed arch, c) the embedded buttressed arch.

1.3 Outline of thesis

In **Chapter 2** of the thesis, an extensive literature survey in principle, addresses three main topics:

- Pseudo-static analysis of masonry arched structures which involves the determination of the governing collapse mechanism depending on the geometrical parameters of each structure
- The dynamic analysis of such structures accelerated on their base by idealised pulses
- Soil-structure interaction employing fully covered arched structures

In **Chapter 3**, seismic response of masonry arches is examined in this study by means of analytical and numerical methods. Emphasis is placed on the low-amplitude levels where linearisation techniques may be efficient. When dealing with monumental arches of fragmented masonry, rocking rotation even in low levels is most often undesirable as it may lead to severe permanent displacements and dislocation of the arch axis, and sometimes to general instability of the structure. It is therefore of great importance to develop simplified procedures for estimating the levels of such low-amplitude arch response in earthquake prone regions. Near-source ground excitation at the base of the structure is idealised with rectangular and cycloidal pulses. The analysis is limited to the prior-to-impact regime in which rocking occurs between successive fragments (voussoirs). Yet, this limitation does not prevent from extracting conclusions, as the prior-to-impact state is the most crucial to rocking response and it can determine whether the structure will undergo rocking vibration or eventually overturns. For simplicity, a specific kinematic mechanism of the fragmented arch, well-known in the literature is implemented throughout the study, thus allowing for comparison of the results with existing solutions. This idealisation is justified as the predominant mechanism from both previous analytical and experimental studies. A good correlation of the results between simplified closed-form solutions and rigorous semi-analytical methods is accomplished. Moreover, these results are also quite close to those of the 2-d finite element analysis.

In **Chapter 4**, a segmental arch consisting of an elliptical upper part (extrados) and a circular lower part (intrados) is introduced. This so-called part-elliptical arch is treated as a rigid monolithic body enabled to rock on a triggering base. The objective of the study is to extend the established methods applicable to the conventional circular arches, particularly in terms of: (a) stability analysis which is performed in static terms to calculate the hinge locations as well as the minimum ground acceleration at the onset of rocking, given the slenderness and the angle of embrace of the arch ($t/R, \beta$), (b) time-history analysis of rocking prior to impact is then feasible as the transition criterion from the full-contact to rocking phase has been established from the previous step. The results are presented comparatively to those extracted from the circular arch of the same geometric characteristics.

In **Chapter 5**, the arch structure supported on buttresses is introduced. Buttresses operate by applying a counterforce opposing the thrust induced by the arch. In addition to the arch geometry, buttress dimensions play a crucial role to the horizontal capacity of the entire structure. Depending on the arch-to-buttress relative proportion, three different hinging mechanisms can arise as mentioned in the literature. The aforementioned states (mechanisms) regard the location of the four ruptures (hinges) that will initiate the rocking mode of the structure. The cases where Mechanism II is mobilised are investigated. Furthermore, a three dimensional finite element model of two different geometries, consisting of individual voussoirs is triggered with idealised pulses of various frequencies and acceleration amplitudes. The nonlinear response of these structures is determined by the produced overturning spectra and the developed collapse mechanisms.

In **Chapter 6**, soil structure interaction effects are implemented to investigate the stability of masonry arches supported on buttresses. Initially, a schematic illustration of the model under its self-weight and the forces acting on it are presented along with two possible cases of pressure redistribution above the structure. In the first case the arch sustains the whole overburden load whilst in the second case the phenomenon of arching effect is associated with the transfer of the load at the surrounding soil. Emphasis is given to the construction sequence of the cut & cover structure throughout

the whole chapter. A series of sophisticated nonlinear FE analysis is performed to models whose soil profiles are described as homogeneous cohesive. The elastoplastic soil behaviour under undrained conditions is described with Von-Mises failure criterion combined with an isotropic and kinematic hardening model in the post-yielding domain. Considerable attention is given to the induced lateral earth pressures and displacements acting on crucial points. The effect of the arch geometric characteristics is also investigated and the results are presented comparatively. Ultimately, the soil stratum is subjected to idealised pulses and records of acceleration time histories. Some of the most iconic monuments of antiquity embedded on soil are depicted in Figure 1.5.

Figure 1.5 Geo-structures of antiquity: (a) vaulted tunnel at the Entrance of Nemea stadium, (b) vaulted tunnel at the Entrance of Sikyon Theatre, (c) tholos tomb in Acharnes, and (d) bored tunnels at the Eupalinian aqueduct.

CHAPTER 2:

Literature Review

2.1 History of Arches

Father Vicente Tosca, architect, philosopher, mathematician and astronomer very wisely stated that:" *The subtlest and more exquisite part of Architecture ….is the formation of every sort of Arches and vaults*" (a part of his Compedio mathematico, 1707-1715). *Arching* as a mechanism of load transfer is inherent to continuum systems such as structural (e.g. a masonry wall with openings) or even natural (i.e soil medium). Master builders of antiquity soon captured this mechanism and acknowledged its benefits on the design of wider spans yet heavily loaded at the same time. Under this perspective, they devised structural forms either 1-dimensional, axial-type (arches) or 2-dimensional, shell-type (vaults, domes), in which arching is the predominant load transfer mechanism.

Two primitive archetypes of spanning a space by diverting the vertical load paths are (a) the post and lintel system and (b) the corbelled (or false) arch. The masonry structures illustrated in Figure 2.1 are prominent examples of these structural forms. which are believed to have set the basis for the evolution of spanning an opening: (a) the Lion Gate at Mycenae with the characteristic relieving triangle dated back to 1300 B.C. (Figure 2.1a), (b) the sanctuary of Hercules in Delos (Figure 2.1b). In particular, the former consists of strong horizontal elements (lintel) which laid across the top surfaces of vertical elements (posts). The latter can be regarded as a precedent step for the master builders until they acquire the empirical skill necessary to construct true stone arches with radial joints. Their similarity is only geometrical as their structural behaviour is fundamentally different. For example: (i) the horizontal stones at the key section are unable to transfer thrust, (ii) not all the structure's tensile stresses caused by the weight

of the superstructure are transformed into compressive stresses, (iii) only friction opposes the stones from sliding.

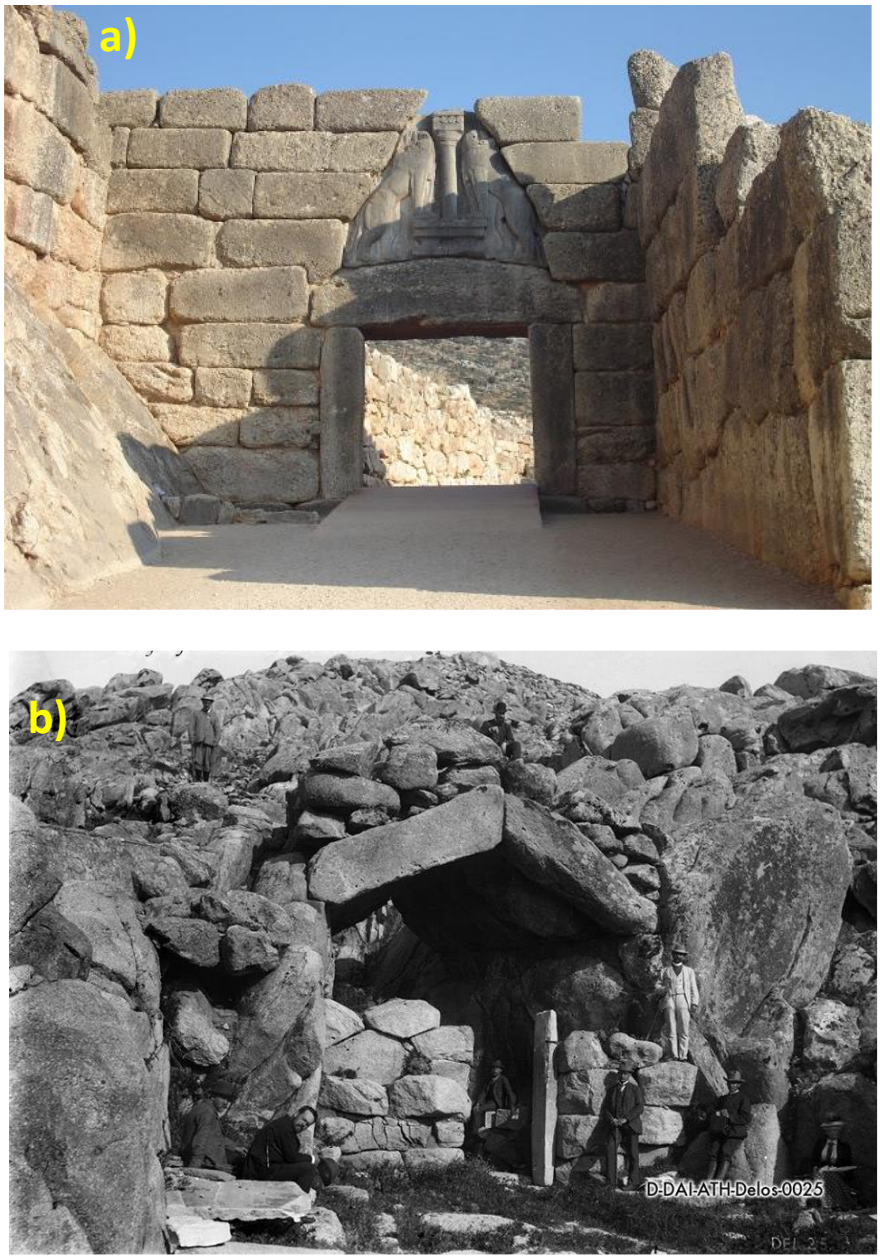

Figure 2.1 Examples of a post and lintel system (a- the Lion Gate at Mycenae) and a false arch (b- the sanctuary of Hercules in Delos).

The history of Curved Architecture dated back to the prehistory. Stone arches were erected in Babylon about 6000 years ago. Outstanding examples of vaulted tombs are the Royal tholos tombs in UR Mesopotamia dated at 3000 B.C and in Greece dated at 1250 B.C (tomb of Agamemnon). Roman builders evolved further the architecture of

arched structures. A better arrangement of the stones at the curved surface along with the usage of mortar between the voussoirs allowed the construction of wide-span vaults and therefore opened a gateway for the widespread usage of the arches in many constructions like bridges and aqueducts.

Vaulted structures in Greece were erected to serve as entrances to ancient stadiums or theatres. Some examples of such structures are the vaulted tunnel at Nemea of 36 m length (built at 400 B.C), the vaulted tunnel at Olympia of 32 m length (built at 300 B.C) and the vaulted tunnel at Sikyon of 16 m length (built at 300 B.C).

As a continuation of the ancient Greek architecture, remarkable new arch typologies were developed in the Byzantine architecture. The distinguished architectural features in medieval structures (which are characteristic examples of Gothic architecture) are the ribbed vaults portrayed in Figure 2.2.

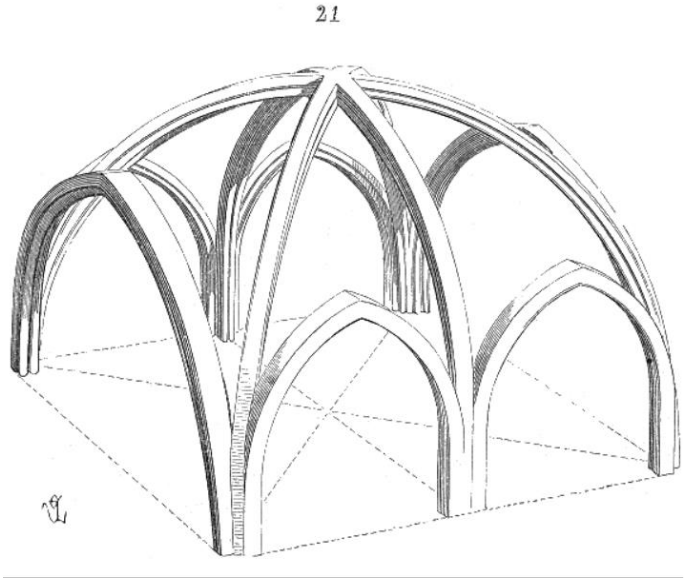

Figure 2.2 A six-part Gothic ribbed vault (Drawings by Eugene Viollet-le-Duc).

2.2 Origins of the statics of the Arch

The first approach of defining the mechanical behaviour of the arch was attributed to **Leonardo Da Vinci** (1451-1519). As reported by Marcolongo he stated that: "*…arch is no more than a strength caused by two weaknesses*, *in that in its construction the arch is composed of two quarter circles each of which*, *being in and of itself very weak tends to fall*, *but as each opposes this tendency in the other*, *the two weaknesses are transformed into one strength*". He made some experimental tests on an arch and came up with a criterion of safety reported in Figure 2.3b and a failure rule reported in Figure 2.3c. He also synthetised the failure rule with these words: "*…the arch will not crack if the chord of the outer arch will not touch the inner arch…*".

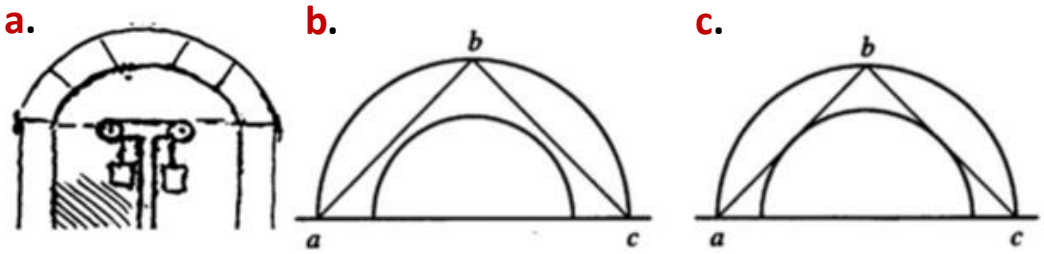

Figure 2.3 a) Experimental test on an arch by Leonardo da Vinci, **b)** the safety criterion and **c)** a failure rule.

In 1675, **Robert Hooke** gave an insightful interpretation of the masonry arch equilibrium: "*…as hangs a flexible cable so*, *but inverted*, *will stand the arch*". The analogy between inverted funicular curve and rigid masonry arches is depicted in Figure 2.4.

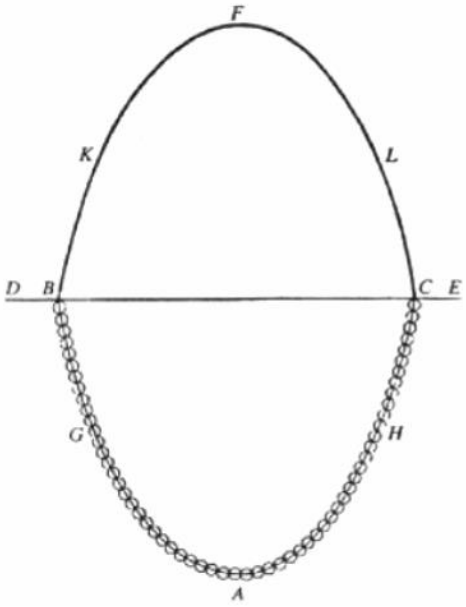

Figure 2.4 Hooke's analogy as schematised by Poleni: the catenary in tension under its own weight and a rigid arch standing in compression.

2.3 The evolution of theories of Arch statics

In the core of these efforts, the following studies confirmed what master builders knew by empirical intuition: arch equilibrium is a pure geometric problem rather than a problem in strength of material.

- Limit equilibrium analysis based on geometrical formulation:

Gregory (1691) understood that the catenary was the proper shape of a uniform arch carrying only its own weight and stated that an arch of any other shape could stand only by virtue of a catenary being contained within its thickness. Interpreting this statement in terms of lines of thrust, it is, as will be seen, as precise preformulation of the lower bound theorem of plastic theory (Heyman 1968).

De la Hire (1695) studied a semi-circular arch as an assemblage of rigid voussoirs and considered no-frictionless joints. He introduced the force polygon and the corresponding funicular polygon for assessing the arch static equilibrium. La Hire's

conception of the funicular polygon triggered the succeeding framework of graphical statics.

Couplet (1729), in his pioneering work, was the first to successfully demonstrate the way a semi-circular arched structure can safely withstand its gravity load, in the framework of a structural mechanics approach. He unveiled the purely geometrical nature of the problem in a sense that collapse is not associated with material crushing but it involves the mobilisation of a kinematic mechanism. Accordingly, a graphical approach can be introduced to determine potential equilibrium or collapse mechanisms through the notion of the thrust line. Equilibrium is established when the thrust line lies inside the arch, whereas collapse occurs as soon as the thrust line intersects the external curves. Couplet calculated the minimum required slenderness, t/R, of the semi-circular arch so that the thrust line be marginally bounded by the outer lines of the arch and limit equilibrium be established. This assumption was based on a failure mechanism through the formation of four hinges but Couplet erroneously predefined the intrados hinges at an angle of 45° with respect to the spring points.

Coulomb's theory (1773), which was developed on his study "*essai sur une application de regies de maximis & minimis a quelques problemes de statique*, *relatifs a l'architecture*", constitutes a milestone in the evolution of the arch equilibrium. The main objectives are: (i) the presence of a pressure line within the arch isn't an indication of the arch safety, hence neighboring admissible mechanisms should be examined, (ii) the arch failure occurs only with the formation of hinges at the joints of the voussoirs, (iii) friction is enough to prevent any sliding, (iv) the lower and upper limit for the value of horizontal thrust is defined through the method of maxima and minima.

Moseley (1843) introduced the terms: a) 'line of resistance' (or line of thrust) which is defined as the geometrical locus of the points of application of the resultant thrust force that develops at any cross section of the masonry arch, and b) 'line of pressure' which was calculated by searching for the optimal position of this curve via the so-called principle of minimum pressure. He also stated that the line of thrust should not pass outside the entire cross-section.

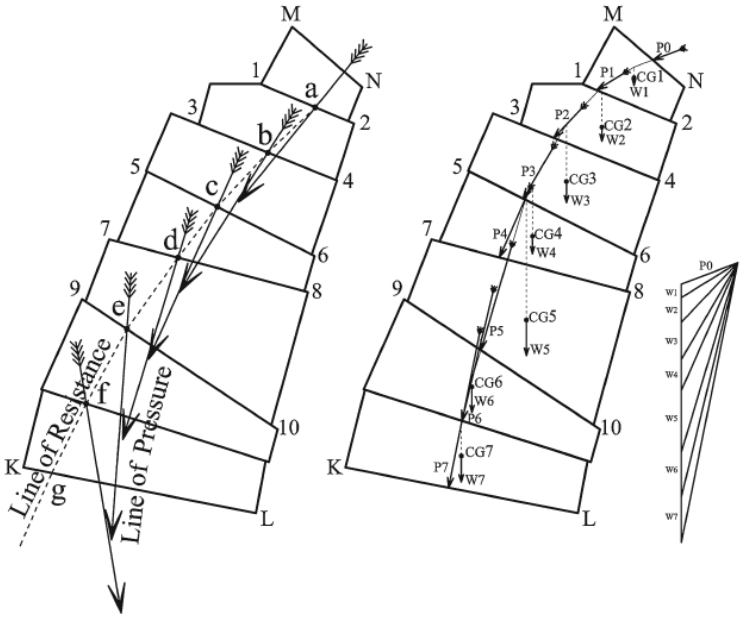

Figure 2.5 A conceptual drawing presented by Moseley which distinguishes the line of resistance (line of thrust) from the line of pressure (funicular polygon).

Milankovitch (1907), on his "well-established" theory over the equilibrium analysis of curved masonry arches, developed the thrust line concept (Drunkkurven) in the most rigorous treatment. Motivated by Couplet's innovative work revisited the theory of thrust line and derived the closed-form expression for the thrust line. He calculated correctly the centre of gravity of an infinitesimal voussoir and computed the exact location of the intrados hinge at 54.5°, thus correcting the minimum required slenderness, t / R, from 0.101 to 0.1075.

Pippard and Baker (1943) concluded that collapse occurs when the arch is transformed into a mechanism with the formation of four hinges (Figure 2.6). Pippard made experimental tests modelling arches of steel voussoirs. But, he erroneously interpreted the results in the light of the elastic theory rather than in terms of the recently ascenting plastic theory.

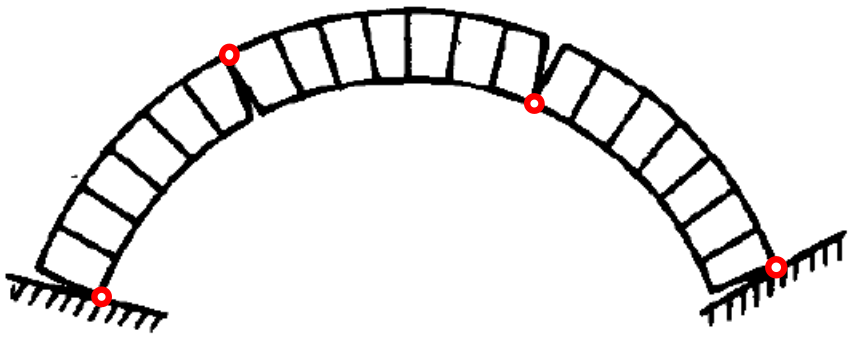

Figure 2.6 Collapse mechanism proposed by Pippard & Baker.

Many other researches in the literature, based on the above fundamental theories, interlarded the static approach of masonry arches.

2.4 Modern theories of arch statics

Kooharian (1952) discovered during his thesis that LA initially formulated for ductile steel structures could also be applied to structure composed of concrete voussoirs. Heyman would later recognise that this result was also valid for masonry structures satisfying the non-tension assumptions. The first systematic investigation of the stability of arches was made by **Heyman**. The equilibrium approach proposed for the static analysis of masonry arches, stemmed from the limit principles of the plastic analysis of steel structures. He also established three fundamental assumptions concerning material properties of the stone blocks: (a) infinite compression strength, (b) zero tensile strength, and (c) the coefficient of friction at the interface adequately large so that sliding be avoided. In so doing, the only way the arch collapses, is through the formation of 4 hinges that turns the arch into a mechanism.

- Limit equilibrium analysis based on energy approach:

As very aptly Alexakis and Makris (2023) pointed out: "*The principle of stationary potential energy is a powerful and simple tool to obtain rigorous solutions for the limit equilibrium state of curved structures without the need to describe geometrically the load path of forces of apply equilibrium in each individual block*".

In recent years, **Alexakis & Makris** investigated thoroughly the stability of a monolithic segmental arch setting the embrace angle, β, as a parameter of the design. They

demonstrated that in a continuous arch the hinge locations should not be predefined but they had to be computed. The fourth hinge position at the downstream of the left springing and the angle of embrace (β) were determined by the authors whereas the effects of the arch thickness *t / R* and the seismic loading ($\ddot{u}_g = e\ g$) on the hinges locations were under examination. In this way, they introduced a variational formulation incorporated in the principle of stationary potential energy to derive the minimum thickness slenderness, t/R, for different values of β. The results demonstrate the favourable role of base confinement, as the minimum required slenderness, t/R, gradually reduces from 0.1075 at the semi-circular arch ($\beta = \pi$) down to 0.0075 at the segmental circular arch of $\beta = \pi/2$. The authors extended the above-mentioned work on circular arches to elliptical ones and on single-nave barrel vaults (circular arch supported on two rectangular buttresses). Figure 2.7 portrays the three systems under examination.

Lame and Clapeyron's findings (1823) over vertical and radial rupture at the hinge position lead them to analyse the arch response for both directions. The solution was based on energy approach and specifically on the application of the principle of stationary potential energy, leaving aside the well-known geometric approach of the thrust line. Moreover, they introduced a twofold transcendental equation suitable for calculating either the arch size for a given loading or the sustainable loading for a predefined arch. Finally, they conclude quoting equations that give the exact positions of the three unknown hinges as well as the minimum thickness t / R for a given angle of embrace.

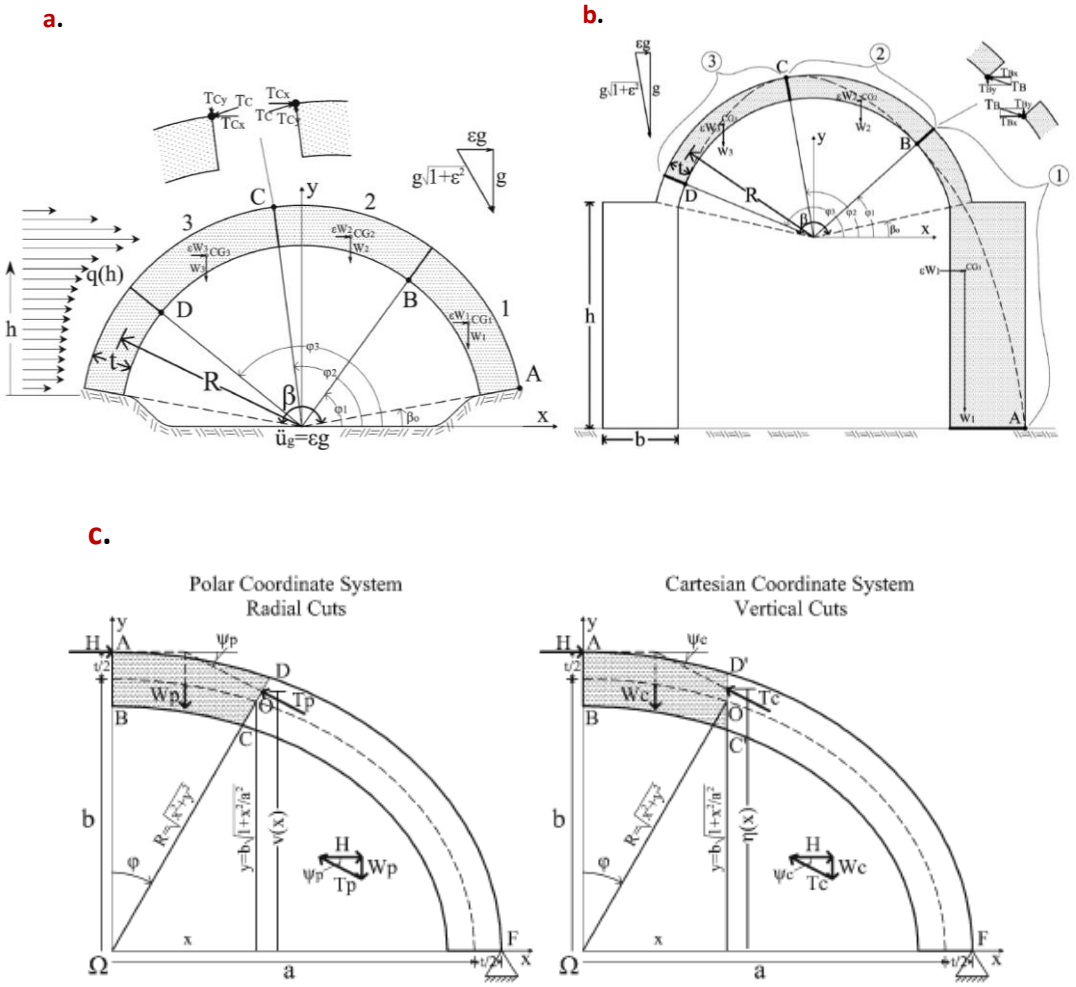

Figure 2.7 Formation of a four-hinge mechanism in: **(a)** a circular arch, **(b)** single-nave barrel vault, **(c)** an elliptical arch when subjected to a horizontal ground acceleration (Alexakis & Makris 2013, 2014, 2017)

2.5 Dynamic analysis methods

Unlike the stability of the masonry arch under self-weight, the response due to lateral dynamic loads didn't receive much attention until **Oppenheim**'s notable work, merely in 1992. Inspired by **Housner's** paper on rigid blocks rocking on a moving base, Oppenheim treated the masonry arch as a rigid body subjected to idealised pulses. He derived the nonlinear equation of motion of a segmental circular arch consisting of seven voussoirs, each one obeying Heyman's limitations, which together with the supporting base form eight radial joints. To derive this equation Lagrangian Mechanics was employed. Since the arch is not considered as a monolithic structure, the imminent

hinges can occur only at these predefined physical joints. Upon the application of rectangular pulses as input base motion, the arch was converted into a four-link mechanism with one degree of freedom of fixed hinge locations. This procedure allowed for the computation of the arch motion before the first impact occurs. Within the framework of time-history dynamic analysis it is critical to determine the criterion for the phase transition from the full contact to rocking regime. Stability analysis in static terms can be used to this respect, on the condition of incipient uplift.

Among all the kinematically admissible mechanisms (each one is characterised by a different equation of motion, and corresponding to a different level of minimum horizontal ground acceleration for the onset of the mechanism motion) Oppenheim addresses the one which is associated with the lowest such minimum $\ddot{x}_g$ for the onset of motion, namely the "theoretical governing mechanism" which was later confirmed by computational and experimental results. Evidently, the dynamic response under base excitation is a geometrical problem and depends on initial conditions.

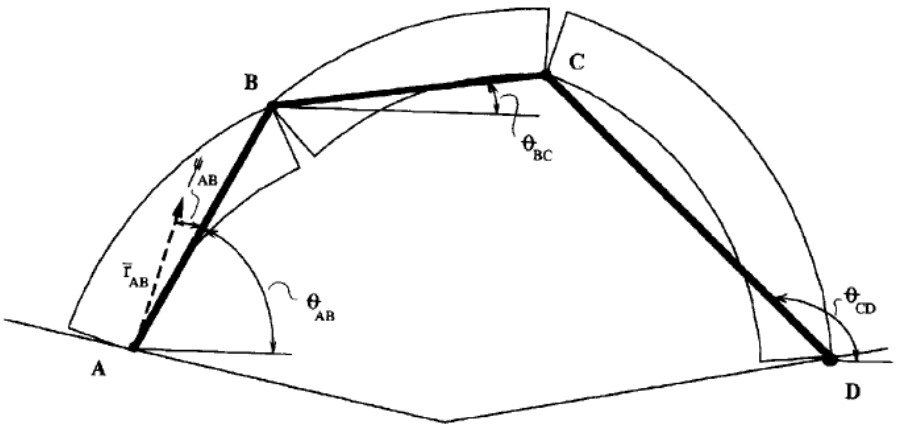

Figure 2.8 Rigid prism mechanism motion of an arch by Oppenheim (1992)

Clemente (1998) on the other hand, addressed dynamic response through pseudo static analysis. An iterative procedure based on energy and geometric approach (via virtual work and thrust line respectively), was used to track down the collapse mechanism of a structure subjected to horizontal acceleration. After defining the minimum accelerations needed to set geometrically different arches into motion, he examined arch response during free vibration as well as under rectangular and

sinusoidal pulses. Emphasis was given on kinematic characteristics (frequency and amplitude) without yet taking impact and damping into consideration.

De Lorenzis (2007) et al moved a step further calculating analytically the arch response after the first impact of rigid blocks, when hinges reopen and a new four-link mechanism is formed.

Ochsendorf (2002), based on Clemente's concept, proposed an alternative iterative procedure for stability analysis under constant horizontal acceleration. A growing interest in the stability assessment of masonry arches using the limit analysis theory has lately been emerged in literature (Dimitri, 2015; Cavalagli, 2017; Di Carlo, 2018; Zampieri, 2017; Stockdale, 2019, 2020). Recent studies further contributed to the arch seismic response under pulse-type ground motion, based either to analytical or to numerical methods (De Lorenzis, 2007; Dimitrakopoulos, 2013; De Santis, 2014; Gaetani, 2017; Leontari, 2018; Kollar, 2019). In the latter, primarily the finite element method (FEM) as well as the discrete element method (DEM) are involved. A thorough comparative study on these methods has been presented by **Sarhosis** et al (2019). Many researchers have extensively implemented the DEM (Dimitri, 2015; Sarhosis, 2019; Cannizzaro, 2018; Pulatsu, 2019; Stockdale, 2020) to assess the collapse behaviour of masonry arches.

While masonry arches of a uniform circular and sometimes elliptical profile have been subjected to thorough scrutiny in the past, only a few studies have addressed the non-uniform arch (Dimitri, 2015; Zampieri, 2019; Tempesta, 2019). As an exception, Milankovitch in his doctoral dissertation developed the theory of the thrust line with reference to a masonry arch of variable thickness (Milankovitch, 1904). In the general case, the intrados and extrados lines are determined by two generic continuous functions so that the variable thickness of the arch ring can be considered. Despite the lack of theoretical background, the non-uniform arch has been implemented in the design of numerous historical bridges around the world. **D' Agostino & Bellomo** (2001) document that historical bridges of a large span have a gradually increasing thickness from the key to the springers at a ratio of 1.1 ÷ 1.6.

CHAPTER 3:

Linearised Response of Arched Structures under Pulse-type Excitation

3.1 Introduction

Arched masonry structures (such as vaulted bridges, cathedral domes etc.) are an important part of the cultural heritage worldwide. Although nowadays construction of this kind of structures is quite rare, the necessity of their preservation has spurred many researchers to thoroughly investigate collapse mechanisms, as well as ways to protect them against natural hazards and decay through time. In this context, Coulomb's (1821) and then Couplet's (1730) studies are highlighted, confirming what master builders knew by empirical intuition: arch equilibrium is a pure geometric problem rather than a problem of strength of material.

Early studies on the stability of masonry arches under gravity loads were made by Heyman (1966, 1969, 1982). The equilibrium approach proposed in these studies stemmed from the plastic analysis principles of steel structures. Within the framework of the limit state analysis, Heyman established three fundamental assumptions concerning material properties of stone blocks: (a) infinite compression strength, (b) zero tensile strength, and (c) coefficient of friction at the interface of subsequent voussoirs adequate large so that sliding be avoided. As a consequence, failure of the arch may occur through the formation of four hinges that turns the arch into a mechanism.

Motivated by Heyman's fundamental work, Clemente (1998) extended the static equilibrium approach to incorporate earthquake lateral loads. In this way the arch is considered to be subjected to a combination of constant horizontal and vertical acceleration (earthquake and gravity load respectively). Then equivalent static analysis

is performed to derive minimum levels of ground acceleration required to collapse the arch. It is denoted however, that this pseudo-static method actually provides the minimum peak ground acceleration required to initiate rocking motion and transform the arch into a mechanism. It depends upon the dynamic properties of the structure and the excitation characteristics whether the structure safely experiences rocking or eventually collapses.

Oppenheim was the first one to incorporate the time-dependent nature of dynamic loading (e.g. earthquake) into the analysis of the masonry arch. In his pioneering study Oppenheim (1992) inspired by Housner's work (1963) on free-standing rigid blocks rocking on an accelerating base and treated the arch as a rigid body assembly subjected to ground motion, through idealised pulses. This typical, circular arch consists of seven voussoirs, each one obeying Heyman's postulates. When subjected to dynamic loading, the rigid blocks may rock one to the other about fixed points, and the arched structure becomes a four-hinge mechanism with one degree of freedom. Among all the kinematically admissible mechanisms (each one is characterised by a different equation of motion, and corresponding to a different level of minimum horizontal ground acceleration for the onset of the mechanism motion) Oppenheim addresses the one which is associated with the lowest such minimum $\ddot{x}_g$ for the onset of motion, namely the governing mechanism. Evidently, the dynamic response under base excitation is a geometrical problem (characterised by the thickness ratio t/R and the angle of embrace β) and depends on initial conditions.

Clemente (1998) implemented time-domain numerical analysis to compute the dynamic response of the masonry arch once the pseudo-statically predicted ground acceleration required for rocking initiation is exceeded. He examined arch response during free vibration as well as under rectangular and sinusoidal pulses. Emphasis was given on kinematic characteristics (frequency and amplitude) without yet taking impact and damping into consideration. De Lorenzis et al (2007) moved a step further by calculating analytically the arch response after the first impact of rigid blocks, when hinges reopen and a new four-link mechanism is formed.

As already discussed, Oppenheim did not consider a continuous monolithic arch with zero tensile strength but rather a circular arch that consists of seven voussoirs. He further simplified the rocking arch to a 4-hinge mechanism whereas the location of the hinges is dictated by the governing mechanism (i.e. the one corresponding to the minimum peak ground acceleration). This theoretical prediction of the rigid body mechanism once rocking occurs was confirmed experimentally by DeJong et al (2008). Recently, Alexakis and Makris (2014) revisited the analysis of a continuous monolithic circular arch through limit equilibrium approach. The location of the hinges is in close agreement to those predicted by Oppenheim.

3.2 STATEMENT OF THE PROBLEM

Consider the model illustrated in Figure 3.1. Originally, the arched structure complies with the supporting base in a purely horizontal motion. When a crucial acceleration is reached, it launches a four-link rocking mechanism. Impacts may occur at four pivot points (A, B', C', D) where hinges are formed. It is assumed thereafter, that hinge formation can't take place in any other point along the arch. In view of this postulation the system can be simplified as a single degree of freedom. In accordance to the Oppenheim's model (1992) the geometric characteristics are: a) the angle of embrace $\beta = 157.5°$, b) the centreline radius R = 10m, and c) the ratio t / R = 0.15. Following Heyman's assumptions (1966), the stone material of the arched structure is of infinite compressive strength, zero tensile strength and a large coefficient of friction to avoid entering the sliding mode at any instant in the rocking motion. In addition, it is assumed that hinges locations are predefined.

3.2.1 Kinematics of arch response

During dynamic motion, a hinge point may move along the arch axis, therefore different instantaneous kinematic mechanisms are being developed. The governing kinematic mechanism according to Oppenheim (1992), is presented in Figure 3.1. This is the one that yields the lowest possible horizontal ground acceleration needed to set the arch to motion, and was chosen as the case study in the present work. A simplified

form of the arch in its initial and displaced state is presented in Figure 3.2, depicting only the links of the three parts (AB, BC, CD) formed before and after hinges (A, B, C, D) open. Links AB and CD perform rotational motion $(u_{AB,}\, u_{CD})$ considering A and D fixed. On the other hand, link BC performs a combination of rotational (u_{BC}) and translational (u_B) motion. Considering combined motion, the total kinetic energy of the rigid body at each moment is the sum of: a) the translational component and b) the rotational component about the instantaneous pole. The rotation of each link θ_ι measured anticlockwise from the horizontal, as well as rotation $\varphi = (\theta_0 - \theta > 0)$ with respect to the original geometry fully determine the motion. The presented kinematic mechanism is the result of the base acceleration to the left $(\ddot{x}_g < 0\ )$, causing a positive rotation (φ) of the arch which initially will rock to the right.

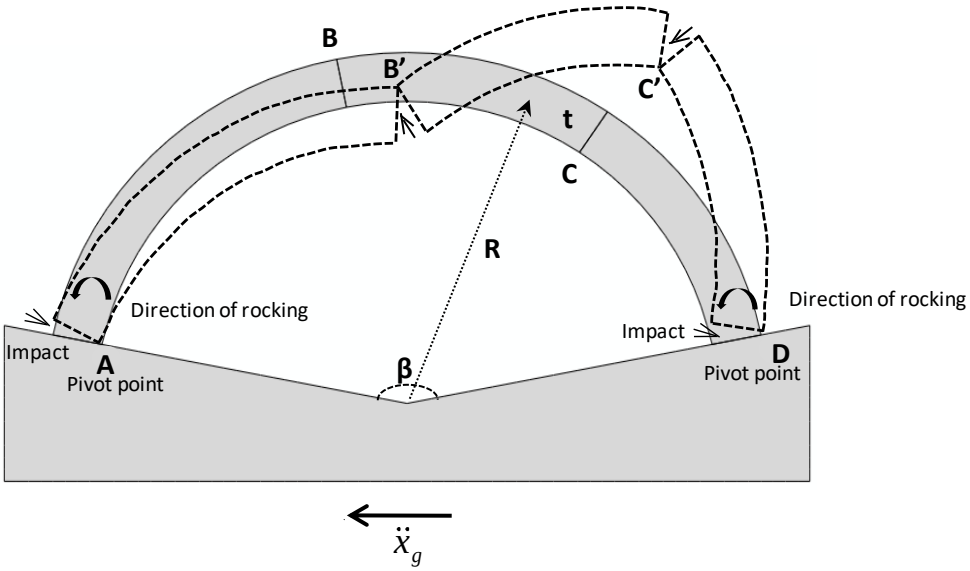

Figure 3.1 Rocking arch on a rigid oscillating base: configuration of the system.

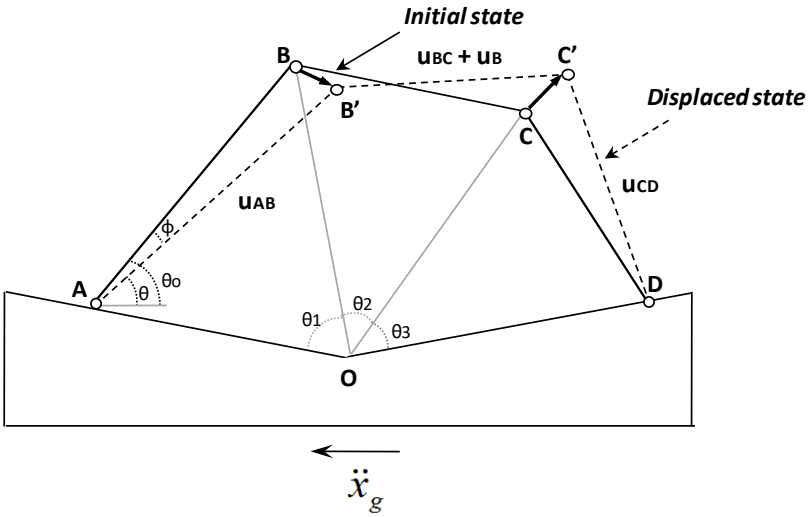

Figure 3.2 Kinematics of mechanism motion as linkage synthesis.

3.2.2 Methods of analysis

The response of such a complicated dynamic nonlinear system may be investigated with various analysis procedures which can be grouped into two categories: a) analytical or semi-analytical methods, b) numerical methods with finite elements. In this study both categories are employed. With regard to the analytical treatment, the Lagrangian method is adopted to derive the equation of motion that describes this kinematic system (Oppenheim, 1992; De Lorenzis et al, 2007). To further reduce the complexity of the problem, linearisation of the nonlinear equation of motion is necessary. Whenever a closed form solution of equation of motion is not feasible, a general software system for mathematical applications "Mathematica" is utilised to compute the response.

On the other hand, numerical analysis is accomplished by using the sophisticated code *Abaqus* and by applying the explicit integration algorithm for solving the nonlinear dynamic response of the system in the time domain. Two dimensional Finite Element (FE) analysis is performed assuming that hinges open at specific and fixed points (A, B, C, D). For the FE model, plane strain elements are used. Each block is idealised as rigid, by using a large enough modulus of elasticity (E = 10 GPa), characterised by density ρ

= 2.2 t/m^3. The base is also considered to be rigid by adopting concrete elastic values (elastic modulus, E = 30 GPa and density, ρ = 2.5 t/m^3). A sophisticated contact algorithm is utilised for modeling contact interface at hinges sections, thus allowing for separation but not for sliding. Hence, the coefficient of friction is adequately large (μ = 0.7). Different types of pulses are imposed to the bottom surface of the base to represent seismic excitation. The major task of the finite element analysis is to evaluate the efficiency of the linearisation techniques in predicting the nonlinear response.

3.2.3 Equation of motion

As already discussed, the Lagrangian method is a convenient tool for the analysis of the above dynamic system. In its general form:

$$\frac{d}{dt}\left(\frac{\partial T}{\partial \dot{\theta}}\right) - \frac{\partial T}{\partial \theta} + \frac{\partial V}{\partial \theta} = Q \tag{3.1}$$

in which, T is the kinetic energy of the system, V the potential energy and Q the generalised forces. For this single-degree-of-freedom system, the angle $\theta = \theta_{AB} = \theta_0$ is chosen arbitrarily and without violating the constraint, as the Lagrangian independent variable (coordinate). The complete expression of these values as a function of θ are given by Oppenheim (1992). For compactness are not retyped herein. Finally, substitution of T, V, and Q to Eq. (3.1) leads to the general nonlinear equation of motion as follows:

$$M(\theta)\ddot{\theta} + L(\theta)\dot{\theta}^2 + F(\theta)g = P(\theta)\ddot{x}_g \tag{3.2}$$

where the coefficients $M(\theta)$, $L(\theta)$, $F(\theta)$, $P(\theta)$ are nonlinear equations of θ given below after replacing $f_{xy} = m_{xy}\bar{r}_{xy}^2 + I_{xy}$:

$$M(\theta) = f_{AB} + f_{BC}\theta'^{2}_{BC} + f_{CD}\theta'^{2}_{CD} + m_{BC}[AB^2 + 2AB\bar{r}_{BC}\theta'_{BC}\cos(\theta - \theta_{BC} - \psi_{BC})] \quad (3.3a)$$

$$L(\theta) = f_{BC}\theta'_{BC}\theta''_{BC} + f_{CD}\theta'_{CD}\theta''_{CD} + m_{BC}AB\bar{r}_{BC}[\theta''_{BC}cos(\theta - \theta_{BC} - \psi_{BC}) - \theta'_{BC}(1 - \theta'_{BC})\sin(\theta - \theta_{BC} - \psi_{BC})] \quad (3.3b)$$

$$F(\theta) = m_{AB}\bar{r}_{AB}\cos(\theta + \psi_{AB}) + m_{BC}[ABcos\theta + \bar{r}_{BC}\theta'_{BC}\cos(\theta_{BC} + \psi_{BC})] + m_{CD}\bar{r}_{CD}\theta'_{CD}\cos(\theta_{CD} + \psi_{CD}) \quad (3.3c)$$

$$P(\theta) = m_{AB}\bar{r}_{AB}\,sin(\theta + \psi_{AB}) + m_{BC}[ABsin\theta + \bar{r}_{BC}\theta'_{BC}\,sin(\theta_{BC} + \psi_{BC})] + m_{CD}\bar{r}_{CD}\theta'_{CD}\,sin(\theta_{CD} + \psi_{CD}) \quad (3.3d)$$

Their physical interpretation has been approached by Oppenheim (1992). Equation 3.2 is valid only when the angle $\theta < \theta_0$, meaning that the computation of the rocking angle θ is limited to the prior-to-impact state. Once θ_0 is exceeded, a new kinematic mechanism is generated which requires a fundamentally different analytical treatment.

3.3 LINEARISATION TECHNIQUES OF ARCH RESPONSE

The coefficients $M(\theta)$, $L(\theta)$, $F(\theta)$, $P(\theta)$ in Eq. (3.2) may be divided by $M(\theta)$ reformulating the equation of motion as follows:

$$\ddot{\theta} + b(\theta)\dot{\theta}^2 = c(\theta)g + d(\theta)\ddot{x}_g \quad (3.4)$$

in which $b(\theta) = L(\theta)/M(\theta)$, $c(\theta) = F(\theta)/M(\theta)$ and $d(\theta) = P(\theta)/M(\theta)$.

This is the general form of the equation of motion, which is nonlinear as coefficients of Eq. (3.4) are complicated functions of the angle θ. For small variations however, it can be postulated that these coefficients remain constant (Oppenheim, 1992). Searching out for the solution of Eq. (3.4) the following transformation is introduced.

$$\theta(t) = \frac{1}{b} log\big(u(t)\big) \tag{3.5}$$

The left side of Eq. (3.4) may be expressed in terms of a new variable *u* as:

$$\ddot{\theta} + b\dot{\theta}^2 = \frac{1}{b}\frac{\ddot{u}}{u} \tag{3.6}$$

Then, the equation of motion yields:

$$\frac{1}{b}\frac{\ddot{u}}{u} = cg + d\ddot{x}_g \tag{3.7}$$

Equation (3.7) may now be written in a standard form of a linear differential equation of 2nd degree:

$$\ddot{u}(t) - b\big(|c|g + d\,\ddot{x}_g\big)u(t) = 0 \tag{3.8}$$

3.3.1 Equation of motion in terms of rotation φ

Alternatively, the equation of motion can explicitly be expressed in terms of φ (defining $\varphi = \theta_0 - \theta$):

$$M(\varphi)\ddot{\varphi} + L(\varphi)\dot{\varphi}^2 + F(\varphi)g = P(\varphi)\ddot{x}_g \tag{3.9}$$

Coefficients *F*, *P* are Taylor series expansions about φ and are approximated by keeping only the first order terms. Clearly, an approximate rather than a detailed solution is sought. In a similar algebraic procedure to that when the variable θ is regarded, Eq. (3.9) finally yields:

$$2\ddot{\varphi} - b\dot{\varphi}^2 - c\varphi - h = 0 \tag{3.10}$$

The above is applicable only for small values of rotation φ, otherwise the expansion does not converge. The general solution of equation (3.10) is unveiled below and it can be characterised as a differential equation in terms of the phase space variables $(\dot{\varphi}, \varphi)$.

$$\dot{\varphi}^2 = \frac{c + bh}{b^2}\left(e^{b\varphi} - 1\right) - \frac{c\varphi}{b} \tag{3.11}$$

3.3.2 Onset of mechanism motion

Recall now Eq. (3.2). The ground acceleration amplitude required to transform the arch into a four-link mechanism is extracted from this equation by applying the criterion for incipient rocking: $\ddot{\theta} = \dot{\theta} = 0$ (Apostolou, 2011; Zhang & Makris, 2001). Hence, for a ground acceleration larger than $|\ddot{x}_g| = F(\theta)/P(\theta)$, the developing inertia forces set the arch on rocking. From that point on, equilibrium becomes unstable and overturning is possible. Nevertheless, there is a thin zone, in terms of the angle θ, in which the structure can safely undergo rocking. This zone is bounded by critical values of $\theta_{max} = \theta_0$ and θ_{min}. The latter is associated with a critical point that Oppenheim called it the "non-recovery" point, as it determines whether the structure will return to its initial position (recovery region) or will eventually collapse (non-recovery region). Energy approach can provide levels of this lower value of θ. Similarly, if the independent variable φ is chosen, the rocking criterion becomes $\ddot{\varphi} = \dot{\varphi} = 0$ and through Eq. (3.9) the critical ground acceleration becomes $|\ddot{x}_g| = F(\varphi)/P(\varphi)$. Then, the critical rotation separates safe from overturning response. All the above are portrayed in Figure 3.3, using the numerical example of the preceding. Hence, for a rocking rotation larger than φ = 0.07 rad, the gravitational force is converted from restoring to overturning meaning that it destabilises structural equilibrium. This conclusion results from the fact

that the coefficient *F(φ)* normalised to its value, becomes negative after the non-recovery point as shown in Figure 3.3. On the contrary, the coefficient *P(φ)* normalised to its value, reveals that the ground acceleration destabilises the four-link mechanism from the beginning, having its contribution increasing almost linearly in relation to the rotation φ.

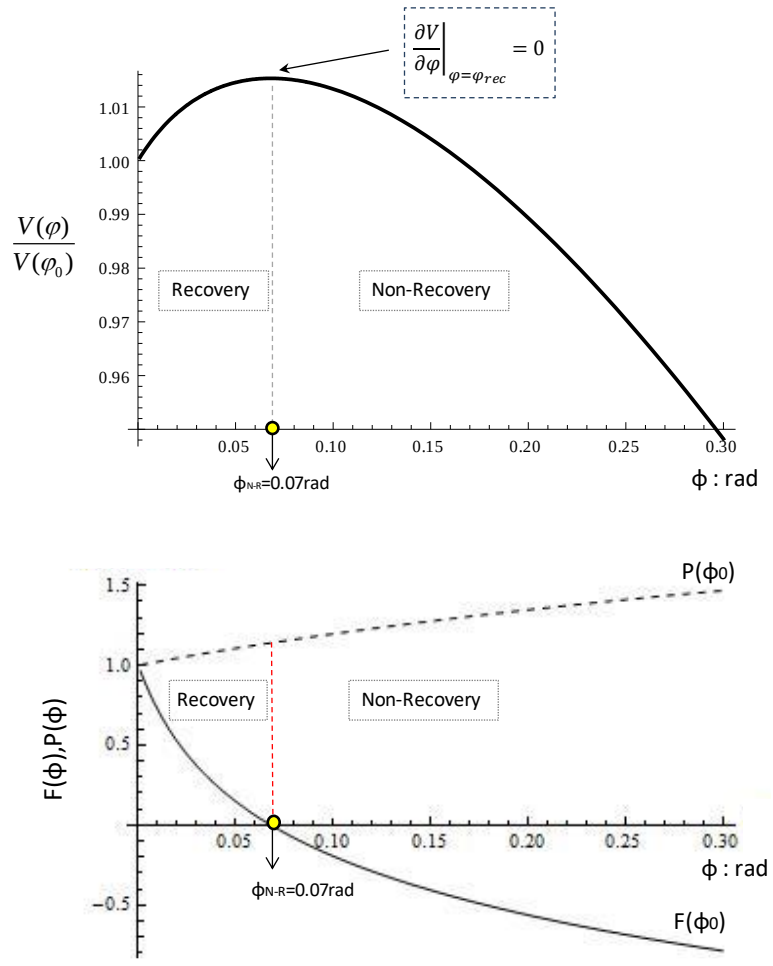

Figure 3.3 Potential energy normalised to its maximum value along with the representative coefficient *F*, and coefficient *P* defined by the non-recovery point.

3.4 LINEARISED RESPONSE UNDER PULSE TYPE MOTION: NUMERICAL EXAMPLES

3.4.1 Constant acceleration pulse

At first, the arch is subjected to a constant acceleration pulse $\ddot{x}_g = -\lambda\, g$. A negative (positive) sign of the ground acceleration denotes clockwise (anticlockwise) rocking rotation (φ) of the structure. Recalling equation of motion in terms of *u* [Eq. (3.8)] and substituting $\ddot{x}_g = -\lambda g$ and $\tilde{c} = (\lambda d - c)g$, it yields:

$$\ddot{u}(t) + b\,\tilde{c}\,u(t) = 0 \tag{3.12}$$

which is a second order differential equation with fixed coefficients and its solution can be built up by a linear combination of trigonometric functions.

$$u(t) = A_1 cos\left(\sqrt{b\tilde{c}}\ t\right) + A_2 sin\left(\sqrt{b\tilde{c}}\ t\right) \tag{3.13}$$

where A_1, A_2 are constants. It is evident that:

$$u(t) = c_2\ cos\left(\sqrt{b\tilde{c}}\,(t - c_1)\right) \tag{3.14}$$

where c_1, c_2 are new constants that can be defined from initial conditions.

Equation (3.14) in combination with the transformation of Eq. (3.5) yields the solution in terms of the angle θ(t).

$$\theta(t) = c_2 + \frac{\log(\cos(\sqrt{b\tilde{c}}\,(t - c_1))}{b} \tag{3.15}$$

At t = 0 angle θ_{AB} is:

$$\theta(0) = c_2 + \frac{\log(\cos\left(\sqrt{b\tilde{c}}\,(-c_1)\right)}{b} \tag{3.16}$$

Or

$$\theta_0 = c_2 + \frac{\log(\cos c_1\sqrt{b\tilde{c}}\,)}{b} \tag{3.17}$$

Derivation of equation (3.15) provides the rotational velocity:

$$\dot{\theta}(t) = -\sqrt{\frac{c}{b}}\tan(\sqrt{b\tilde{c}}\,(t - c_1)) \tag{3.18}$$

At $t = t_0$, the rotational velocity is zero therefore:

$$\dot{\theta}(0) = 0 = \tan(\sqrt{b\tilde{c}}\,(-c_1) => c_1 = 0 \tag{3.19}$$

Substitution of the value of c_1 to Eq. (3.17) allows for c_2 to be calculated:

$$\theta(0) = c_2 + \frac{\log(\cos\left(\sqrt{b\tilde{c}}\ 0\right)}{b} = \theta_0 => c_2 = \theta_0 \tag{3.20}$$

Eventually, the analytical solution yields in terms of θ:

$$\theta(t) = \theta_0 + \frac{\log\left(cos\left(\sqrt{b\tilde{c}}t\right)\right)}{b} \tag{3.21}$$

Numerical implementation is presented next based on the above solution. The coefficients *M*, *L*, *F*, *P* of the equation of motion are calculated considering the aforepresented numerical example (geometric characteristics: arch radius a =10 m, angle of embrace $\beta = 157.5°$, ratio thickness/radius (t / R) = 0.15). For this specific case, Eqs. (3.2) and (3.4) become respectively:

$$4370\ \ddot{\theta} + 59249\dot{\theta}^2 - 87.7\ g = 239\ \ddot{x}_g \tag{3.22}$$

$$\ddot{\theta} + 13.56\dot{\theta}^2 - 0.02\ g = 0.055\ \ddot{x}_g \tag{3.23}$$

It is noted the computed response is associated with the specific kinematic mechanism adopted so far. (A different kinematic mechanism would respond to different values of these coefficients).

Figure 3.4 depicts the development of rotation θ_{AB} over time for different constant pulses based on the above equation. Initially, the static angle of the link AB is $\theta_0 = 0.8972\ rad$, and consequently the starting point of all curves. The ground acceleration amplitude that transforms the arch into a four-link mechanism is extracted from Eq. (3.22) by applying the criterion for incipient rocking: $\ddot{\theta} = \dot{\theta} = 0$. For a ground motion larger than $|\ddot{x}_g| = F(\theta)/P(\theta) > 0.37g$, the developing inertia forces set the arch on rocking. From that point on, equilibrium becomes unstable and overturning is inevitable as depicted from the time histories of Figure 3.4.

This value of φ corresponds to $\theta = \theta_{min} = 0.8272rad$ (in displaced state) and it is highlighted in Figure 3.4 with black dashed line. Curves that cross that line (i.e. $|\ddot{x}_g|$ = 0.39 g, 0.45 g, 0.56 g, 0.61 g, 0.71 g) represent arches that fail as rotation θ drops below

the critical value. In contrast, curve 0.37 *g* represents a rocking arch in marginal equilibrium. The stronger the impulse the sooner the arch collapses.

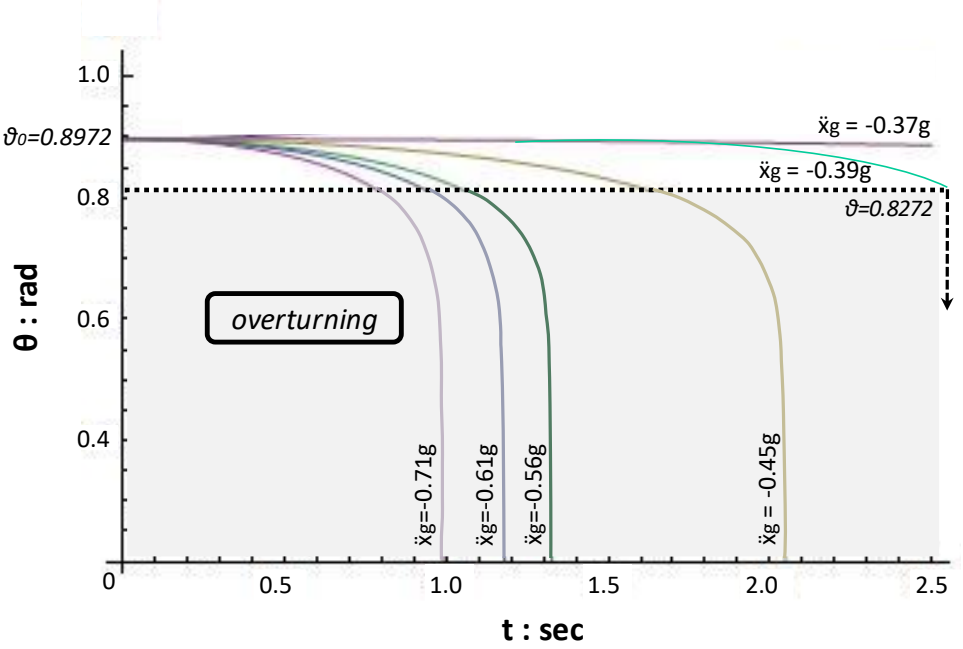

Figure 3.4 Time history of angle θ_{AB} for different levels of ground excitation.

3.4.2 One-sine pulses

Herein, the linearised equation of motion is readjusted for a sinusoidal ground motion. Cycloidal pulse of type-A approximates a forward pulse of near fault ground motion and is chosen over one cosine pulse (Type-B Pulse) because of its more destructive effects [Makris & Roussos, 1998]. Within the limits of the linear approximation and for a ground acceleration,

$$\ddot{x}_g = -\, a_p \sin(\omega_p\, t) \qquad (3.24)$$

(where, a_p and ω_p are the acceleration amplitude and the angular frequency of the pulse respectively, *t* is the time and the minus sign designates positive rotation φ), the governing eq. (3.8) becomes:

$$\ddot{u}(t) - b\big(|c|g - da_p \sin(\omega\, t)\big)u(t) = 0 \tag{3.25}$$

A suitable transformation of variable [Eq.(3.26)] is used to convert Eq. (3.25) to a linear second-order homogeneous differential equation similar to the well-known from the literature Mathieu Equation [Eq.(3.27)].

$$\omega\, t = 2x + \frac{\pi}{2} \tag{3.26}$$

$$\ddot{u}(x) + (A - 2Qcos(2\, x))u(x) = 0 \tag{3.27}$$

Mathieu Equation commonly occurs in nonlinear vibration problems, a) in systems in which there is periodic forcing, and b) instability studies of periodic motions in nonlinear autonomous systems. Recall the case of a pendulum whose support is periodically forced in a vertically direction as a typical example. Obviously, the coefficient of the differential equation is periodic without entailing that the equation possesses only periodic solutions. Only for specific values of the constants *A*, *Q* (which are often referred as characteristic number and parameter respectively) a periodic solution is achieved. Both of them are expressed in terms of excitation parameters and of the coefficients of the equation of motion (*b*, *c*, *d*) [Eqs. (3.28-3.30)]. As already mentioned, the latter are complicated functions of angle θ but assuming small variations of θ, they remain constant. Adopting initial formulae, they may be rewritten as in Eqs. (3.29-3.30). It is noted that *A* encompasses the potential energy which is proportional to θ at any displaced configuration of the arch. Similarly, *Q* describes the applied external force, emphasised on the excitation amplitude a_p.

$$A = \frac{4gbc}{\omega^2} \qquad\qquad Q = \frac{2a_p bd}{\omega^2} \tag{3.28}$$

$$A = \frac{4gL(\theta)F(\theta)}{[\omega M(\theta)]^2} \qquad \text{Or} \qquad A = 2EF(\theta)g \tag{3.29}$$

$$Q = \frac{2a_p L(\theta) P(\theta)}{[\omega M(\theta)]^2} \qquad \text{Or} \qquad Q = EP(\theta)a \tag{3.30}$$

where, $$E = \frac{2L(\theta)}{[\omega M(\theta)]^2}$$

According to superposition principle, Equation (3.27) possesses a solution which is a linear combination of two independent solutions, $u_1(x)$ and $u_2(x)$. This solution is obtained below:

$$u(x) = c_1 u_1(x) + c_2 u_2(x) \tag{3.31}$$

The arbitrary constants c_1 and c_2 are defined by the boundary conditions supposing that for $x = x_0$, the general solution is $u(x) = u(x_0)$ and its derivative is $u'(x_0) = 0$.

To be more specific, the example of the afore-discussed arch will be used. The numerical solution of equation (3.31) is obtained with a computational algorithm. It is omitted however, due to the intricacy of the coefficients $c_{1,2}$ and of the solutions $u_{1,2}$. It is worth mentioning that no periodic solutions correspond to this system. For convenience, although, the differential equation [Eq.(3.27)] can be presented numerically. Hence, for various sine pulses (a_p, ω_p) it yields:

$$\ddot{u}(x) + \frac{1}{\omega^2}\big(10.6 - 2.96a_p cos(2\,x)\big)u(x) = 0 \tag{3.32}$$

As already discussed, the motion initiates when the ground acceleration $\ddot{x}_g$ exceeds the value of 0.37 g. For the sine pulse case, the aforementioned applies when

$a_p \sin(\omega_p t) > |-0.37|g \Rightarrow t_0 = \frac{1}{\omega_p} sin^{-1}\left[\frac{(|-0.37|g)}{\alpha_p}\right]$. At that time hinges are formed, and as a result the arch is transformed into a mechanism. The arch rocking response can be further described with the excitation parameters, the acceleration amplitude (a_p) and the excitation frequency ($\omega_p = 2\pi / T_p$). It is therefore interesting to develop diagrams of rotation θ_{AB} for different levels of the former parameters (Figure 3.5). Thus, the way the pulse characteristics affect the overturning response is analysed separately. Notably, the selected pulses to be examined can adequately resemble recorded time histories of zero final ground velocity. In the first case, the excitation frequency remains constant and equal to $\omega_p = \pi$ ($T_p = 2$ sec) whereas, the acceleration amplitude fluctuates between -(4/3) g to -1 g and -0.75 g (Figure 3.5a$_1$). Evidently, the detrimental effect of the increasing a_p is clear as higher values lead more rapidly the arch to overturning (when the angle θ_{AB} exceeds the critical value of 0.8272 rad as mentioned above). For the most unfavourable case of the maximum a_p = -(4/3) g, the system is set into motion at t_0=0.089 sec and overturning occurs at t_{over} = 0.67 sec, at the second quarter of the pulse, whereas, for the other two levels of the acceleration amplitude, the motion onsets later at t_0 = 0.12 for a_p = -1 g and at t_0 = 0.16 sec for a_p = -0.75 g, and collapse time is defined at t_{over} = 0.8 sec (second quarter of the pulse), 1.05 sec (third quarter of the pulse) respectively. In the second case, as seen on Figure 3.5b$_1$, decreasing the ω_p from π (T_p = 2 sec) to 0.75π (T_p = 2.66 sec) and 0.5π (T_p = 4 sec) (consequently increasing the excitation period T_p) and keeping constant the acceleration amplitude a_p (= -3/4 g) affects favourably the overturning response. Additionally, for all the examined cases, the results indicate that the arch rocks and collapses straightforward to the right, with no impacts to occur. 3D diagrams presented on Figures 3.5b$_1$, b$_2$, are constructed to give insight of the predicted collapse mechanism.

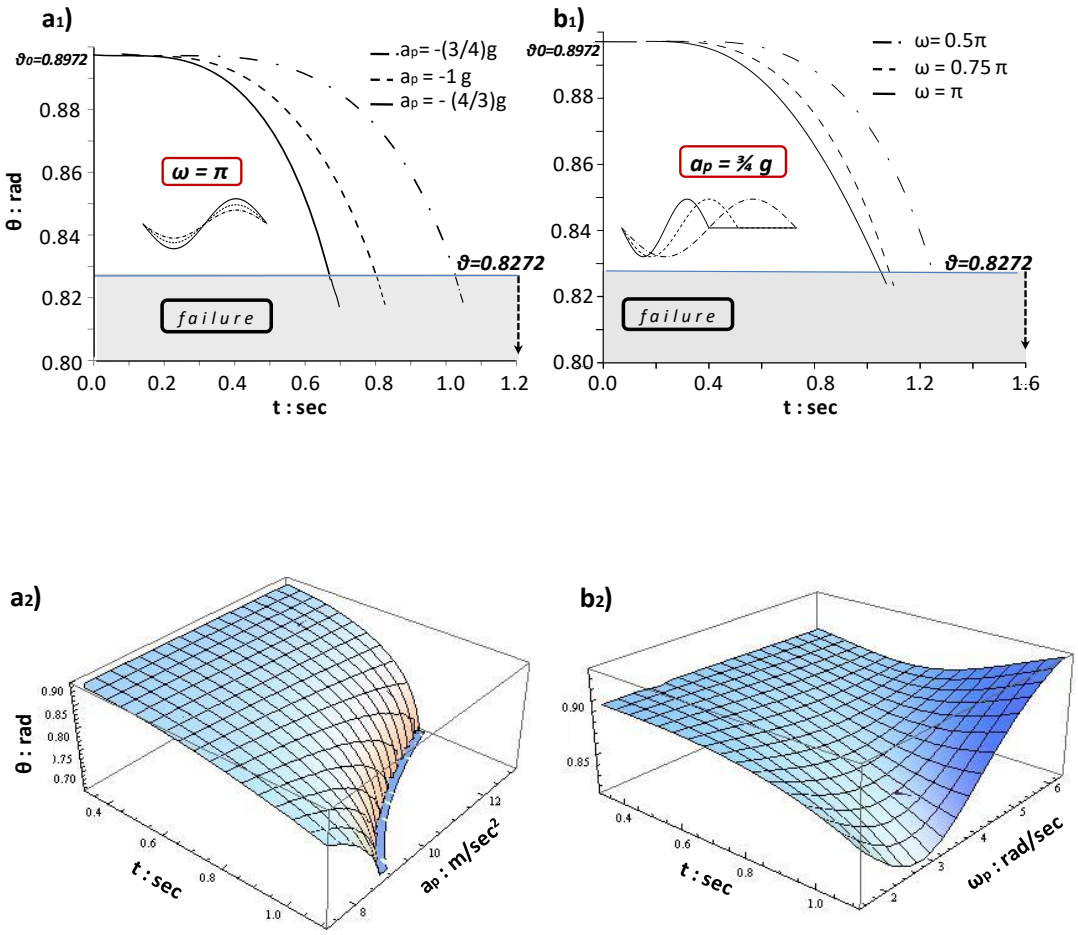

Figure 3.5 Effect of the acceleration amplitude a_p (a_1, a_2) and of the excitation frequency ω_p (b_1, b_2) on the rocking response presented in 2D and 3D.

Initially, the equation of motion is transformed for sinusoidal pulses into a Mathieu kind differential equation. Appropriate solution of this equation is found corresponding to this specific arch geometry [Eq.(3.32)]. In this respect, the computed time history of angle θ_{AB} for various one-sine pulse excitations with period ranging from T_p = 0.75 sec to 4sec is presented in Figure 3.6. The study of the impulse response is feasible till the first impact. Alternatively, the arch response under the same set of one-sine pulses may be repeated by implementing two additional methods: (a) a semi-analytical solution, in which the linearised equation of motion of Eq.3.9 is solved iteratively through a numerical solver available in Mathematica code, (b) two-dimensional finite element analysis using Abaqus code. The results are comparatively

portrayed in Figure 3.6 along with those extracted from Mathieu Equation. The comparison among the three methods proves to be remarkably good indicating the validity of the linearisation techniques. Nevertheless, as the finite element method provides rigorous solution for the four-link mechanism it still remains to be checked the accuracy of this simplified model.

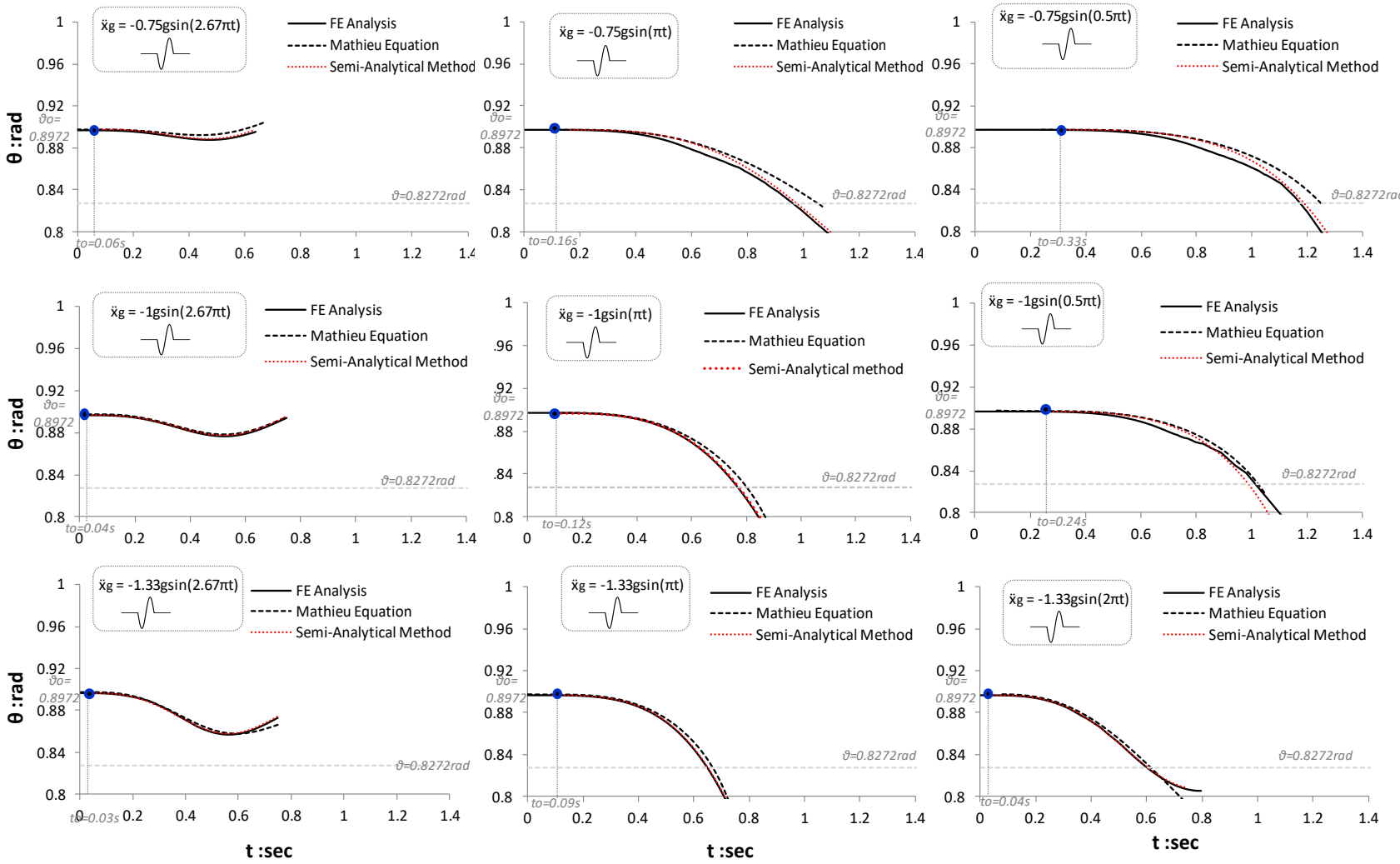

Figure 3.6 Time histories of the angle θ_{AB} under one-sine pulse base excitation: (line 1) a_p = -0.75g, T_p = 0.75, 2, 4 sec, (line 2) a_p = -1g, T_p = 0.75, 2, 4 sec, (line 3) a_p = -1.33 g, T_p = 0.75, 1, 2 sec: comparison between finite element analysis and linearised analytical solutions (semi-analytical solution of Eq. (3.9) and closed-form solution with Mathieu equation).

In the preceding, Mathieu equation has been proven a useful tool to extract closed-form solutions for low amplitudes of rocking. It is also reminded that in this series of analyses, a unique value of the ratio t / R was considered (t / R =0.15). Simplified analysis of the rocking response based on Mathieu equation is extended next, by introducing more values of the ratio t / R. As before, the arched structure is subjected to cycloidal pulse-type excitation at the base. Whether the structure can safely experience rocking vibration or immediately collapses is illustrated with the overturning spectra of Figure 3.7. For lower values of the period T_p, higher values of the acceleration amplitude are required to overturn the arch. In addition, for a specific period T_p, the higher the ratio t / R is, the higher the minimum acceleration is required to collapse. A long-period pulse (T_p = 2 sec or ω_p = π rad) is chosen from Figure 3.7 as suitable to enlighten the rocking response at marginal equilibrium (Figure 3.8). Time histories of the normalised angle θ_{AB}, the normalised rotation φ, and the phase portrait confirm the influence of the geometrical parameters on the arch limit response. The heavier arch (t / R = 0.18) sustains larger rotations which is a rational conclusion given the larger inertia.

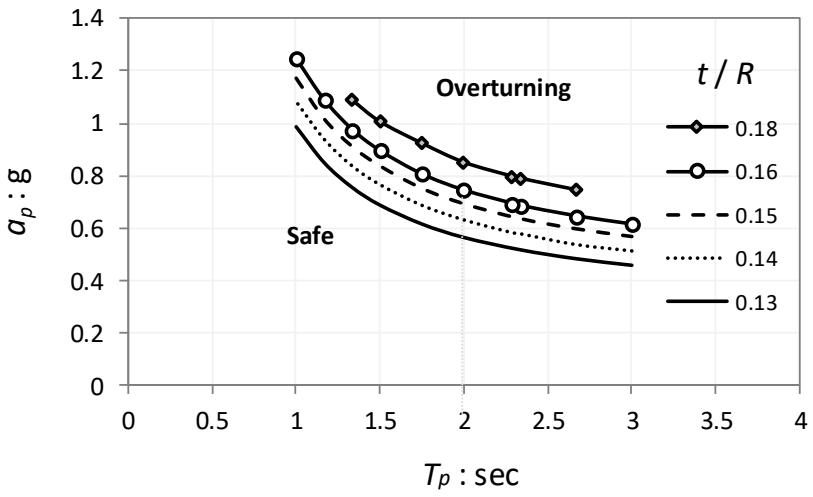

Figure 3.7 Safe and overturning region formed by acceleration-period pairs under sine pulses for different arches. Safe mode refers to the first impact moment. Overturning after one impact cannot be excluded.

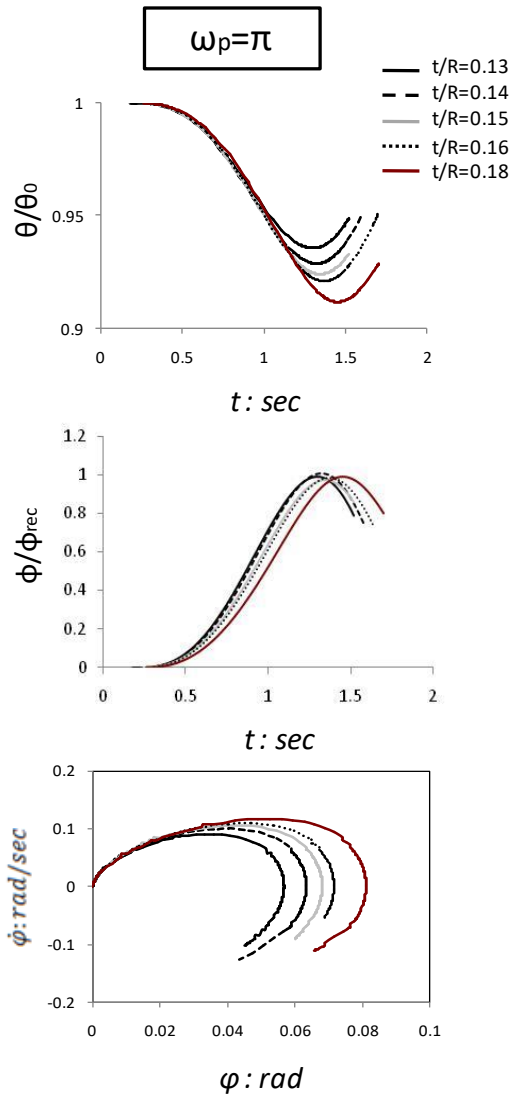

Figure 3.8 Time histories of the normalised angle θ_{AB}, rotation φ and phase diagram of a marginally safe arch subjected to sine pulses (ω_p = π) for different values of *t / R*.

3.4.3 Rectangular pulses

The two-step rectangular pulse as an excitation to study the arch rocking response was introduced by Oppenheim (1992). Later, this extreme pulse was also used by De Lorenzis et al (2007). In this context, the time history of the acceleration consists of a large negative pulse ($a_p = -1g$) of duration t_p, followed by a smaller positive pulse of half magnitude ($a_p = 0.5g$) and of double duration $2t_p$. These pulse shape parameters lead to zero terminal ground velocity (Figure 3.9). Two different values of the duration t_p have been adopted by Oppenheim, namely 0.40 sec and 0.44 sec. These values of t_p are also applied herein so that comparative results can be extracted. General remarks for both cases regard mainly the movement of the base. The

maximum value of the base velocity occurs when the acceleration changes sign, and it vanishes at the end of the pulse. On the other hand, the displacement time history indicates the change in curvature with the sign change and a residual displacement after the end of the pulse.

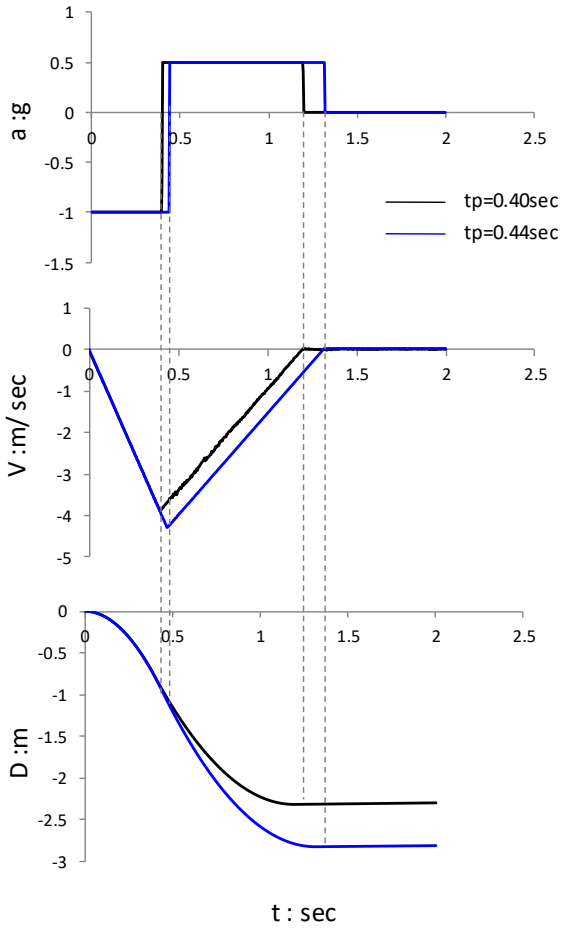

Figure 3.9 The impact of the impulses, with durations t_p = 0.40, 0.44sec and acceleration magnitude a = 1 g, on velocity and displacement time histories of the arch base.

A computational solution of the equation of motion in terms of rotation φ (Eq. 3.9) is accomplished with *Mathematica* code, after properly adjusting the coefficient $P(\varphi)$ to implement ground shaking idealised with the two rectangular pulses illustrated in Figure 3.9.

$$445\ddot{\varphi} - 6017.75\dot{\varphi}^2 + 87.86 = (-1g)(-237.45) \qquad 0 \le t \le t_p \qquad (3.33)$$

$$445\ddot{\varphi} - 6017.75\dot{\varphi}^2 + 87.86 = (+0.5g)(-237.45) \qquad t_p \leq t \leq 3t_p \qquad (3.34)$$

The results obtained with the above method along with the results derived by Oppenheim are portrayed in Figure 3.10. Moreover, the finite element method through *Abaqus* code is implemented to evaluate these analytical solutions. The comparison of these three methods is satisfying. When t_p = 0.40 sec, the arch after rocking for a while, returns to its initial position (φ = 0). On the other hand, when t_p = 0.44 sec, the rotation φ gradually increases leading to overturning.

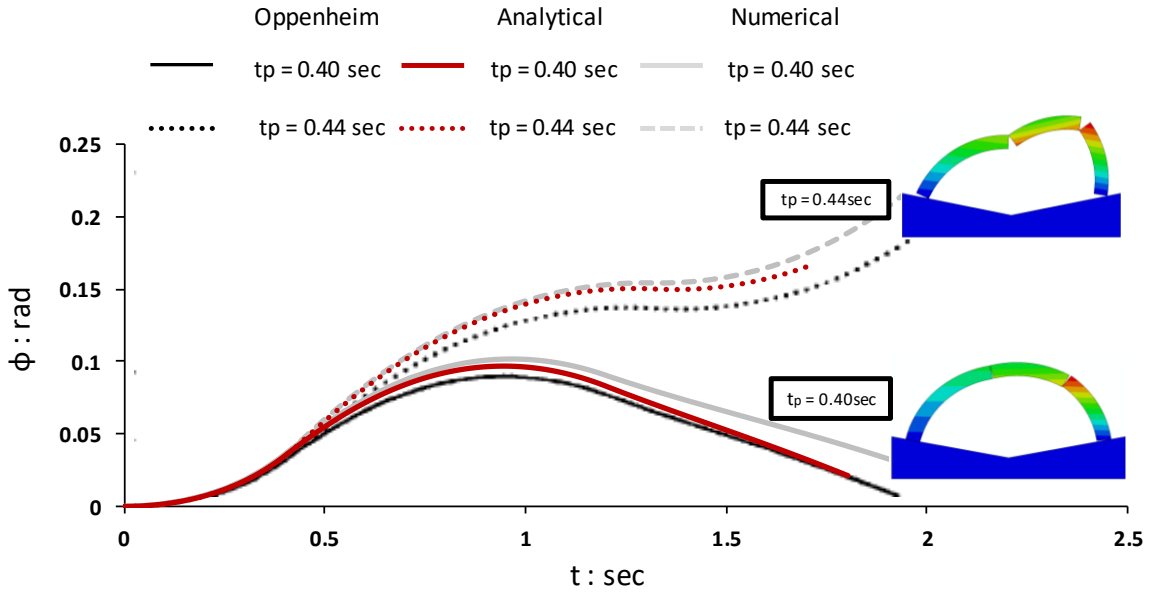

Figure 3.10 Response to idealised ground motion pulse.

Similar results of the comparison between two methods of analysis can be extracted when the excitation period is significantly lower. In this way, a new set of rectangular pulses is adopted with duration values 0.20 sec and 0.27 sec. Time histories of the computational solution of Eq.(3.9) (*Mathematica*) and comparison with the finite element analysis (*Abaqus*) are illustrated in Figure 3.11.

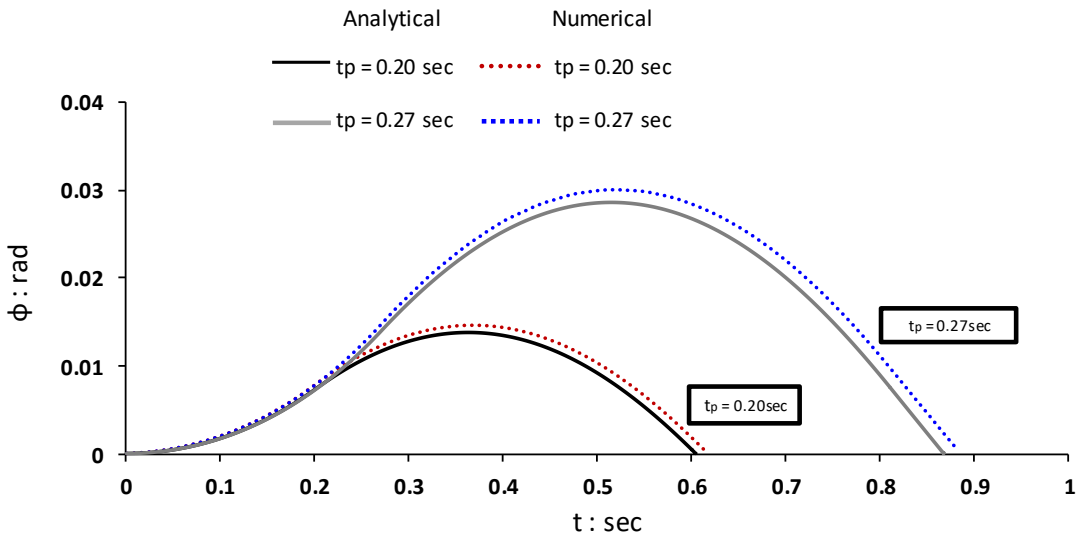

Figure 3.11 Response to idealised ground motion pulse.

3.5 Applicability and limitations

3.5.1 Influence of the number of blocks

As mentioned above, the hinge locations are assumed fixed during the rocking vibration. The accuracy of the simplification of a four-hinge mechanism is strengthened by computational and experimental results of earlier studies (Clemente, 1998). The applicability of the four-hinge model is investigated herein by conducting analyses through finite element formulation of a seven-rigid block arch. The same type of pulses used in previous analyses are implemented to simulate ground excitation at the base of the model: (a) one-sine pulses (b) rectangular pulses. Time histories of angle θ_{AB} in the case of a seven-block arch, are in a good agreement with the numerically and analytically computed results of a three-block arch as illustrated in Figure 3.12. On the other hand, in the case of rectangular pulses, the results indicate not only a larger rotation φ (especially for t_p = 0.27sec) but also a slower return from θ to θ_0. Although It is a complicate task to describe the behaviour of each voussoir of the arch, it is also challenging for future research.

3.5.2 Influence of sliding

The effect of friction on the arch response is also investigated. Influence of sliding has met only limited investigation in the past. A few experimental studies have revealed that the results aren't generally influenced as initiation of sliding is difficult to occur. According to the results of finite element analyses the coefficient of friction (μ) has practically no appreciable effect on the arch behaviour in the case of a 3-blocks arch imposed on both rectangular and sine pulses (Figures 3.14, 3.15 left). On the other hand, for an arch of seven voussoirs, some differentiations are observed. Particularly, from Figure 3.14 (right), where time history of rotation φ is depicted, it is extracted that a low coefficient of friction (μ=0.51) is accompanied with larger rotations. It is important to note that such values of μ are less than the typical ones. The numerical investigation continues with specific sine pulses (Figure 3.15 left). In the first half cycle of high frequency shaking, the coefficient of friction doesn't play any particular role. Larger deviations in angle θ_{AB} under various coefficients are observed for higher values of acceleration amplitudes a_p. Differentiations in rotations or angles are totally expected due to accumulated small displacements on each joint.

From the investigation that took place, as presented on the diagrams below, sliding doesn't essentially affect the collapse mechanism. Small-scale experiments offer a strong corroboration to the above conclusion. De Jong et al (2008) performed harmonic and seismic testing on two geometrically different arches finding out that no sliding occurs. They remarked that "failure occurred as a result of hinging and rocking".

To this end, the above findings give a glimpse of how the number of blocks and coefficient of friction affect the arch response. They should await considerably more analytical and experimental testing before being evaluated

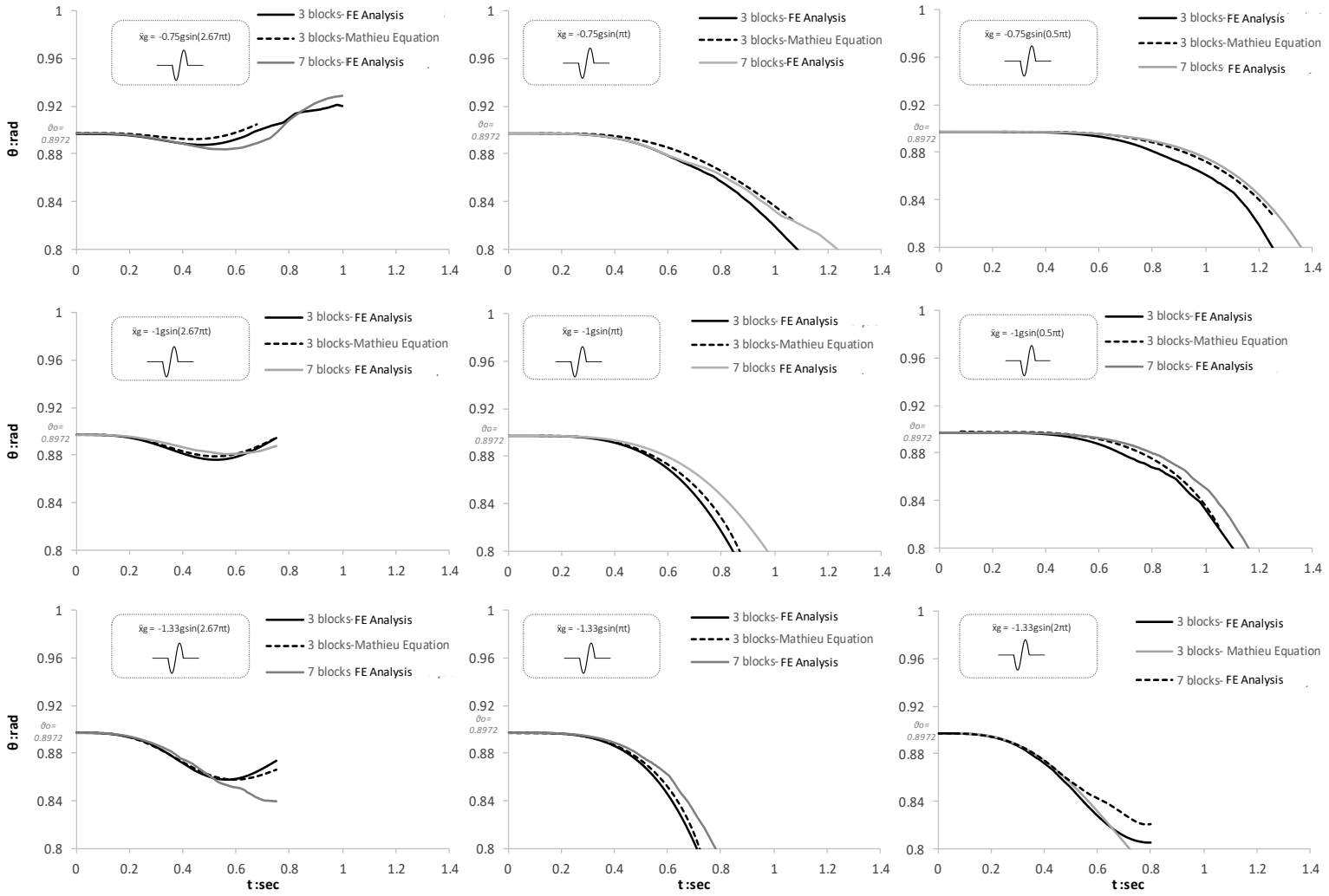

Figure 3.12 Time histories of the angle θ_{AB} under one-sine pulse base excitation: (line 1) a_p = -0.75 g, T_p = 0.75, 2, 4sec, (line 2) a_p = -1 g, T_p = 0.75, 2, 4sec, (line 3) a_p = -1.33 g, T_p = 0.75, 1, 2sec: Comparison between arches consisting of three blocks and seven blocks.

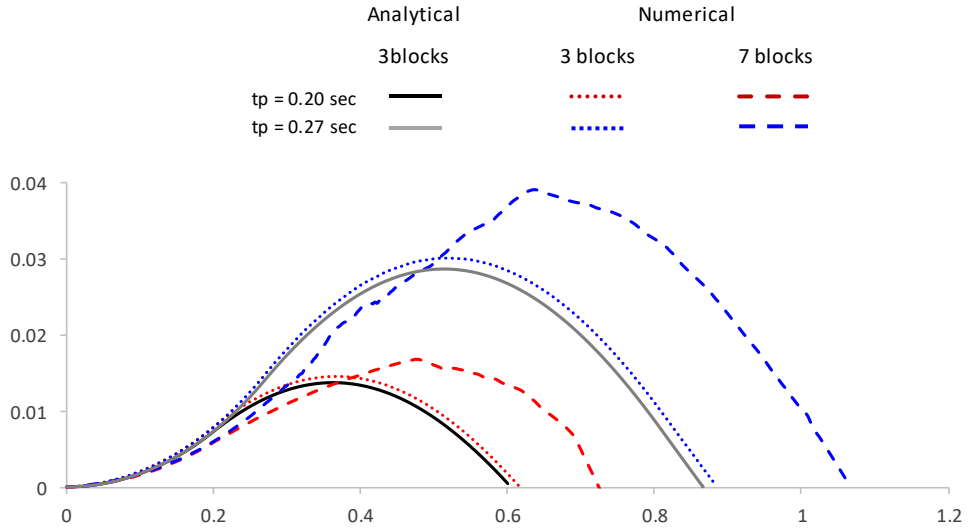

Figure 3.13 Response to idealised rectangular pulses for arches consisting of three and seven blocks.

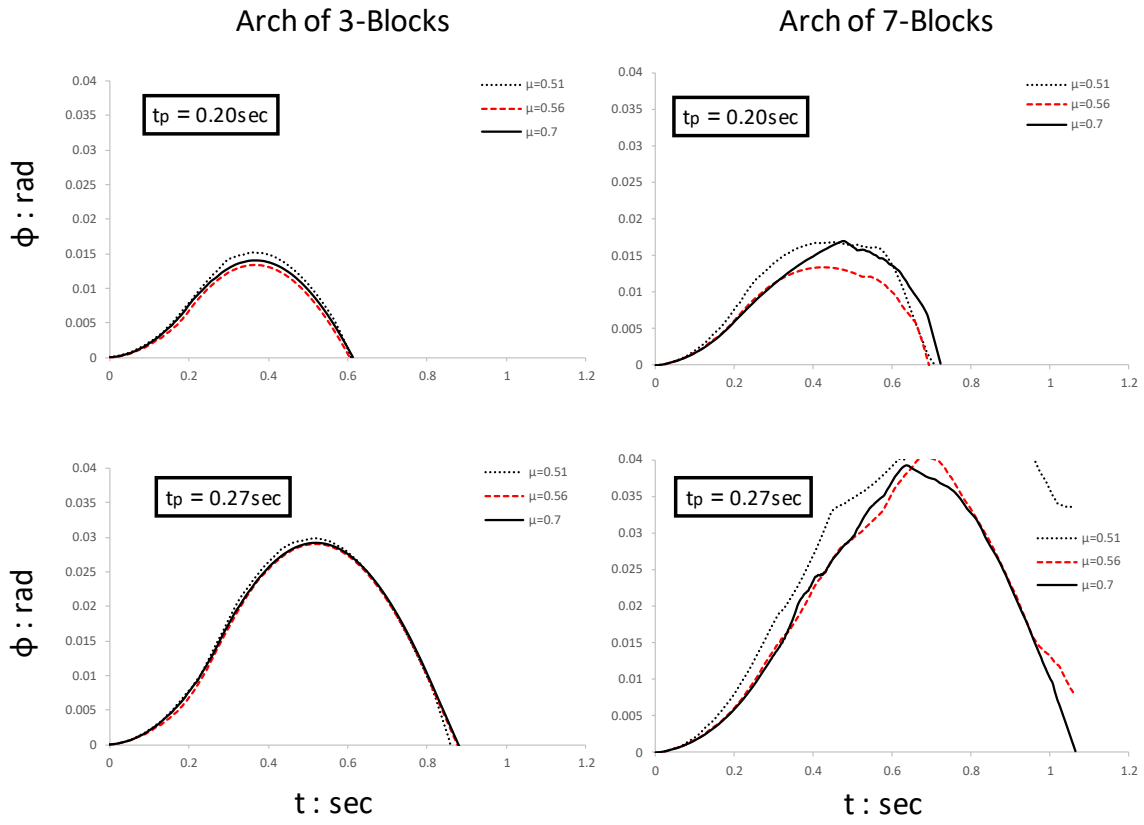

Figure 3.14 Effect of the coefficient of friction on the behaviour of arches consisting of three (left column) and seven blocks (right column) under rectangular pulses.

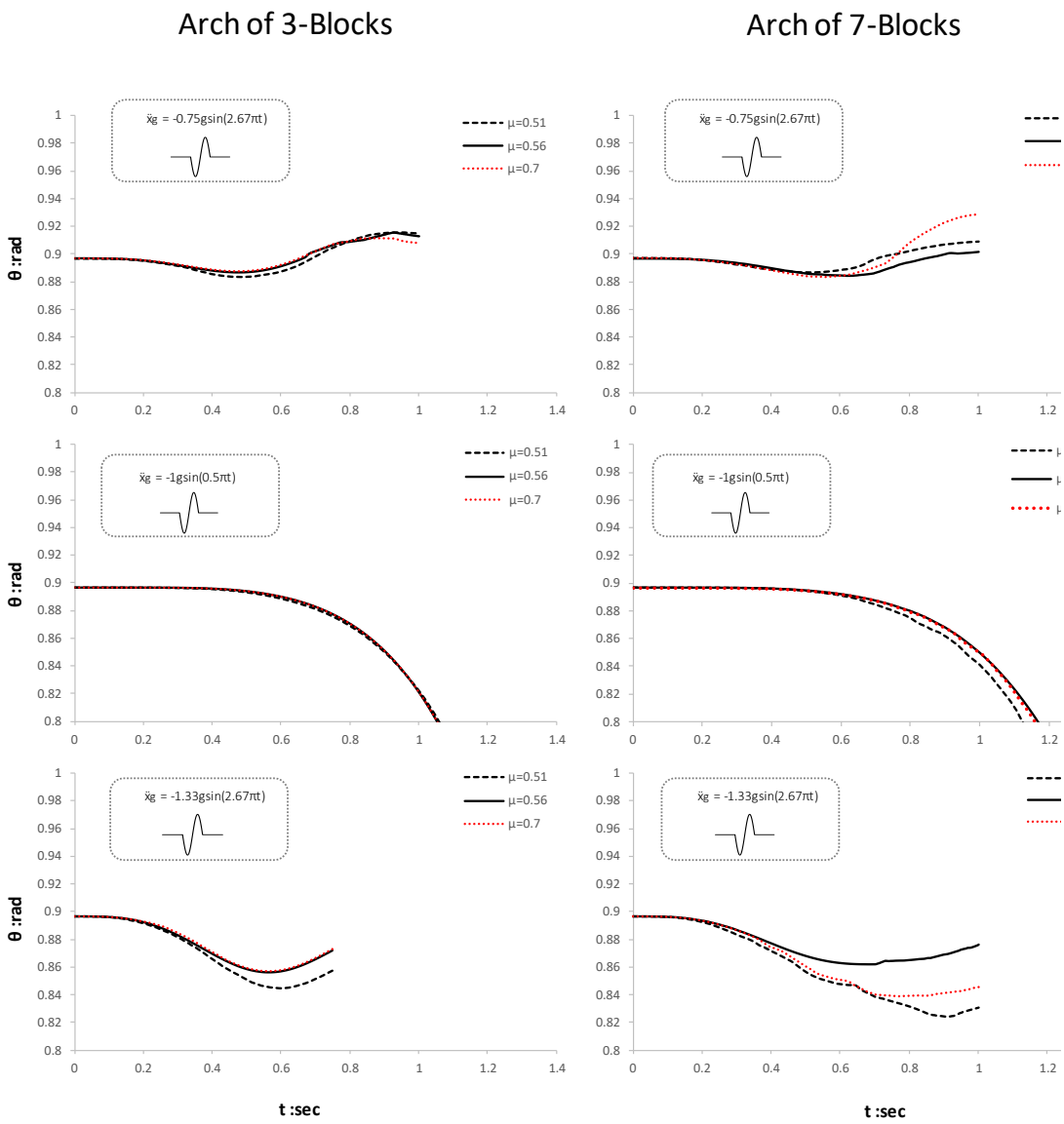

Figure 3.15 Effect of the coefficient of friction on the behaviour of arches consisting of three (left column) and seven blocks (right column) under sine pulses.

3.6 CONCLUSIONS

The study revisits the dynamic behaviour of a part-circular masonry arch subjected to ground motion, as introduced by Oppenheim in 1992. The examined model, under horizontal acceleration applied at its base, is transformed into predefined rigid body assemblies. This concept of arch modeling founds a direct application to monumental masonry arches. In such stiff structures, rocking rotation even in low-amplitude levels

is most often undesirable as it may lead to severe permanent displacements accompanied with possible dislocation of the arch axis, and sometimes to general instability of the structure. It is therefore of great importance to develop simplified procedures for estimating the levels of the low-amplitude response. In this context, simplified analytical techniques are applied to calculate the linear response. These methods comprise both closed-form solutions and numerical integration of the equation of motion. Applicability of linearised response is evaluated mainly through comparison with rigorous 2-dimensional finite element analysis. Moreover, where available, the results are compared with those of the literature. Near-source earthquake shaking is represented with idealised cycloidal and rectangular pulses. In addition, constant acceleration pulses are involved.

A general solution of the resulting linear equation of motion, extracted with the Lagrangian method, suitable for any arch geometry is presented. The impact of the gravitational and the external forces to the system, represented by the coefficients, $F(\varphi)$ and $P(\varphi)$ respectively, is also discussed. Then, a first application of this general solution is given through the examination of constant acceleration pulses. Simplified forms of the rotation θ_{AB} (Lagrangian variable) with respect to time are presented.

One-sine pulses are also introduced to represent ground excitation. In this respect, a linear second-order homogeneous differential equation of motion is derived, similar to Mathieu equation. According to superposition principle, each solution of the Mathieu equation is a linear combination of two independent solutions, thus allowing for a closed-form solution to be obtained. In parallel, numerical integration of the equation of motion is involved to compute the response. A parametric comparative study is presented for different values of the peak ground acceleration and excitation period. Nonlinear finite element analysis in the time domain is also employed to further strengthen the comparison. The results reveal a close agreement between these methods and justify the applicability of the linear simplification of the response. The benefit of the Mathieu equation to easily derive reliable results in large amounts is applied to the study of the overturning response of the arch. The parametric study reveals that overturning of the arch according to the minimum overturning acceleration spectrum, is more sensitive to high values of a_p and low values of T_p.

Another interesting finding is that overturning and imminent collapse occur without impact.

Rectangular asymmetric pulses are also involved in the study of the earthquake response. The type of the pulse and the values chosen are those used by Oppenheim (1992) so that a comparative study is possible. The results indicate convergence between linear analytical and nonlinear finite element methods. The reliability of these results is further strengthened by the comparison with Oppenheim's results for rectangular pulses.

CHAPTER 4:

STABILITY and ROCKING RESPONSE of NON-UNIFORM MASONRY ARCHES: THE 'PART-ELLIPTICAL' PROFILE

4.1 Introduction

Stability of masonry arches has always been a challenging task for architects and builders over the centuries. Nevertheless, the scientific community has started to be intrigued by this subject merely at the eighteenth century. Couplet, in his 1729's pioneering work, was the first to successfully demonstrate the way a semi-circular arched structure can safely withstand its gravity load, in the framework of a structural mechanics approach. He unveiled the purely geometrical nature of the problem in a sense that collapse is not associated with material crushing but it involves the mobilisation of a kinematic mechanism. Accordingly, a graphical approach can be introduced to determine potential equilibrium or collapse mechanisms through the notion of the thrust line. Equilibrium is established when the thrust line lies inside the arch, whereas collapse occurs as soon as the thrust line intersects the external curves. Couplet calculated the minimum required slenderness, t/R, of the semi-circular arch so that the thrust line be marginally bounded by the outer lines of the arch and limit equilibrium be established. This assumption was based on a failure mechanism through the formation of four hinges but Couplet erroneously predefined the intrados hinges at an angle of 45° with respect to the spring points. Milankovitch (1904), motivated by Couplet's innovative work revisited the theory of thrust line and computed the exact location of the intrados hinge at 54.5°, thus correcting the minimum required slenderness, t/R, from 0.101 to 0.1075. In recent years, Alexakis & Makris (2013, 2014) investigated thoroughly the stability of a monolithic segmental arch setting the embrace angle, β, as a parameter of the design. They demonstrated that in a continuous arch the hinge locations should not be predefined but they had to be computed. In this way, they introduced a variational formulation incorporated in the principle of stationary potential energy to derive the minimum thickness slenderness, t/R, for different values of β.

The results demonstrate the favourable role of base confinement, as the minimum required slenderness, t/R, gradually reduces from 0.1075 at the semi-circular arch ($\beta = \pi$) down to 0.0075 at the segmental circular arch of $\beta = \pi/2$. Inherent to the afore-discussed analytical studies are the so-called Couplet-Heyman postulates, considering for the masonry infinite compressive strength, zero tensile strength, and the coefficient of friction large enough to prevent sliding (Heyman 1982).

Unlike the stability of the masonry arch under self-weight, the response due to lateral dynamic loads didn't receive much attention until Oppenheim's notable work, merely in 1992. He derived the nonlinear equation of motion of a segmental circular arch consisting of seven voussoirs which together with the supporting base form eight radial joints. Since the arch is not considered as a monolithic structure, the imminent hinges can occur only at these predefined physical joints. Upon the application of rectangular pulses as input base motion, the arch was converted into a four-link mechanism of fixed hinge locations. This procedure allowed for the computation of the arch motion before the first impact occurs. Within the framework of time-history dynamic analysis it is critical to determine the criterion for the phase transition from the full contact to rocking regime. Stability analysis in static terms can be used to this respect, on the condition of incipient uplift. Clemente (1998) adopted an iterative procedure based on an energy approach to derive minimum levels of ground acceleration, as well as to calculate the hinge locations at the onset of rocking mode, for different values of the slenderness, t/R, and the angle of embrace, β. Ochsendorf (2002), based on Clemente's concept, proposed an alternative iterative procedure for stability analysis under constant horizontal acceleration. A growing interest in the stability assessment of masonry arches using the limit analysis theory has lately been emerged in literature (Dimitri, 2015; Cavalagli, 2017; Di Carlo, 2018; Zampieri, 2019; Stockdale, 2019, 2020). Recent studies further contributed to the arch seismic response under pulse-type ground motion, based either to analytical or to numerical methods (De Lorenzis, 2007; Dimitrakopoulos, 2013; De Santis, 2014; Gaetani, 2017; Leontari, 2018; Kollar, 2019). In the latter, primarily the finite element method (FEM) as well as the discrete element method (DEM) are involved. A thorough comparative study on these methods has been presented by Sarhosis et al (2016). Many researchers have extensively

implemented the DEM (Dimitri, 2015; Sarhosis, 2019; Cannizzaro, 2018; Pulatsu, 2019; Stockdale, 2020) to assess the collapse behaviour of masonry arches.

While masonry arches of a uniform circular and sometimes elliptical profile have been subjected to thorough scrutiny in the past, only a few studies have addressed the non-uniform arch (Dimitri, 2015; Zampieri, 2019; Tempesta, 2019). As an exception, Milankovitch in his doctoral dissertation developed the theory of the thrust line with reference to a masonry arch of variable thickness (1904). In the general case, the intrados and extrados lines are determined by two generic continuous functions so that the variable thickness of the arch ring can be considered. Despite the lack of theoretical background, the non-uniform arch has been implemented in the design of numerous historical bridges around the world. D' Agostino & Bellomo (2001) document that historical bridges of a large span have a gradually increasing thickness from the key to the springers at a ratio of 1.1 ÷ 1.6. Two representative examples of such stone bridges are portrayed in Figure 4.1.

Prompted by the lack of detailed investigation, the present study is oriented to non-uniform arches with the following geometrical particularity: elliptical at the extrados (upper curve) yet circular at the intrados (lower curve). For simplicity, this profile will be referred from now on as *a part-elliptical*. The objective is to investigate the role of the extrados curve on the structural performance of the arch under base horizontal motion.

In light of the above, the analysis of rocking response is divided in two steps (Alexakis, 2014; Oppenheim, 1992): (a) stability analysis is performed in static terms to calculate the hinge locations as well as the minimum ground acceleration at the onset of rocking, given the slenderness and the angle of embrace of the arch (t/R, β), (b) time-history analysis of rocking prior to impact is then feasible as the transition criterion from the full-contact to rocking phase has been established from the previous step. Regarding the first step, a rigorous variational formulation is implemented by adopting the principle of minimum total potential energy, $P = U + V$, where U is the elastic strain energy and V is the potential energy associated with force of gravity. According to this principle, the total energy is at a stationary position when an infinitesimal variation from such position involves no change in energy meaning that $\delta P = 0$. As no elastic deformation is considered $(U = 0)$, it eventually yields that $\delta V = 0$. The second step deals with the time-history analysis of rocking response with analytical or

numerical methods. Similar to the circular case, rocking of the arch ring is associated with a one-degree-of-freedom vibration once a four-link kinematic mechanism is developed. In the analytical procedures, the equation of motion derived with Lagrangian formulation is employed. Whenever a closed-from solution of equation of motion is not tractable the software system "Mathematica" is utilised to extract

the analytical solution. For the purposes of the numerical procedures, a two-dimensional finite element modelling is implemented. Numerical results are then discussed and compared to those provided by the analytical method. A comprehensive approach to gain insight to the geometrically nonlinear response of part-elliptical arches in the time-domain is through idealised pulses. Simple pulses are employed in the analysis not just to represent near-fault ground motion but also because in many cases the time history of the recorded acceleration can effectively be trimmed to a one-cycle pulse.

Prior to the analysis of the part-elliptical profile the study revisits the uniform circular arch in *Section 4.2*, in terms of calculation of the imminent hinges. Hence, the afore-described principle of minimum potential energy is engaged to extract closed-form solution of the hinge locations whereas the results are presented comparatively to those of the semi-analytical approach (Alexakis, Makris 2014). In *Section 4.3*, the response of the part-elliptical arch subjected to a horizontal acceleration is investigated. In particular, the model parameters are described in *Section 4.3.1*. Stability analysis is then presented in static terms in *Section 4.3.2* through variational and Lagrangian formulation (*Sections 4.3.2.1* and 4.*3.2.2* respectively). In *Section 4.3.3*, a time-history analysis of the response is performed through analytical and finite element approaches (described in *Sections 4.3.3.1* and 4.*3.3.2* respectively). To this end the results of a comparative study are presented in *Section 4.3.3.3*. The performance of the part-elliptical arch is evaluated with reference to the uniform, circular arch. Moreover, the two methods of analysis are also compared in the same section, in terms of time-histories of the problem parameters.

It is worthy of note that this study regards only the weight of the arch ring. This simplification allows to isolate the response of the arch itself excluding the effect (beneficial or detrimental) of additional dead loads of spandrels, backfills etc. Moreover, it enables comparison of the results with some well-established studies of the literature. An extension of the analytical and

numerical model that will simulate realistic conditions comprising of more complex loads and boundaries is worth contemplating in future work.

a.

b.

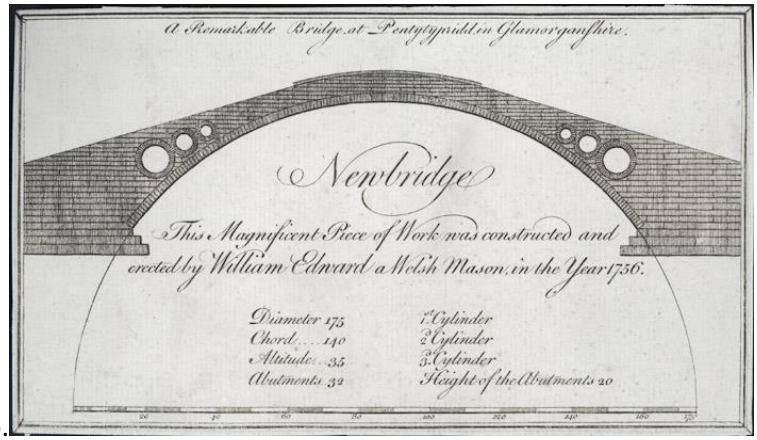

Figure 4.1 Two typical part-elliptical bridges: a. Templas bridge, Aetolia-Akarnania, Greece b. The Bridge at Pontypridd, Wales.

4.2 Revisiting the circular arch

4.2.1 Calculation of hinge locations in previous studies

As stone is a material strong enough to crush under compression, the only failure mode of a masonry arch is through the formation of no-tension hinges that turns the structure into a rocking mechanism. In dynamic terms, as soon as the critical uplift acceleration is reached, a stone arch of mid-thickness radius R, thickness t, and of angle-of-embrace β, becomes a four-hinge mechanism and the blocks rock one to the other as portrayed in Figure 4.2 (left side). It is implied that the structural stiffness is large enough so that in the full-contact phase no flexural displacements are developed. Evidently, in this regime the arch performs as a rigid body that follows the ground motion.

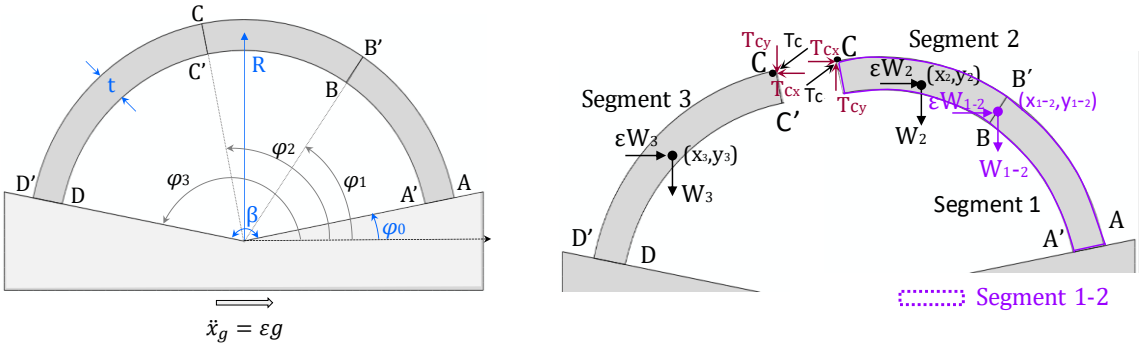

Figure 4.2 The circular arch with mid-thickness radius *R*, thickness *t* and angle of embrace β becomes a four-hinge mechanism when subjected to horizontal ground acceleration $\ddot{x}_g = \varepsilon g$ (left). Limit equilibrium analysis applied to the arch (right).

The question arising is to locate the points of rupture under a specific horizontal acceleration. A first approach was to consider that hinges develop at the physical joints of the blocks (Oppenheim 1992). In a subsequent approach the circular stone arch was treated as monolithic and the imminent hinges were determined by a method based on a variational formulation and the application of the principle of stationary potential energy (Alexakis & Makris 2014). This procedure is presented briefly and emphasis is given to the proposed analytical solution. In Figure 4.2 (left side) the location of the four hinges of the rocking mechanism developed by

horizontal acceleration $\ddot{x}_g = \varepsilon g$ is depicted in which ε is the seismic coefficient, and g is the acceleration of gravity. In this work, a two-springing collapse mechanism is studied which means that hinges A and D form at the extrados right springing (position φ_0) and the intrados left springing (position φ_3) respectively. On the other hand, hinges B and C form at the main arch body at positions φ_1 and φ_2 respectively. The weights (W_i) and the coordinates of the centre of gravity (x_i, y_i) of segment 2 (segment BC), segment 3 (segment CD) and the combined segment 1-2 (segment ABC) are presented in Eqs. (4.1) and (4.2). The limit equilibrium state of each segment (2,3, 1-2) is described below through Eqs. (4.3) and (4.4). The internal thrust force at point C (T_c) is analysed to the unknown horizontal and vertical components (T_{cx}), (T_{cy}) respectively (Figure 4.2 right).

For segments 2 and 3 (BC and CD respectively) it yields:

$$W_i = \rho g 2R^2 r'(\varphi_i - \varphi_{i-1})$$
$$x_i = R\left(1 + \frac{r'^2}{3}\right)\frac{\sin\varphi_i - \sin\varphi_{(i-1)}}{\varphi_i - \varphi_{(i-1)}}, y_i = -R\left(1 + \frac{r'^2}{3}\right)\frac{\cos\varphi_i - \cos\varphi_{(i-1)}}{\varphi_i - \varphi_{(i-1)}} \quad (4.1)$$

where i = 2 or 3, and $r' = \frac{t}{2R}$. Likewise, for the combined segment 1-2 (ABC) it yields:

$$W_{(i-1)-i} = \rho g 2R^2 r'(\varphi_i - \varphi_{(i-2)})$$
$$x_{(i-1)-i} = R\left(1 + \frac{r'^2}{3}\right)\frac{\sin\varphi_i - \sin\varphi_{(i-2)}}{\varphi_i - \varphi_{(i-2)}} \quad , \quad y_{(i-1)-i} = -R\left(1 + \frac{r'^2}{3}\right)\frac{\cos\varphi_i - \cos\varphi_{(i-2)}}{\varphi_i - \varphi_{(i-2)}} \quad (4.2)$$

where i = 2, and $r' = \frac{t}{2R}$. In both sets of Eqs. (4.1) and (4.2), density ρ is considered constant.

Moment equilibrium of segments 2, 3 about hinge B and C respectively, in a slightly different formulation to that developed in (Alexakis & Makris, 2014) yields:

$$a_i T_{c_x} + b_i T_{c_y} + f_i = 0$$

$$a_i = R\left((r' \pm 1)sin\varphi_i - (1 \mp r')sin\varphi_{(i-1)}\right)$$

$$b_i = R\left((1 \mp r')cos\varphi_{(i-1)} - (1 \pm r')cos\varphi_i\right) \quad (4.3)$$

$$f_i = \frac{2r'R^3}{3\cos\xi}((r'^2 + 3)\left(\sin(\xi - \varphi_{(i-1)}\right) - \sin(\xi - \varphi_i)) + 3(r' - 1)(\varphi_i - \varphi_{(i-1)})\cos(\xi - \varphi_*))$$

where i = 2 or 3, $\varphi_* = \varphi_{(i-1)}$ for segment 2 and $\varphi_* = \varphi_i$ for segment 3. Likewise, moment equilibrium of the combined segment 1-2 about hinge A yields:

$$a_{(i-1)-i} T_{c_x} + b_{(i-1)-i} T_{c_y} + g f_{(i-1)-i} = 0$$

$$a_{(i-1)-i} = (r' + 1)R\left(sin\varphi_i - sin\varphi_{(i-2)}\right)$$

$$b_{(i-1)-i} = (r' + 1)R\left(cos\varphi_{(i-2)} - cos\varphi_2\right) \quad (4.4)$$

$$f_{(i-1)-i} = \varepsilon W_{(i-1)-i}\left(y_{(i-1)-i} - (r' + 1)Rsin\varphi_{(i-2)}\right) + W_{(i-1)-i}\left(x_{(i-1)-i} - (r' + 1)Rcos\varphi_{(i-2)}\right)$$

where the multiplier of the horizontal earthquake $\varepsilon = \tan\xi$ and i = 2. By solving the above Eqs. (4.3), (4.4) it yields:

$$T_{c_x} = \frac{b_2 f_3 - b_3 f_2}{a_2 b_3 - b_2 a_3} \;\; and \;\; T_{c_y} = \frac{a_3 f_2 - a_2 f_3}{a_2 b_3 - b_2 a_3} \quad (4.5)$$

$$\left(a_{(1-2)}b_2 - b_{(1-2)}a_2\right)f_3 + \left(b_{(1-2)}a_3 - a_{(1-2)}b_3\right)f_2 + (a_2 b_3 - b_2 a_3)f_{(1-2)} = 0 \quad (4.6)$$

The horizontal (T_{c_x}) and the vertical (T_{c_y}) components of the internal thrust force T_c are unfolded on Eq. (4.5). Moreover, Eq. (4.6) involves only the radius *R*, the slenderness r' and the angles φ_i (i =1,2,3). Some of the formulae presented above (Eqs.4.1-4.4) can also be found in literature (Alexakis & Makris, 2013, 2014) however they are also included herein to facilitate independent reading.

4.2.2 Analytical calculation of hinge locations

Alternatively to what presented so far in literature (Alexakis & Makris, 2013, 2014), the left-hand side of Eq.(4.6) can be defined as a new function *G* of the independent variables *r'*, *R*, φ_i, ξ, which should be zero: $G(R, r', \varphi_1, \varphi_2, \varphi_3, \xi) := 0$. The fourth power of the radius *R* is an overall factor, therefore, multiplying by the inverse R^{-4} a new function *F* independent of *R* is defined: $F(r', \varphi_1, \varphi_2, \varphi_3, \xi) = 0$, which can be written as a fourth-degree polynomial with respect to *r':*

$$F(r', \varphi_1, \varphi_2, \varphi_3, \xi) = \sum_{k=1}^{4} c_k r'^k = c_4 r'^4 + c_3 r'^3 + c_2 r'^2 + c_1 r' + c_0 = 0 \qquad (4.7)$$

The coefficients c_k are known functions of the angles. Therefore, the solution of Eq. (4.4) can be expressed in terms of the roots of the polynomial (Eq. 4.7). It is noteworthy that the roots can be extracted analytically as functions of the angles φ_i. After algebraic manipulations, the coefficients of the fourth-degree polynomial (Eq.4.7) are presented on Eq. (4.8) presented below:

$$c_4 = \kappa, c_3 = \mu - \lambda, c_2 = 3\kappa + \nu, c_1 = -(3\lambda + \mu), c_0 = \nu \qquad (4.8)$$

$$\frac{\kappa}{2} = \sin(\varphi_1 - \varphi_3)\,(\sin\xi - \sin\varphi_2) + \sin(\xi - \varphi_2)\,(\sin\varphi_1 - \sin\varphi_3) \qquad (4.9)$$

$$\frac{\lambda}{2} = \sin(\varphi_1 - \varphi_3)\,(\sin\xi - \sin\varphi_2) - \sin(\xi - \varphi_2)\,(\sin\varphi_1 - \sin\varphi_3) \qquad (4.10)$$

$$\begin{aligned}\frac{\mu}{12} = {} & (\varphi_1 - \varphi_2)\cos\varphi_1 \cos\frac{\xi - \varphi_3}{2}\cos\frac{\varphi_2 - \varphi_3}{2}\sin\frac{\xi - \varphi_2}{2} \\ & + (\varphi_2 - \varphi_3)\cos\varphi_3 \cos\frac{\xi - \varphi_1}{2}\cos\frac{\varphi_1 - \varphi_2}{2}\sin\frac{\xi - \varphi_2}{2} + (\varphi_2 \\ & - \xi)\cos\xi \cos\frac{\varphi_1 - \varphi_2}{2}\cos\frac{\varphi_2 - \varphi_3}{2}\sin\frac{\varphi_1 - \varphi_3}{2}\end{aligned} \qquad (4.11)$$

$$\frac{v}{3} = [(\varphi_2 - \varphi_1)\cos\varphi_1 + \sin\varphi_1 - \sin\varphi_2][\sin(\xi - \varphi_2) + \sin(\varphi_2 - \varphi_3) + \sin(\varphi_3 - \xi)][(\xi - \varphi_2)\cos\xi - \sin\xi + \sin\varphi_2][\sin(\varphi_1 - \varphi_2) + \sin(\varphi_2 - \varphi_3) + \sin(\varphi_3 - \varphi_1)] + [(\varphi_2 - \varphi_3)\cos\varphi_3 - \sin\varphi_2 + \sin\varphi_3][\sin(\xi - \varphi_1) + \sin(\varphi_1 - \varphi_2) + \sin(\varphi_2 - \xi)] \quad (4.12)$$

According to the principle of stationary potential energy, every system in stable static equilibrium should have its potential energy minimised and therefore its partial derivatives with respect to the angles φ_i should be set equal to zero. The potential energy and the partial derivatives are given by the following forms, Eqs. (4.13) and (4.14) respectively:

$$V(r') = 4\,\rho R^3\,\sin\frac{\beta}{2}\,r'\left(1 + \frac{r'^2}{3}\right) \quad (4.13)$$

$$\frac{\partial V}{\partial \varphi_i} = 4\,\rho R^3\,\sin\frac{\beta}{2}(1 + r'^2)\,\frac{\partial r'}{\partial \varphi_i} = 0, \qquad i = 1,2,3 \quad (4.14)$$

where

$$\frac{\partial r'}{\partial \varphi_i} = 0, \qquad i = 1,2,3 \quad (4.15)$$

The derivative of r' (Eq. 4.15) can be extracted when differentiating Eq. (4.7):

$$\frac{\partial r'}{\partial \varphi_i} = -\frac{\sum_{k=1}^{4} c_k^{(i)} r'^k}{\sum_{k=1}^{4} k\,c_k r'^{k-1}} \qquad \text{where} \qquad c_k^{(i)} = \frac{d\,c_k}{d\,\varphi_i}, i = 1,2,3 \quad (4.16)$$

Where $c_k^{(i)}$ defined in Eq. (4.8), are computed in terms of the angles φ_i through Eqs. (4.9-4.12). In this way, the location of the hinges can be determined by setting the numerator of the right-hand side of Eq. (4.16) equal to zero. Therefore, solution is sought where Eqs. (4.7) and (4.16) hold simultaneously. Denote that Eq. (4.16) provides the analytical solution of the polynomial

function in contrast to the approach presented in Alexakis & Makris (2014), that was based on numerical procedures. A graphic illustration of the solution can yield the location of the hinges. In the diagram of Figure 3, the results of the analytical solution are compared to those derived numerically by Alexakis & Makris. The comparison is based on matching the location of the imminent hinges φ_1 and φ_2 of a circular arch for various angles of embrace β (β = 90°, 125°, 157.5°, 180°) and slenderness t / R. The range of seismic coefficient ε associated with the curves is: ε = 0.05 ÷ 1 for β = 90°, 125° and ε = 0.07 ÷ 1 for β = 157.5°, 180°. The comparison is proved remarkably good indicating the accuracy of the proposed analytical solution. The slight difference observed in the case of β = 157.5° is attributed to the comparison of the analytical solution with the other authors results of an arch of β = *155* °.

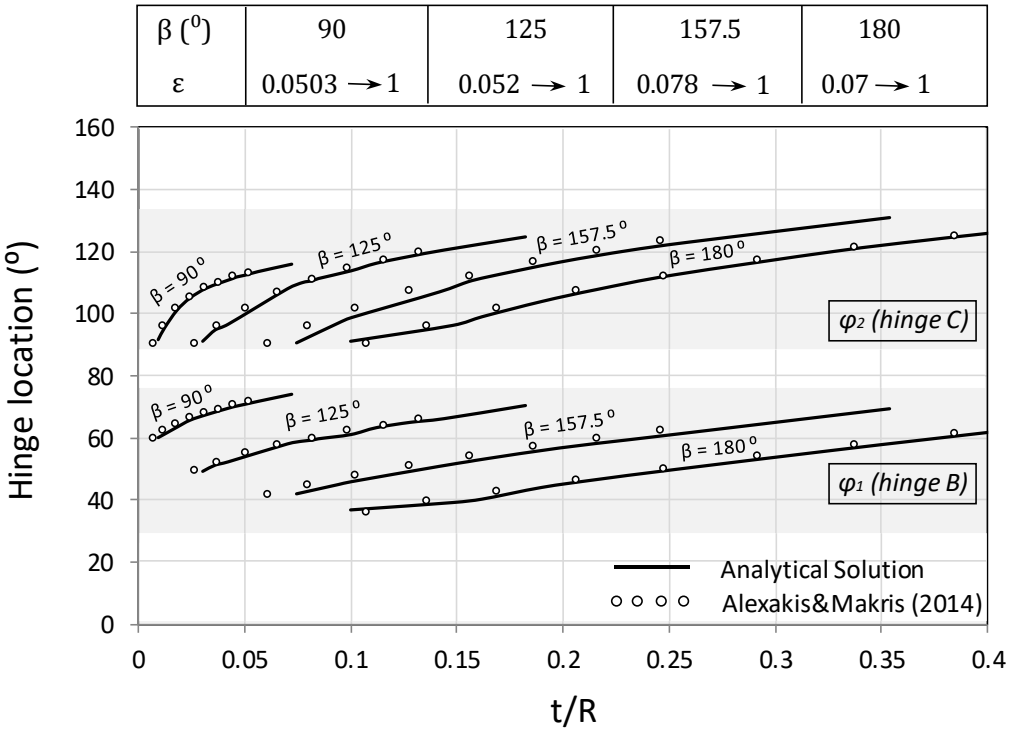

Figure 4.3 Location of the imminent hinges φ_1 and φ_2 at points B, and C respectively of a circular arch with a given angle of embrace β and slenderness t / R. Results of this work are compared with those obtained by Alexakis & Makris.

4.3 Part-Elliptical Arch

4.3.1 Model parameters

Consider now the rigid masonry arch shown in Figure 4.4 with the following particularity: circular on the inside (intrados) yet elliptical on the outside (extrados). In geometrical terms, this type of arch which from now on will be referred as part-elliptical, can be defined by the angle of embrace β, the thickness radius $R(\varphi)$, along with the shape parameters of the ellipse: the semi major and minor axes (a and b respectively, where $a > b > R\ (90°)$). In addition, as thickness t gradually decreases from the edge to the center, a nominal value has to be defined, which herein is set $t = t_{min}$ (i.e. the thickness at the mid-point axis). The aforementioned choice of the minimum value is considered more suitable not only for comparison purposes with arches of uniform thickness but also for computational simplicity as t in this position (φ =90°) is independent of the angle of embrace β. The position of each focus of the ellipse is given in vector notation:

$$\vec{r}(\varphi) = \frac{ab}{\sqrt{b^2 cos^2\varphi + \alpha^2 sin^2\varphi}}(icos\varphi + jsin\varphi) \tag{4.17}$$

in which, φ is the angle formed by the radius of the ellipse at a random point and the horizontal axis, whereas i and j represent the unit vectors with reference to the abscissa and the ordinate respectively. Accordingly, the thickness of the arch as a function of the angle, φ, is:

$$t(\varphi) = R_e(\varphi) - R_i = \frac{b}{\sqrt{1 - \frac{a^2 - b^2}{a^2}\cos^2\varphi}} - R_i \tag{4.18}$$

in which, R_e and R_i are the external and internal radii respectively.

Similar to the circular case, when a critical horizontal acceleration $\ddot{x}_g = \varepsilon\ g$ is applied at its supporting base, the arch transforms into a four-hinge mechanism. The presumable hinge

locations *A*, *B*, *C*, *D* defined by the angles φ_0, φ_1, φ_2, and φ_3 respectively are illustrated in the schematic of Figure 4.4. Hinge A forms at the right extrados of the springing at position $\varphi_o = (\pi-\beta)/2$ while hinge *D* is bounded by an unknown location φ_3. In this work a two-springing collapse mechanism is studied which means that hinge D forms at the intrados left springing (position $\varphi_3 = \pi - \varphi_o$). On the other hand, hinges *B* and *C* lie on the intrados and the extrados of the arch respectively.

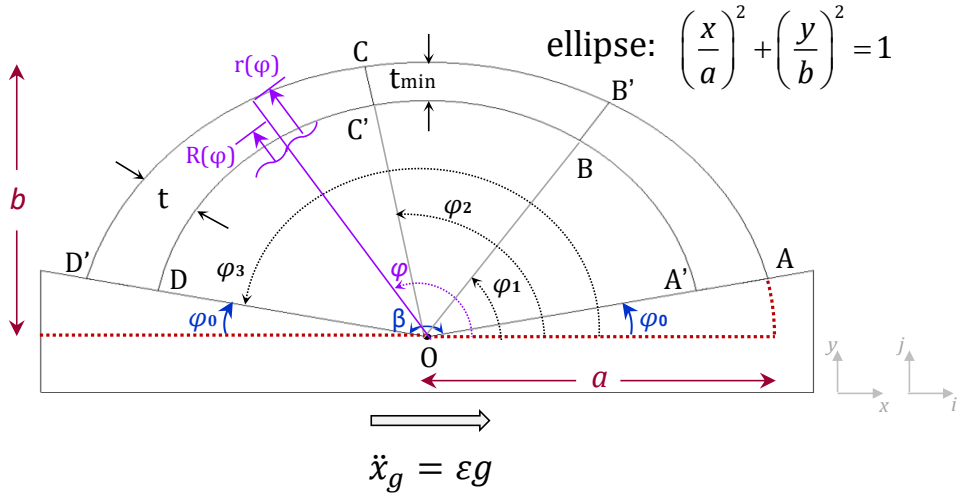

Figure 4.4 Schematic of the part-elliptical arch.

4.3.2 Stability analysis

4.3.2.1 Variational formulation

Equilibrium analysis is applied for the segments formed, as described above. Each segment is characterised by its weight *W* and the coordinates of the centre of gravity x_{cm}, y_{cm} (Figure 4.5). Alike the circular arch case, the cartesian components of the internal thrust force T_c (T_{c_x}, T_{c_y}) acting at the hinge *C* are considered as the unknown parameters of the equations below.

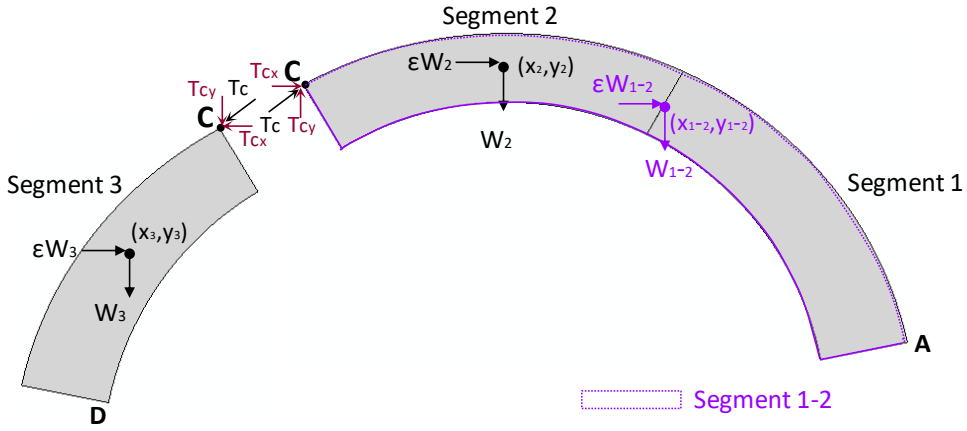

Figure 4.5 Limit equilibrium analysis applied to the part-elliptical arch.

For segment 2 (BC), its weight W_2 and the centre of gravity (x_2, y_2) yield:

$$W_2 = \rho g \frac{1}{2}\left[(\varphi_1 - \varphi_2)(r'-1)^2 + \frac{(r'+1)^2\left(\pi - \tan^{-1}\left(\frac{\tan\varphi_1}{\lambda}\right) + \tan^{-1}\left(\frac{\tan\varphi_2}{\lambda}\right)\right)}{\lambda}\right] \tag{4.19}$$

$$x_2 = \frac{\left[-(r'-1)^3(\sin\varphi_1 - \sin\varphi_2) + \frac{(1+r')^3\left(-\frac{\tan\varphi_1}{\sqrt{\lambda^2+\tan{\varphi_1}^2}} - \frac{\tan\varphi_2}{\sqrt{\lambda^2+\tan{\varphi_2}^2}}\right)}{\lambda^2}\right]}{3W_2}$$

$$y_2 = \frac{\left[-(r'-1)^3(\cos\varphi_1 - \cos\varphi_2) + \frac{(1+r')^3\left(-\frac{1}{\sqrt{\lambda^2+\tan{\varphi_1}^2}} - \frac{1}{\sqrt{\lambda^2+\tan{\varphi_2}^2}}\right)}{\lambda}\right]}{3W_2} \tag{4.20}$$

in which, r' is the slenderness ratio t / $2R$, and λ is the width-to-the-height ratio of the ellipse b / a. Likewise, for segment 3 (CD) its weight W_3 and the centre of gravity (x_3, y_3) yield:

$$W_3 = \rho g \frac{1}{2}\left[(\varphi_2 - \varphi_3)(r'-1)^2 - \frac{(r'+1)^2\left(\tan^{-1}\left(\frac{\tan\varphi_2}{\lambda}\right) - \tan^{-1}\left(\frac{\tan\varphi_3}{\lambda}\right)\right)}{\lambda}\right] \tag{4.21}$$

$$x_3 = \frac{\left[-(r'-1)^3(\sin\varphi_2 - \sin\varphi_3) + \frac{(1+r')^3\left(\frac{\tan\varphi_2}{\sqrt{\lambda^2+\tan{\varphi_2}^2}} - \frac{\tan\varphi_3}{\sqrt{\lambda^2+\tan{\varphi_3}^2}}\right)}{\lambda^2}\right]}{3W_3}$$

$$y_3 = \frac{\left[-(r'-1)^3(\cos\varphi_2 - \cos\varphi_3) + \frac{(1+r')^3\left(\frac{1}{\sqrt{\lambda^2+\tan{\varphi_2}^2}} - \frac{1}{\sqrt{\lambda^2+\tan{\varphi_3}^2}}\right)}{\lambda^2}\right]}{3W_3} \tag{4.22}$$

For the combined segment 1-2 (ABC) its weight $W_{1\text{-}2}$ and the centre of gravity ($x_{1\text{-}2}$, $y_{1\text{-}2}$) yield:

$$W_{1-2} = \rho g \frac{1}{2}\left[(\varphi_0 - \varphi_2)(r'-1)^2 + \frac{(r'+1)^2\left(\pi - \tan^{-1}\left(\frac{\tan\varphi_0}{\lambda}\right) + \tan^{-1}\left(\frac{\tan\varphi_2}{\lambda}\right)\right)}{\lambda}\right] \tag{4.23}$$

$$x_{1-2} = \frac{\left[-(r'-1)^3(\sin\varphi_0 - \sin\varphi_2) + \frac{(1+r')^3\left(-\frac{\tan\varphi_0}{\sqrt{\lambda^2+\tan{\varphi_0}^2}} - \frac{\tan\varphi_2}{\sqrt{\lambda^2+\tan{\varphi_2}^2}}\right)}{\lambda^2}\right]}{3W_{1-2}}$$

$$y_{1-2} = \frac{\left[-(r'-1)^3(\cos\varphi_0 - \cos\varphi_2) + \frac{(1+r')^3\left(-\frac{1}{\sqrt{\lambda^2+\tan{\varphi_0}^2}} - \frac{1}{\sqrt{\lambda^2+\tan{\varphi_2}^2}}\right)}{\lambda}\right]}{3W_{1-2}} \tag{4.24}$$

Moment equilibrium of the combined segment 1-2 (*ABC*) around hinge *A* yields:

$$
\begin{aligned}
&T_{c_x}\left(\frac{R\,(1+r')\sin\varphi_2}{\sqrt{1-\varepsilon^2\,\cos^2\varphi_2}}-\frac{R\,(1+r')\sin\varphi_0}{\sqrt{1-\varepsilon^2\,\cos^2\varphi_0}}\right)\\
&+T_{c_y}\left(\frac{R\,(1+r')\cos\varphi_0}{\sqrt{1-\varepsilon^2\,\cos^2\varphi_0}}-\frac{R\,(1+r')\cos\varphi_2}{\sqrt{1-\varepsilon^2\,\cos^2\varphi_2}}\right)\\
&+\epsilon\,W_{1-2}\left(y_{cm}^{1-2}-\frac{R(1+r')\sin\varphi_0}{\sqrt{1-\varepsilon^2\,\cos^2\varphi_0}}\right)\\
&+W_{1-2}\left(x_{cm}^{1-2}-\frac{R(1+r')\cos\varphi_0}{\sqrt{1-\varepsilon^2\,\cos^2\varphi_0}}\right)=0
\end{aligned}
\tag{4.25}
$$

Likewise, moment equilibrium of (i) segment 2 (*BC*) around hinge *B* and (ii) segment 2 (*CD*) around hinge *D* yields Eqs. (4.26) and (4.27) respectively:

$$
\begin{aligned}
&T_{c_x}\left(\frac{R\,(1+r')\sin\varphi_2}{\sqrt{1-\varepsilon^2\,\cos^2\varphi_2}}-R\,(1+r')\sin\varphi_1\right)\\
&+T_{c_y}\left(R\,(1+r')\cos\varphi_1-\frac{R\,(1+r')\cos\varphi_2}{\sqrt{1-\varepsilon^2\,\cos^2\varphi_2}}\right)\\
&+\varepsilon\,W_2\,(y_2-R\,(1+r')\sin\varphi_1)+W_2\,(x_2-R\,(1+r')\cos\varphi_1)=0
\end{aligned}
\tag{4.26}
$$

$$
\begin{aligned}
&T_{c_x}\left(\frac{R\,(1+r')\sin\varphi_2}{\sqrt{1-\varepsilon^2\,\cos^2\varphi_2}}-\frac{R\,(1+r')\sin\varphi_0}{\sqrt{1-\varepsilon^2\,\cos^2\varphi_0}}\right)\\
&+T_{c_y}\left(\frac{R\,(1+r')\cos\varphi_0}{\sqrt{1-\varepsilon^2\,\cos^2\varphi_0}}-\frac{R\,(1+r')\cos\varphi_2}{\sqrt{1-\varepsilon^2\,\cos^2\varphi_2}}\right)\\
&+\varepsilon\,W_3\left(y_3-\frac{R(1+r')\sin\varphi_0}{\sqrt{1-\varepsilon^2\,\cos^2\varphi_0}}\right)+W_3\left(x_3-\frac{R(1+r')\cos\varphi_0}{\sqrt{1-\varepsilon^2\,\cos^2\varphi_0}}\right)\\
&=0
\end{aligned}
\tag{4.27}
$$

The subtraction of the potential energy of a purely elliptical (V_{el}) and a purely circular (V_c) arch gives the potential energy of this particular arch geometry (see Appendix A):

$$V = g\,\rho\,\frac{2\,R^3}{3}\left(\frac{(1+r')^3}{\sqrt{1-\varepsilon^2\,\cos^2\varphi_0}} - (1-r')^3\right)\cos\varphi_0 \tag{4.28}$$

Next, the principle of stationary potential energy is revisited. Equilibrium is achieved when the potential energy is stationary meaning that the partial derivatives with respect to the critical angles φ_1, φ_2, φ_3 are equal to zero (Eq. 4.29). By differentiating Eq. (4.28) with respect to the angles φ_i yields:

$$\frac{\partial V}{\partial \varphi_i} = \frac{d V}{d r'}\frac{\partial r'}{\partial \varphi_i} = 0$$

$$\frac{\partial r'}{\partial \varphi_i} = 0, i = 1,2,3 \tag{4.29}$$

Evidently, Eqs. (4.25) ~ (4.27) are implicit functions of the independent variables (the slenderness ratio r' and the acceleration ε as well as the dependent variable φ_i). Iterative procedures available in the code *Mathematica* are implemented to separate the dependent variable φ_i from r' and ε and therefore to derive the locus of the solution. The solution leads to the unknown locations of the ruptures $\varphi_{1,2}$ as well as the minimum thickness t / R for given angles of embrace.

Figure 4.6 depicts comparatively a circular and a part-elliptical ($\lambda = b / a = 0.95$) arch for different levels of slenderness t / R and angles of embrace β, in terms of the critical acceleration needed to initiate motion. In particular, Figure 4.6 implies that for a given slenderness, higher acceleration values are required to initiate uplift of a part-elliptical arch compared to those required for a circular one. In the first case, the slenderness t / R due to thickness variation is considered with regard to the smallest values of t (thickness) and R (radius). Each pair of curves with the same angle of embrace, has a lower bound determined by a minimum t / R and a common upper bound at $\varepsilon = 1$ (arbitrarily chosen). Figure 4.7 illustrates the locations of hinges B and C forming when the arch is subjected to various values of uplift acceleration $\varepsilon\, g$, for given angles of embrace β. It is noted that the angle φo depends only upon β ($\varphi_0 = [\pi\text{-}\beta] /$

2). Interestingly, it is also observed that as confinement of the arch is gradually enforced (larger values of φ_0) the kinematic mechanism tends to be independent to the seismic coefficient, ε. On the other hand, for the unconfined arch ($\varphi_0 = 0$) a rather linear trend is established between the angles φ_1, φ_2 and the coefficient ε. The endpoints of the curves (minimum and maximum values of the seismic coefficient ε) are in one-to-one matching with the endpoints of the curves of Figure 4.6. Figure 4.8 yields that the ratio λ (= b / a) is linear to slenderness t / R for various levels of the seismic coefficient ε. It is confirmed that the arch thickness is favourable to the stability of the structural system, in a way that higher acceleration levels are required to induce rocking as the thickness is gradually increasing. Moreover, when comparing two arches of the same slenderness t/R but of different angles of embrace β it is concluded that the one of larger β becomes a four-hinge mechanism for a smaller horizontal acceleration εg.

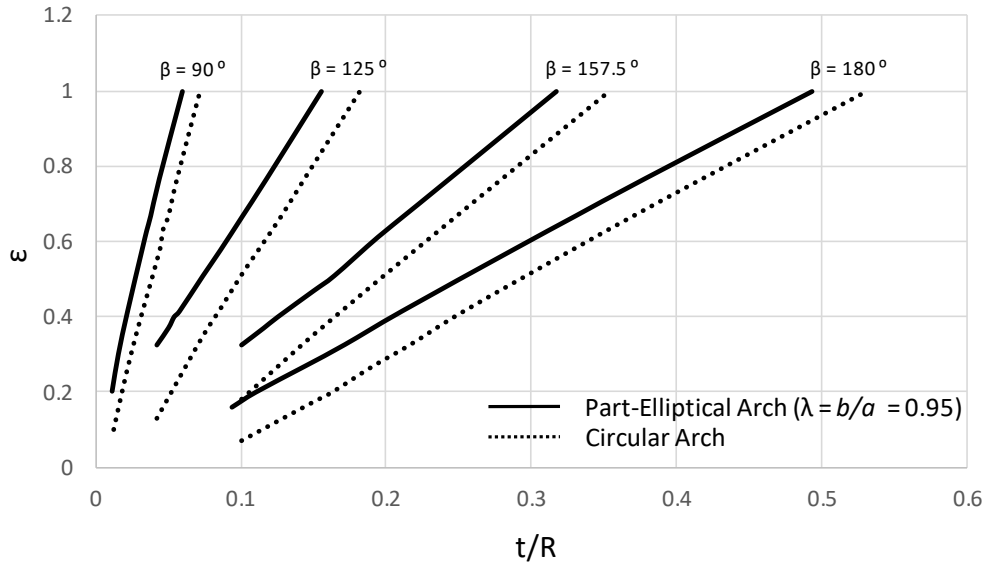

Figure 4.6 Seismic coefficient ε of circular arch and part-elliptical arch ($\lambda = b / a = 0.95$) for given angles of embrace β corresponding to different slenderness t / R.

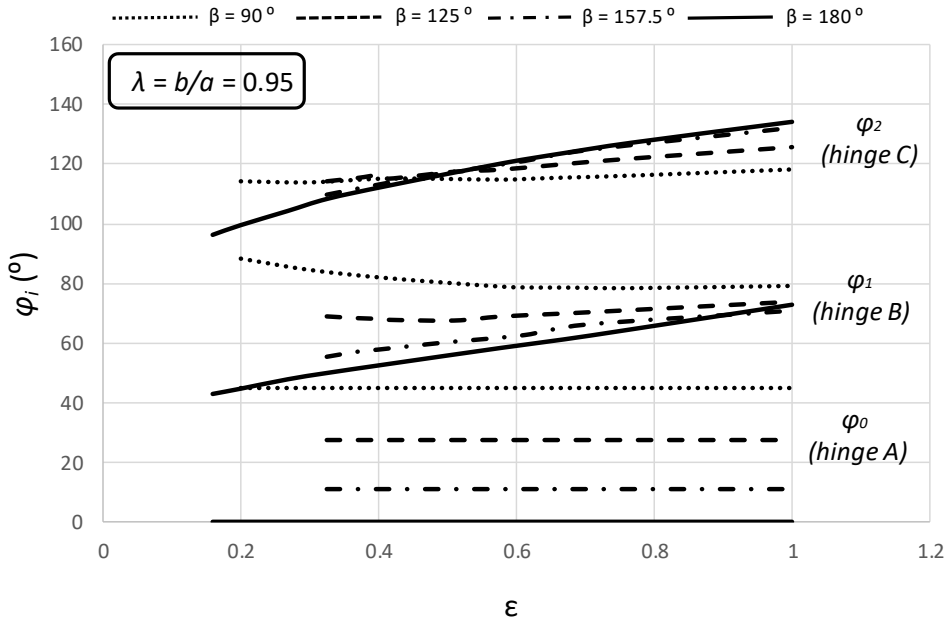

Figure 4.7 Location of the imminent hinges φ_i where i = 0, 1, 2 (points A, B, and C respectively) of a part-elliptical arch ($\lambda = b / a = 0.95$) with a given angle of embrace β.

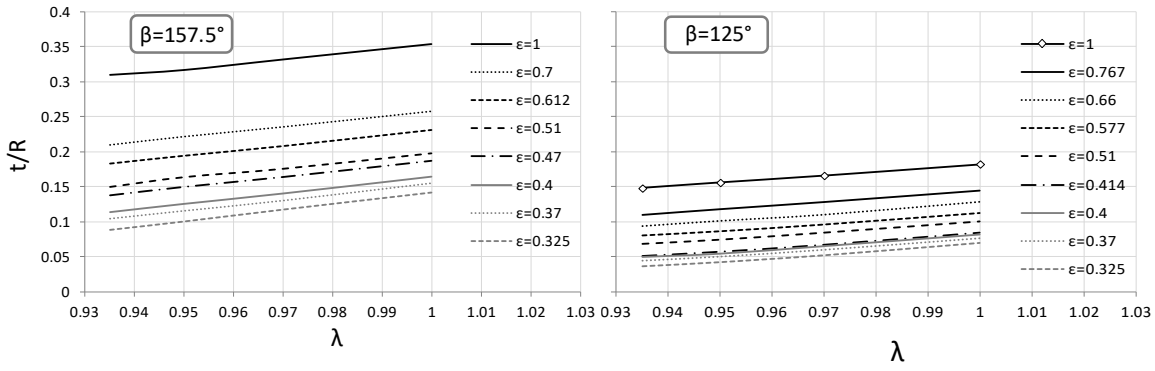

Figure 4.8 Minimum required slenderness as a function of $\lambda = b / a$ for different levels of the uplift horizontal acceleration $\ddot{x}_g = \varepsilon g$.

A numerical example can further elucidate the interplay of the geometrical parameters and the acceleration required for incipient uplift. The numerical values are chosen from the graphs of Figures 4.6 and 4.7. Let us consider the case where $\beta = 157.5°$ and $t / R = 0.194$. A circular arch uplifts for a horizontal ground acceleration, $\ddot{x}_g = 0.51\ g$, whereas a part-elliptical one when $\ddot{x}_g = 0.61$ g. In the first case, hinges form at $\varphi_1 = 56.622°$, $\varphi_2 = 116.611°$ and $\varphi_3 = 168.75°$,

whilst in the second case at φ_1 = 62.6°, φ_2 = 121.076° and φ_3 = 168.75°. Other geometrical parameters are: (a) the mid-radius R (R = 10 m), the thickness t (t / R = 0.194 => t = 1.94 m), the internal radius b ($b = R + t/2$ = 10.971 m) which are identical in both cases and (b) the ratio λ ($\lambda = b / a$ = 0.95) and a ($a = b / \lambda$ = 10.971/0.95 = 11.5484) which are additional for the part-elliptical arch (Figure 4.4).

4.3.2.2 Lagrangian formulation

The kinematic mechanism in combination with the Lagrangian non-linear formulation can contribute to extract the governing equation of motion. To this extent, the Lagrangian equation can be expressed in the following compact form.

$$\frac{d}{dt}\left(\frac{\partial T}{\partial \dot{\theta}}\right) - \frac{\partial T}{\partial \theta} + \frac{\partial V}{\partial \theta} = Q \tag{4.30}$$

in which, T is the kinetic energy of the system, V the potential energy and Q the generalized forces. For this single-degree-of-freedom system the angle $\theta = \theta_{AB} = \theta_0$ is chosen arbitrarily and without violating the constraint, as the Lagrangian independent variable (coordinate).

The kinematics of the system employed to formulate the Lagrangian equation of motion is portrayed in Figure 4.9. The horizontal supporting base is represented with a rigid plane free to undergo horizontal vibration. The rocking arch consists of 3 rigid segments (AB, BC, CD) that correspond to different portions of the angle of embrace β ($= \theta_1 + \theta_2 + \theta_3$). The initial and the displaced state are determined with the angles θ_0 and θ respectively measured anticlockwise from the horizontal. The rotation of such a system, is denoted as ϕ, is $\theta_0 - \theta$ with respect to the original geometry. The horizontal acceleration applied to the base from right to left ($\ddot{x}_g < 0$) causes a positive rotation (ϕ) of the arch which initially will rock to the right.

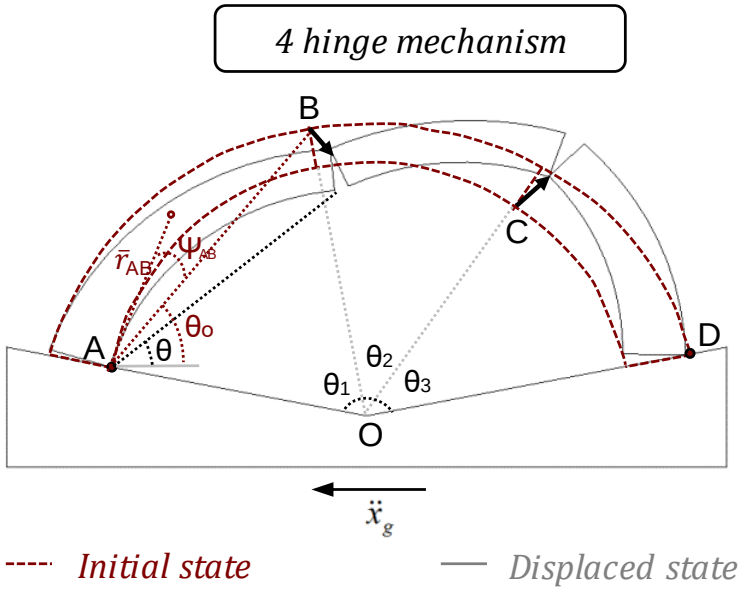

Figure 4.9 Kinematic mechanism of the part-elliptical arch.

Consequently, the equation of motion takes the compact form:

$$M(\theta)\ddot{\theta} + L(\theta)\dot{\theta}^2 + F(\theta)g = P(\theta)\ddot{x}_g \tag{4.31}$$

in which the coefficients $M(\theta)$, $L(\theta)$, $F(\theta)$, $P(\theta)$ are nonlinear equations of θ given below after replacing $f_{xy} = m_{xy}\bar{r}_{xy}^2 + I_{xy}$. Where m_{xy}, $\bar{r}_{xy}$, I_{xy} and ψ_{xy} are the mass, the distance to the centre of mass measured from the downstream joint corresponding to each link, the centroidal polar moment of inertia and the angular offset respectively (xy = AB, BC, CD) (Figure 4.9).

$$M(\theta) = f_{AB} + f_{BC}\theta'^2_{BC} + f_{CD}\theta'^2_{CD} + m_{BC}[AB^2 + 2AB\bar{r}_{BC}\theta'_{BC}\cos(\theta - \theta_{BC} - \psi_{BC})]] \tag{4.32}$$

$$L(\theta) = f_{BC}\theta'_{BC}\theta''_{BC} + f_{CD}\theta'_{CD}\theta''_{CD} + m_{BC}AB\bar{r}_{BC}[\theta''_{BC}cos(\theta - \theta_{BC} - \psi_{BC}) - \theta'_{BC}(1 - \theta'_{BC})\sin(\theta - \theta_{BC} - \psi_{BC})] \tag{4.33}$$

$$F(\theta) = m_{AB}\bar{r}_{AB}\cos(\theta + \psi_{AB}) + m_{BC}[AB\cos\theta + \bar{r}_{BC}\theta'_{BC}\cos(\theta_{BC} + \psi_{BC})] + m_{CD}\bar{r}_{CD}\theta'_{CD}\cos(\theta_{CD} + \psi_{CD}) \tag{4.34}$$

$$P(\theta) = m_{AB}\bar{r}_{AB}\, sin(\theta + \psi_{AB}) + m_{BC}[ABsin\theta + \bar{r}_{BC}\theta'_{BC}\, sin(\theta_{BC} + \psi_{BC})] + m_{CD}\bar{r}_{CD}\theta'_{CD}\, sin(\theta_{CD} + \psi_{CD}) \quad (4.35)$$

These functions have been presented in literature in similar forms (Oppenheim, 1992; Clemente, 1998; Leontari, 2018). In addition, their physical interpretation has also been elucidated (Oppenheim, 1992). Eq. (4.31) is valid only when $\theta < \theta_o$, meaning that the computation of the rocking angle θ is limited to the prior-to-impact state. Evidently, the equation of motion is dependent upon the geometrical characteristics of the structure. A similar procedure has been followed for a circular arch (Oppenheim, 1992; Clemente, 1998; Leontari, 2018). Nevertheless, the part-elliptical arch requires a larger computational effort due to geometric complexities. The horizontal ground acceleration needed to initiate uplifting about the predefined hinges can also be extracted from Eq. (4.31) by applying the criterion for incipient rocking: $\ddot{\theta} = \dot{\theta} = 0$. The above condition states that the supporting base should experience acceleration larger than $|\ddot{x}_g|$ = *F(θ) / P(θ)* = 0.61 g in order the developing inertia forces to set the arch on rocking. Compared to the circular arch case where $|\ddot{x}_g|$ = *F(θ) / P(θ)* = 0.51 g, the part-elliptical arch performs enhanced-resistance to entering the rocking mode. The above values of uplift acceleration can also be extracted from the diagram of Figure 4.6.

A comparison between the part-elliptical and the circular arches is performed in Figure 4.10 in terms of the potential energy normalised to its value as a function of the rotation ϕ. A turning point of the system is at the moment the potential energy reaches its peak value which corresponds to maximum rotation ϕ_c and ϕ_e for the circular and part-elliptical arch respectively. For these critical values of rotation, velocity and kinetic energy are instantaneously zero and the system "decides" whether it eventually collapses or not. For the circular case the point of non-recovery is reached after a relatively small rotation. In fact, as already pointed out by Oppenheim (1992) "*a typical arch has considerable resistance to the onset of mechanism motion but relatively little capacity to absorb forced excursions into such motion*". This finding is even more amplified in the part-elliptical arch in which the critical rotation ϕ drops from 0.25 rad down to 0.20 rad at a maximum energy ratio *V(ϕ) / V(ϕ₀)* even higher.

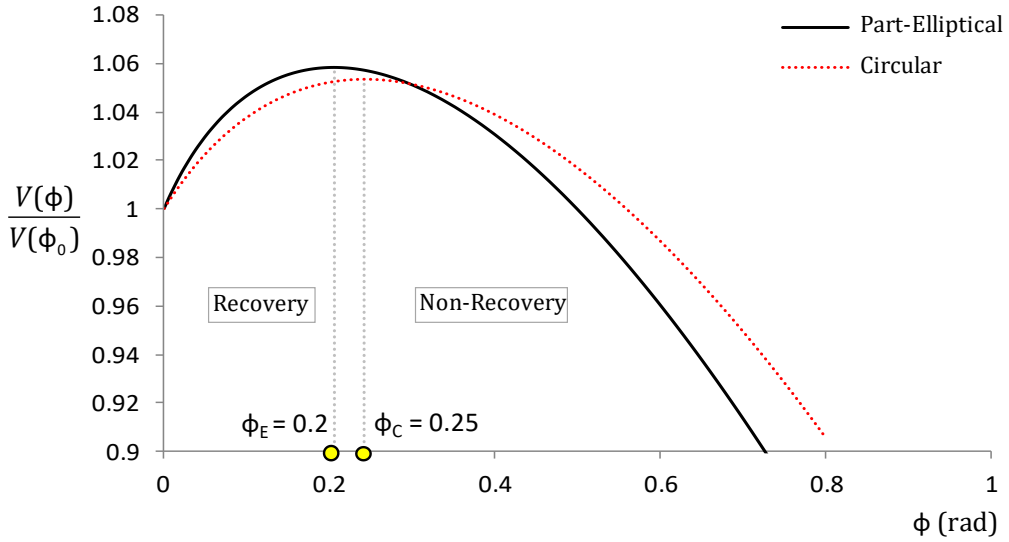

Figure 4.10 Recovery and non-recovery domain introduced by the normalized potential energy for both circular and part-elliptical arch (dotted and continuous lines respectively).

For a rocking masonry arch, gravity is the restoring mechanism that brings the structure back to static equilibrium. In Figure 4.11, both the restoring and the driving mechanism for each profile are portrayed. The alternation of sign in the case of the coefficient $F(\theta)$ denotes that the mechanism the gravitational force imposes to the system turns from restoring to driving. For the part-elliptical arch (continuous line) gravity leads the system to overturning faster compared to the circular arch (dotted line). Therefore, the point of non-recovery ϕ_{cr} is reached earlier in the first case. This is a reasonable finding as the part-elliptical arch is heavier, due to its geometry. On the other hand, during the entire motion, the ground acceleration contributes to the system as a destabilising factor. In concluding, a circular arch requires smaller acceleration amplitudes to uplift while the part-elliptical exhibits substantial resistance to earthquake pulses. On the other hand, the part-elliptical arch reaches the threshold of collapse in smaller rotations than the circular arch for a specific thickness/radius ratio.

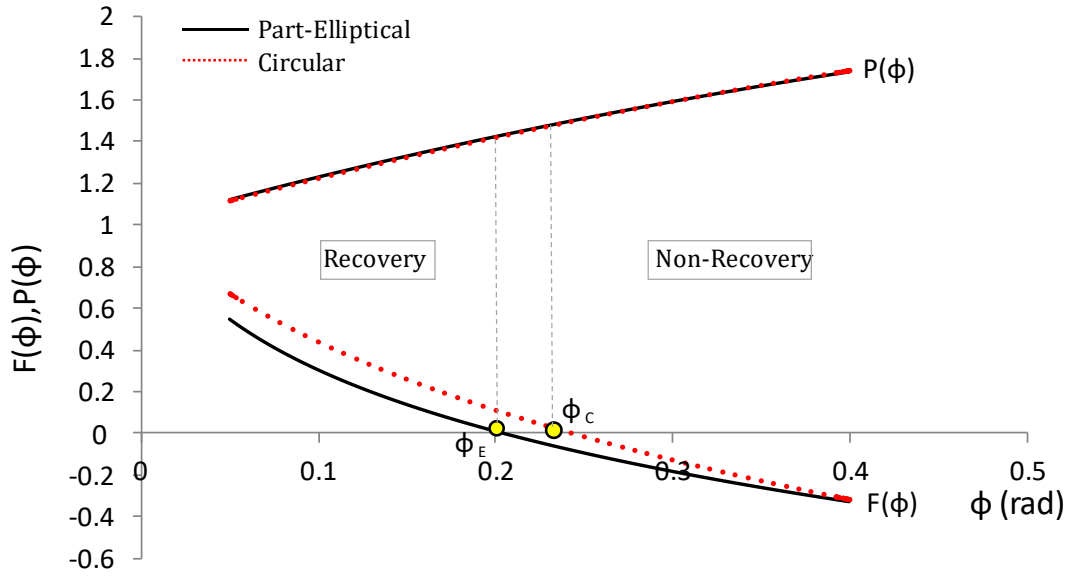

Figure 4.11 Representative coefficients *F* and *P* defined by the non-recovery point for circular and part-elliptical arch (dotted and continuous lines respectively).

4.3.3 Time-history analysis

4.3.3.1 Lagrangian formulation

The governing equation of motion as derived from Lagrangian formulation (Eq. 4.31) in combination with the nonlinear coefficients (Eqs. 4.32 ~ 4.35) is implemented to compute the time-history of rocking rotation. A numerical solution of the differential equation of motion in terms of rotation ϕ (or the angle θ) is accomplished with *Mathematica* code, after properly adjusting the coefficient $P(\phi)$ (or $P(\theta)$) to implement ground shaking. The linearised equation of motion is solved iteratively through a numerical solver (ND solve) in the Wolfram Mathematica 8 environment. To determine the solutions of the equation, initial conditions are denoted in the form $\phi\,(0) = 0$ and $\phi'\,(0) = 0$. Mathematica can switch methods many times if the situation asks for it. The explicit integration settings for the applied methods are the "Runge-Kutta" (Implicit or Explicit), the "Adams" methods or implicit backward differentiation formulas (BDF or IDA).

4.3.3.2 Finite element modelling

Nonlinear analysis of a free-standing arch on accelerating base is implemented numerically in the time-domain with the finite element method. To this extent, the software suite *Abaqus* is utilised for the mesh generation as well as for the analysis execution. Both the arched structure and the supporting base are represented with quadrilateral, continuum plain strain elements. A reasonably refined mesh of the model is generated, composed of elements varying from 0.33 m to 0.47 m in width for the arch and from 0.17 m to 0.39 m for the base. The linearly elastic behaviour of the masonry arch is determined by elastic modulus, E = 10 GPa, Poisson ratio, ν = 0.20, and density, ρ = 2.2 t/m^3. In the same way, for the supporting base the material properties are E = 30 GPa, ν = 0.20, and ρ = 2.5 t/m^3. For such high levels of the elastic moduli, flexural deformations are rather negligible, and therefore each structural element can practically be considered as rigid. The arch is partitioned in three monolithic voussoirs which together with the base form four interfaces (hinges). A surface-based kinematic contact algorithm has been adopted allowing for rigorous treatment of finite separation (uplifting) and sliding at each interface. The latter is governed by a Coulomb-type frictional law at the interface. Experimental studies have pointed out that for masonry stones the coefficient of friction can roughly be estimated at 0.7 (Marino M. 2014). Geometric nonlinearity attributed to $P-\delta$ effects is taken into account through appropriate large displacement formulation. A direct integration of the equations of motion is performed at each time increment through an explicit algorithm incorporated in the finite element code. This dynamic analysis procedure is based upon the implementation of the explicit central-difference integration rule of the kinematic variables (Eq. 4.36):

$$\dot{u}^N{}_{\left(i+\frac{1}{2}\right)} = \dot{u}^N{}_{\left(i-\frac{1}{2}\right)} + \frac{\Delta t_{(i+1)} + \Delta t_{(i)}}{2} \ddot{u}^N_{(i)} \tag{4.36}$$

where u^N is a degree of freedom (a displacement or rotation component) and the subscript i refers to the increment number. In addition, the use of diagonal ("lumped") element mass matrices allows for the accelerations at the beginning of the increment to be computed according to Eq. (4.37).

$$\ddot{u}^N_{(i)} = (M^{NJ})\left(P^J_{(i)} - I^J_{(i)}\right) \tag{4.37}$$

where M^{NJ} is the mass matrix, $P^J_{(i)}$ is the applied load vector, and $I^J_{(i)}$ is the internal force vector.

The afore-discussed explicit procedure is computationally efficient in a sense that it requires no iterations and no tangent stiffness matrix. The computational cost is further minimised by choosing reduced integration elements (CPE4R) available in Abaqus/Explicit code. The finite element configuration of the model is illustrated in Figure 4.12.

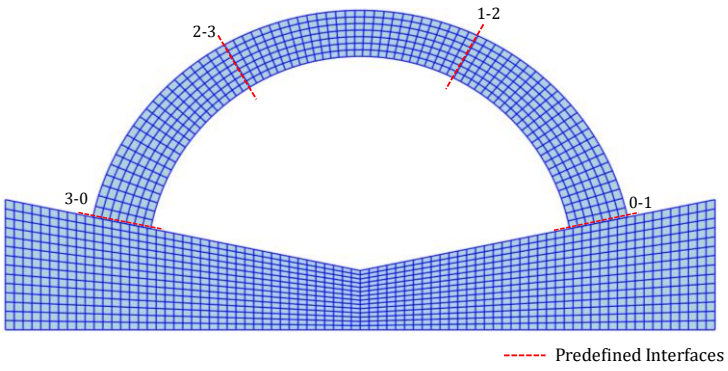

Figure 4.12 2-dimensional finite element model of the non-uniform arch and the supporting base. The four predefined interfaces are also depicted.

The lateral boundaries of the model are free to move horizontally unlike the vertical movement of the base which is restricted. Concerning the horizontal loading, different types of pulses are in all cases uniformly imposed to the bottom surface of the base for representing seismic

excitation. On the other hand, vertical loading is restricted to the self-weight of the structure excluding the effect of other gravitational loads caused by the backfill or live loads.

4.3.3.3 Comparative study

Effect of the non-uniform profile. The response of the part-elliptical arch is first computed with the finite element method for different levels of geometrical ratio λ. In this way the results can be comparatively presented with those of the circular arch (λ =1). A series of one-cycle trigonometric pulses is applied as excitation at the base. This sort of pulses approximates the kinematic characteristics of recorded near-source excitations and may lead to considerable permanent displacements. They are discretised to Type A (forward pulse or one sine pulse), Type B (forward-and-back pulse or cosine pulse) and Type C_n (exhibits n cycles). The present study is limited to the first type due to its more detrimental effects. This so-called one-sine pulse is presented in Figure 4.13. It is characterised by the amplitude a_p, the period T_p, and the time for the onset of rocking t_{on} expressed in terms of amplitude a_p, frequency $\omega_p = \frac{2\pi}{T_p}$, and the ratio $F(\theta)$ / $P(\theta)$. Figure 4.14 portrays time-histories of the normalised angle, θ, for three different values of λ: 0.95, 0.97, 1. Hence, three arches of different upper curve (extrados) are selected, in which the minor axis (b = 10.97 m) is kept constant whereas the value of the major axis (a) ranges from $a = b$ = 10.97 m (circular case) to a = 11.31 m and a = 11.5484 m (elliptical cases). In light of the above, a salient comparison among the three arches can be performed. During arch rocking, two different states can be distinguished: (a) rocking with impact during the excitation or (b) overturning at the first half of the cycle. For high frequency pulses (ω_p = 2π) the increase in the acceleration amplitude, from 0.75 g to 1 g and eventually to 1.33 g, doesn't essentially affect the arch behaviour for any of the arches. For lower values of frequency ω_p (π, 0.5π) though, the acceleration amplitude plays a crucial role to the arch response. For instance, a pulse of ω_p = π may lead to collapse for a_p = -1.33 g whereas for lower amplitudes the arch survives failure. Another interesting response is the one caused by a pulse of $\omega_p = 0.5\pi$ and a_p = -0.75 g where the arch of λ = 0.95 manages to survive failure unlike the other two arches. The following one-cycle pulses induce larger rotations for circular arches which in some cases may lead to collapse. In view of the above findings, it may be stated that part-elliptical arches due to their slightly different geometry are more stable

structures than the circular arches. Particularly the more "elliptical" the upper curve is the less prone is the arch to failure. Their stability decreases as the geometrical ratio λ increases till the value of $\lambda = 1$ where the arch becomes circular.

Comparison between analytical and numerical solution. The results of the time-history analysis obtained with the semi-analytical method are comparatively presented next with those of the finite element method for a part-elliptical arch with geometrical ratio $\lambda = 0.95$. Such a comparison is essential due to the assumptions and simplifications involved in these two methods. Hence, the analytical approach adopts the rigid, no-tension model of a monolithic arch in which sliding along the joints is prevented. On the other hand, the finite element approach considers for the masonry a very stiff structure (E = 30 GPa), yet not ideally rigid. In addition, the imminent hinges are predefined as a prevailing kinematic mechanism under dynamic lateral load is regarded, whereas sliding is not prevented. A two-step rectangular pulse is introduced to the analysis as an excitation to the supporting base. It contains a large negative pulse (a_p = -1 g) of duration t_p followed by a smaller positive pulse of half magnitude (a_p = 0.5 g) and of double duration $2t_p$. Such pulses were introduced to the analyses and used in recent studies (Heyman, 1982; Oppenheim, 1992; Dimitri, 2015). Their particularity is the lack of residual velocity. In Figure 4.15, the arch response to pulses with duration t_p = 0.75 sec and t_p = 0.80 sec is illustrated using both the analytical and the numerical method. For a pulse of t_p = 0.75 sec as a base motion (black lines), the arch safely exhibits rocking and returns to equilibrium state (rotation ϕ = 0 rad) regardless of the method, analytical or numerical (solid or dotted line respectively). On the contrary, for a pulse of t_p = 0.80 sec (red lines) both solutions predict that the arch is rocking and eventually overturns as rotation ϕ increases exponentially. More importantly, a good agreement is also observed between analytical and numerical solution for both pulses. A sequence of snapshots resulted from the deformed FE mesh model is portrayed in Figure 4.16. These snapshots portray the arch in the last increment of the pulse (state of recover and overturning).

The comparative study of the two methods implemented to compute rocking response is extended next as illustrated in Figure 4.17. To this end, the part-elliptical arch of the numerical example of *Section 4.2.1* is once more adopted (β = 157.5° and t / R = 0.194). Ground motion applied to the supporting base is simulated with a one-sine pulse of acceleration amplitude values 0.75 g, 1.0 g, and 1.33 g. It is worthy of note that all three values exceed the threshold

acceleration at incipient uplift (0.61 g), hence rocking motion is expected. In addition, three values of the excitation period are adopted: 1.0 sec, 2.0 sec, 4.0 sec. The above values of a_p and T_p form a set of 9 analyses, all representative of very strong motion under quasi-static conditions. A remarkable agreement between the two methods is observed, which highlights the reliability of both approaches in the context of a dynamic time-history analysis. A slight deviation is observed in the case of ω_p = 0.5π and a_p = 0.75 g where the semi-analytical method gives more conservative results.

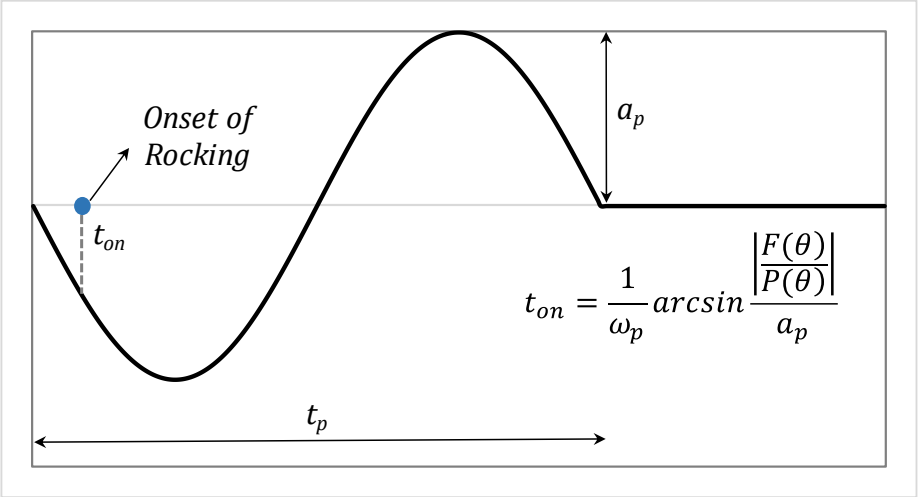

Figure 4.13 One-sine pulse (cycloidal Type A pulse).

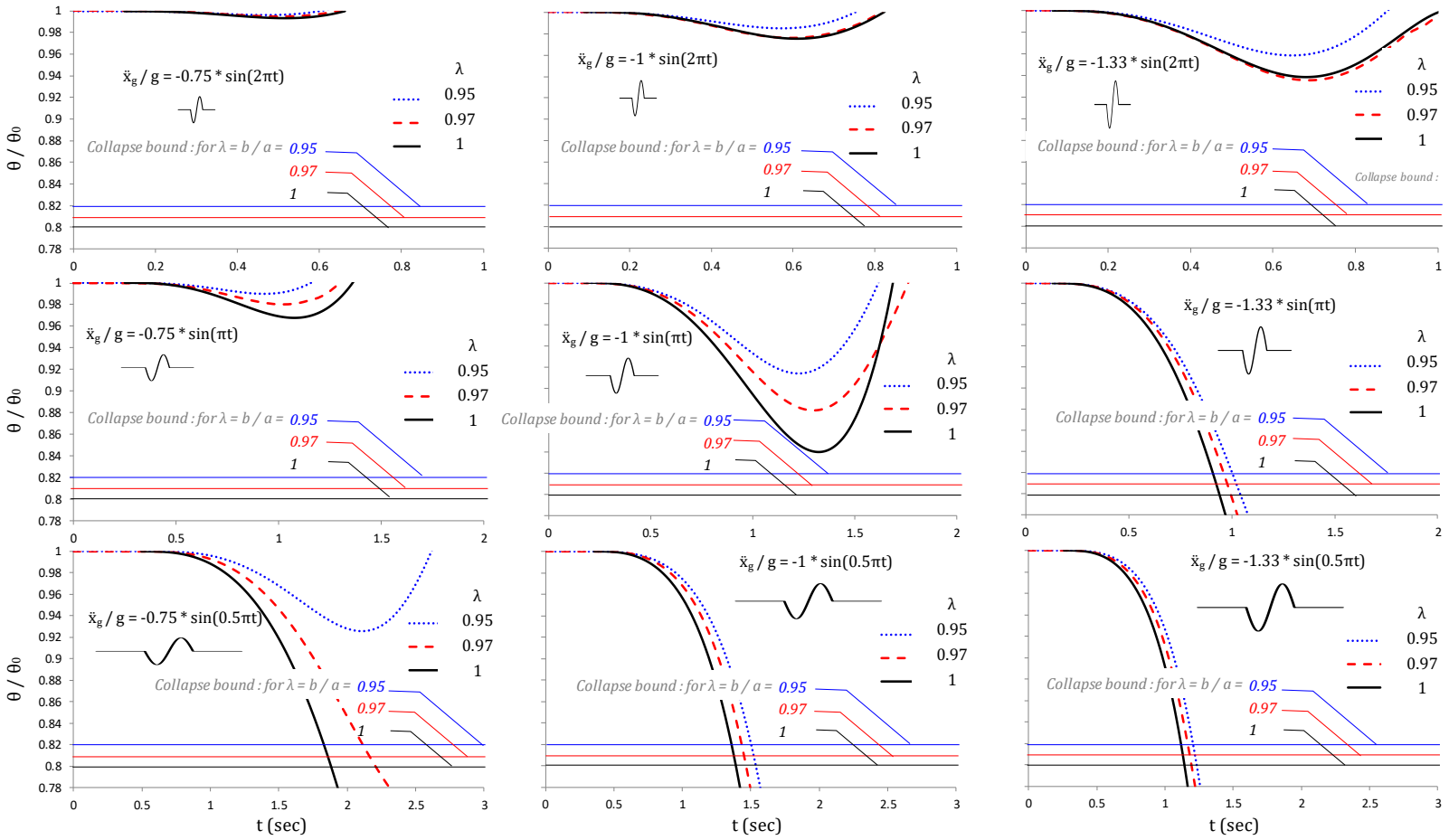

Figure 4.14 The influence of the geometrical ratio λ on the time history of the normalised angle θ when the arch is subjected to various one-sine pulses. Three different cases are investigated: (a) for λ = 0.95 (part-elliptical arch), (b) λ = 0.97 (part-elliptical arch), and (c) λ = 1 (circular arch). Collapse bounds for each case are depicted.

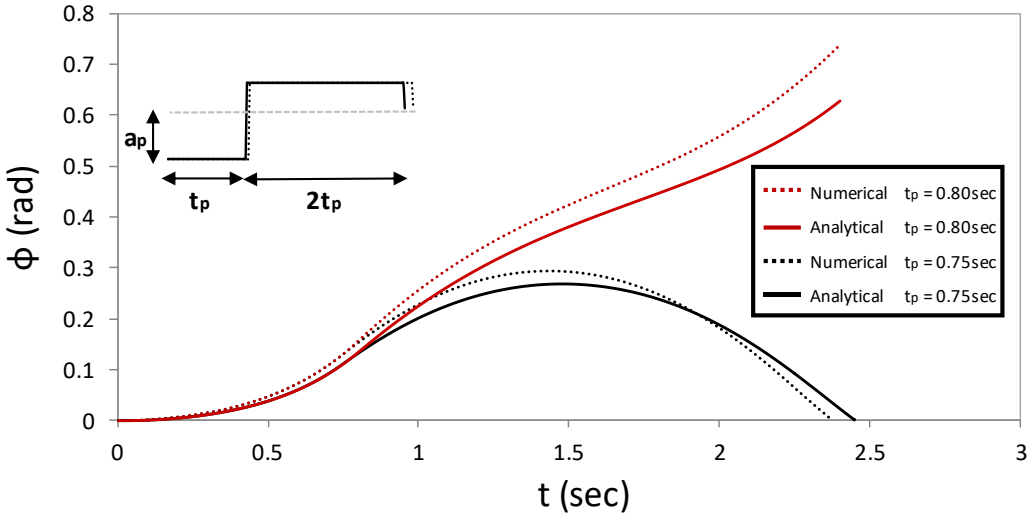

Figure 4.15 Rotation time histories of the part-elliptical arch subjected to different rectangular pulses. Black lines: t_p = 0.75 sec. Red lines: t_p = 0.80 sec. Solid lines: analytical solution. Dashed lines: numerical solution.

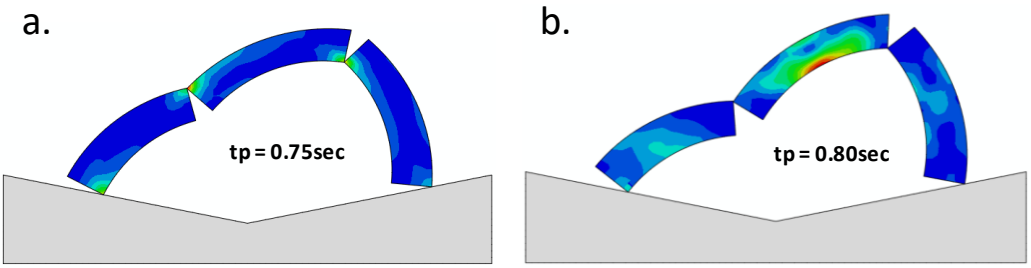

Figure 4.16 Illustration of snapshots of the part-elliptical arch subjected to rectangular pulses: (a) Recover, *tp* = 0.75 sec (left), (b) Overturning, *tp* = 0.80 sec (right).

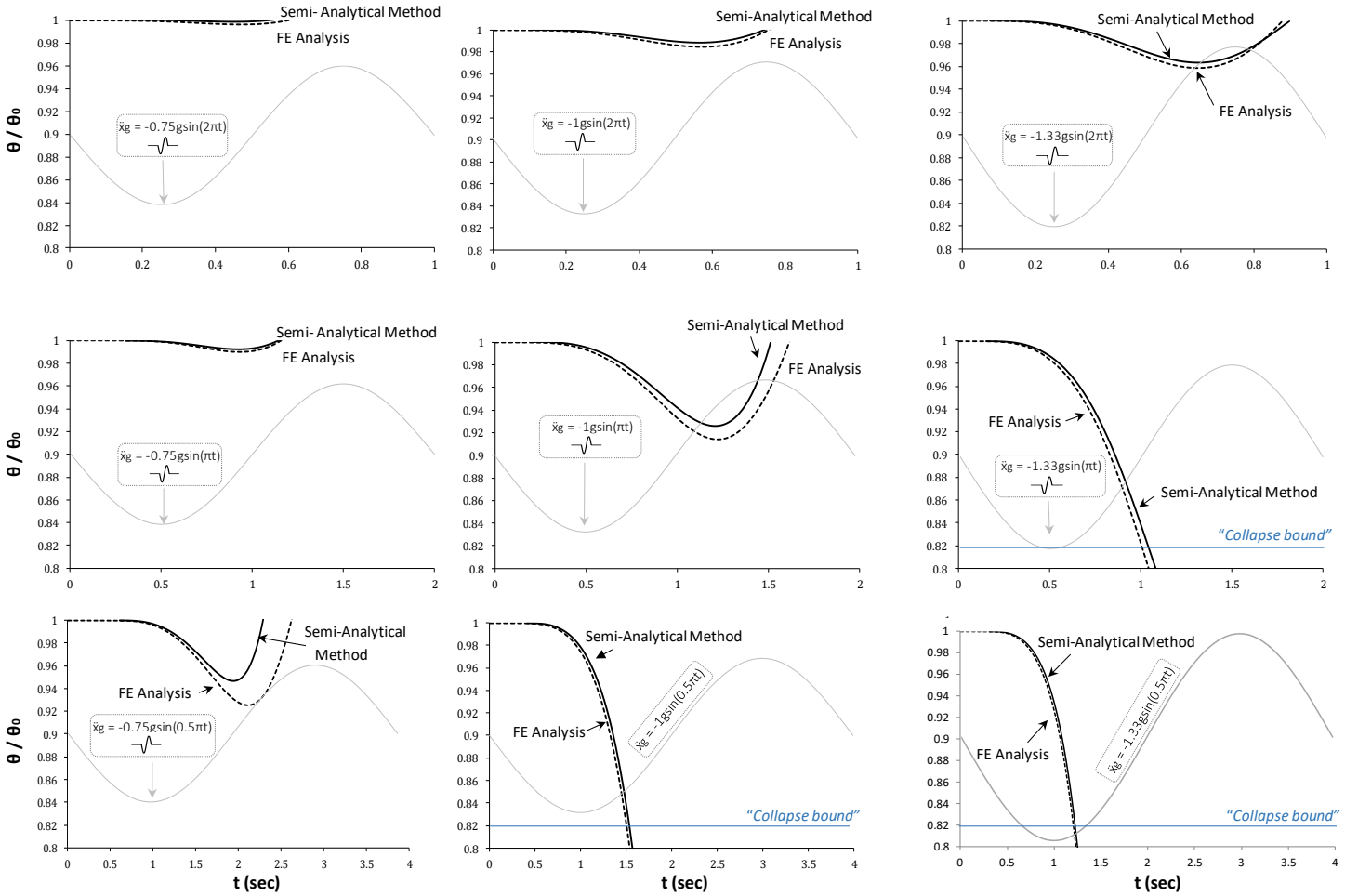

Figure 4.17 Time histories of the normalised angle θ of a part-elliptical arch (λ = 0.95) excited by one-sine pulses at the base. Comparison between FE (dotted line) and semi-analytical solution (continuous line).

4.4 Conclusions

An arch ring of non-uniform thickness subjected to rocking is employed in this study. This so-called part-elliptical arch is described with an elliptical (upper) and a circular (lower) curve, and is frequently encountered in long-span masonry bridges. This chapter investigates the response of such a structure in comparison with the uniform circular arch.

Based on the existing method of a variational formulation in literature (Alexakis & Makris 2014), in the beginning, the hinge locations of a continuous monolithic circular arch are calculated when subjected to a given level of acceleration $\ddot{x}_g$. What is new in this study is that the locations of the imminent hinges are calculated analytically through closed-form solutions. The results are in excellent agreement with those derived from the semi-analytical approach of previous study (Alexakis & Makris 2014).

Regarding the part-elliptical arch, (i) stability analysis and (ii) dynamic response analysis are engaged. Stability analysis involves both variational and Lagrangian formulation. In the context of a demand assessment, namely for a given slenderness, it is found that systematically higher acceleration levels are required to set a part-elliptical arch on rocking compared to those required for a circular one. This implies that an arch with increasing thickness from the key to the springers (as described with λ) performs enhanced resistance to hinge formation and rocking when subjected to ground horizontal excitation. Therefore, it has reasonably been adopted in the past as an improved profile in terms of seismic performance, for long-span masonry bridges. Moreover, when comparing two arches of the same slenderness t / R but of different angles of embrace β it is concluded that the one of larger β becomes a four-hinge mechanism for a higher horizontal acceleration $\varepsilon\ g$. Dynamic response analysis is performed in the time domain through analytical and numerical methods. In the former, time-histories of the rocking response are computed from the analytical solution of the Lagrangian equation of motion. Idealised pulses are used as base excitation to represent conditions of near-source ground shaking. Once rocking occurs it turns out that the non-uniform profile impacts the response but not in a

straightforward fashion. Evidently, the response is very sensitive to the excitation period unveiling the profoundly non-linear nature of the problem. Apart from the analytical treatment, two-dimensional numerical analysis with finite elements is performed. The results are presented comparatively with those of the analytical method for long-duration pulses. Both methods provide time-histories of the dynamic response which in general lines are in remarkable agreement. This is very important taking into account the essentially different assumptions adopted in two approaches: The analytical method considers a rigid, monolithic arch of zero tensile strength in which sliding at the joints is prevented. On the contrary, the numerical model implies a stiff but not ideally rigid structure with a predefined hinge mechanism, where interfaces are reasonably rough allowing theoretically sliding.

It has to be mentioned that in the analyses presented herein only dead loads due to the arch ring weight have been considered neglecting additional gravity loads mainly due to backfill or overburden material. This simplifying approach is conservative and allows for the comparison with a plethora of previous studies already presented in literature on the pure arch behaviour (Alexakis, 2013, 2014; Heyman, 1982; Oppenheim, 1992; Gaetani, 2017, Leontari, 2018; Kollar, 2019; Cannizzaro, 2018; Pulatsu, 2019; Stockdale, 2020; Tempesta, 2019). A more realistic simulation of the arch as a part of a structure (e.g bridge, entrance, vault) is a topic for future research. A complete masonry arch configuration could be implemented, including apart from the arch ring, the spandrel structure and the fill material above. The development of the semi-analytical method could expand taking into consideration more complicated loading and boundary conditions. The presence of spandrels, backfill soil, and piers is expected to strongly affect the arch stress distribution and its load-bearing capacity (Sarhosis, 2016, 2019; Pulatsu, 2019; Reccia, 2014; da Porto, 2016). Finally, regarding the finite element model, the analysis can be extended in a future study to address a monolithic, no-tension arch.

CHAPTER 5:

Masonry arched structures on buttresses

5.1 Introduction

The fundamental structure of many masonry monuments worldwide is the buttressed arch. Masonry bridges, aqueducts, gothic cathedrals, byzantine churches, arcades and barrel vaults among others are supported by this typical structure. Masonry arches at their springings, exert inclined thrust forces which are loading the buttresses. The latter contribute favourably to the structure stability as they carry this thrust from the arch and transmit it to the supporting soil. In this chapter the ultimate capacity of simple masonry arched structures supported on buttresses under combined static and seismic loading is investigated. It is assumed, that they are composed of masonry voussoirs resting on top of each other, freely supported.

Arched structures have already been discussed and analysed in previous chapters (chapter 3 & 4) as a vivid paradigm of structures whose stability is dependent solely on their equilibrium. The monolithic structural model allows for investigating their mechanical behaviour through Limit Equilibrium Analysis. Similar to the cases of circular and part-elliptical arches the same procedure is followed for the analysis of buttressed arches. What is new in this case is a possible hinge formation on one or on both buttresses leading to more complicated computations. Contingent upon the arch-to-buttress height ratio, rocking could turn out crucial for stability. Alexakis and Makris (2017, 2018) in their pioneering work investigated the hinging mechanisms and the minimum uplift horizontal acceleration of masonry single-nave barrel vaults subjected to lateral and gravity loads by employing the principle of stationary potential energy. Lastly, a numerically based approach with the aim of the finite element method can be a very useful tool for the rocking overturning analysis under seismic excitation when the structure is considered as an assemblage of voussoirs.

5.2 Limit analysis of masonry buttressed arches subjected to lateral and gravity loads

5.2.1 Geometry and loading conditions

Buttressed arched structures either as principal components of heritage buildings or as individual structures can be found in many different geometries. The arch part can be of uniform section (circular) or of non-uniform section (non-circular such as part-elliptical, pointed, ogee). Depending on the angle of embrace they can be segmental or semi-circular. Buttress geometry also varies to thick or slender. In this chapter the circular buttressed arch is studied. The parameters that define the arch geometry are analytically presented below.

Loading conditions can also vary. The buttressed arch must support its self-weight or other additional dead loads (e.g. overburden soil, fill of other materials). For masonry arch bridges live loading should also be considered. Horizontal forces of increasing intensity may also influence the loading conditions of the structural system. Seismic excitation exerts lateral loading that can be crucial for the structure sustainability. Herein, loading conditions comprise the gravity load of each part of the structure (arch and buttresses) and the lateral inertial loading produced by the applied constant horizontal acceleration.

5.2.2 Assumptions for the application of L.A and hinging mechanisms

The most suitable approach to address the stability of unreinforced masonry (URM) arches under horizontal loads is through Limit Analysis (L.A.). For the application of this method, the following postulates for the masonry behaviour as proposed by Heyman should be taken under consideration: infinite compressive strength, zero tensile strength, and the coefficient of friction large enough to prevent sliding. Under these requirements, the masonry becomes an assemblage of rigid parts held in by mutual pressure and the failure mode of the system is activated by the formation of no-tension hinges that turns the structure into a rocking mechanism.

Stability analysis of the arched masonry structures through the kinematic theorem requires the identification of the hinging mechanisms. As already discussed analytically in previous chapters, a voussoir-arched structure transforms into a mechanism when relative separation and rotation occur at four deformable joints simultaneously, leading to the formation of hinges. In a parallel approach, when the arch is treated as monolithic, the principle of stationary potential energy unveils the four locations of the structure where the partial derivatives of the potential energy become zero.

Depending on the structure geometry and precisely on the arch-to-buttress relative proportion, the following hinging mechanisms in Figure 5.1 (initially proposed by De Luca, 2004) are distinguished:

(i) Mechanism I (Local or Arch Mechanism) usually occurs in the case of slender arches atop of stocky buttresses where all four hinges form at the most vulnerable part, the arch, and none at the buttresses,

(ii) Mechanism II (semi-global or mixed Mechanism) occurs when apart from the arch, one buttress also participates in the hinging mechanism. Specifically, one hinge opens at the bottom corner of the buttress while the other three across the arch and

(iii) Mechanism III (global Mechanism) occurs when two hinges develop at the arch and the other two at each buttress. The last two mechanisms are usually formed for thick arches and slender buttresses (Mech.III for even more slender and therefore more vulnerable buttresses).

If hinge B or D exceeds the arch springing and forms horizontally across the buttresses then Mechanism IV is activated, which is a variation of the Mechanism II. Boundary conditions are implemented to avoid the latter mechanism.

Some representative examples of the above kinematic mechanisms on buttressed arches are portrayed in Figure 5.2 (Brandonisio 2017).

The failure mechanisms of the buttressed arches were recently studied by Calderini and Lagomarsino (2014) who carried out an experimental program on the 1:10 scaled buttressed arch with the aim of studying the structural response under seismic excitation. Dimitri & Tornabene (2015) examined the effect of geometry on the seismic

capacity of buttressed arches. Bradonisio et al (2017) proposed a numerical procedure based on the application of Limit Analysis combined with non-linear programming techniques to calculate the actual horizontal load multiplier λ and the location hinge that defines the most probable failure mechanism. In his succeeding work (Bradonisio et al, 2020), 128 buttressed arches of different geometries, with emphasis to the angle of embrace (β), were analysed under seismic motion in order to capture their precise mechanical behaviour.

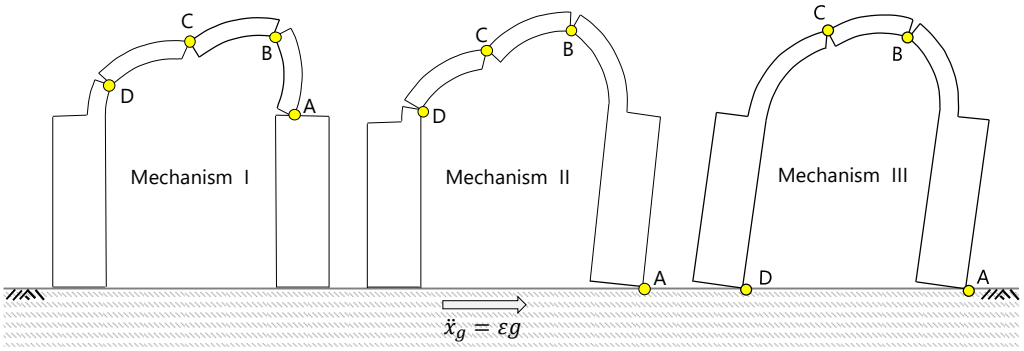

Figure 5.1 Three different kinematic mechanisms (I, II, III) that can be possibly activated under the implementation of a ground acceleration $\ddot{x}_g$ from the left to the right.

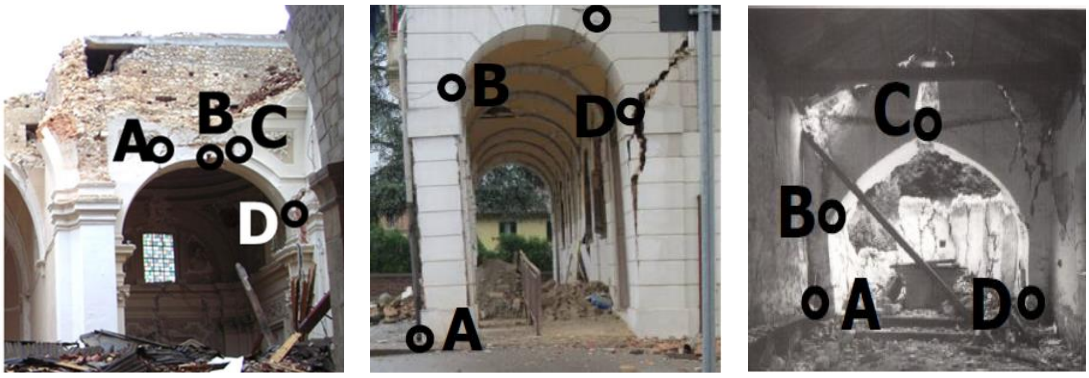

Figure 5.2 Representative examples of the above kinematic mechanisms on buttressed arches: Santa Maria di Collemaggio church in L'Aquila (Italy) during the 2009 L'Aquila earthquake, Town Hall in San Agostino (Italy) during the 2012 Emilia Romagna earthquake, and Santa Caterina church in Venzone (Italy) during the 1976 Friuli earthquake (Brandonisio 2017).

5.2.3 Thick arches atop of slender buttresses

The horizontal capacity of slender buttresses that support a circular thick arch which are common parts of monumental structures such as vaulted entrances, bridges etc. are examined next. According to the previous section, when the minimum horizontal ground acceleration for the onset of rocking applies at the base, Mechanism II (or mixed or semi-global) is activated. The buttress geometry (b, h) plays a dominant role to the structure stability in contrast to the minor role of the arch geometry. Their contribution is investigated in the following sections.

i. Model Parameters

Consider now the rigid masonry buttressed arch shown in Figure 5.3. The model below consists of a thick arch supported by slender buttresses and it can be geometrically defined by (i) the arch parameters: the angle of embrace β, the thickness t, the mid-thickness radius R and (ii) the buttress parameters: the height h and the width b. The buttress slenderness s is usually defined by the ratio of width to height. Given that the equilibrium of masonry arches (as already discussed) is a purely geometrical problem, the collapse of the overall structure is governed by the above parameters which are normalised to the mid-thickness radius R.

When a critical horizontal acceleration $\ddot{x}_g = \varepsilon\, g$ is applied at the structure base from the left to the right, the buttressed arch transforms into a four-hinge mechanism. The presumable hinge locations A, B, C, D are illustrated in the schematic of Figure 5.3 which portrays a Mechanism II-model. Hinge A is placed at the bottom right corner of the right buttress (given the direction of the excitation) while the rest of the hinges are defined by the angles φ_1, φ_2, and φ_3 respectively (from the horizontal). Specifically, hinge B is activated at position $\varphi_0 \leq \varphi_1 < 90^\circ$ (hinge at the right springing when "$\varphi_1 = \varphi_0$"), hinge C is formed somewhere at the left semicircle, while hinge D is bounded by a location $\varphi_3 \leq (\pi - \varphi_0)$. When "$\varphi_1 = \varphi_0$"and "$\varphi_3 = \pi$", happen simultaneously (hinges forms at the right and left springing respectively) a "two-springing" mechanism is

formed. From the above limitations (boundaries at the springings), Mechanisms IV is automatically excluded.

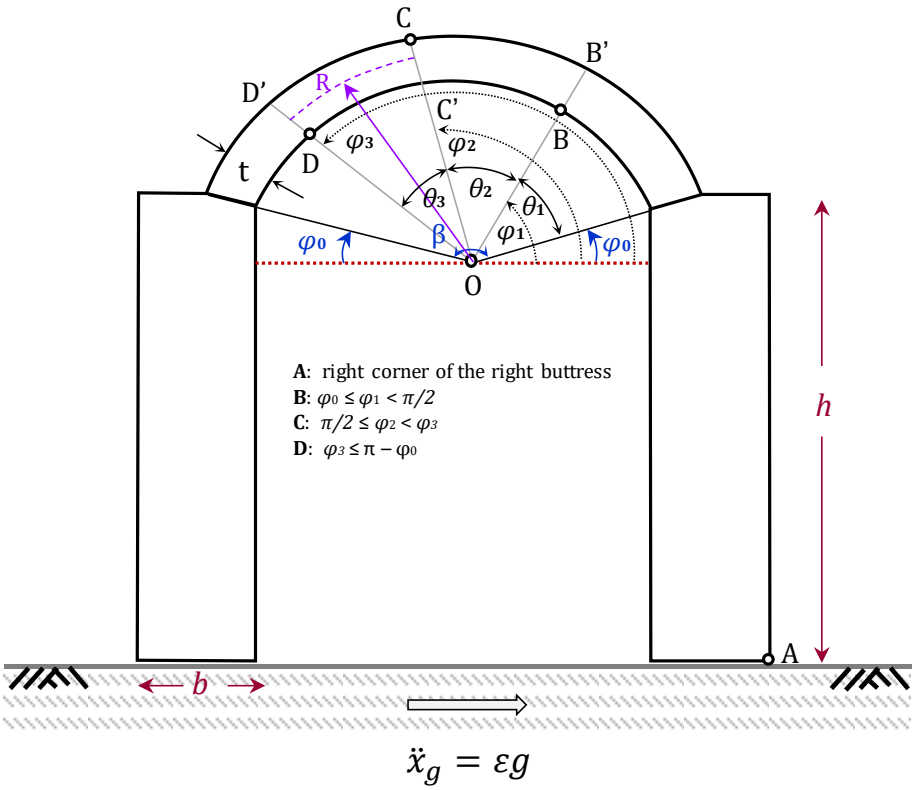

Figure 5.3 Schematic of a thick circular masonry arch supported by slender masonry buttresses. Mechanism II is activated under horizontal acceleration acting from the left side to the right. The main arch and buttress geometric parameters that influence the system stability are depicted.

ii. Stability analysis at incipient uplift – Variational formulation

Stability analysis is pre-formed in static terms to calculate the hinge locations as well as the minimum ground acceleration at the onset of rocking.

In the framework of limit equilibrium analysis, a proper configuration of the model under examination should be selected. The illustration of the L.A model is depicted in Figure 5.4 where three basic parts for the analysis are distinguished: segment 1 (or part AB), segment 2 (or part BC) and the combined segment 2-3 (or part BCD). It should be

noted here that segment 1 consists of two areas, the arch portion and the buttress area which embodies two parallelepipeds and a little triangle at their intersection. Segments 2 and 2-3 are portions of the arch body.

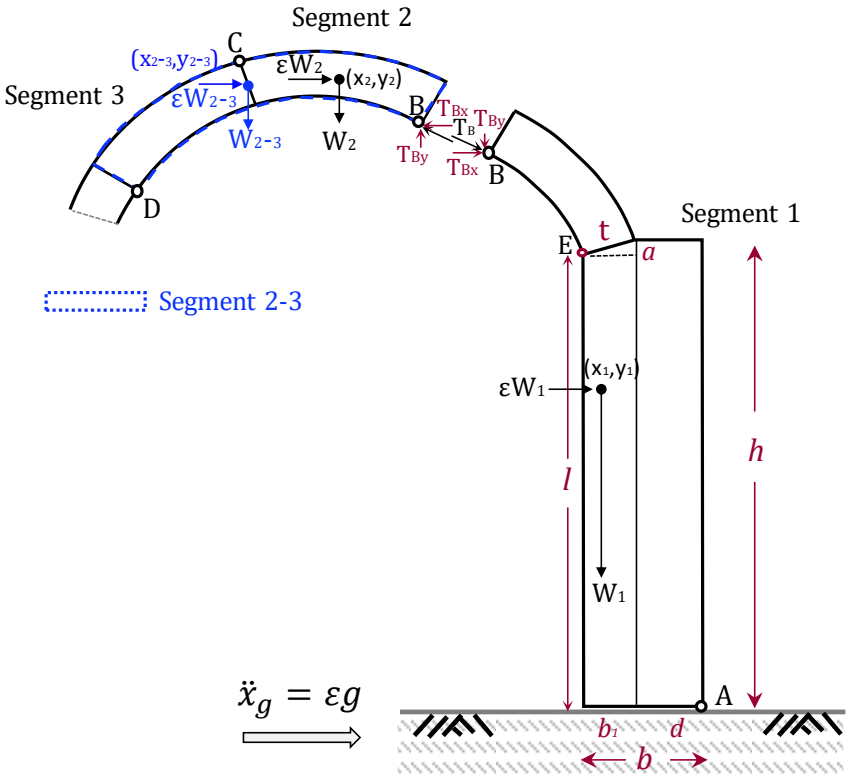

Figure 5.4 Illustration of the limit equilibrium analysis. The three segments of the four-link mechanism II and the combined segment 2-3 used for the analysis are depicted in detail. Horizontal (ε W_i) and vertical (W_i) forces acting on the centre of gravity (x_i, y_i) for each segment are also highlighted.

Next step is the determination of the applied forces on the centre of gravity (x_i, y_i are the Cartesian components) of each segment. The horizontal forces εW_i are developed by the horizontal component of the seismic excitation $\ddot{x}_g = \varepsilon g$ while the vertical ones, W_i are the self-weights, where "i" identifies the three segments (1, 2, 2-3) of the dominant hinging mechanism. When "ε" reaches a value capable to transform the arched structure into a mechanism, the thrust line (the resultant of both vertical and horizontal forces) reaches the surface of the masonry and touches the intrados at

points B and D, and the extrados at point C. Specifically, the unknown internal thrust force at hinge B is analysed to the horizontal and vertical components T_{Bx} and T_{By}. The weights and the Cartesian components of the center of gravity for each part are:

$$x_1 W_1 = x_{arc} W_{arc} + x_{triangle} W_{triangle} + x_{paral1} W_{paral1} + x_{paral2} W_{paral2} \quad (5.1)$$

$$y_1 W_1 = y_{arc} W_{arc} + y_{triangle} W_{triangle} + y_{paral1} W_{paral1} + y_{paral2} W_{paral2} \quad (5.2)$$

$$W_1 = W_{arc} + W_{triangle} + W_{paral1} + W_{paral2} \quad (5.3)$$

$$x_2 = R\left(1 + \frac{r^2}{3}\right)\frac{sin\,\varphi_2 - sin\,\varphi_1}{\varphi_2 - \varphi_1} \quad (5.4)$$

$$y_2 = -R\left(1 + \frac{r^2}{3}\right)\frac{cos\,\varphi_2 - cos\,\varphi_1}{\varphi_2 - \varphi_1} \quad (5.5)$$

$$W_2 = 2R^2 r(\varphi_2 - \varphi_1) \quad (5.6)$$

$$x_{2-3} = R\left(1 + \frac{r^2}{3}\right)\frac{sin\,\varphi_3 - sin\,\varphi_1}{\varphi_3 - \varphi_1} \quad (5.7)$$

$$y_{2-3} = -R\left(1 + \frac{r^2}{3}\right)\frac{cos\,\varphi_3 - cos\,\varphi_1}{\varphi_2 - \varphi_1} \quad (5.8)$$

$$W_{2-3} = 2R^2 r(\varphi_3 - \varphi_1) \quad (5.9)$$

Equations 5.1-5.3 are presented analytically on the Appendix C due to their complexity.

Moment equilibrium of segments 1 (AB) and 2 (BC) about hinges A and C respectively yields:

$$c_{x1}T_{Bx} + c_{y1}T_{By} + f_1 = 0 \tag{5.10}$$

$$c_{x2}T_{Bx} + c_{y2}T_{By} + f_2 = 0 \tag{5.11}$$

Moment equilibrium of the combined segment 2-3 (BD) about hinge D yields:

$$c_{x2-3}T_{Bx} + c_{y2-3}T_{By} + f_{2-3} = 0 \tag{5.12}$$

$$c_{x1} = R\big((1-r)\,sin\,\varphi_1 - (1+r)\,sin\,\varphi_0 + 2c_h\big) \tag{5.13}$$

$$c_{y1} = R\big((1-r)\,cos\,\varphi_1 - (1-r)\,cos\,\varphi_0 - 2s_b\big) \tag{5.14}$$

$$f_1 = \big(W_{1x} + \varepsilon * W_{1y}\big) - W_1 * R\big((1-r)\,cos\,\varphi_0 + \varepsilon * (1+r)\,sin\,\varphi_0 + 2(s_b - \varepsilon * c_h)\big) \tag{5.15}$$

$$c_{x2} = R\big((1+r)\,sin\,\varphi_2 - (1-r)\,sin\,\varphi_1\big) \tag{5.16}$$

$$c_{y2} = R\big((1+r)\,cos\,\varphi_2 - (1-r)\,cos\,\varphi_1\big) \tag{5.17}$$

$$f_2 = W_2(x_2 - R(1+r)\,cos\,\varphi_2) + \varepsilon W_2(y_2 - R(1+r)\,sin\,\varphi_2) \tag{5.18}$$

$$c_{x2-3} = R\big((1-r)\,sin\,\varphi_3 - (1-r)\,sin\,\varphi_1\big) \tag{5.19}$$

$$c_{y2-3} = R\big((1-r)\,cos\,\varphi_3 - (1-r)\,cos\,\varphi_1\big) \tag{5.20}$$

$$f_{2-3} = W_{2-3}(x_{2-3} - R(1-r)\,cos\,\varphi_3) + \varepsilon W_{2-3}(y_{2-3} - R(1-r)\,sin\,\varphi_3) \tag{5.21}$$

where T_{BX}, T_{By} are the unknown Cartesian components of the internal thrust force T_B and c_{xi}, c_{yi}, f_i (where i=1, 2, 2-3) are coefficients which are defined below.

The parameters c_h, s_b are half the normalized to R, height and width of the buttress. By solving the equations (5.11) and (5.12) the components of the thrust force T_B take the following form:

$$T_{BX} = \frac{c_{y2-3}f_2 - c_{y2}f_{2-3}}{c_{y2}c_{x2-3} - c_{x2}c_{y2-3}} \tag{5.22}$$

$$T_{BY} = \frac{c_{X2}f_{2-3} - c_{X2-3}f_2}{c_{y2}c_{x2-3} - c_{x2}c_{y2-3}} \tag{5.23}$$

By substituting the thrust force components as functions of the coefficients c_{xi}, c_{yi}, f_i into Eq. (5.10), the following simplified form is yielded:

$$c_1f_1 + c_2f_2 + c_{2-3}f_{2-3} = 0 \tag{5.24}$$

The coefficients c_i and the functions f_i (where i represent each segment) are combinations of: (i) the arch parameters (r, φ_0), (ii) the buttress parameters (s_b, c_h) and (iii) the characteristic parameters (ε, φ_i) of the dominant hinging mechanism (Eqs. 5.13-5.21). Their detailed form is presented in the Appendix. A subject of interest is the rupturing acceleration $\varepsilon\ g$ and, the presumable rupture-points over the arch body defined by angles of embrace φ_1, φ_2, φ_3. Therefore, equation (5.24) is solved for the parameter ε which is expressed as a function of the angles φ_i (i=1, 2, 3) (Eq.5.25).

$$\varepsilon = f(\varphi_i) \tag{5.25}$$

According to the principle of stationary potential energy, every system in stable static equilibrium should have its potential energy minimised and therefore its partial derivatives with respect to the angles φ_i should be set equal to zero (Eq.5.26).

$$\frac{\partial V}{\partial \varphi_i} = \frac{\partial \varepsilon}{\partial \varphi_i} = 0, \qquad i = 1,2,3 \tag{5.26}$$

iii. Numerical results

The effect of the buttress geometry (*b*, *h*) is depicted in the following diagrams (Figures 5.5-5.8). Four different buttress geometries are considered (Table 1). The buttress slenderness $s = b / h$ is set from 0.25 to 0.75. The arch parameters ranges: (i) for the angle of embrace β, values fluctuate from 90˚ (very segmental arch) to 180˚ (semi-circular arch) and (ii) for the mid-thickness ratio t / R, from 0.025 to 0.275 considering respectively very thin to thick arches.

Table 1 Buttress geometries

	1	**2**	**3**	**4**	**5**	**6**
b/R	0.50	0.75	0.50	0.75	0.50	0.75
h/R	1	1	1.5	1.5	2	2
s	0.50	0.75	0.33	0.50	0.25	0.375

For relatively very slender arches (proportional to the buttresses), the curves ε-β don't cover the whole range of the angle of embrace or they may not exist at all. This happens either because they can't stand their own weight or because for such vulnerable arches Mechanism I is activated.

For each pair of diagrams where the height h / R is fixed and the width b / R increases to 50% (b / R = 0.50 to 0.75), it is concluded that:

-The seismic coefficient ε is almost doubled meaning that as the slenderness *s* increases the structure obtains better resistance to the mechanism motion.

- For the case $b / R = 0.75$ & $h / R = 1$ (relatively stocky buttress), all the curves corresponding to various t / R end at the angle of embrace β = 165˚. For larger angles Mechanism I is activated.

- The minimum horizontal ground acceleration for the onset of motion will decrease with a larger angle of embrace.

Generally, a buttressed semi-circular arch (angle of embrace β = 180˚) is more unstable than a segmental one (angle of embrace β = 90˚). For a given t / R, the difference in seismic resistance between these extreme cases, is smaller as the normalised height h / R increases.

Buttresses with the same coefficient of slenderness s but with different size (for example b / R = 0.5 & h / R = 1 and b / R = 0.75 & h / R = 1.5) don't display the same resistance to the onset of motion. The larger buttress is more stable than the smaller one (Housner 1963).

By doubling the height from h / R=1 to 2, the buttress becomes slenderer (slenderness ratio s decreases) which entails a more unstable structure that enters the rocking mode for low value of horizontal ground acceleration.

As has already been clarified from the previous diagrams, the illustrated curves of Figure 5.7 likewise, represent only the buttressed arches that can support their own weight and correspond to collapse mechanism II (mixed or semi-global). For arches with angle of embrace β = 90˚ and 125˚ regardless of their thickness, the location of the fourth hinge (hinge D) resulting from Eq. (5.26), exceeds the left springing boundary representing Mechanism IV. In that case, hinge D is set to the left springing. Concerning hinge B location, for some thickness range of the very segmental arches (β = 90˚), it is calculated beyond the right boundary and is readjusted to the right springing. The angle of embrace β seems to play a minor role to the rupture locations. Specifically, the curves that correspond to hinge C location (φ_2) almost coincide regardless of the arch embrace. As the arch becomes slenderer (t / R decreases) hinge B curve slopes upwards meaning that it diverges from the springing.

For the cases that no adjustment is necessary, it has been observed that the angle φ_2 equals to:

$$\varphi_2 = \frac{(\varphi_1 + \varphi_3)}{2} \tag{5.27}$$

If each particular one of the angles above (measured from the horizontal) is expressed as a function of the angles corresponding to the three links of the four-link mechanism, it yields:

$$\varphi_1 = \varphi_0 + \theta_1\,, \quad \varphi_2 = \varphi_0 + \theta_1 + \theta_2\,, \ \varphi_3 = \varphi_0 + \theta_1 + \theta_2 + \theta_3 \qquad (5.28)$$

Where θ_1, θ_2, θ_3 are the angles forming between the horizontal and hinge B, the latter and hinge C and, the latter and hinge D respectively. Replacing Eq. (5.28) to Eq. (5.27) it results to $\theta_2 = \theta_3$ meaning that this configuration always gives the governing mechanism which yields the minimum horizontal ground acceleration.

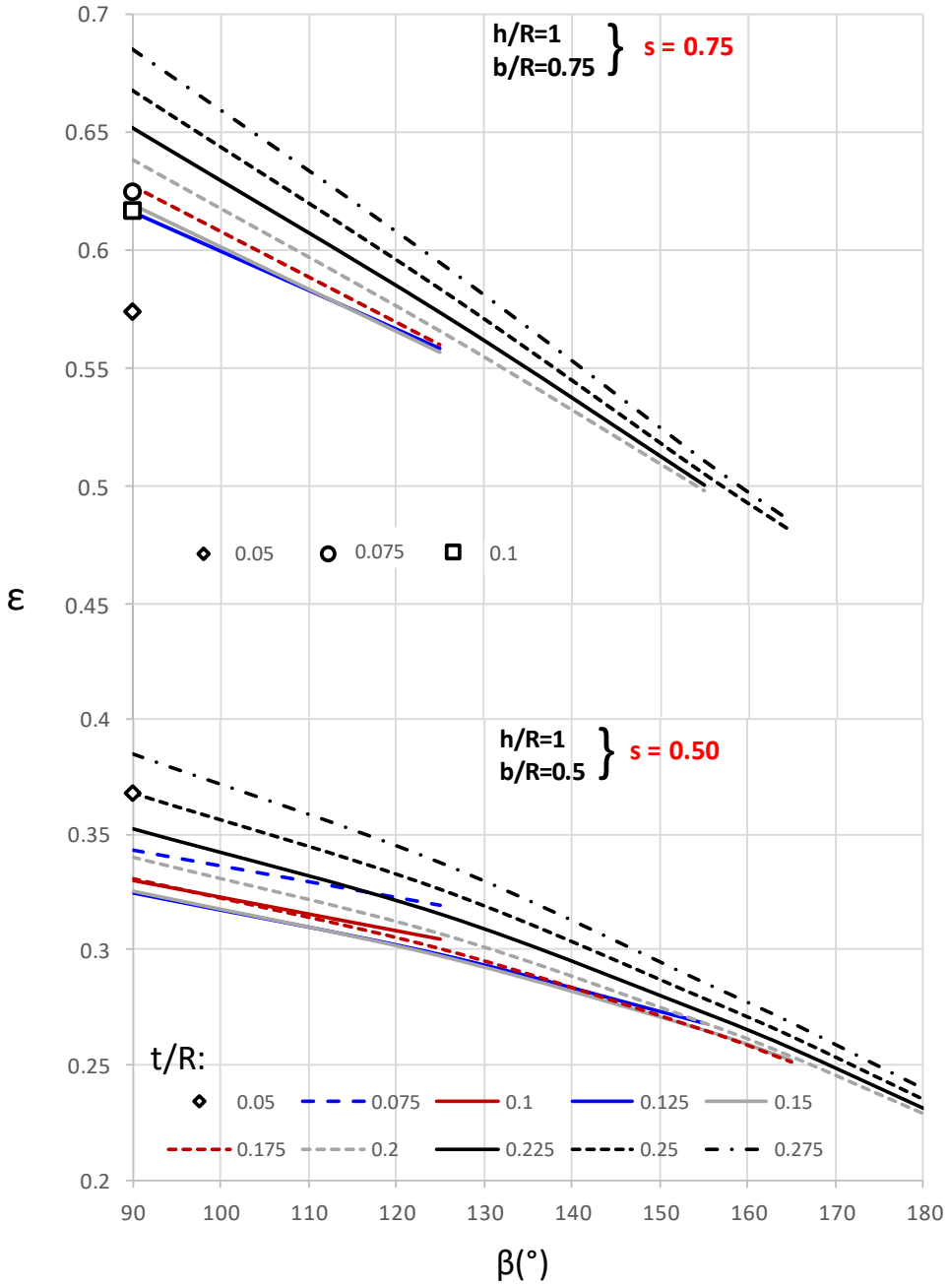

Figure 5.5 Effect of the width increase (b / R = 0.5 to 0.75) of a buttress with a given h (h / R =1) on the seismic coefficient ε for various arch geometries (t / R, β).

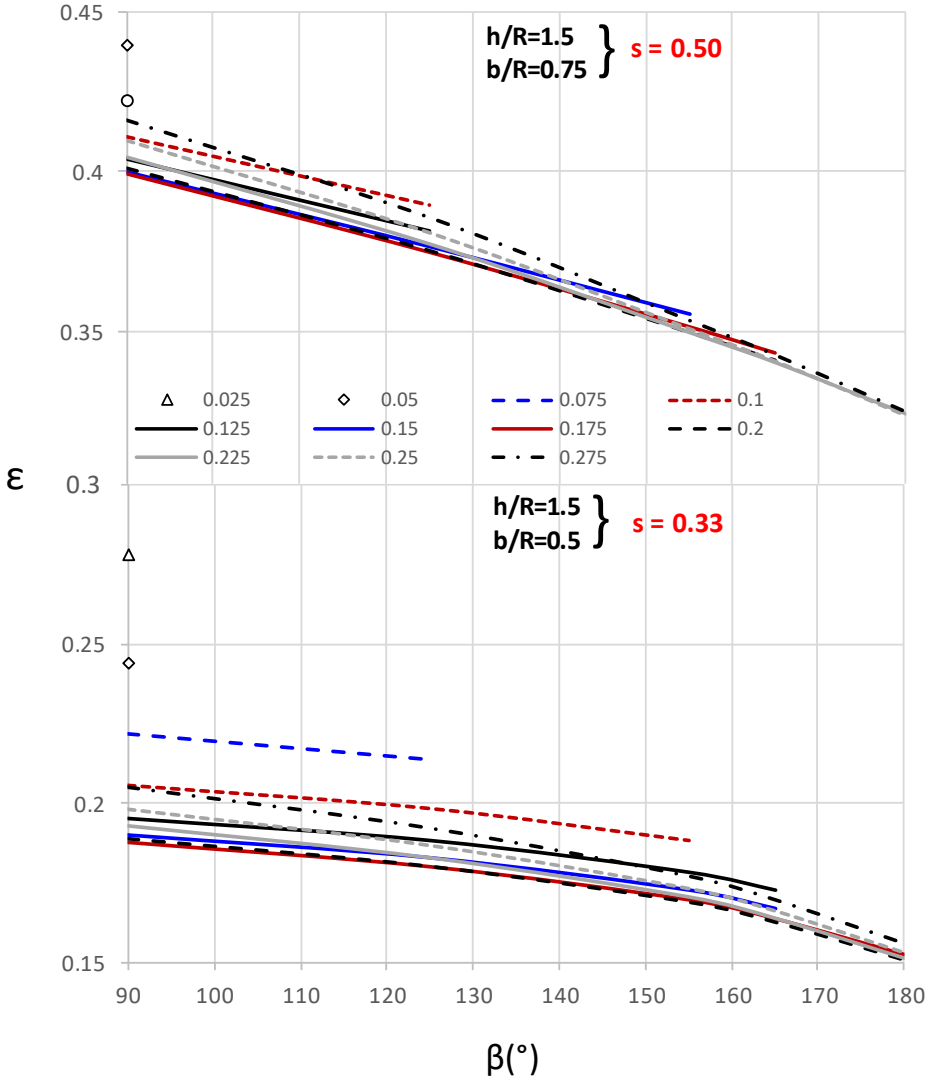

Figure 5.6 Effect of the width increase (b / R = 0.5 to 0.75) of a buttress with a given h (h / R =1.5) on the seismic coefficient ε for various arch geometries (t / R, β).

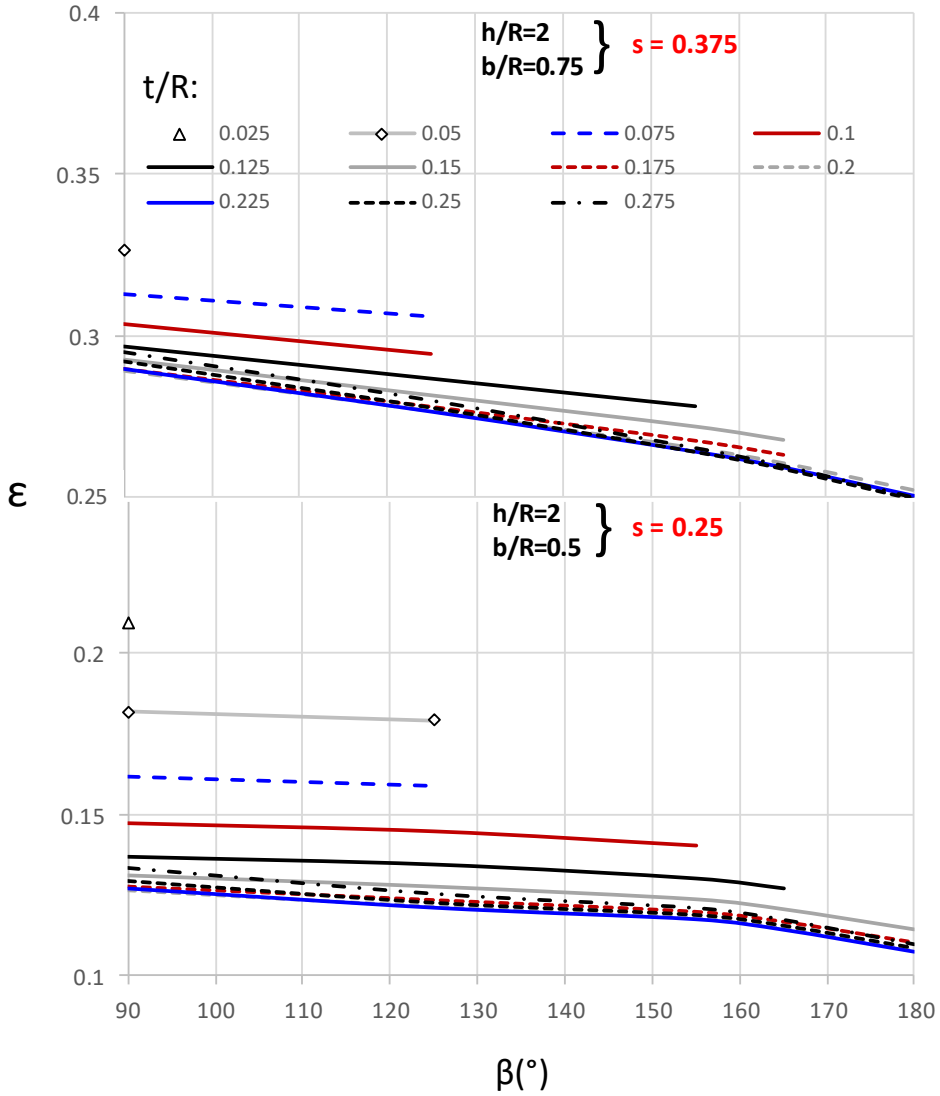

Figure 5.7 Effect of the width increase (*b / R* = 0.5 to 0.75) of a buttress with a given *h* (h / R =2) on the seismic coefficient *ε* for various arch geometries (*t / R*, *β*).

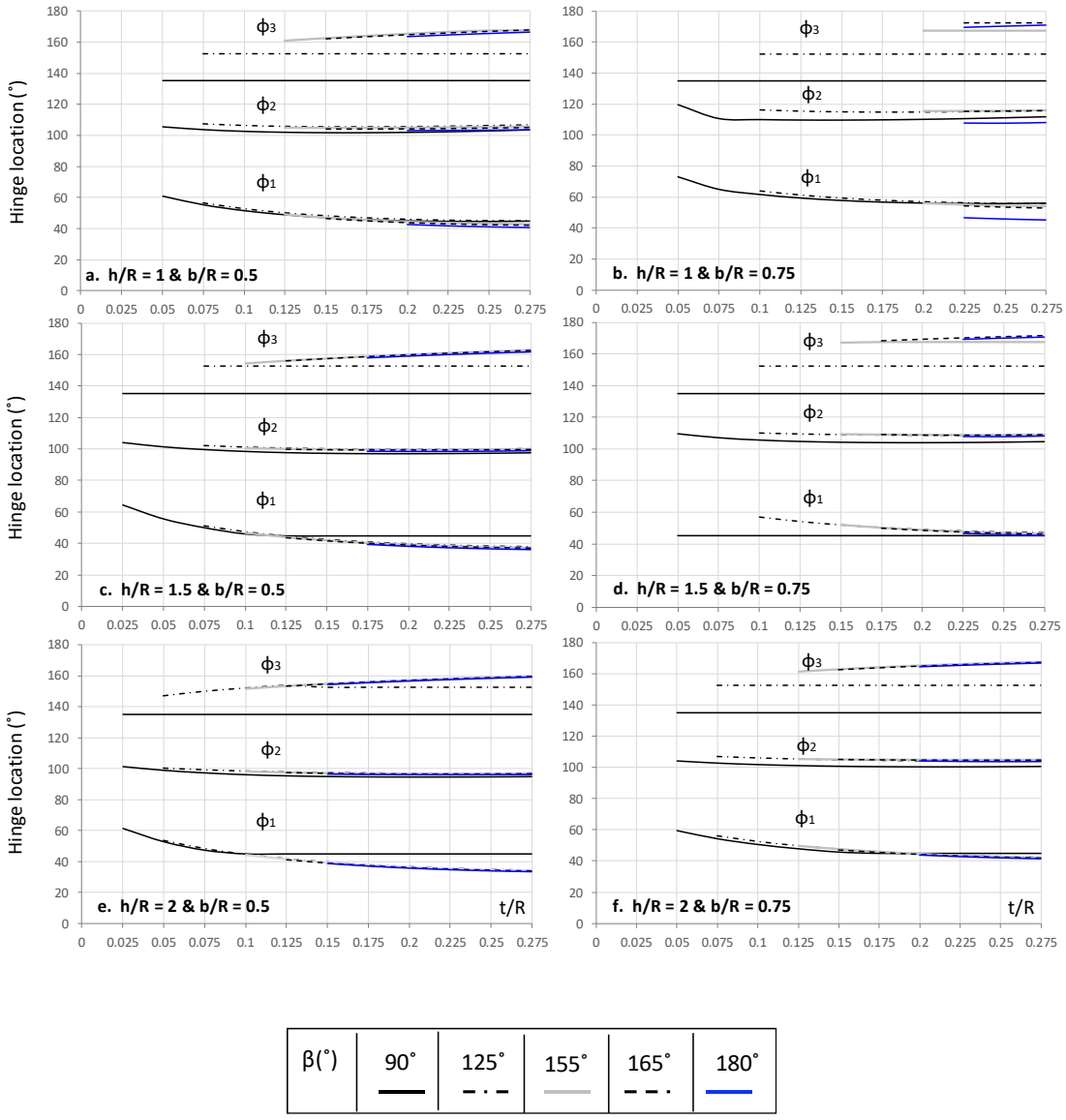

Figure 5.8 Location of the imminent hinges φ_1, φ_2, φ_3 at points B, C, D (Figure 5.2) respectively of a buttressed arch with given buttress geometries (b/R, h/R). Arch parameters (β and t/R) cover a satisfying range of values.

5.3 Time history analysis

5.3.1 Finite element Modelling

In the foregoing pseudo-static analyses, buttressed arches of various geometries idealised as monolithic structures were examined for their ability to resist in the rocking mode. Inherent to the monolithic model is that the imminent hinges may occur at any possible location permitting the development of any admissible mechanism.

Within the framework of a time-history analysis, buttressed arches consist of individual stones (voussoirs) assembled each other without mortar. When uplifting takes place hinges can only form at predefined locations which are the interfaces of voussoirs. The dimensions and proportions considered for our model (Figure 5.9) were defined through real historic structures (in particular the tunnel entrance of an ancient Greek stadium located in Nemea, Peloponnese). The model under examination consists of a segmental arch, assemblage of nine voussoirs each one of thickness t = 0.4 m, with embrace β = 146˚ and radius R = 1.33 m. Each one of the supporting buttresses is h = 1.66 m in height and b=0.40 m in width and is structured with four voussoirs. The contribution to stability that larger buttresses may offer to the system is examined by applying a higher value of the width (b' = 0.535 m). Figure 5.9 presents the two structural models: the arch atop of buttresses of uniform cross-section and, the arch atop of buttresses of non-uniform cross section (dotted line).

Nonlinear analysis of rocking and uplifting response under seismic excitation is implemented numerically in the time domain with the finite element method. To this extent, the comprehensive code Abaqus is used and the explicit integration algorithm for solving the nonlinear dynamic response of the system in the time domain is implemented. Finite Element (FE) analysis is performed assuming that hinges open at specific and fixed points (interfaces of voussoirs). The structure is presented with plane-strain elements. Each block is idealised as rigid, by using a large enough modulus of elasticity (E = 6.5 GPa), characterised with density ρ = 2.2 kg/m^3. The base is also considered to be rigid by adopting concrete elastic values (elastic modulus, E = 25 GPa

and density, ρ = 2.5 kg/m^3). A sophisticated contact algorithm is utilised for modeling contact interface at hinges sections, thus allowing for separation but not for sliding. Hence, the coefficient of friction is adequately large (μ = 0.7). The finite element model is excited in the horizontal direction along the base of the soil layer with trigonometric pulses of one cycle and Ricker wavelets. This idealised motion is commonly used to represent directivity affected near-fault ground excitation. In particular, Ricker wavelets represent records with long-duration pulses which result of the "rupture directivity" effect and "permanent offset" effect.

Our interest in this section focuses on the structural response of yielding masonry buttressed arches under distinguishable pulses which substitutes the earthquake induced response adequately.

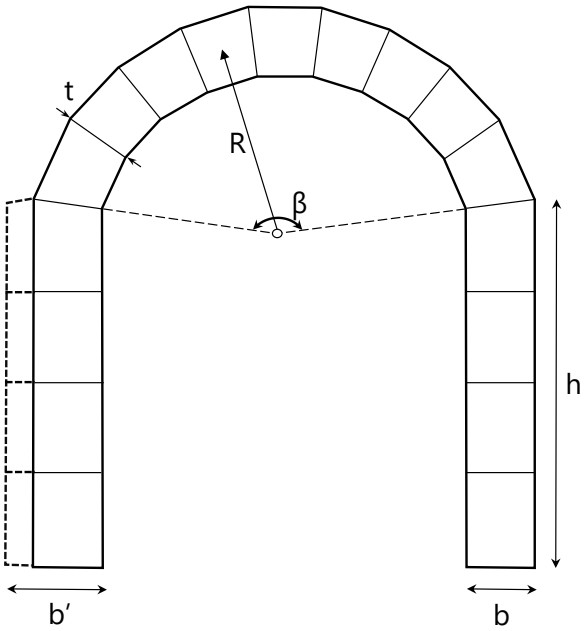

Geometric parameters	
R	1.33 m
t/R	0.3
β	146°
h	1.66 m
b	0.40 m
b′	0.535 m

Figure 5.9 Geometric parameters of the buttressed arch models.

5.3.2 Arch atop of buttresses of uniform cross-section

The 3-d finite element model of Figure 5.10 depicts a buttressed arch supported on a rigid accelerating base. A reasonably refined mesh of the model is generated from Abaqus.

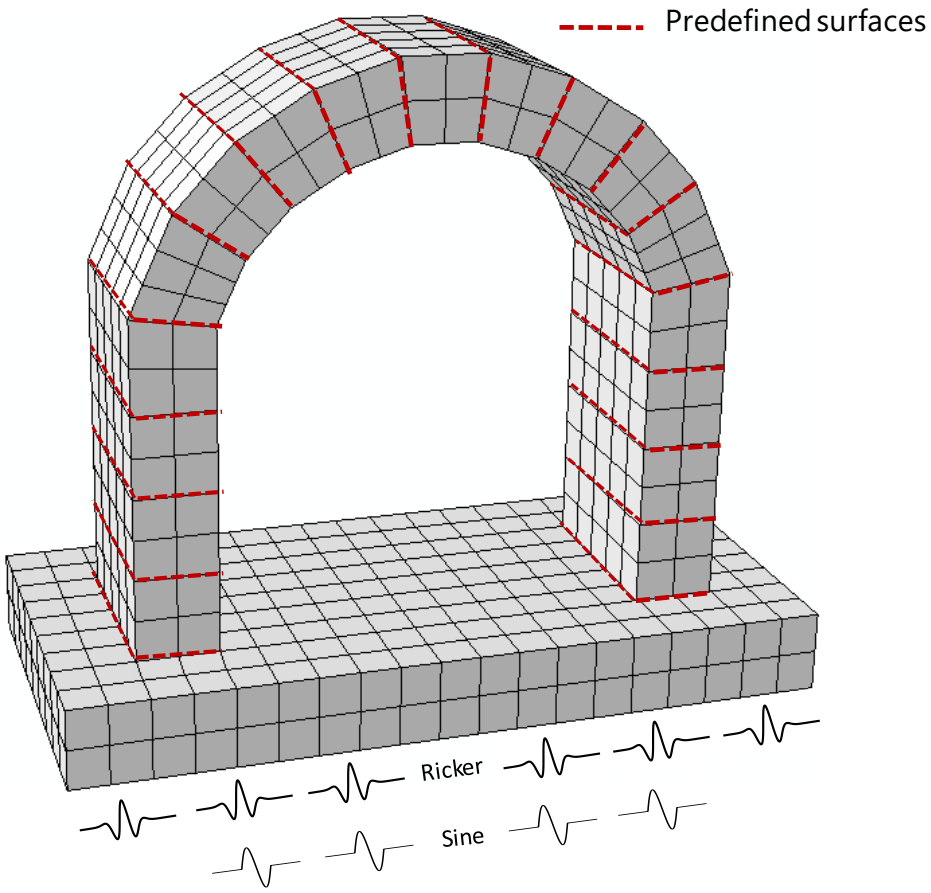

Figure 5.10 3-dimensional finite element model of a buttressed arch of uniform cross-section supported on a rigid base. The predefined interfaces between voussoirs where hinges may occur are highlighted with red dotted line. The base is excited with idealised pulses (Ricker & one-sine pulse).

The mortar-free interfaces are highlighted with red dotted lines suggesting the presumable locations of hinges forming when the vault is excited with idealised pulses (Ricker & one-sine pulse).

Minimum acceleration levels for toppling (a_p) are computed in terms of the excitation period (T_E) of the buttressed arch. The overturning spectra are plotted in Figures 5.11,

5.12. The dominant collapse mechanism, as suggested on previous section for slender buttresses, is Mechanism II (or Mixed or Semi-global) except from the cases D (T_E = 0.6 sec) and E (T_E = 0.9 sec) where five-hinge mechanism prevails. Cases A and B that correspond to high frequency pulses (T_E=0.2 sec & 0.3 sec respectively) activate two-springing mechanisms which occur to be diametrically opposite. The structural system displays a significant resistance to such low duration pulses and specifically a Ricker wavelet of period T_E = 0.2 sec (case A) is practically impossible to overturn the illustrated buttressed arch (a_p = 3 *g*!!).

For values of T_E increasing at levels higher than 0.2 sec the minimum PGA to overturn the buttressed arch is rapidly decreasing. Eventually, for sufficiently large periods (T_E > 0.9 sec) the minimum acceleration relatively approaches the pseudo-static value. Evidently, these long duration wavelets have a detrimental effect on the stability of the buttressed arch.

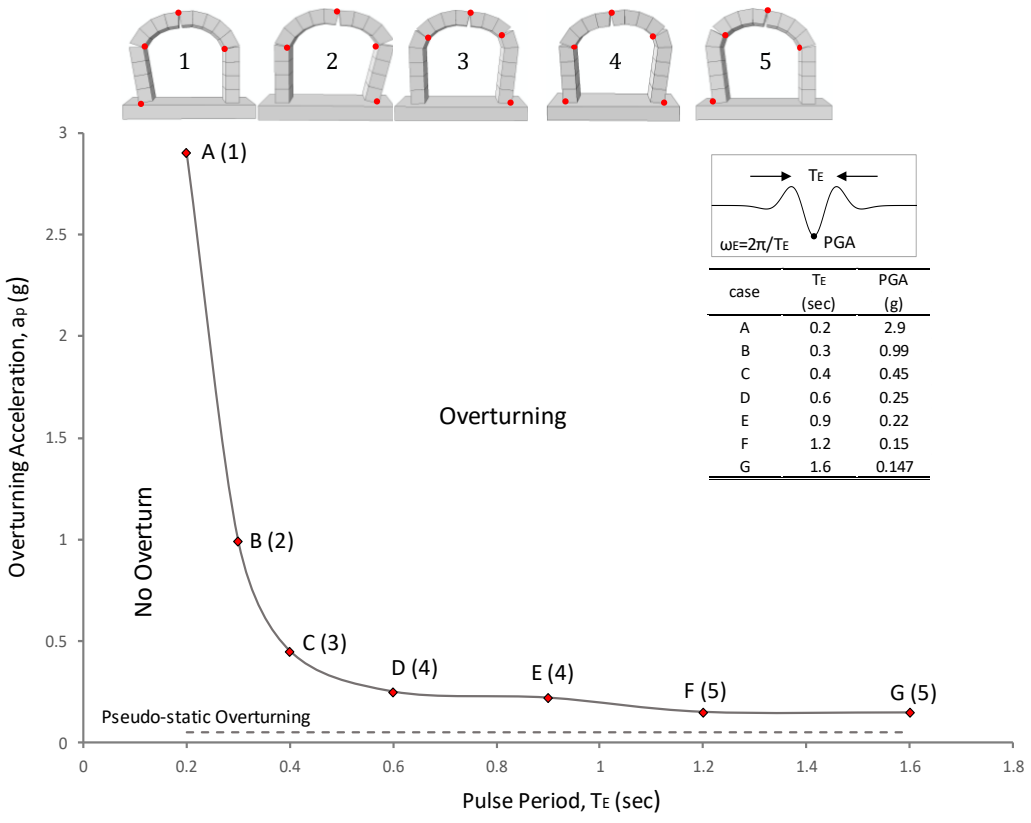

case	T_E (sec)	PGA (g)
A	0.2	2.9
B	0.3	0.99
C	0.4	0.45
D	0.6	0.25
E	0.9	0.22
F	1.2	0.15
G	1.6	0.147

Figure 5.11 Overturning Spectrum of the vaulted structure on buttresses with uniform cross-section (Figure 5.9) subjected to Ricker pulses at the base. For each pulse A-G (pulse periods T_E: 0.2, 0,3, 0.4, 0.6, 0.9, 1.2, 1.6 sec) the hinge locations are marked on the deformed FE mesh models (1-5).

The overturning spectra of Figures 5.11 and 5.12 are comparatively highlighted to determine the potential destructiveness that each utilised pulse exercises to the buttressed arch of Figure 5.10. Hence, it can be seen that among these motions, the one-sine pulse is the most detrimental in comparison with the Ricker wavelet, especially for low duration pulses. For moderate and long period pulses the effect of the type of motion is minimal. Nevertheless, the hinge locations that correspond to each pulse period differ. For Ricker pulses, five different combinations are obtained. On the other hand, for sine pulses, two different combinations dominate. One for T_E < 0.9 sec (Mechanism III or global) and one for $T_E \geq 0.9$ sec (Mechanism II or semi-global) as depicted in Figure 5.12.

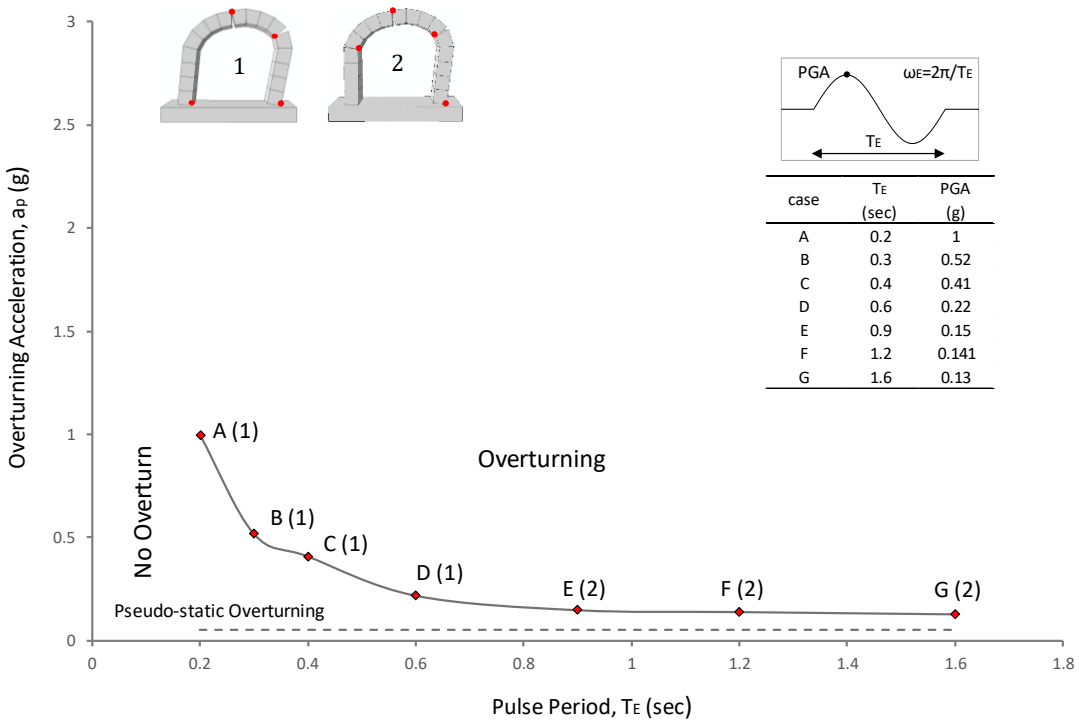

Figure 5.12 Overturning Spectrum of the vaulted structure on buttresses with uniform cross-section (Figure 5.9) subjected to sinusoidal pulses at the base. For each pulse A-G (pulse periods T_E: 0.2, 0.3, 0.4, 0.6, 0.9, 1.2, 1.6 sec) the hinge locations are marked on the deformed FE mesh models (1-5).

5.3.3 Arch atop of buttresses of non-uniform cross-section (buttresses of thicker section)

After examining the collapse behaviour of a buttressed arch with uniform cross-section along the structure, we can now further investigate the effect of a nonuniform thickness along the buttressed arch. In this way, the buttress slenderness (b / R) increases by 25% namely from b / R = 0.3 to b'/ R = 0.4 while all the other geometrical characteristics (t / R, h / R, β) remain constant. For the Abaqus analysis, the mesh model is modified by adding a series of elements at the external sides of the buttresses as depicted in Figure 5.13. The results are presented through the overturning spectra calculated for different ground shakings: Ricker wavelets and one-sine pulses with a period ranging from 0.20 sec to 1.60 sec. The aforementioned diagrams are plotted in Figures 5.14 & 5.15 respectively. Snapshots of the collapse mechanisms of the structural model for all the cases (A -> G) are also included to the graphs.

The reformed model is also subjected to the aforementioned idealised pulses so that the results can be comparable to the previous geometry. It is obvious from the overturning spectra of Figures 5.14 & 5.15 the remarkable difference of the overturning amplitude levels caused by each type of short period impulses (Ricker & one-sine). The beneficial effect of the Ricker pulses with respect to the one-sine pulses is attributed merely to the favorable asymmetry which offers an additional "safety net". For moderate and long period pulses the response is almost identical. From the comparison of the different geometries it is revealed that even a small increase in the buttress width offers stability to the structure regardless the impulse type.

In all cases, the Mechanism II is the governing one. The only exception is when the structural model is accelerated by a long period Ricker wavelet (T_E = 1.2 sec) and Mechanism III (global) is activated. Hence, the possibility of activation of one mechanism in place of another not only depends on the arch-to-buttress relative geometrical proportion but on the loading distributions too.

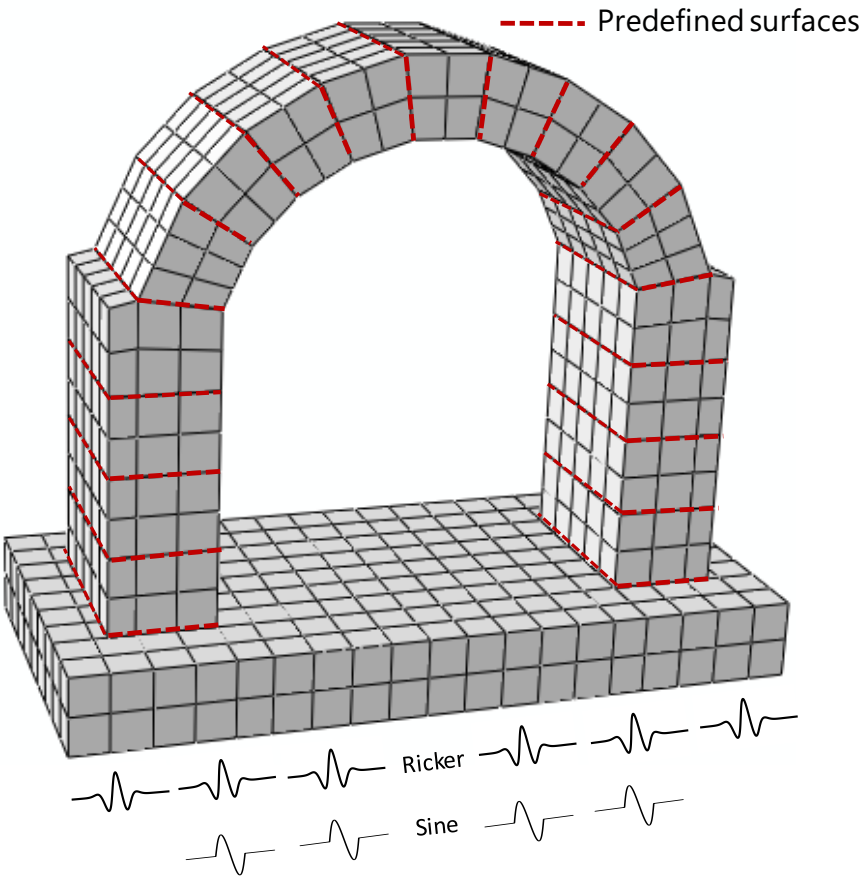

Figure 5.12 3-dimensional finite element model of a buttressed arch of non-uniform cross-section supported on a rigid base. The predefined interfaces between voussoirs where hinges may occur are highlighted with red dotted line. The base is excited with idealised pulses (Ricker & one-sine pulse).

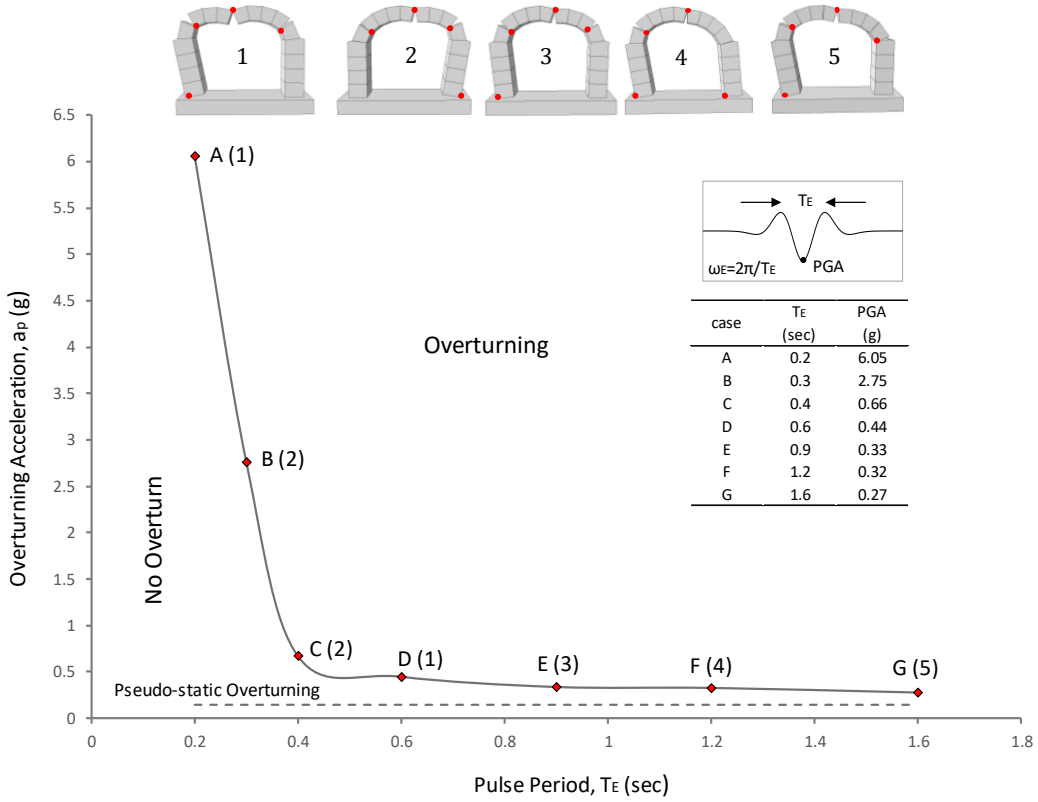

Figure 5.14 Overturning Spectrum of the vaulted structure on buttresses with non-uniform cross-section (Figure 5.12) subjected to Ricker pulses at the base. For each pulse A-G (pulse periods T_E: 0.2, 0.3, 0.4, 0.6, 0.9, 1.2, 1.6 sec) the hinge locations are marked on the deformed FE mesh models (1-5).

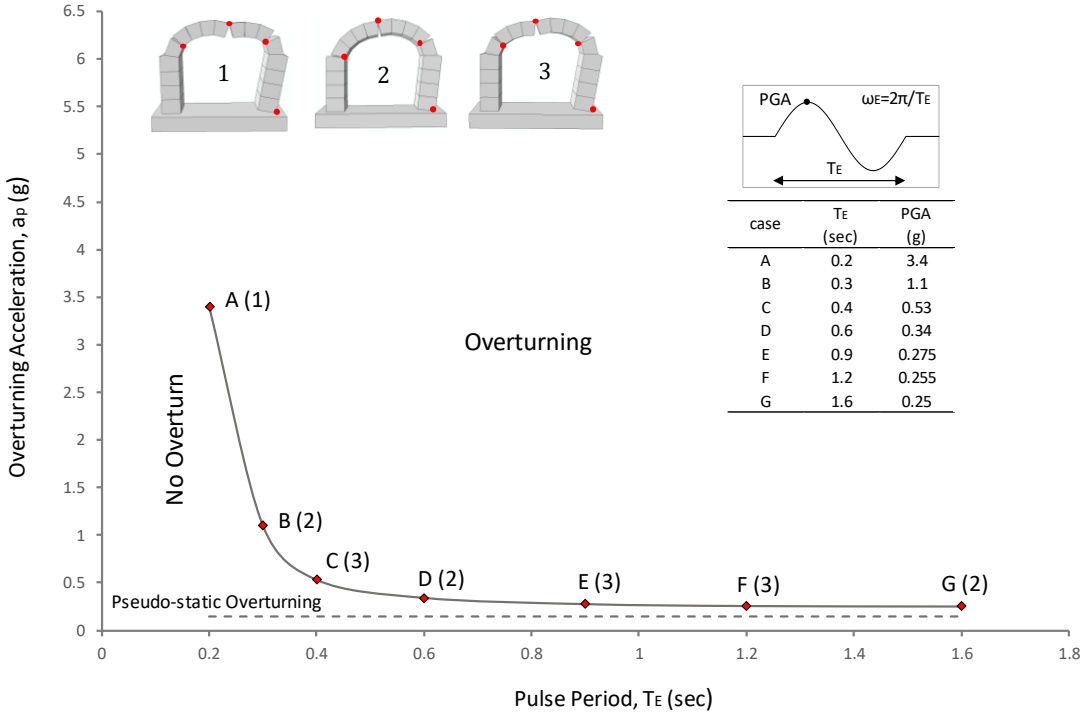

Figure 5.15 Overturning Spectrum of the vaulted structure on buttresses with non-uniform cross-section (Figure 5.12) subjected to sinusoidal pulses at the base. For each pulse A-G (pulse periods T_E: 0.2, 0.3, 0.4, 0.6, 0.9, 1.2, 1.6 sec) the hinge locations are marked on the deformed FE mesh models (1-5).

5.4 Conclusions

At the first part, a monolithic circular buttressed arch under seismic action is examined. Among the three possible failure mechanisms, the so-called Mechanism II (or mixed or semi-global) is studied. This mechanism is associated with the formation of three hinges in the arch and one hinge at the corner of the buttress. It develops under specific geometries and particularly when thick arches are supported by slender buttresses. A variational formulation utilising the principle of stationary potential energy as

proposed by Alexakis & Makris (2014, 2017, 2018) is revisited for the four different buttress geometries. Some of the main conclusions are:

1. Increasing the buttress width ensures stability as it requires higher values of acceleration to transform the structure into a mechanism. For example, a 50% increase of the width leads to 50% higher values of critical accelerations. Generally, when the slenderness *s* increases, either by increasing the buttress width or by decreasing the height, the structure becomes more stable as it entails higher values of acceleration to impose rocking.
2. Smaller values of embrace β have a favourable effect to the stability.
3. The case of a relative stocky buttress (b / R =0.75, H / R = 1) is a limit state where for larger buttresses the arch becomes relatively vulnerable and under a critical acceleration another mechanism is mobilised where all four ruptures occur at the arch.
4. Concerning the buttresses, Housner's finding (1963) is confirmed. According to that, between two equally slender structures but different in size the larger one is the more stable.
5. An important observation from Figure 5.7 where the locations of the imminent hinges are depicted, concerns the angles φ_i (i=1, 2, 3). It is found that they satisfy the relation $\varphi_1 + \varphi_3 = 2\varphi_2$ as it is described by equation (5.10). Expressing the angles φ as functions of the angles of each link (θ_i) (see equation 5.11), it leads to the critical mechanism that yields the minimum ground acceleration. This configuration consists of two equal links (with the same angle θ_i) and one larger and resembles the one that Oppenheim (1992) has considered as a *representative arch* in his study.

   At the second part, a time history analysis at the buttressed arches consisting of individual voussoirs (with predefined hinge locations) is conducted. The nonlinear rocking behaviour of 3d buttressed arch models is highlighted with the aid of the explicit algorithm available in the FE code Abaqus. The seismic

excitation is introduced in the horizontal direction along the base of the soil layer with trigonometric pulses of one cycle and Ricker wavelets. The sensitivity of the 3d model to the pulse characteristics is depicted in the overturning spectra of Figures 5.11, 5.12, 5.14 & 5.15. It is concluded that:

1. The structural system exhibits a significant resistance to low duration pulses. In this way, a Ricker wavelet of period T_E = 0.2 sec (case A) is practically impossible to overturn the illustrated buttressed arch (a_p = 3 *g*!!).
2. The dominant failure mechanism is Mechanism II (or semi-global)
3. The long duration Ricker wavelets have a detrimental effect on the stability of the buttressed arch. Specifically, for sufficiently large periods (T_E > 0.9 sec) the minimum acceleration gradually approaches very close to the pseudo-static value.
4. The one-sine pulse is the most detrimental in comparison with the Ricker wavelet, especially for low duration pulses. For moderate and long period pulses the effect of the type of motion is minimal. The beneficial effect of the Ricker pulses with respect to the one-sine pulses is attributed merely to the favorable asymmetry which offers an additional "safety net".
5. From the comparison of the different buttress geometries (Figure 5.10 & 5.12) it is inferred that even a small increase in the buttress width offers stability to the structure regardless the impulse type.

CHAPTER 6:

Embedded Vaulted Structures: Soil-Structure Interaction

6.1 Introduction

In Chapter 5, a masonry arch supported by two buttresses on free contact with a rigid base was investigated thoroughly. Stability analyses were performed on monolithic structural models whereas dynamic analyses were implemented on articulated models with predefined interfaces. This *vaulted structure*, is revisited now by taking into consideration that either the pair of buttresses alone or the entire structure is covered with soil. In the latter case the crest of the arch lies at a depth *d* underneath the soil surface. For simplicity this type of structure will be appointed from now on as an *embedded vaulted structure*. Unlike in the case of the simple vaulted structure of Chapter 5, the foundation base is replaced with soil which performs as a supporting medium in the foundation level. Moreover, in this case the surrounding soil medium, apart from supporting the structure, contributes to the static equilibrium in two more, distinct ways. In particular, the backfill soil is retained by the structure, especially by the two buttresses and additionally, in fully embedment conditions it may also impose loads to the structure through overburden pressures.

Two prominent examples of such monumental masonry *geostructures* are illustrated in Figure 6.1: A vault with embedded lateral walls, used as the entrance to the ancient stadium of Olympia, Western Peloponnese (Figure 6.1a), and a vaulted tunnel, used as the entrance to the ancient stadium of Nemea, Northeastern Peloponnese (Figure 6.1b). Other examples of cut and cover tunnels are the vaulted entrances at the Sikyon theatre, the tumulus tombs in Kasta, Amphipolis and in Acharnes, Attica. In addition, bored tunnels such as the Eupalinian aqueduct are supported by masonry arch and therefore these can be regarded as embedded vaulted structures. Although the scope of this study is focused on geostructures in which a cut-and cover construction

procedure has been adopted, the findings extracted herein can also be extrapolated to bored tunnels with masonry support, by adopting some conservative assumptions.

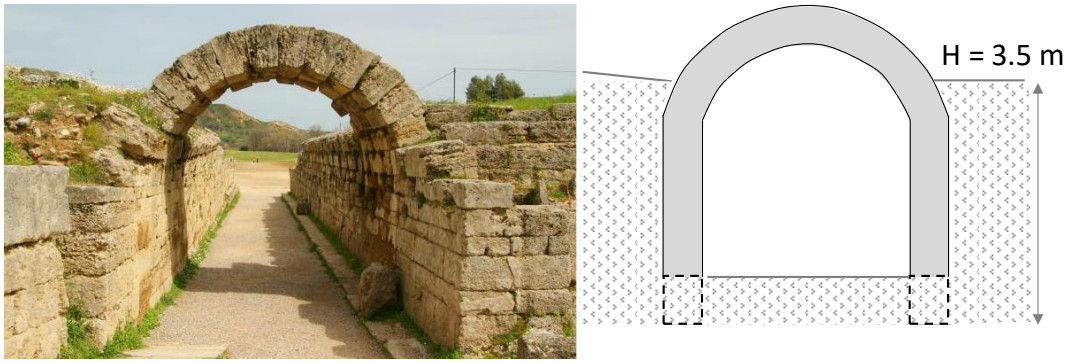

(a) *Type I embedded vaulted structures*

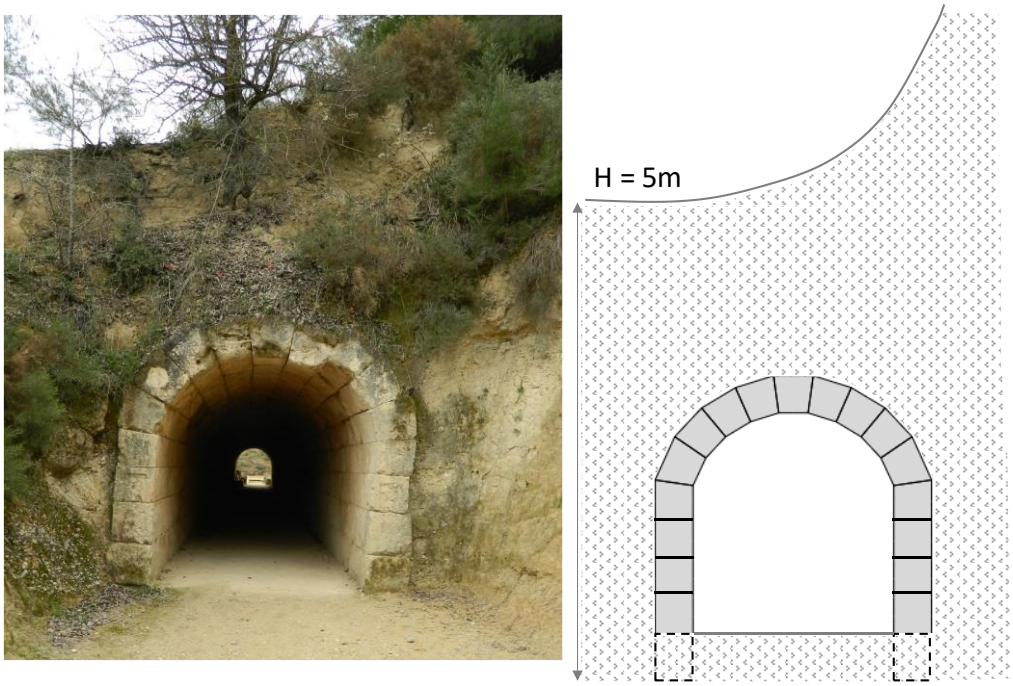

(b) *Type II embedded vaulted structures*

Figure 6.1 Embedded vaulted structures in Ancient Greece: (a) masonry vault with embedded lateral walls, used as the entrance to the ancient stadium of Olympia, western Peloponnese, (b) masonry vaulted tunnel, used as the entrance to the ancient stadium of Nemea, northeastern Peloponnese.

6.2 System Configuration incorporating the Construction Sequence

The free body diagram of the embedded vaulted structure is illustrated in Figure 6.2. When the structure is "wished in place" at the excavated area the gravity loads of the structure parts (W_{arch} and $W_{buttress}$) mobilise reaction forces from the foundation soil (N, T_{base}). (The term "wished in place" refers to the neglection of the reduction of the horizontal stresses into the trench due to ground relaxation at the FE analysis).

The reaction force T_{base} is tangential to the soil-foundation interface outwards and depends on the coefficient of the friction μ along the interface. Sliding of the structure will be avoided if this force is less than the product of μ*N (N: is the force normal to the stone interface). The larger the coefficient of friction μ the less possible the structure to slide.

When the gaps on either side of the walls are filled with soil, the voussoirs are subjected additionally to the horizontal earth pressures p_{hor}. The infill zone (30cm in width) is set on compression providing counterbalance to the soil-foundation reaction. The lateral earth pressure distribution depicted on the schematic configuration of Fig. 6.2 develops according to Rankine's and Coulomb's theory of linear increase of lateral pressure with depth.

Eventually when the overburden soil is placed upon the structure its weight will be received by the curved surface of the arch as distributed vertical earth pressures (p_{ver}) depicted in Fig. 6.2. Depending on the height of the overburden soil as well as the structure's rigidity the distress of the arch may be accompanied with a finite displacement. This compliance may impose in return soil settlement. The unfavorable case where the structure and the infill zone receive all the overburden load is illustrated in Fig. 6.2a. On the other hand, shearing resistance within the contact zone of the yielding and stationary masses may oppose to this movement and tends to maintain it in its original position. As a consequence, the pressure of the yielding mass reduces while the pressure on the adjoing stationary mass

increases. This transfer of pressure is called the arching effect. The stress path along a curved line resembles to a fictitious arch over the yielding zone. The mechanism that allows for this diversion of stress paths from the vertical direction stems from the redundancy of the two-dimensional soil medium. Similar phenomena can be encountered in a solid masonry wall above an opening. This state though is a rather temporary behaviour of soil mass in the yielding zone than a stable one, which evolves with the structure's displacement (Fig. 6.2b).

Conventionally, active lateral pressure against rigid walls was calculated using classical earth-pressure theories such those developed by Coulomb and Rankine. While Coulomb's theory considers the forces acting on a failure wedge with a plane of rupture, Rankine's theory assumes that the distribution of lateral earth pressure against the wall is triangular and increases linearly with depth with the maximum value at the lowest point of the wall and extended up to the crest of the wall. Numerous studies however, have revealed that a more realistic distribution of lateral pressure on the back of a retaining wall is curvilinear or other nonlinear forms (Terzaghi 1943; Tsagareli 1965; Spangler and Handy 1982; Fang and Ishibashi 1986; Wang 2000; Ghosh and Saha 2014). The reduction and the redistribution of stresses within the backfill is resulted from arching effects in the backfill due to roughness of the retaining wall. Lateral earth pressure increases at the upper portion of the wall while decreases at the lower portion. The afore-discussed theories are summarised in Figure 6.3.

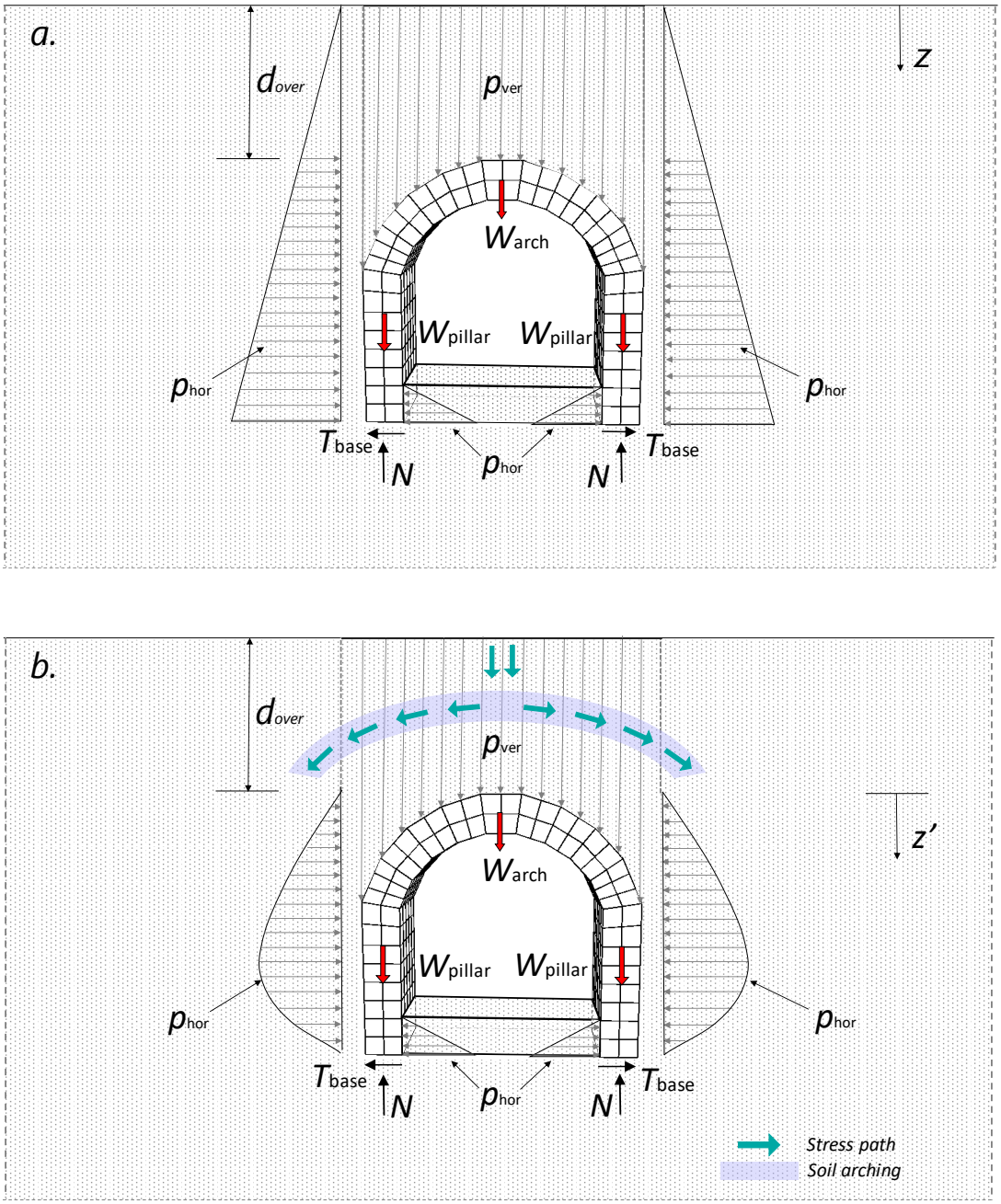

Figure 6.2 Illustration of the free body diagram of a masonry vaulted structure underneath a layer of d_5 = 2.20 m overburden soil. a) The unfavorable case of neglecting soil arching: 1) Forces tangential and normal to the foundation interface T_{base} and N respectively, 2) gravity loads of masonry vaulted structure (W_{arch}, W_{pillar}) and 3) horizontal and vertical earth pressures p_{hor} and p_{ver} respectively. b) Considering soil arching: stress path and soil arching are highlighted. Horizontal earth pressures are considered from the keystone level.

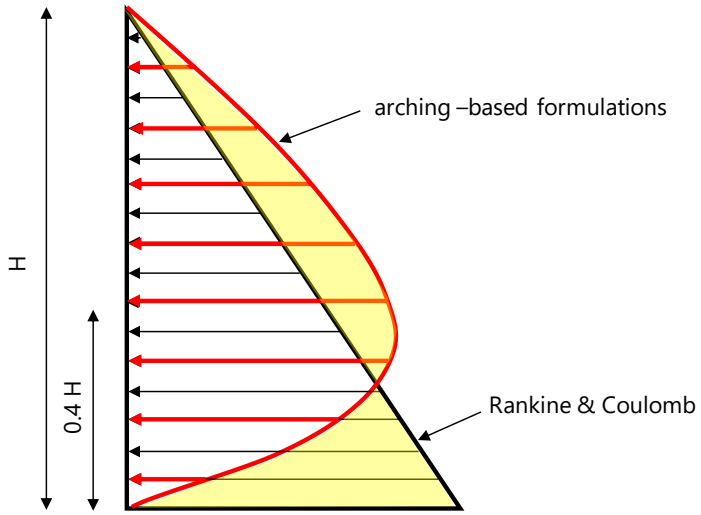

Figure 6.3 Illustration of the linear earth pressure distribution against rigid retaining wall by Rankine & Coulomb (black line) in comparison with the rounded earth pressure distribution by arching based formulation (red line). The zones of increased and decreased earth pressures resulting from the comparison are highlighted with yellow.

6.3 Finite Element Modelling

6.3.1 Two-dimensional Configuration

Nonlinear analysis of the response under static and earthquake loading is implemented numerically with the Finite Element Method. To this extend, the sophisticated code ABAQUS is utilised. Figure 6.4 portrays the finite element discretisation of the model along with a schematic layout of modelling details. A masonry vaulted structure consisting of a finite number of voussoirs is constructed in a trench at a depth of 5.50 m which is excavated in cohesive soil. The structure and the surrounding soil are represented with plane-strain elements. For the purposes of the two-dimensional modelling, soil medium is represented with quadrilateral, continuum elements. Regarding the finite element mesh, a sufficiently refined one is required especially in the area around the structure to ensure the adequacy of the results from the Abaqus

simulation. A fairly fine mesh is selected for an area of 30 m length and 15 m height where the magnitude of stresses is of high interest. It is meshed with quadrilateral plane strain continuum elements of 0.25 m x 0.20 m (detail a). Towards lateral boundaries the mesh is coarser with quadrilateral elements of 0.50 m x 0.20 m (detail b). Table 1 compiles the material properties of the structure. General section beam elements are utilised to support the structure which are gradually removed as the backfill height increases.

A static step is preceding any static or dynamic analysis to establish geostatic conditions within. An implicit direct-integration algorithm incorporated in the code Abaqus is employed to compute the nonlinear dynamic response of this system. With this technique the global equations of motion are integrated through time using the implicit Hilber-Hughes-Taylor operator. Equilibrium solution within each time increment is obtained with an iterative process applying Newton's method. An automatic incrementation scheme is also used with the general implicit dynamic integration method. The scheme uses a half-step residual control to ensure an accurate dynamic solution. The half step residual is the equilibrium residual error (out-of-balance forces) halfway through a time increment. This half-step residual check is the basis of the adaptive time incrementation scheme. If the half-step residual is small, the accuracy of the solution is high and the time step can be increased safely; conversely, if the half-step residual is large, the time step should be reduced. The automatic incrementation scheme is especially effective in case where a sudden event is introduced to the dynamic problem. In such studies small time increments are required immediately after the sudden event. At later times the response can be modelled accurately with large time increments because most of the high frequency content of the solution has been damped out by the dissipation mechanisms present in the model.

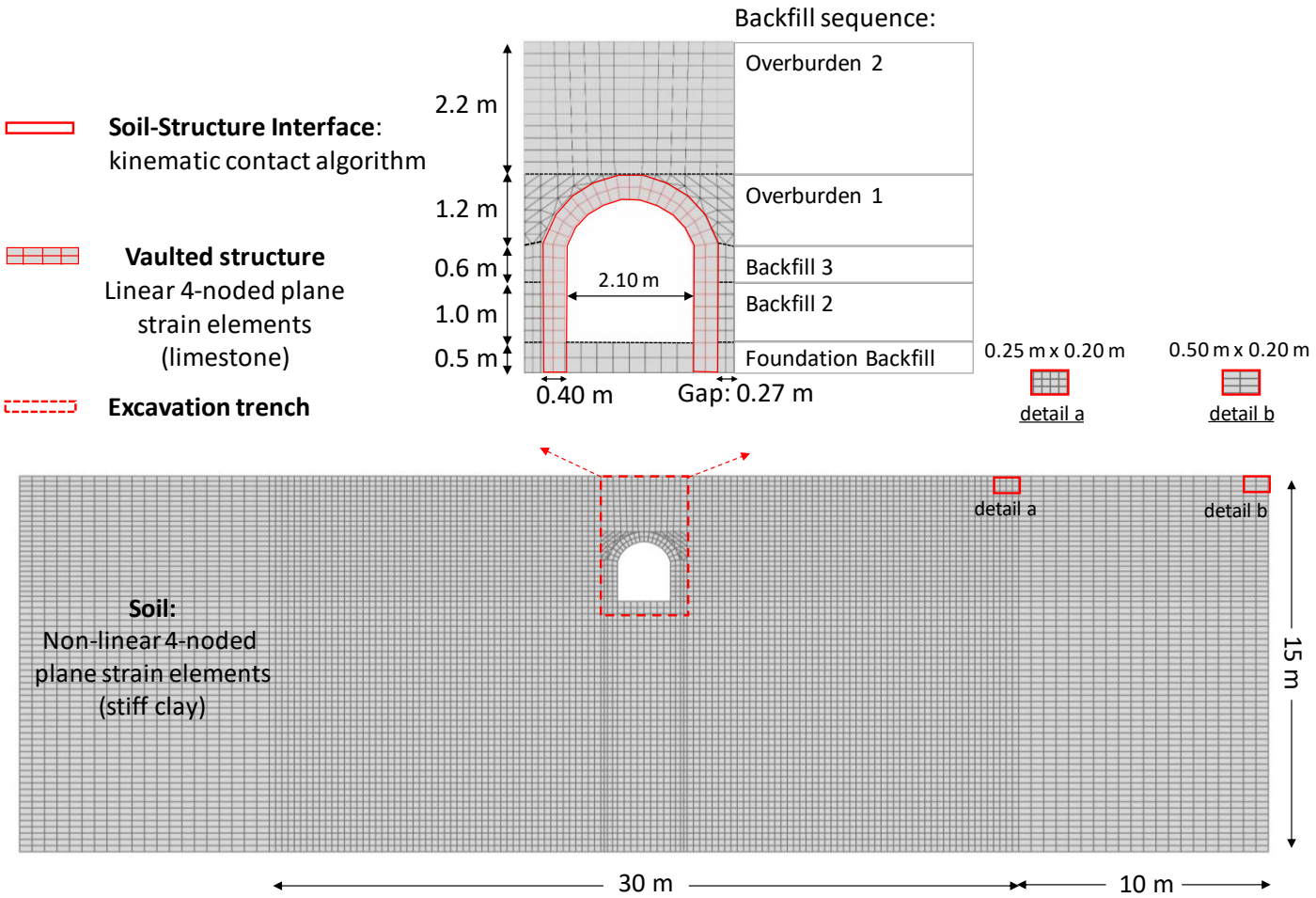

Figure 6.4. The excavation trench, the masonry vaulted structure, and details of the backfill and overburden layers; geometry and finite element discretisation assuming plane strain conditions.

Table 6.1: Material Properties of the structure

Material	**El.Modulus** (*GPa*)	**Poisson ratio** (-)	**Density** ($kg\ /m^3$)
limestone	6.5	0.25	2.2

Boundary conditions

Location and type of boundaries require special consideration. Under static loading (either monotonic or cyclic) these boundaries can be placed as close as possible to the embedded structure (just outside the ''pressure bulb'' of the foundation) given that free field conditions are ensured along any soil profile. Under static loading (either monotonic or cyclic) such a threshold between free field and new field can be placed fairly close to the embedded structure. On the other hand, in dynamic loading there is a significantly larger soil mass around the excavation which interacts with the structure. In this case the aforementioned threshold line should be shifted away from the structure. Vertical boundaries measure 10 m approximately from the excavation bottom. Regarding lateral boundaries, the corresponding nodes at the opposite vertical sides of the same elevation are tied together and forced to move simultaneously only in the horizontal direction preventing any rotation. The side nodes of the excavation are also constrained, as temporary retaining scheme to avoid ground movements. During the backfill procedure these constraints are deactivated to allow the physical development of horizontal earth pressures. Vertical component of the displacement is constrained along the base of the soil medium (vertical movement of the base is restricted).

Interface model

A sophisticated contact algorithm is utilised for modeling contact interface at hinges sections [voussoir-to-voussoir and voussoir-to- buttress (monolithic)] as well as at soil-structure interface. A sufficiently large coefficient of friction (μ = 0.7) was chosen to

approach pure rocking conditions associated with slender systems. The effect of sliding on the response is negligible.

Construction Sequence

The construction sequence of Figure 6.5 is modelled through FE analyses to rigorously capture the effects associated with the interaction between the vaulted structure and the surrounded soil. The arched structure is initially "wished in place" in a trench of 5.5 m depth and the buttresses are temporarily supported. The excavation area is gradually backfilled first with a layer of height d_1 = 0.5 m which is placed to both the exterior sides of the buttresses to form the foundation (foundation backfill). Next, the backfill height increases by d_2 = 1 m (backfill 2) and in a third phase the buttresses are fully backfilled (backfill 3, d_3 = 0.60 m). The first layer of overburden soil covers the arch laterally to its top surface (overburden 1) and lastly a 2.2 m overburden soil reaches the trench upper surface (overburden 2).

By increasing the backfill height gradually, the following can be underscored:

- the backfill and overburden soil affect the structure stability
- detailed profiles of the earth pressures that develop in every step
- possible development of soil arching phenomena at the arch base

The significance of installation sequence on the earth pressures acting on retaining walls and on wall movements relative to the retained soil were mentioned by several authors (Poulos et al, 2001, Potts & Fourie, 1984, Clayton et al, 1993). Finite element analyses conducted on previous works have also highlighted the importance of the construction sequence.

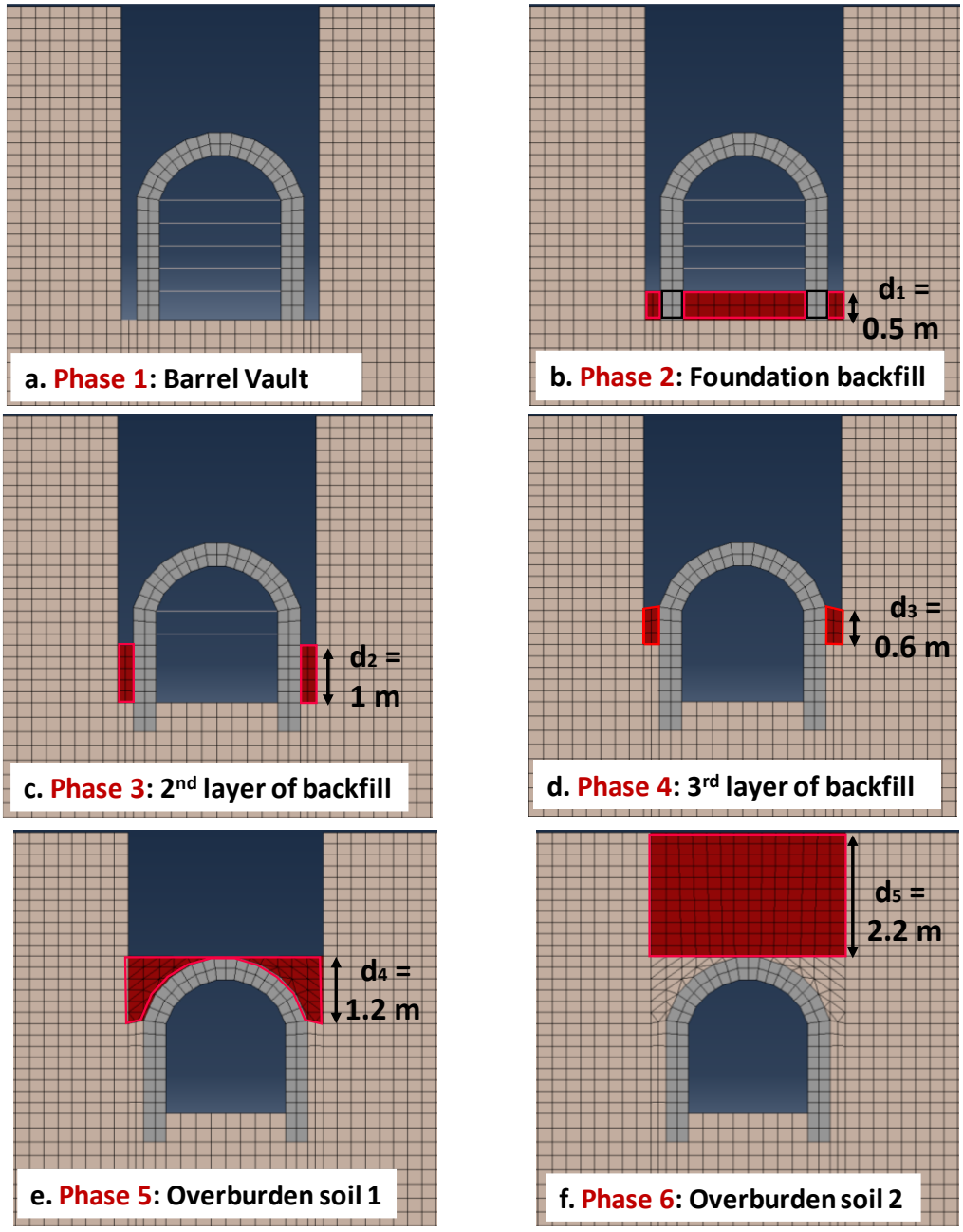

Figure 6.5 Representation of the construction sequence with finite elements: (a) Phase 1: the arched structure is built in a trench and the buttresses are temporarily supported, (b) Phase 2: a backfill layer of height d_1 = 0.5 m is placed to both the exterior sides of the buttresses to form the foundation (foundation backfill), (c) Phase 3: backfill height increases by d_2 = 1 m (backfill 2), (d) Phase 4: the buttresses are fully backfilled (backfill 3, d_3 = 0.60 m), (e) Phase 5: the first layer of overburden soil, d_4 = 1.20 m covers the arch laterally to its top surface (overburden 1) , and (f) Phase 6: a d_5 = 2.2 m overburden soil reaches the trench upper surface (overburden 2).

6.3.2 Soil material modelling

A soil profile of homogeneous cohesive soil in which stiffness and strength are gradually increasing with depth is implented in this study. Soil properties of the stiff clay stratum such as the undrained shear strength (S_u), the Modulus of Elasticity (E), and the shear Modulus (G) are portrayed in Figure 6.6.

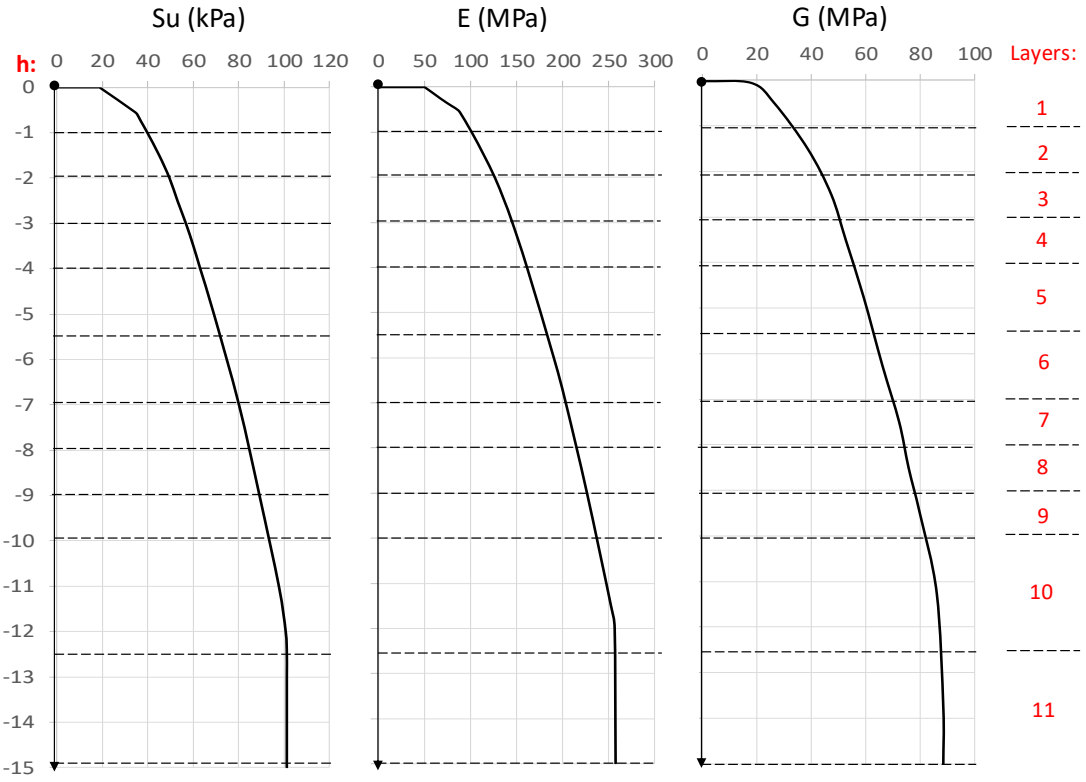

Figure 6.6 Soil profile of a stiff cohesive soil. Height distribution of the undrained shear strength S_u (kPa), the modulus of Elasticity E (MPa), and the shear modulus G (MPa).

The elastoplastic soil behavior of cohesive soils under undrained conditions is described with Von-Mises failure criterion, available in the finite element code Abaqus. Representation of the yield surfaces in principal stress coordinates is illustrated in Figure 6.7 along with Tresca's hexagonal yield surface. The post-yield behavior is simulated by an isotropic/ kinematic hardening and the associated plastic flow rule.

During two-dimensional (plane strain) conditions, the yield surface can be expressed in the principal stress space by the following function:

$$F = (\sigma_1 - \sigma_2)^2 + (\sigma_2 - \sigma_3)^2 + (\sigma_3 - \sigma_1)^2 - 2 * \sigma_y^2 = 0 \quad (1)$$

In which $\sigma_{1/2/3}$ are the principal stresses and σ_y is the maximum yield stress. For $F < 0$, the stress levels are inside the yield surface and soil behavior is elastic. The latter is determined by the visco-elastic parameters E, ν and ξ.

The evolution law consists of two components:

- a nonlinear kinematic hardening component, which describes the translation of the yield surface in stress space and is defined through a "back-stress" parameter α;
- an isotropic hardening component, which describes the change of the equivalent stress defining the size of the yield surface σ_0 as a function of plastic deformation.

The evolution of the kinematic component of the yield stress is defined as:

$$\dot{\alpha} = C\,\dot{\bar{\varepsilon}}^{pl}\,\frac{1}{\sigma_o}(\sigma - \alpha) - \gamma\,\alpha\,\dot{\bar{\varepsilon}}^{pl} \quad (2)$$

Where C is the initial kinematic hardening modulus and γ is the parameter determining the rate of decrease of the kinematic hardening with increasing plastic deformation (Ziegler 1959, Chaboche 1990). The plastic flow rate is $\dot{\varepsilon}^{pl}$

$$\dot{\varepsilon}^{pl} = \dot{\bar{\varepsilon}}^{pl}\frac{\partial F}{\partial \sigma} \quad (3)$$

Where $\dot{\bar{\varepsilon}}^{pl}$ is the equivalent plastic strain rate.

The maximum yield stress for clays can be defined as

$$\sigma_y = \sqrt{3}S_u \quad (4)$$

In that case the hardening parameter γ may be expressed as

$$\gamma = \frac{C}{\sqrt{3}S_u - \sigma_0} \tag{5}$$

Calibration of the kinematic hardening component is based on the equation $C = E = 2(1+\nu)$ for very small strains (where E is the modulus of elasticity and ν is the Poisson's ratio). The stress at zero plastic strain σ_0 is taken as 1/10 to 1/3 of the undrained shear strength S_u for smaller computational cost reasons. Model parameters are calibrated against G-γ curves of the literature, as described in Gerolymos et al (2005). In this study, model parameters are calibrated to fit published G: γ curves of Vucetic and Dobry (1991) for a plasticity index, PI=15.

Regarding the profile of the backfill and overburden soil, it resembles with the surrounding soil (Figure 6.6) but the behavior under undrained condition is neatly/ simply elastic linear.

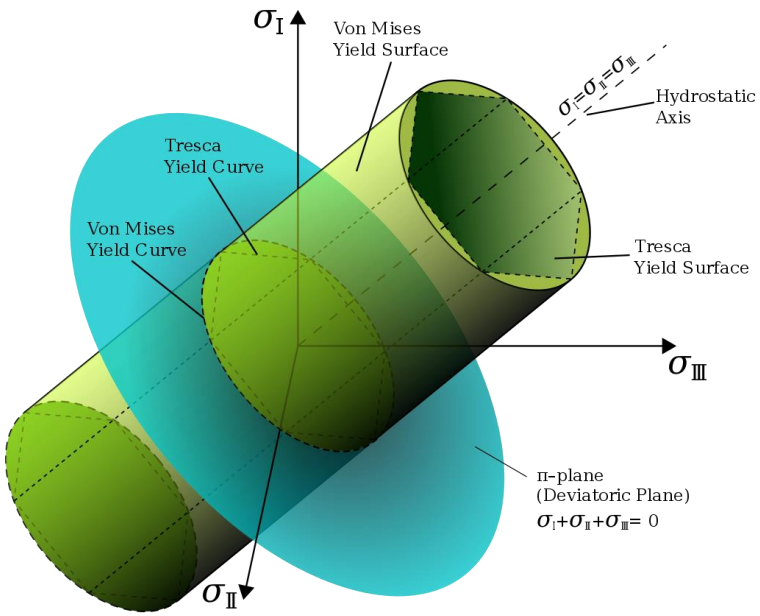

Figure 6.7 Representation of the three-dimensional extended pressure dependent Von Mises failure criterion in the principal stress space. Tresca yield surface is also seen in a hexagonal prism.

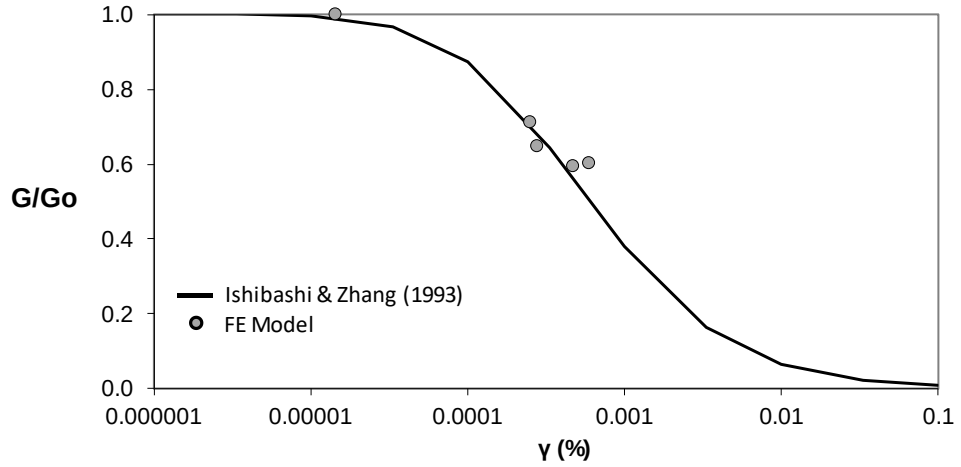

Figure 6.8 Constitutive model calibration for stiff clay. Comparison of FE-computed against G-γ curves with published curves of Ishibashi & Zhang (1993) for plasticity index PI = 15.

6.4 Establishment of Static Equilibrium

6.4.1 Earth pressures on a vaulted structure of uniform section

In a soil that currently exists under the condition of zero horizontal deformation with principal planes that are horizontal and vertical the coefficient of earth pressure at rest, K_o, is the ratio of the effective horizontal pressure σ_h at any depth below the soil surface to effective vertical pressure σ_v:

$$K_o = \sigma'_{ho} / \sigma'_{vo} \quad (6)$$

Based on the movement of the retaining wall the following types of lateral earth pressure can be exerted on retaining walls. Active earth pressure state is developed on the wall when the wall moves away from its initial "at rest" condition. In that case the horizontal stress is reduced which leads to an increase in shear stresses.

The latter mobilises the full shear strength of soil which eventually fails. The coefficient of active lateral pressure K_a at a given depth is defined as

$$K_a = \sigma'_{ha} / \sigma'_{v} \quad (7)$$

Where $\sigma'_v > \sigma'_{ha}$

Passive earth pressure state is developed when the wall moves towards the soil. The horizontal pressure σ'_h is increased whilst the vertical stress σ'_v, which is controlled by self-weight and wall friction, remains constant. As the wall moves in towards the soil the shear stress changes and eventually when the applied shear stress reaches the available shear strength, soil failure will occur. In order to increase the '*at rest*' pressure to limiting passive values, larger displacements are

required. The coefficient of passive lateral pressure K_p at a given depth is defined as

$$K_p = \sigma'_{hp} / \sigma'_v \quad (8)$$

Where $\sigma'_v < \sigma'_{hp}$

The following investigates the effect of the construction sequence of the embedded barrel vault on the stress field of the soil. In Figure 6.9 four sections at near field (x = 1 m), middle field (x = 6 & 12 m) and far field (x = 25 m) of soil medium are highlighted (where x is the distance from the excavation boundary line).

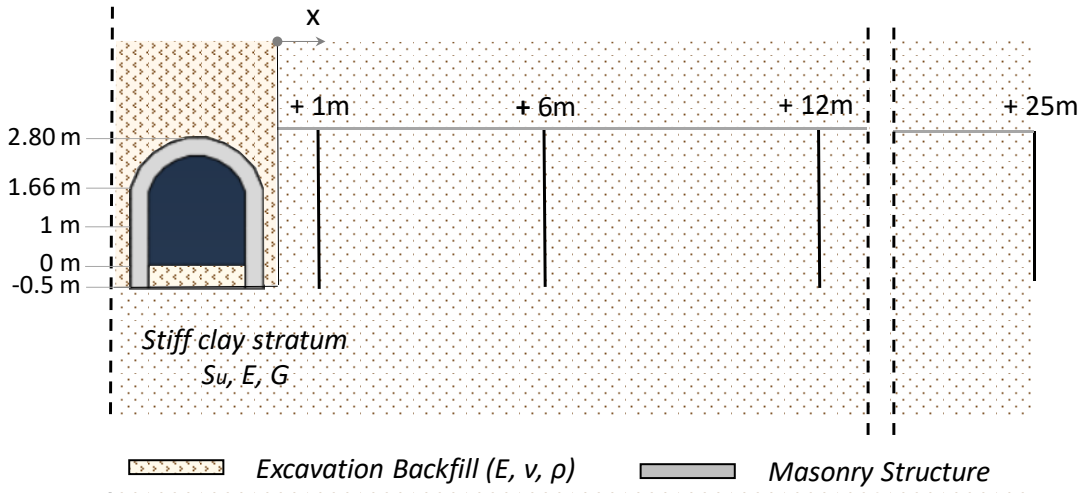

Fig.6.9 Four sections at the soil medium: a) near the excavation trench (x =1 m), b) at a distance of x =6 m, c) at the mid-axis (x =12 m) and d) at the boundary (x =25 m). Horizontal distance "x" is measured from the trench edge. The height levels of each backfill layer are also depicted.

Figure 6.10 depicts the earth pressure coefficient "K" distribution from the bottom edge of the excavation to the soil surface. Each diagram corresponds to a different phase of the construction sequence as presented analytically in Figure 6.3.

- Sign convention for stresses is as follows: Normal stresses are positive, meaning that they induce tension, when they are directed away from the retained medium and negative are those directed towards it. Concerning the vertical stresses, negatives are those directed downwards. Therefore, the negative values of the coefficient *K* are resulting from tensile horizontal stresses (σ_h) whilst the positive values indicate that horizontal stresses induce compression.
- The coefficient K is calculated according to equation 6, in which both horizontal and vertical stresses are computed numerically.
- Generally, for the interpretation of the results it should be taken into consideration that the coefficient *K* is influenced by various factors such as the previous stress history of the retained soil, the friction between the wall and the soil, the soil cohesion, the wall inclination and rigidity.
- After the excavation, the surrounding soil relaxes and the stresses "at rest" are increased near the excavation bottom. Without the imposed kinematic restrains, soil would have failed resulting in excessive deformations at the excavation base. The impending of the deformations at the sidewall (vertical) surfaces leads to "passive" conditions near the bottom and "active" conditions at the surface (these conditions can be referred as "initial conditions" of construction sequence).
- Once the supported material is placed (backfill procedure) the near field lateral earth stresses (x = 1 m) are intensely affected especially when the wall is fully covered and loaded with overburden soil. As the backfill height increases into the gap from the foundation stones to the keystone, the retained soil deforms laterally (active state) and "pushes" the walls inwards. In order the structure to receive the torque, the arch pushes the soil and reaches the passive state. These masonry walls are non-yielding structures which usually undergo relatively very small movements.
- The horizontal earth pressures at the structure base are noticeable relieved by the partial embankment of the gaps next to the buttresses (phase 2, 3). When the structure is fully covered with backfill soil (phase 5), the structure

receives these pressures with slightly higher compliance and conditions of active state are developed. During phase 4, passive state is developed at the backfill surface. The boundary that separates the two states moves upwards when the arch is covered to its key and lowers again when a 2.20 m overburden soil is placed (phase 6).

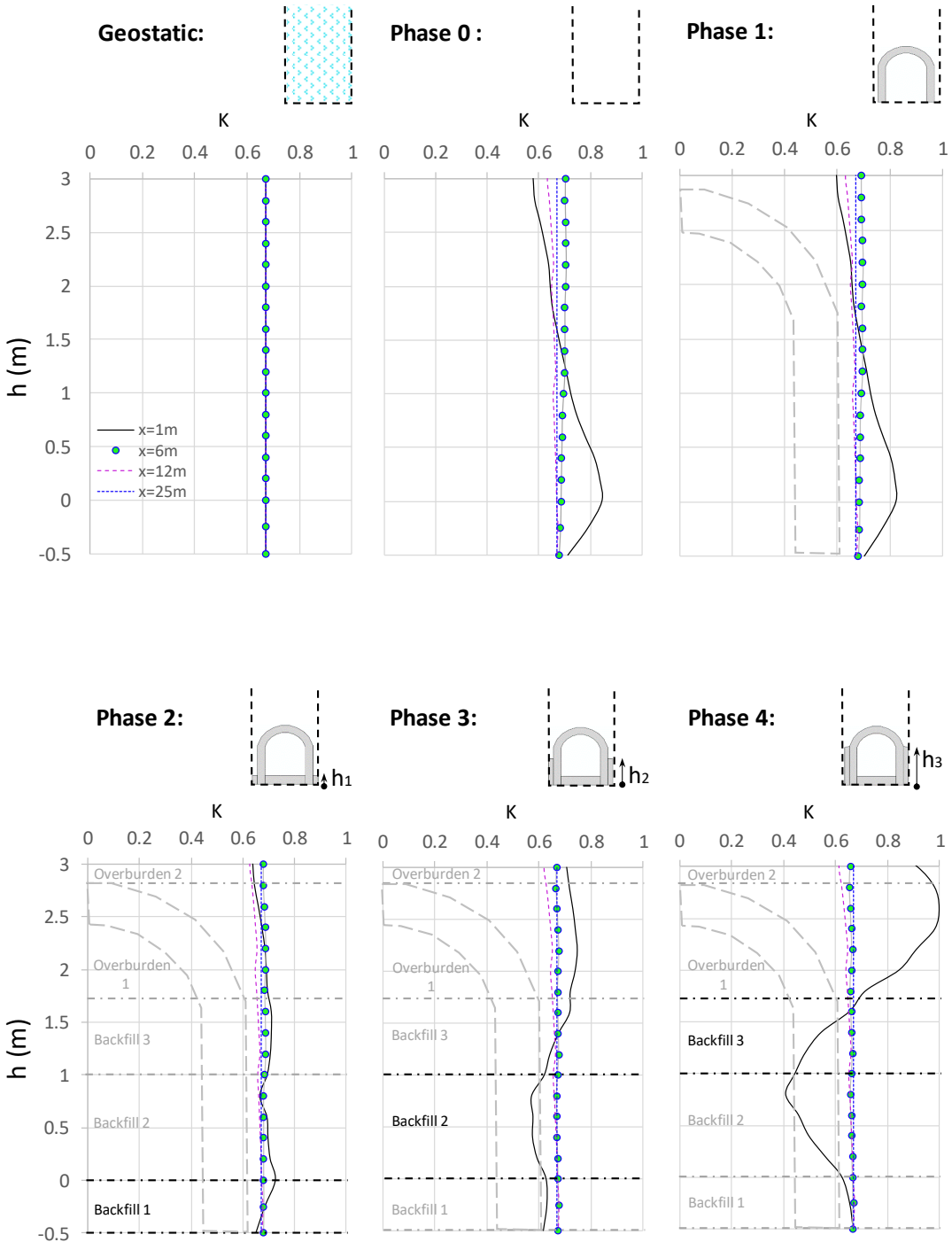

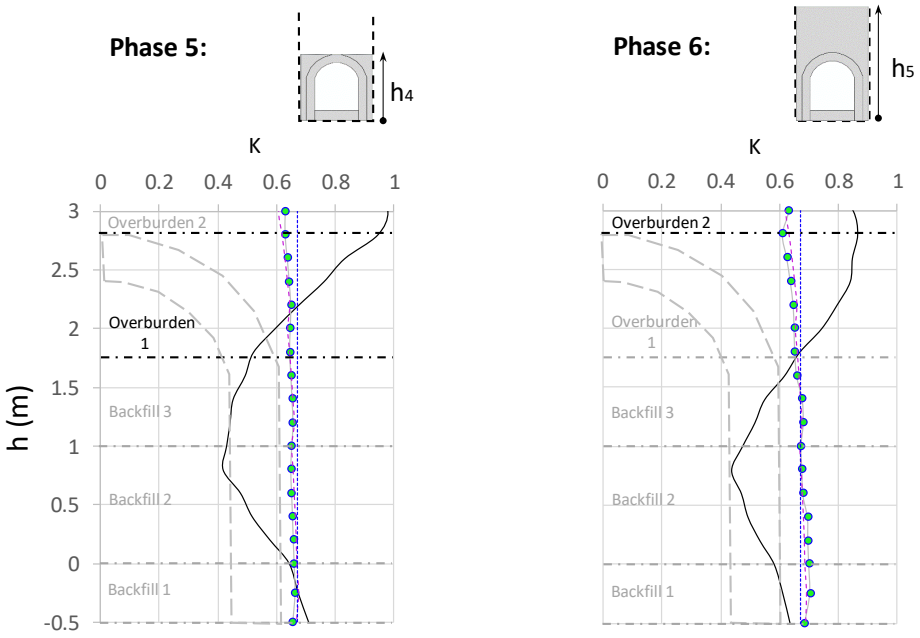

Figure 6.10 Heightwise distribution of the lateral earth pressure coefficient *K* at four different sections of the soil stratum (Figure 6.10) during each step of the construction of a vaulted structure of uniform section: (a) geostatic, (b) excavation of the trench (phase 0), (c) construction of the vaulted structure (phase 1), (d) 1st layer of the backfill soil (h_1=0.50 m) (phase 2), (e) 2nd layer of the backfill soil (h_2=1.50 m) (phase 3), (f) 3rd layer of the backfill soil (h_3=2.10 m) (phase 4), (g) 1st layer of the backfill soil (h_4=3.30 m) (phase 5), and (h) 2nd layer of overburden soil (h_5=5.50 m) (phase 6).

Horizontal Earth Pressures

During the progressive embankment of the excavated trench after the vaulted structure has been placed, soil-structure interaction occurs and both the responses of the interacted parts depend on the following factors:

1) Structure-soil placement techniques. In our case the structure is "wished in place" and the backfill soil is placed successively.
2) The coefficient of friction at the soil-structure interface which in our case is high enough to prevent sliding (μ =0.7)
3) The ability of the wall movements, which are related to the limestone inertia, to mobilise the soil shear strength capacity

Of interest are the stresses arising in the backfill soil in the vicinity of the structure. According to the aforementioned sign convention for stresses, the earth pressures presented in Fig.6.11 are compressive stresses acting on the vicinity of the wall. Soil contact pressures can be redistributed along the interface in such a way the developed fluctuations of the linear profile provide moments to stabilise the buttress in vertical position. Upon the refill of the overburden soil the demand of outward dislocation of the arch at its supporting base mobilises significant soil forces to ensure the structural integrity of the arch. This pair of symmetrical horizontal forces is demonstrated with a local peak in the profile of soil contact forces, around the supports of the arch. In this way structural arching effect is attained and thus static equilibrium of the structure is established with minimal displacements.

To further elucidate the favorable role of backfill soil the development of horizontal earth pressures on the excavation section is presented in Figure 6.12. The enforcement of kinematic constraints among the vertical boundaries of the excavation results to additional horizontal earth pressures. The concentration of these pressures is observed at positions that deformation would develop if these constraints didn't impose. During the backfill procedure (phases 3-6) a stress relief is observed at the soil next to buttresses. As the backfill height increases larger amount of soil mass contributes to the tension redistribution. At the last phase of the construction sequence (phase 6), the stresses at the interface with overburden 1 are quite larger than the geostatic due to the structural arching whereas at the interface with overburden 2 are slightly larger due to soil arching.

The backfill soil contributes in two ways:

1) When the arch is loaded by the overburden soil, resulting to the development of the structural arching phenomenon, it offers the horizontal reaction at the arch base to limit the arch flattening,
2) It receives a portion of the overburden load and generally behaves as a "cushion mechanism".

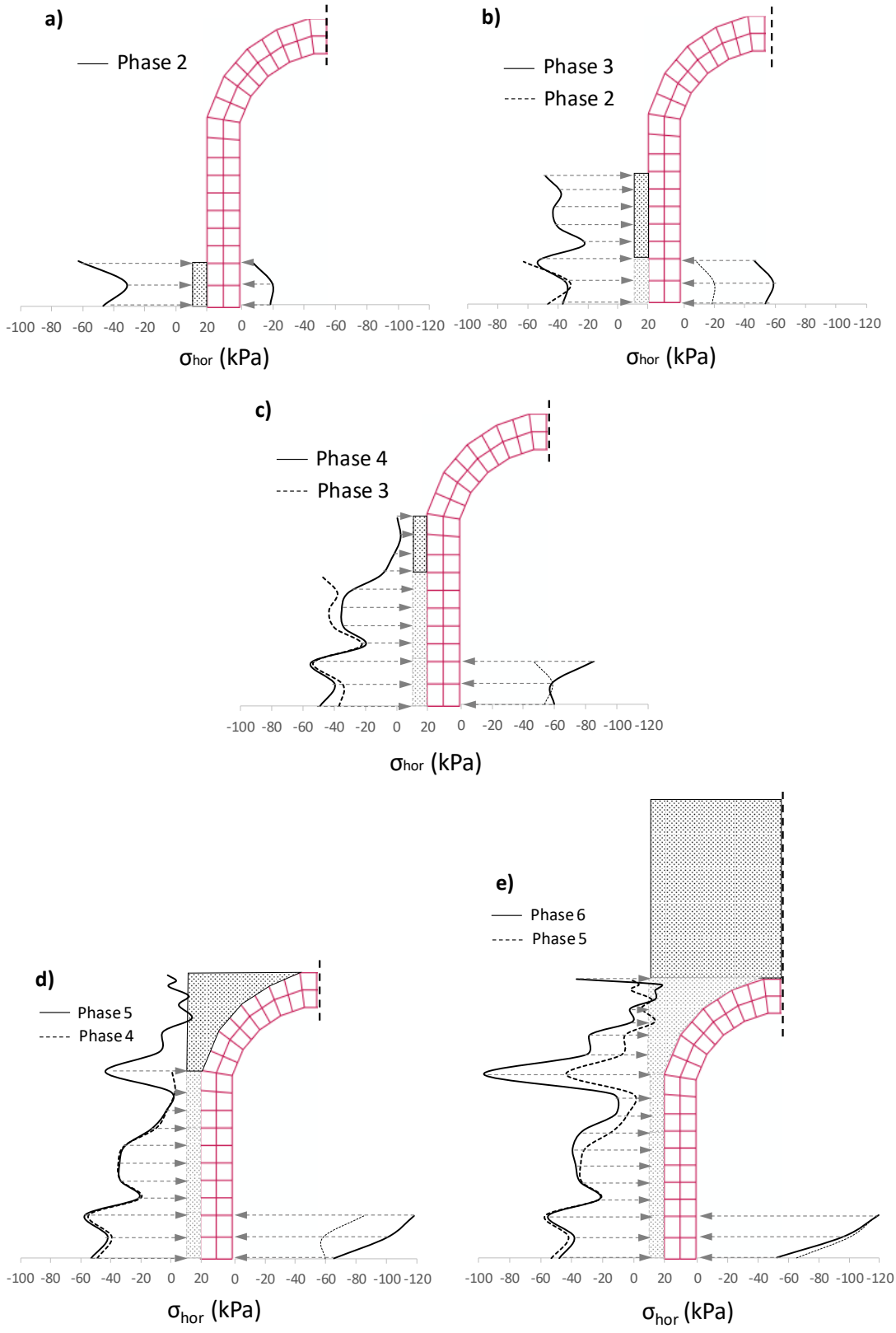

Figure 6.11 Heightwise distribution of the lateral earth stresses acting on the buttress-arch surface during every step of the backfill procedure after the construction of the vaulted structure.

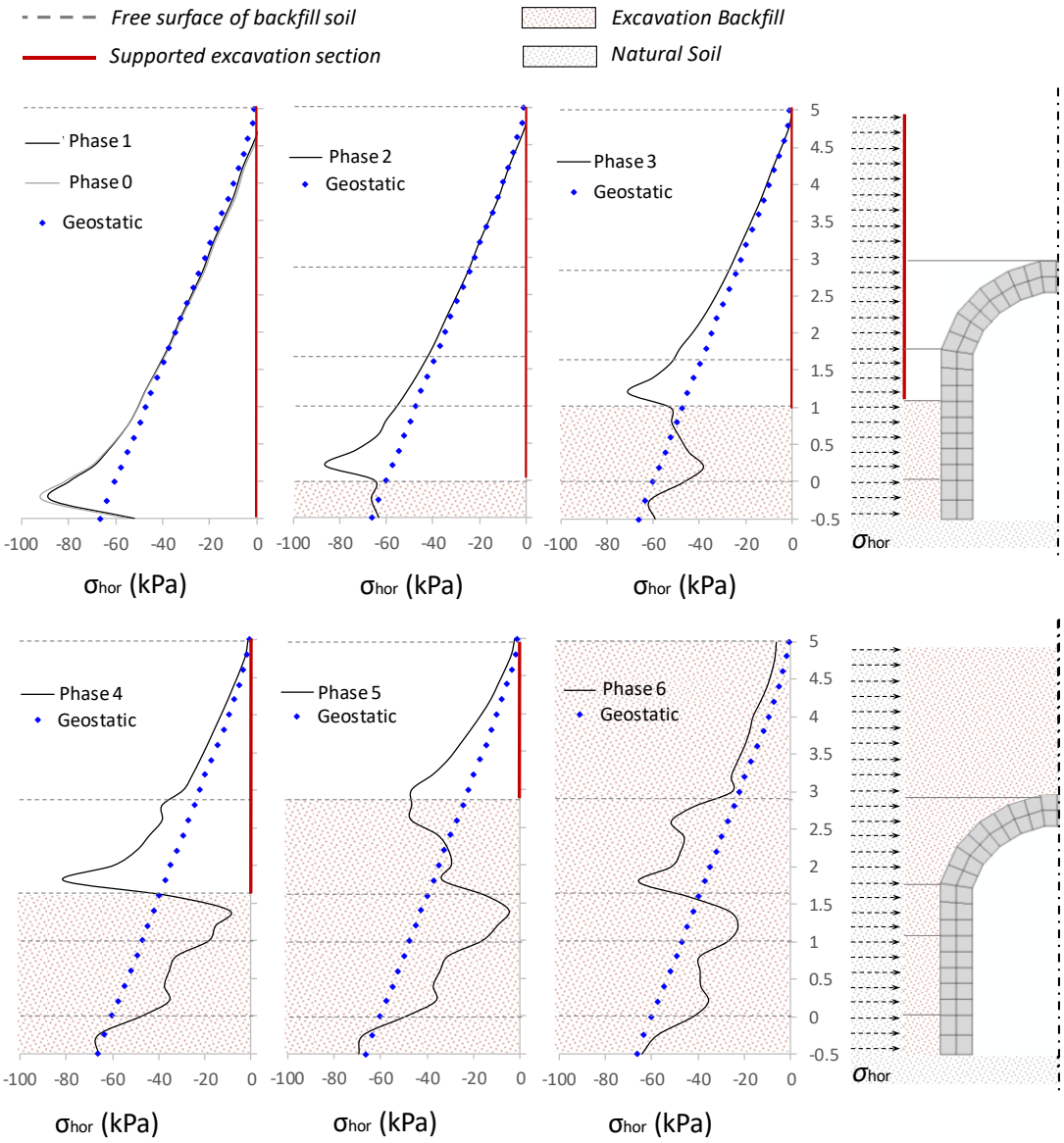

Figure 6.12 Lateral soil pressures along the excavation section (supported with numerical constraints at nodes). The stress distribution on each step is illustrated along with the triangular earth pressure distribution. The latter is utilised as a yardstick for evaluating the effect of the construction sequence to the stresses.

Horizontal and vertical displacements

Apart from horizontal earth pressure distributions, remarkable conclusions can be drawn from the displacement curves. Figure 6.13 illustrates the contours of structural displacements on x and y components due to the successive embankment of the structure. The response of the structure is governed primarily by the response of the soil adjacent to the structure. The changing forces from the backfill or overburden soil that are applied to the vaulted structure mobilise different deformation modes. The magnitude of these displacements depends on: a) the structure geometry, b) masonry stiffness, c) soil stiffness and d) the construction sequence. For the sake of convenience displacements are positive when they are directed along the positive direction of the corresponding co-ordinate axis.

Three essential phases of the structure's embankment are distinguished: (i) the buttresses are fully backfilled (the soil arises at the height of h_3 = 2.16 m from the foundation base), (ii) the arch is covered to its crown (h_4 =3.30 m) and (iii) the placement of overburden soil above the arch forms the final soil surface at a height of h_5 =5 m from the foundation base.

Upon completion of backfill, the compliance of the buttress is fully mobilised as depicted in Figure 6.13i. These inwards translational and rotational displacements of each buttress (horizontal displacement of 0.4 mm) are restrained by the arch as severe friction forces are developed along each buttress-to-arch interface. Static equilibrium at the end of this phase is established resulting in contact forces which are reduced along the buttress and increased along the arch (tendency for active and passive state respectively). As backfill proceeds, and the arch is covered with soil up to its top point (Figure 6.13ii), soil contact forces impose bending of the arch accompanied with inward horizontal displacements as well as upward movement especially of its central voussoirs (1.8 mm approximately). Eventually, when the excavation is fully recovered with soil, the crown is gradually depressed and the overburden pressures restore the undeformed geometry.

Static equilibrium is then established as the overburden load is undertaken through two arching mechanisms:

i) by the structural arch as the voussoirs are stressed with predominantly axial compression and severe horizontal forces are developed at the arch supports to ensure arching mechanism. These forces are transmitted to the soil medium around these supports which are demonstrated as concentration of the contact pressures in the profile of Fig. 6.11e,

ii) by soil arching. This mechanism is developed at the back and above the arch and allows of stress paths to divert the structural arch transmitting a part of the overburden load directly to soil medium

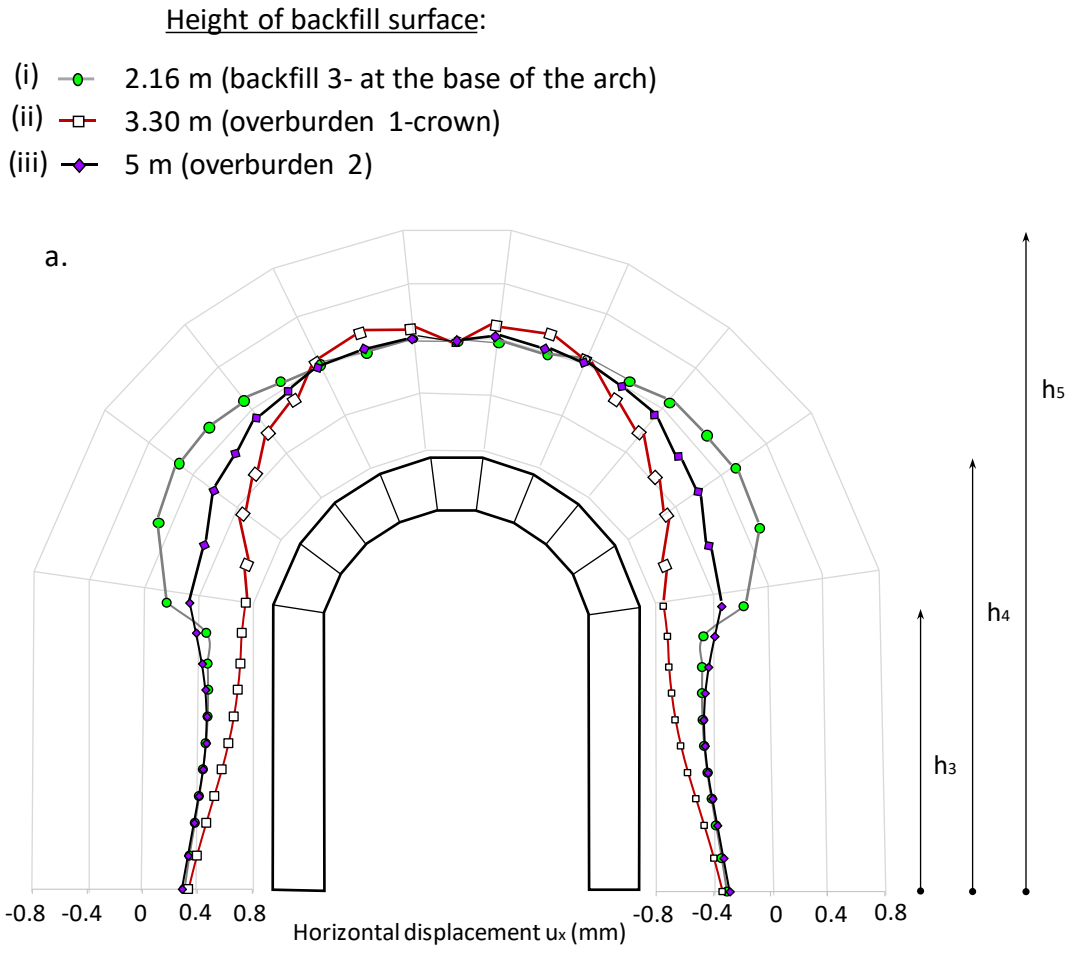

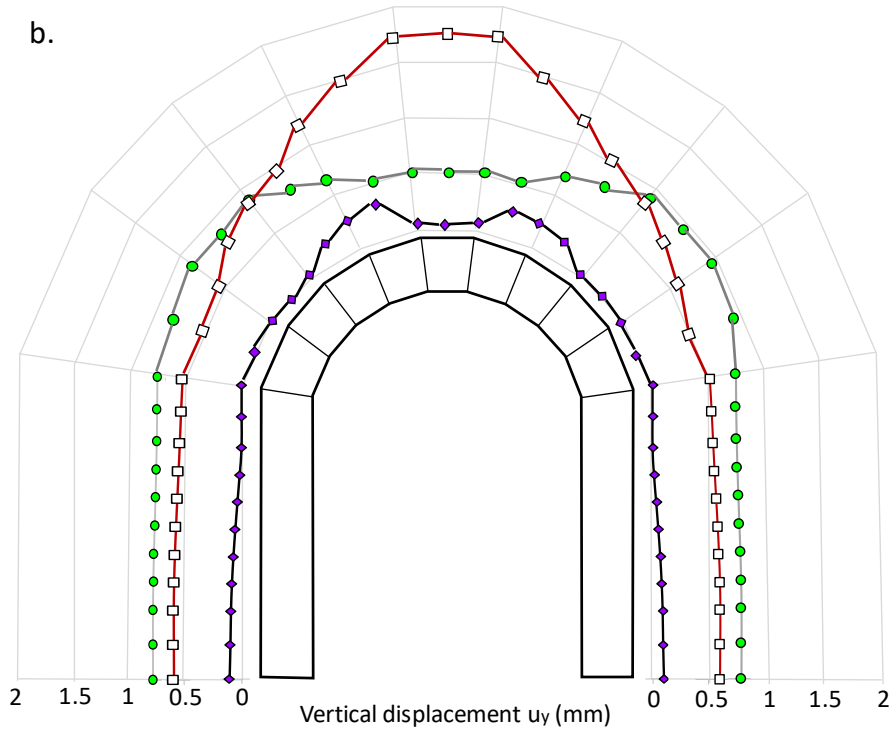

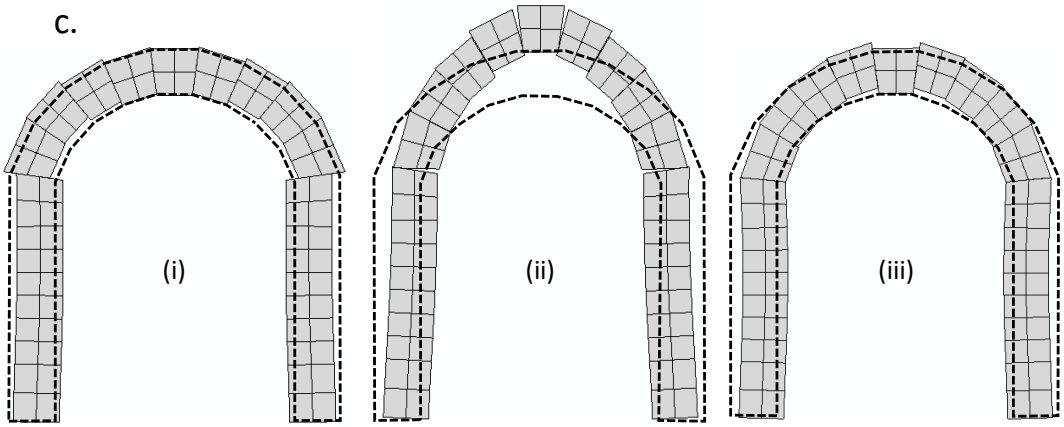

Figure 6.13 Contours of (a) horizontal u_x and (b) vertical displacements u_y, (c) deformation mode with a scale factor of 200% of the structure calculated for three distinguished loading increments: (i) the buttresses are fully backfilled to the height of h_3 =2.16 m, 2) the backfill arises at the height of the crown, h_4 =3.30 m and 3) overburden load is placed above the arch, h_5 =5 m from the foundation base.

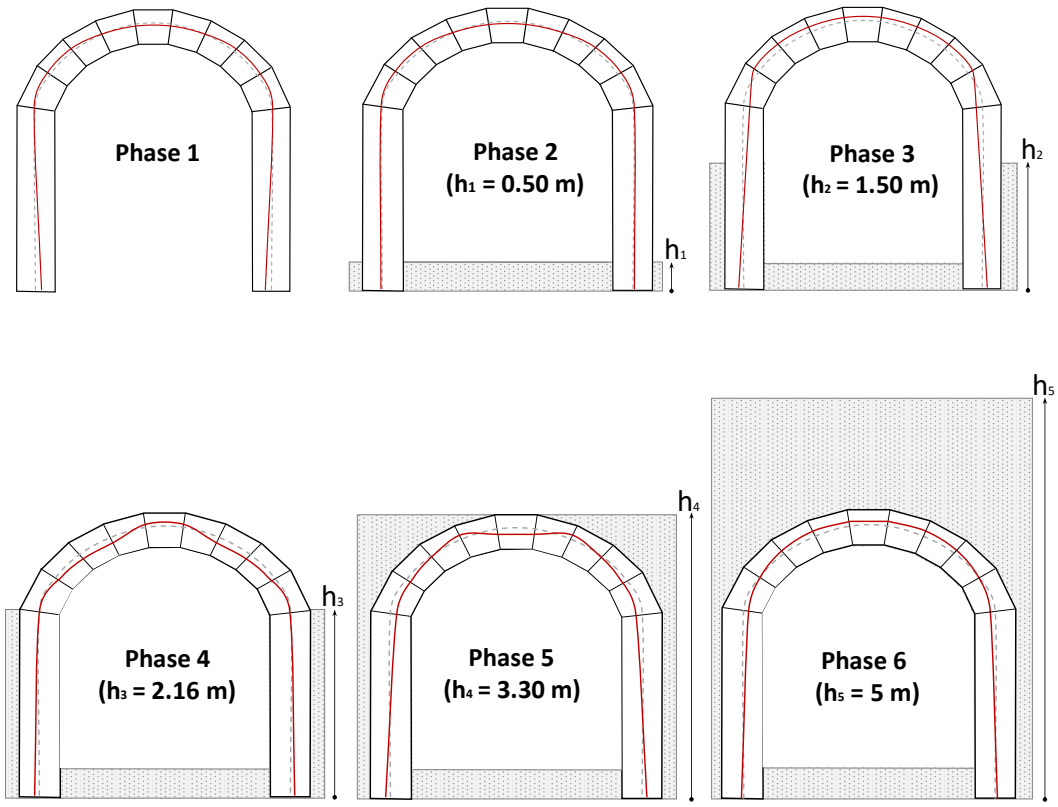

Figure 6.14 Evolution of the thrust line of the vaulted structure for the different phases of the construction sequence of Fig.6.4.

In Figure 6.14 the evolution of the thrust line of the vaulted structure for the different phases of the construction sequence is depicted. The definition of the thrust line lies upon the following phrase: *"For a structure in pure compression to be in equilibrium with the applied loads there must be a line of thrust that lies entirely within the section of the structure. The thrust line (or line of resistance) is defined as the geometrical locus of the points of application of the resultant thrust force that develops at any cross section of the masonry arch."*

As already had been mentioned, buttresses are simulated as monolithic. Therefore, line of thrust isn't representative along their height. Furthermore, buttresses are supported by vertical beams which are removed as the backfill height increases.

6.5 Effect of a stiffen buttress

In this section, the effect of enlarged buttresses to the stability of an embedded structure, and to its interaction with soil is explored. The geometry of the barrel vault portrayed in Figure 5.3.1, where the buttress slenderness increases only by 25% (from b / R =0.3 to b'/R =0.4), is considered. Interestingly, part of the overburden load is undertaken directly by the two buttresses as the 2d configuration dictates. The arched structure on the enlarged buttresses are more safe and heavier structures. The applied loads aren't distributed in a vertical direction but they are obliquely directed outwards. This outward transferred thrust is absorbed by the additional part. The previous FE analyses for a barrel vault of uniform section are repeated for the non-uniform section and the results are presented in comparison. The sketched representation of the model under examination is shown in Figure 6.15. Detail of the forces applying on the left skewback is also portrayed in Figure 6.15 (ii).

The resultant of the compressive forces induced by the voussoir (thrust T) is opposed by the passive soil resistance (P), the frictional resistance at the bottom "skewback-type" voussoir (F) and the overburden weight above the skewback (W). When the horizontal component of thrust overcomes the frictional resistance at the interface ($T_x > F$), mobilisation of passive restraining pressures from the surrounding soil is required.

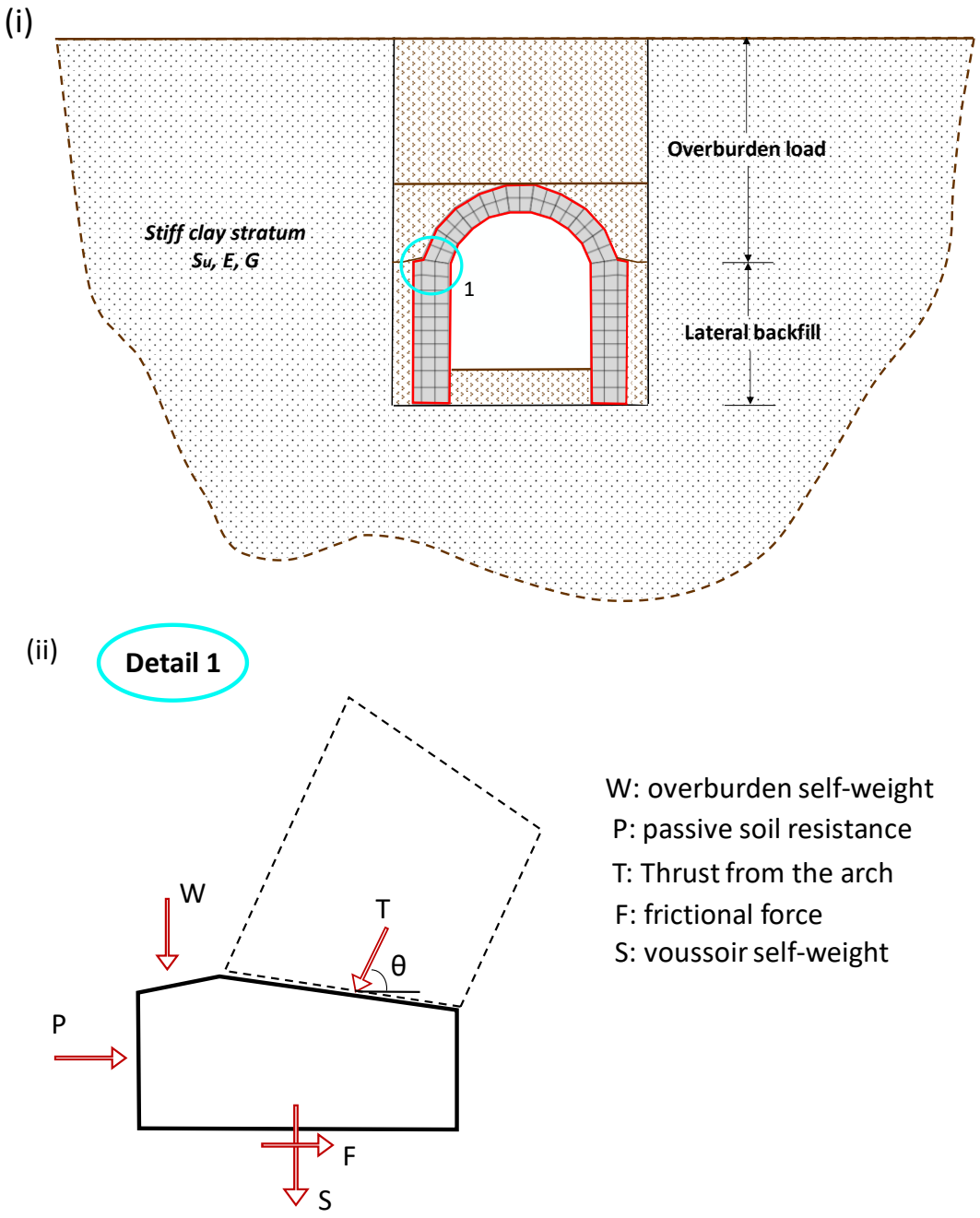

Figure 6.15 (i) Illustration of a vaulted structure with enlarged buttresses embedded on the stiff clay stratum of Fig.6.5. The backfill layers are separated with continuous grey lines, (ii) free body force diagram of a buttress voussoir.

6.5.1 Earth pressures on a vaulted structure of non-uniform section

Similar to the case of the vaulted structure of uniform section, the distribution of lateral earth pressure coefficient *K* is presented below (Figure 6.16). With a cursory glance, the distributions for both the vaulted structures (Figures 6.2 & 6.15) are almost identical. Distribution of the coefficient K during Phase 2 is quite similar with the previous phases. It seems that the placement of the first layer of backfill is incapable of mobilising reactions from the enlarged buttresses which in return will cause changes to the soil stress state. At Phase 4, it is observed that the ability of the arch to move outwards is more limited when the buttresses have larger width than the supported arch (the case of a vaulted structure of non-uniform section). A larger part of the vaulted structure (from the foundation to almost the height of the keystone) mobilise an active state to the surrounding soil when the arch is covered up to the crown (Phase 5: overburden 1). An overburden load upon the structure has a stabilising effect on the system's equilibrium in all cases.

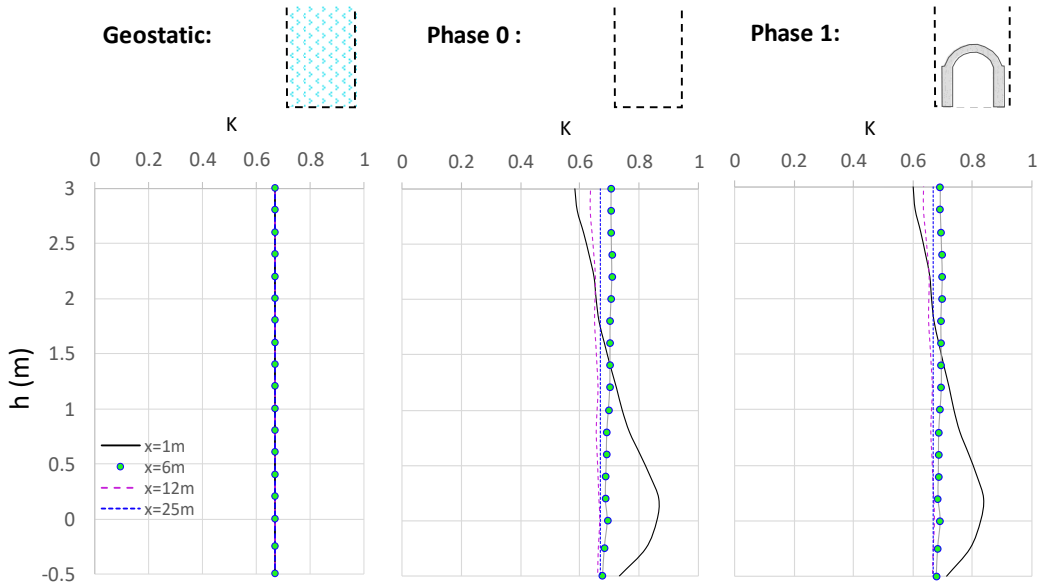

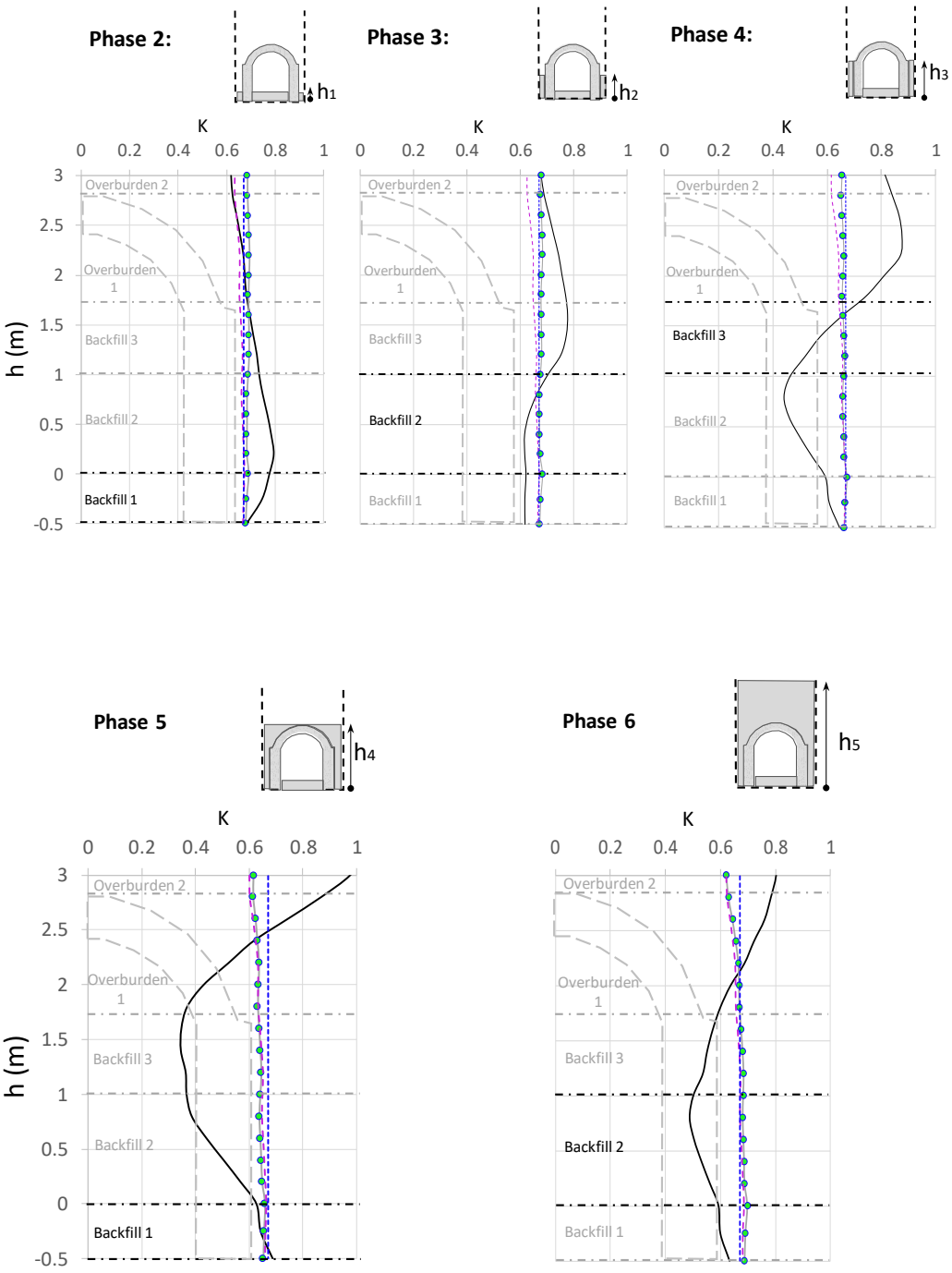

Figure 6.16 Heightwise distribution of lateral earth pressure coefficient K at four different sections of the soil stratum (x=1 m, x=6 m, x=12 m and x=25 m) during each step of the construction of a barrel vault of non-uniform section: a) geostatic, b) excavation of the trench (phase 0), c) construction of the vaulted structure (phase 1), d) 1st layer of the backfill soil (h_1=0.50 m) (phase 2), e) 2nd layer of the backfill soil (h_2=1.50 m) (phase 3), f) 3rd layer of the backfill soil (h_3=2.10 m) (phase 4), g) 1st layer of the backfill soil (h_4=3.30 m) (phase 5) and h) 2nd layer of overburden soil (h_5=5.50 m) (phase 6).

Conspicuous recession of the horizontal earth reaction at the arch base in comparison with the vaulted structure of uniform section is observed at the diagrams of Figure 6.17 during phase 5 & 6 of construction sequence. It seems that part of the horizontal force needed to support the arch is now received by the buttresses as shear mechanism. The stiffen buttress in now capable of receiving moment loading from the arch tendency to flatten.

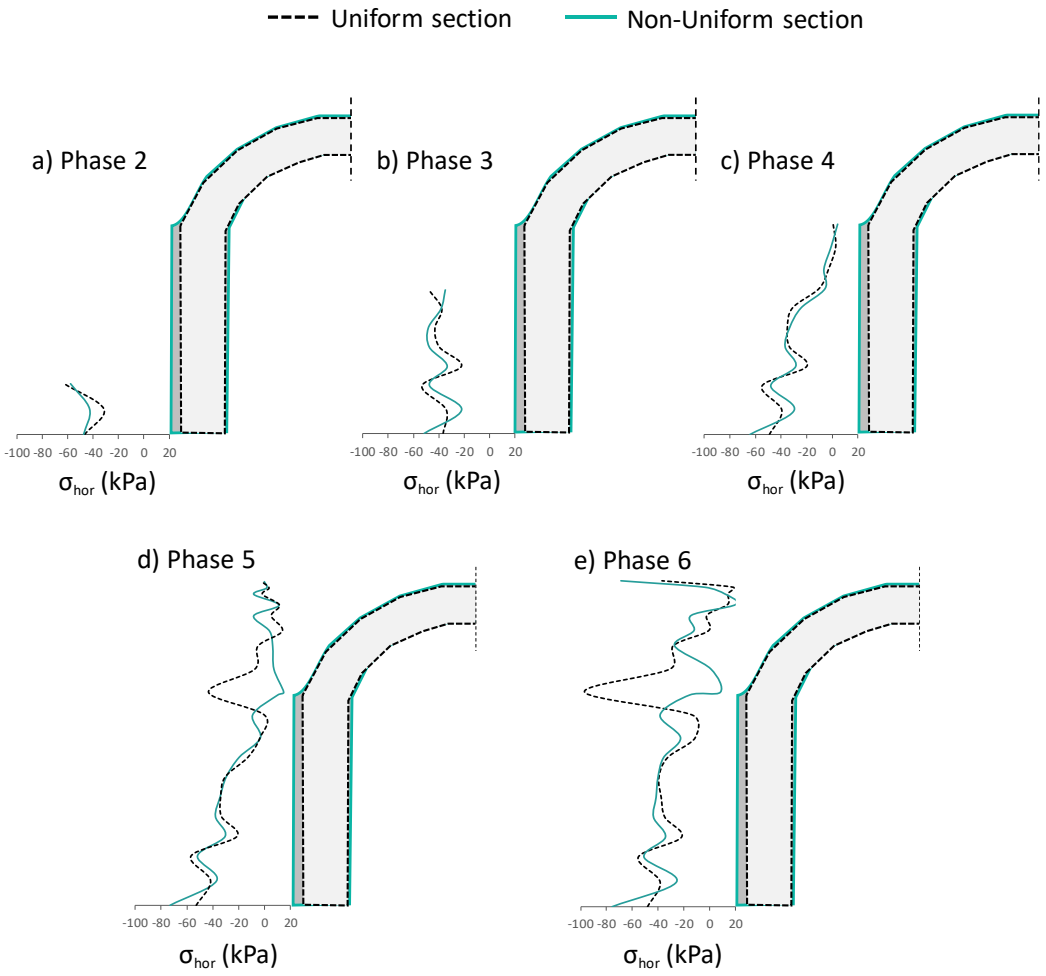

Figure 6.17 Comparison of the heightwise distribution of the lateral earth stresses acting on the wall surface during every step of the backfill procedure after the construction of the vaulted structure of uniform and non-uniform section.

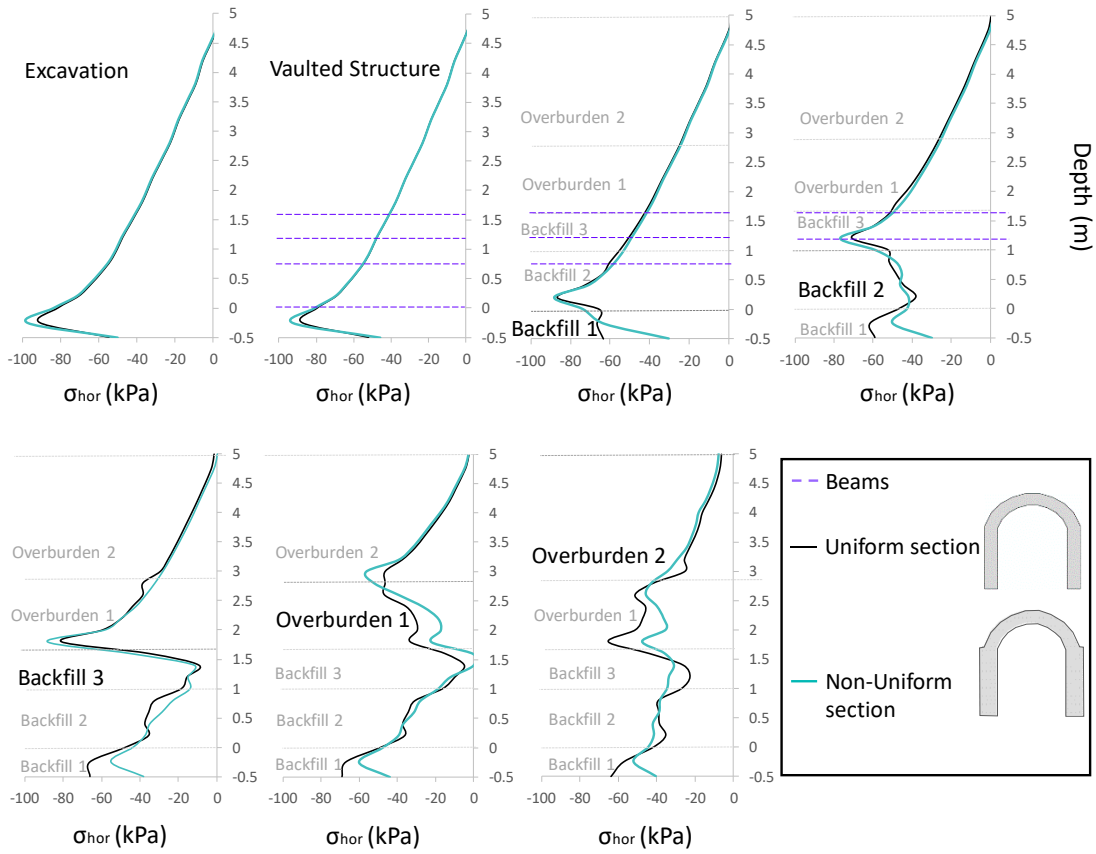

Figure 6.18 Comparison of the lateral earth pressures that develop along the excavation section as the soil interacts with a vaulted structure of either uniform or non-uniform section (black and green line respectively). Distributions are presented for each step of the construction sequence (Fig.6.4). The backfill and overburden layers as well as the position of the beams (which are removed as the backfill layers are gradually placed) are highlighted.

When the buttresses are embedded from their outer side (Figure 6.19(i)) the developed soil pressures push them inwards. This movement is prevented not only by the mobilization of the friction at the arch-buttress surface but by the new geometry as well. The latter factor impends the arch from moving outwards and eventually from flattening. As a consequence, rocking initiates about the pivot point which is formed at the contact point of the arch extrados with the buttress. During phase 5 (Figure 6.19(ii)), the backfill soil levels up to the arch crown leading to the application of soil pressures at the whole structure's perimeter. Comparing with the corresponding deformation mode of the configuration of Figure 6.13, the

upward movement of the arch is apparently smaller but rocking between the voussoirs in the vicinity of the keystone is more intense. Finally, the placement of the overburden soil restores the system to its initial position regarding the buttresses but resulting to larger permanent local dislocations of the upper voussoirs in comparison with previous geometry.

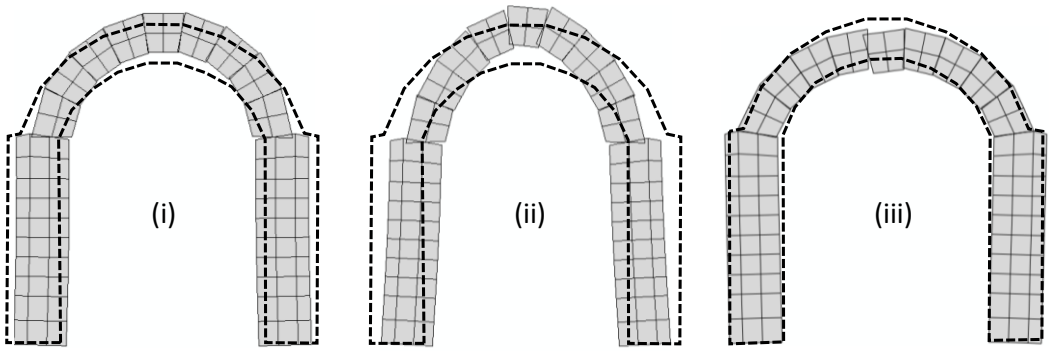

Figure 6.19 Deformation mode with a scale factor of 200% of the structure with the stiffen buttresses calculated for three distinguished loading increments: (i) the buttresses are fully backfilled to the height of h_3 =2.16 m (phase 4), (ii) the backfill arises at the height of the crown, h_4 =3.30 m (phase 5), and (iii) overburden load is placed above the arch, h_5 =5 m from the foundation base (phase 6).

6.6 Seismic Response

The seismic response of embedded structures is a complex soil-structure interaction problem. Structure movements and dynamic earth pressures depend on the response of the soil underlying the structure, the response of the backfill, the inertial and flexural responses of the buttresses, and the nature of the input motions.

The vaulted structure is dynamically excited using a variety of records as base excitations. Specifically, the soil base is horizontally shaked by a set of both idealised mathematical pulses (Ricker Wavelets) and real earthquake records. The first category comprises one significant pulse, preceded and followed by two smaller pulses. The selected wavelets are characterised by low (0.4 *g*) and strong (1 *g*) intensity and two different periods T_E (see Figure 6.20 (i) ~ (iv)). Concerning the real acceleration time histories, they cover a wide range of frequencies and intensities (Figure 6.20 (v) ~ (vi)).

For example:

(1) a medium intensity record as that of the 2003 Lefkada M_s 6.4 earthquake: peak ground acceleration (PGA) = 0.42 *g*, dominant period-range T_p = 0.2-0.65 *sec* (Gazetas et al 2005).

(2) very strong accelograms such as the Japan Mountaineering Association (JMA) record of the 1995 M_w = 7.2 Kobe earthquake: PGA=0.82 *g*, T_p=0.25-1 *sec*, and the Rinaldi-228˚ record of the 1994 M_w = 6.8 Northridge California earthquake: PGA=0.84 *g*.

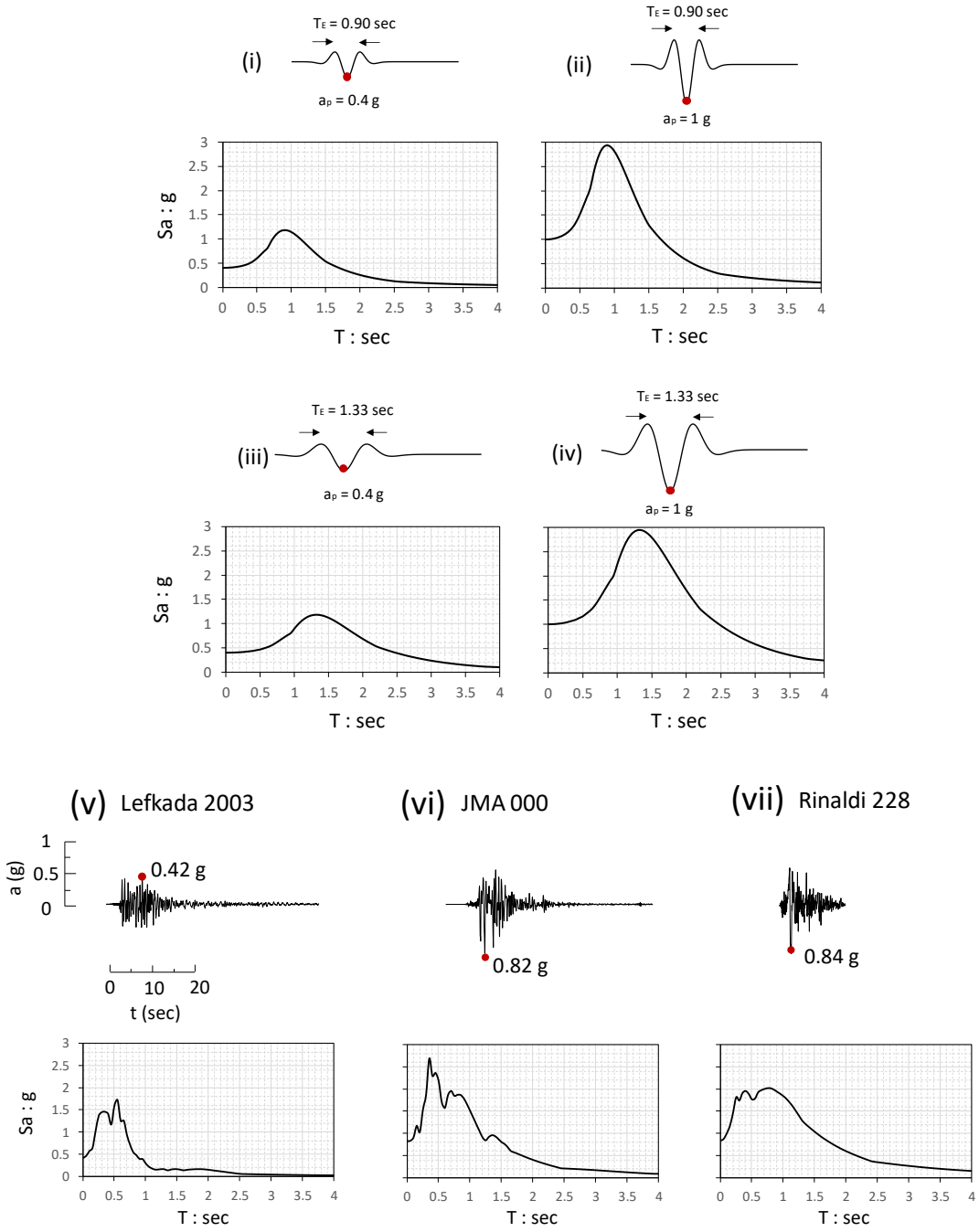

Figure 6.20 Ricker pulses (i), (ii), (iii), (iv) and three different real earthquake records (v), (vi), (vii) utilised to trigger the soil base of the embedded vaulted structure. The acceleration spectra are also depicted.

Initially, the role of soil amplification will be examined. In this context, the acceleration distributions developed to three different selected sections, the one at the centreline of excavation (x=0 m), the second behind the excavation (x=0.25 m) and the third at the far field (x=25 m) will be presented in Figure 6.21. The most important observations are:

- Shakings of the same acceleration amplitude a_p give similar acceleration distributions throughout each section.
- In moderate shakings of acceleration amplitude of a_p = 0.4 g, the three distributions of maximum acceleration corresponding to different positions in the soil medium are identical. The explanation for this observation lies on the fact that the soil structure interface follows the shear deformation of the soil strata.
- The increase of the pulse period from T_E = 0.90 sec to 1.33 sec seems to have negligible effect to the acceleration distribution.
- Interestingly, the maximum accelerations, developed above the structure (z =2.8 m to 5 m) at cases (i) & (iii) remain constant whilst at cases (ii) & (iv) are distorted significantly from the distribution "route". The presence of the structure tents to reinforce certain harmonic components of the incident seismic waves. The soil amplification phenomenon is observable from the level of the structure foundation to the surface. It is amplitude-dependent and roughly related to pulse frequency.
- The sharp peak of the maximum acceleration at the base is due to the soil plastification.

It can be readily seen from Figure 6.22 that for the case of Lefkada 2003, a low-intense earthquake: (i) the maximum horizontal acceleration at the surface takes values about twice the acceleration of the input motion, (ii) the distributions of the maximum accelerations at the three sections (a-a′, b-b′, c-c′) are identical, (iii) the soil amplification of the seismic motion is apparent from the base to the surface.

For the cases of JMA 000 & Rinaldi 228, which are strong seismic shakings that have produced high peak accelerations (~ 0.80 g), a different behaviour governs the response. In particular, along the sections there exists both amplification and de-

amplification of the input motions. The latter is observed up to the level of the structure foundation whilst from this level to the ground surface the phenomenon is twisted. The amplification is generally larger in the vicinity of the free-field. The effect of boundaries is obvious. The incident wave is trapped within the boundaries undergoing reflections.

Horizontal Earth Pressures

Increasing acceleration levels form weak to strong intensity amplitudes have been implemented in the analysis (PGA: 0.2 g ~ 1 g). For each loading case the maximum and minimum dynamic earth pressures at the backfill-buttress interface are calculated. For Ricker pulses of period T_E = 0.90, 1.33 *sec* (Figure 6.23 & 6.24), intense soil reactions are observed at the arch-buttress interface, suggesting the crucial demand of the arch to flatten.

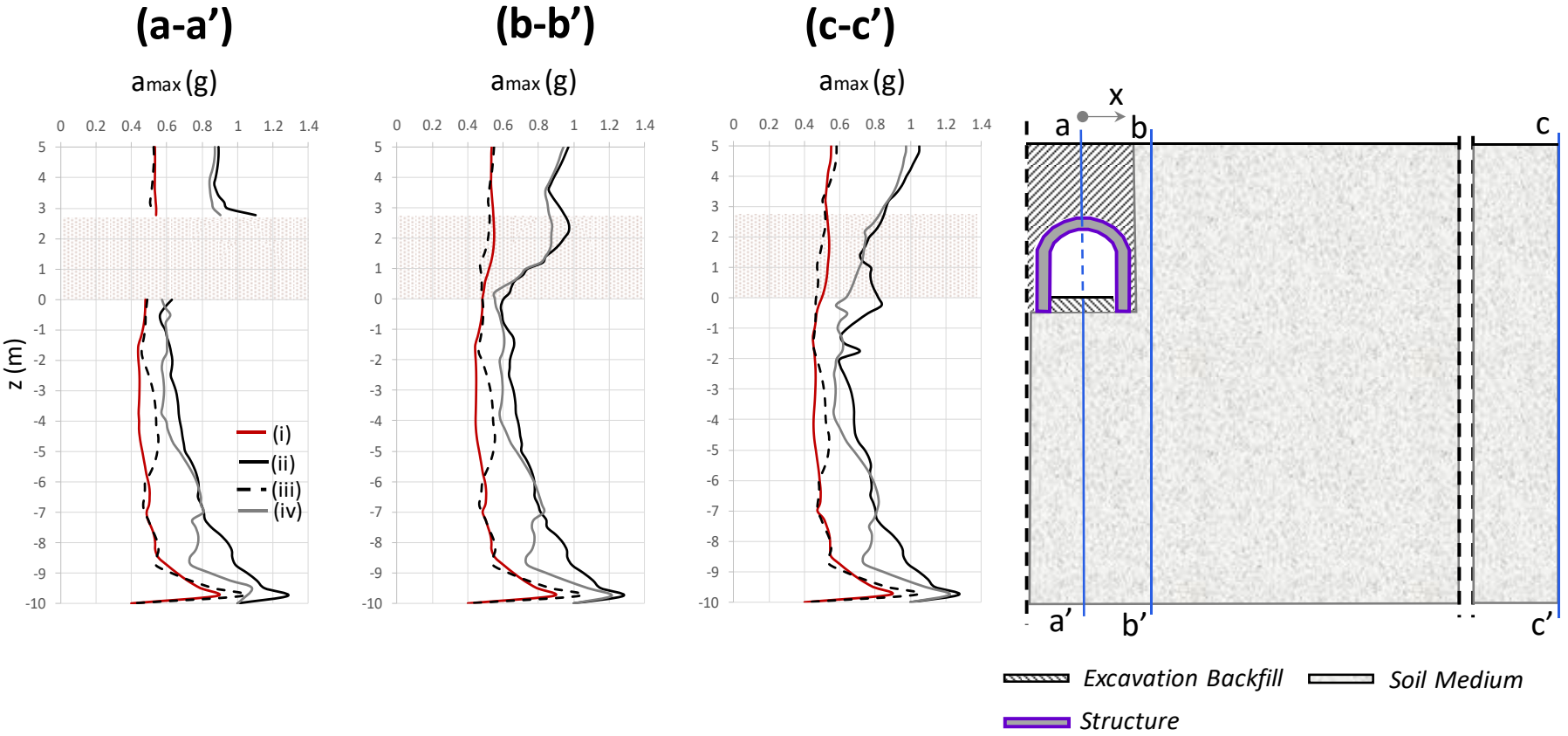

Figure 6.21 Lines a, b and c show the position of three selected sections on the soil stratum where acceleration distributions will be developed: (a) centreline of excavation (x = 0 m), (b) behind the excavation (x = 0.25 m), (c) far-field (x = 25 m)Distribution of maximum horizontal acceleration along sections a, b and c (position of each section is shown in Fig.6.18) when the bedrock level is triggered with Ricker pulses: (a_1) a_p = 0.4 g & T_E = 0.90 sec, (a_2) a_p =1 g & T_E = 0.90 sec, (b_1) a_p = 0.4 g & T_E = 1.33 sec and (b_2) a_p =1 g & T_E = 1.33 sec.

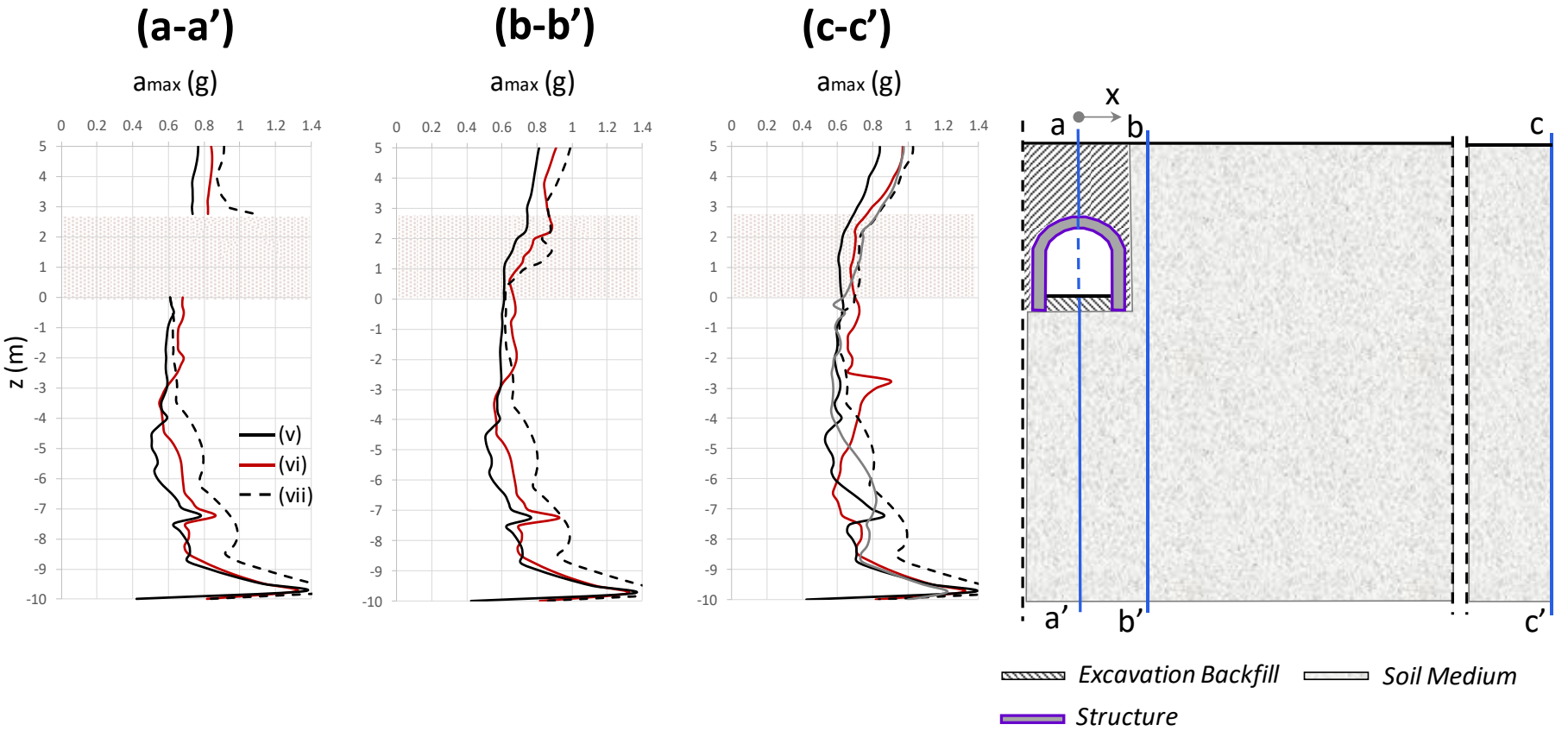

Figure 6.22 Distribution of maximum horizontal acceleration along sections a, b and c when the bedrock level is triggered with three different real earthquake records. The selected ensemble of these three records range from medium intensity (Lefkada 2003) to very strong accelerograms characterized by forward-rupture directivity effects, large number of significant cycles (Rinaldi 228 & JMA 000).

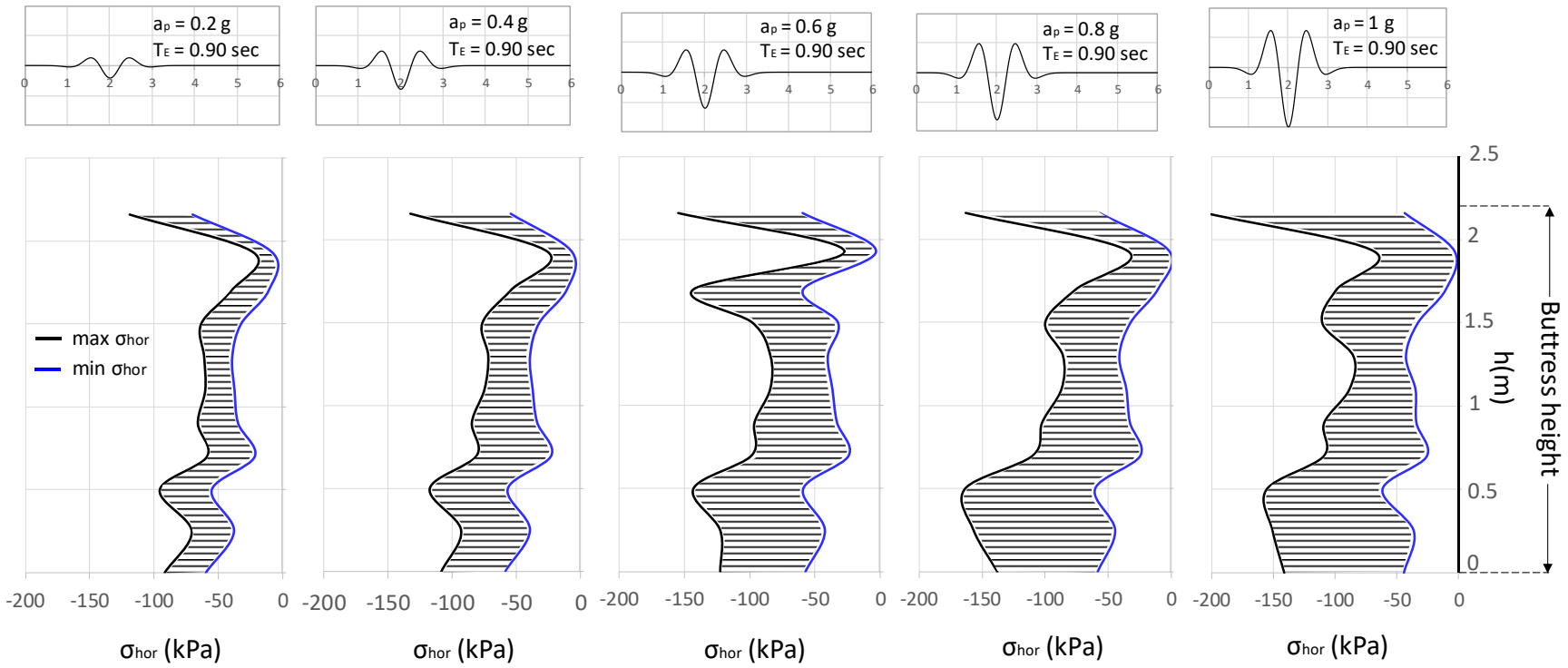

Figure 6.23 Illustration of the maximum & minimum dynamic earth pressures at the backfill-buttress interface when the base is subjected to Ricker wavelets of fixed duration T_E = 0.90 sec and increasing acceleration amplitude from a_p = 0.2 *g* to 1 *g*.

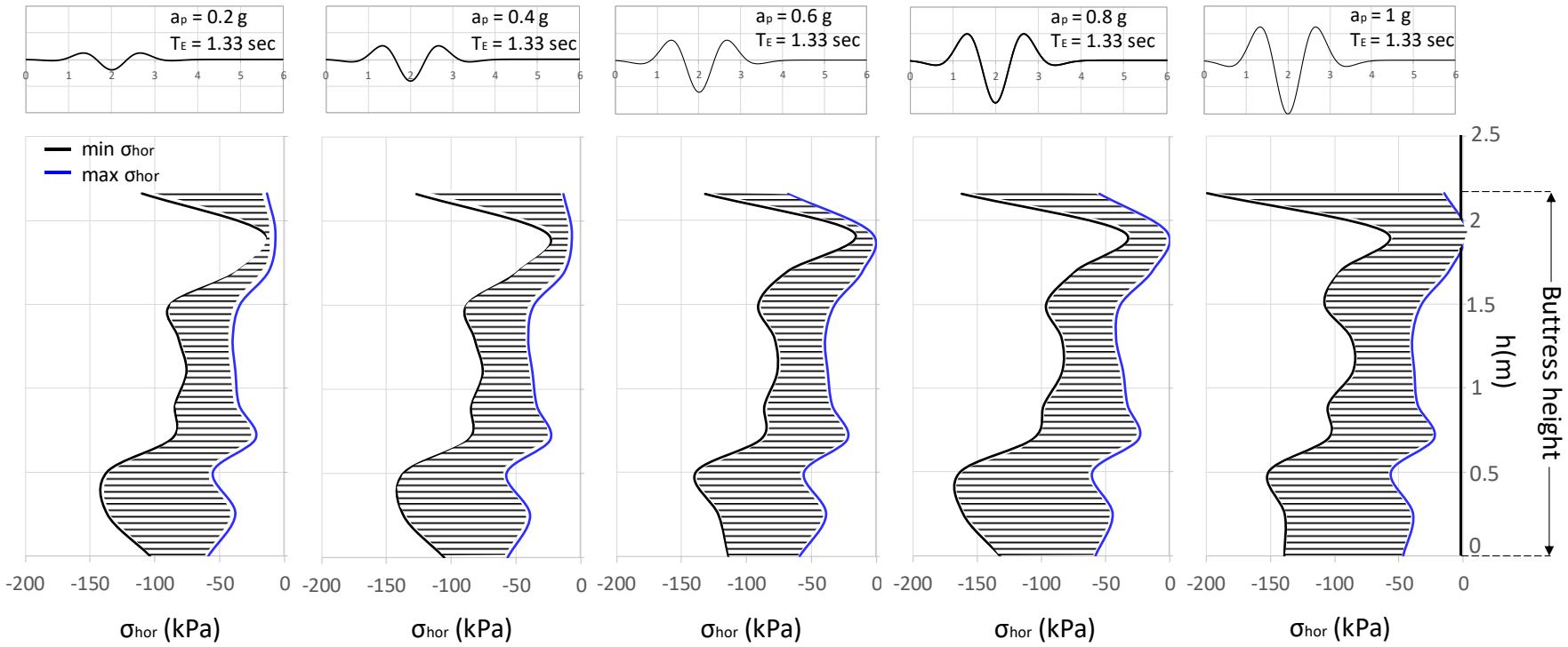

Figure 6.24 Illustration of the maximum & minimum dynamic earth pressures at the backfill-buttress interface when the base is subjected to Ricker wavelets of fixed duration T_E = 1.33 sec and increasing acceleration amplitude from a_p = 0.2 *g* to 1 *g*.

Next, the relieving role of the backfill to the surrounding soil is examined. The evolution of the lateral stresses that develop along the left excavation boundary when Ricker wavelets of three different durations (T_E = 0.6 sec, 0.90 sec & 1.33 sec) are applied at the base is calculated. For each duration the structure is subjected to a wide range of acceleration amplitudes a_p from very low values (0.2 *g*) to moderate (0.4 *g*, 0.6 *g*) and to very strong (1 *g*). The distribution of the lateral stresses under static condition is used as a yardstick for the comprehension of the effect of the pulse characteristics (a_p, T_E). In the view of the calculated results obtained from the numerical analyses, depicted in Figure 6.25 it is clear that:

- the predominant period of Ricker pulses doesn't seem to affect the horizontal earth pressures that develop beyond the backfill soil.
- The earth pressure distribution at the level of the overburden soil (*h*=2.8 m -5 m) is linear regardless the pulse characteristics (a_p, T_E).
- The arch mechanism influences the surrounding soil increasing the pressures locally at *h* = 1.66 m.
- There is a notable increase in the lateral earth pressures when larger acceleration amplitudes are applied.
- The shape of the distribution is similar and irrespective of the prescribed seismic input motion and consequently from the pulse characteristics. They have a minor role on the modulation of the distribution shape which is determined by the static response.

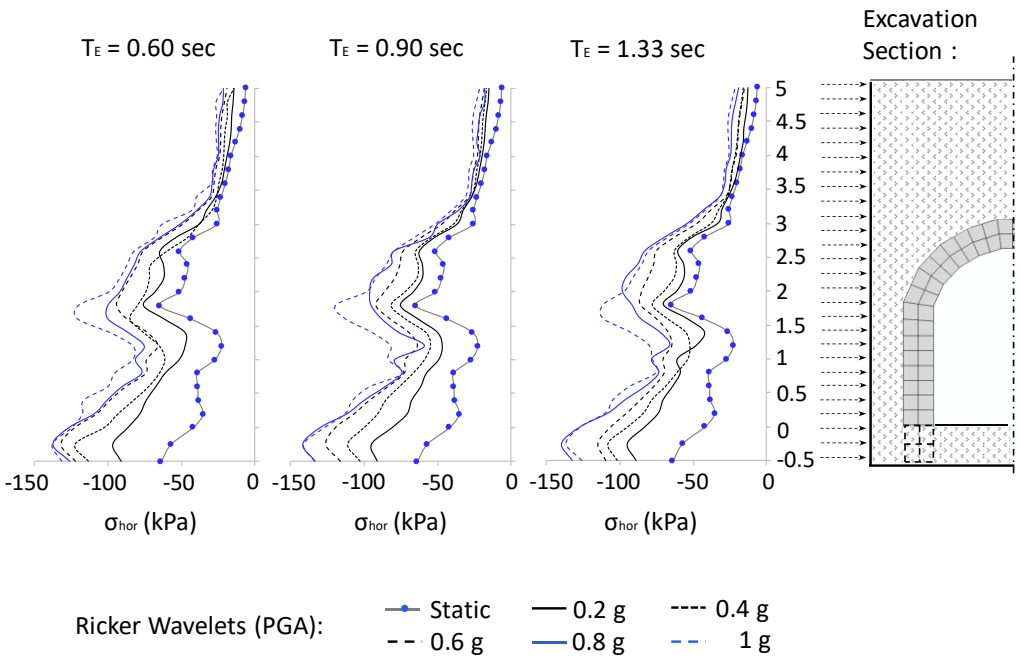

Figure 6.25 Evolution of the lateral stresses that develop along the left excavation boundary when Ricker wavelets of three different durations (T_E = 0.6 sec, 0.90 sec & 1.33 sec) are applied at the base. For each duration the structure is subjected to a wide range of acceleration amplitudes a_p from very low values (0.2 *g*) to moderate (0.4 *g*, 0.6 *g*) and to very strong (1 *g*). Distribution of the lateral stresses under static condition is also depicted.

Inspection of the maximum and minimum principal stresses (Figure 6.26) helps to visualise the most vulnerable locations of the structure when a cluster of idealised Ricker pulses of different intensity trigger the model.

1-D kinematic analysis

Considering the nonlinear behaviour of the model, the fundamental eigen period of the soil column is calculated T_E = 0.30 sec. Therefore, a Ricker pulse with the above predominant period is chosen as seismic excitation. In Figure 6.27 the results of the 1-D analysis are presented in the following way: at the left side, the shear wave velocity and the maximum acceleration distribution at the excavation section, in the middle bottom the input motion while above the resulting ground surface motion, and at the right side of the figure the acceleration response spectrum of the base and the surface. The Peak Ground Acceleration (PGA) is 0.68 *g* which corresponds to a maximum *SA* =

2.11 *g* for eigen value period T_E =0.30 sec. The ground amplification at that point is A = 2.1.

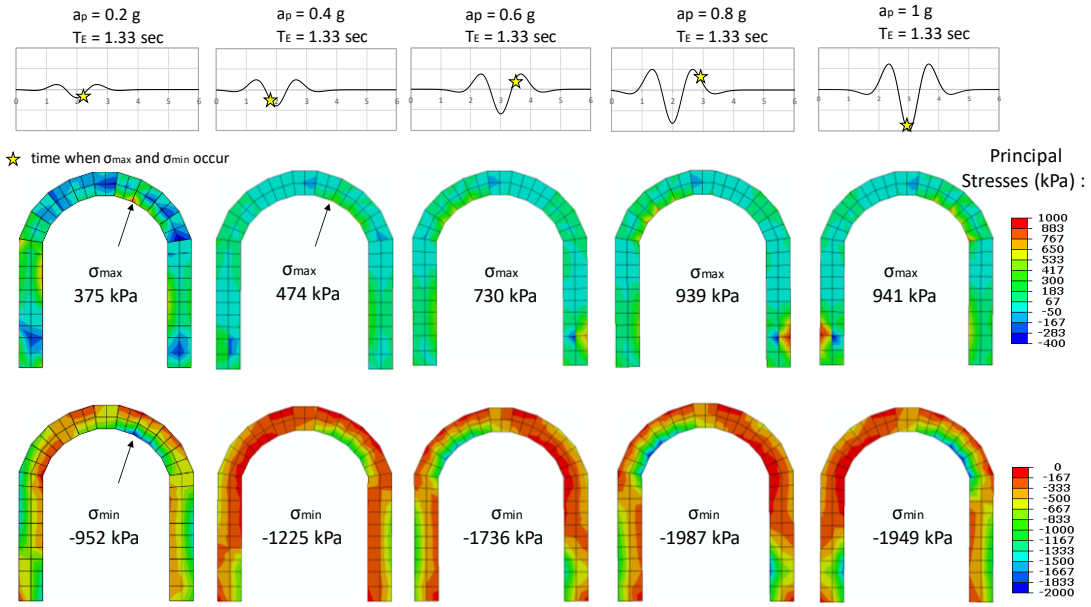

Figure 6.26 Structural distress when the embedded vaulted structure is subjected to a Ricker wavelet of duration T_E = 1.33 sec. For each acceleration amplitude a_p (0.2 *g*-1 *g*) contours of the maximum and minimum principal stresses are presented.

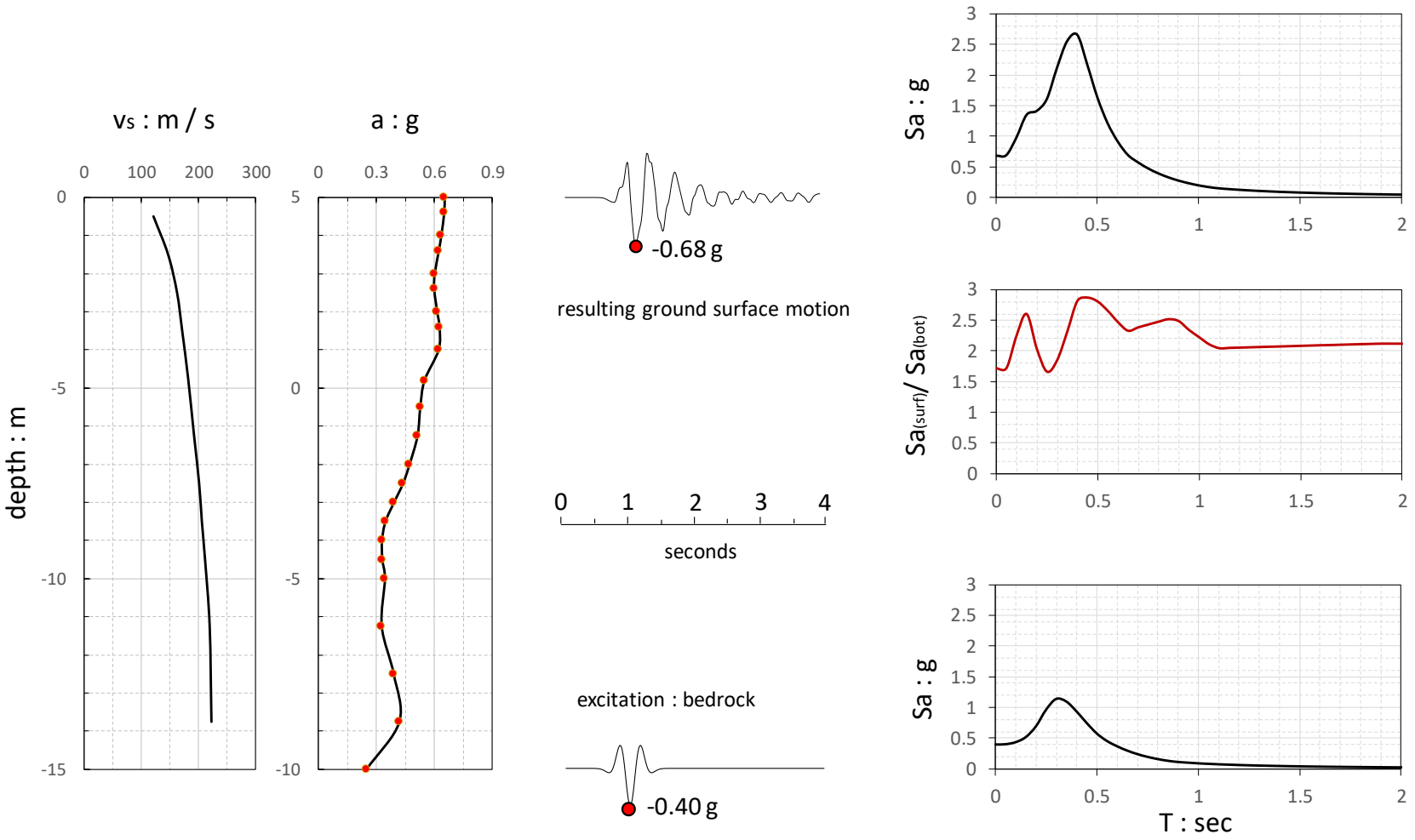

Figure 6.27 1-D kinematic analysis at the excavation section.

6.7 Conclusions

This chapter presents the overall response of an embedded vaulted tunnel into a stiff clay soil under vertical and lateral loading with the aim of identifying the developed physical and structural mechanisms affecting the static and seismic capacity of the structure. The pivot points of this chapter are:

(1) The assembly of an advanced finite-element model of the aforementioned structure

(2) The step-by-step analysis of the construction sequence which allows a spherical observation of the soil-structure interaction

(3) The two arching mechanisms developed to receive the applied loads by the structural arch and the soil arching

(4) The contribution of the backfill soil as a cushion mechanism for the embedded structure

(5) the accumulation of permanent displacements as well as at the maximum soil reactions that can develop in the structural elements.

(6) The crucial role of the structure geometry studying and analysing a vaulted structure with slightly enlarged buttresses

(7) The seismic response of this category of structures (embedded arched structures) and their vulnerability to a variety of ground motions.

Regarding (**1**), an advanced finite-element modeling of the soil-structure system is developed, incorporating the construction sequence. Special attention has been given choosing the appropriate boundary conditions, the interface and the soil material modelling.

Regarding (**2**), when observing the structure's response during the construction sequence the following can be extracted:

- The prevailing initial conditions at the excavated trench are passive at the bottom whilst active at the surface.

- As the backfill height gradually increases, two different conditions of the earth pressures are established behind the structure: An active state behind the buttress accompanied with a passive state behind the arch.

- The deformed configurations of the structure enclose the ongoing developed structural mechanism of a vaulted tunnel through the whole procedure of its embankment.

Regarding (**3**), A fictitious arch is developed within soil medium to carry the overburden load, along with the structural arch. According to this 'soil arching' mechanism, stress paths are diverted within soil medium around the embedded vault. The remaining part of the overburden load is sustained by the structural arch and transferred to the buttresses with a combined shear and vertical load. This severe shear force developed at the bottom of the arch is demonstrated as concentration of contact pressures in the profile of Figure 6.11e.

Regarding (**4**), backfill soil contributes as a cushion mechanism for the embedded structure: (i) it offers the horizontal reaction at the arch base to prevent arch from flattening upon the overburden load, (ii) by virtue of two-dimensional redundancy it receives directly a portion of the overburden load (soil arching).

Regarding (**5**), arches on enlarged buttresses are more safe and stiff structures. The applied loads aren't distributed in a vertical direction but they are obliquely directed outwards. This outward thrust is safely transferred downwards along the additional part. Evidently, part of the horizontal force needed to support the arch is now received by the buttresses as shear mechanism. In addition, the stiffen buttress offers enhanced capacity under moment loading due to the arch tendency to flatten.

Finally, regarding (**6**), the seismic response of such structures and their vulnerability to a variety of ground motions is investigated. In this perspective, idealised Ricker pulses are imposed to the base as input motion and the influence of their characteristics (a_p, T) are highlighted. For different periods T_E, different structural mechanisms are mobilised resulting in excessive horizontal earth reactions at different positions. At the

excavation interface the earth pressures development is rather irrelevant to the pulse period, it depends yet on the pulse amplitude.

CHAPTER 7:

Conclusions

7.1 Main Findings

As stated in the introduction the scope of this Thesis was to study the stability, the seismic response and the soil-structure interaction of masonry arches structures. The aim was to contribute to the better understanding of a 300-year old problem which in some way it is not yet fully investigated.

Some of the key conclusions of the Thesis are as follows:

The study revisits the dynamic behaviour of a **part-circular masonry arch** subjected to ground motion, as introduced by Oppenheim in 1992. The examined model, under horizontal acceleration applied at its base, is transformed into predefined rigid body assemblies. In such stiff structures, rocking rotation even in low-amplitude levels is most often undesirable as it may lead to severe permanent displacements accompanied with possible dislocation of the arch axis, and sometimes to general instability of the structure. It is therefore of great importance to develop simplified procedures for estimating the levels of the low-amplitude response. In this context, simplified analytical techniques are applied to calculate the linear response. These methods comprise both closed-form solutions and numerical integration of the equation of motion. Applicability of linearised response is evaluated mainly through comparison with rigorous 2-dimensional finite element analysis. Near-source earthquake shaking is represented with idealised cycloidal and rectangular pulses. In addition, constant acceleration pulses are involved.

- A general solution of the resulting linear equation of motion, extracted with the Lagrangian method, suitable for any arch geometry is presented. The impact of the gravitational and the external forces to the system, represented by the coefficients, F(φ) and P(φ) respectively, is also discussed. Then, a first application of this general

solution is given through the examination of constant acceleration pulses. Simplified forms of the rotation θ_{AB} (Lagrangian variable) with respect to time are presented.

- One-sine pulses are also introduced to represent ground excitation. In this respect, a linear second-order homogeneous differential equation of motion is derived, similar to Mathieu equation. According to superposition principle, each solution of the Mathieu equation is a linear combination of two independent solutions, thus allowing for a closed-form solution to be obtained. In parallel, numerical integration of the equation of motion is involved to compute the response. A parametric comparative study is presented for different values of the peak ground acceleration and excitation period. Nonlinear finite element analysis in the time domain is also employed to further strengthen the comparison. The results reveal a close agreement between these methods and justify the applicability of the linear simplification of the response. The benefit of the Mathieu equation to easily derive reliable results in large amounts is applied to the study of the overturning response of the arch. The parametric study reveals that overturning of the arch according to the minimum overturning acceleration spectrum, is more sensitive to high values of a_p and low values of T_p. Another interesting finding is that overturning and imminent collapse occur without impact.
- Rectangular asymmetric pulses are also involved in the study of the earthquake response. The type of the pulse and the values chosen are those used by Oppenheim so that a comparative study is possible. The results indicate convergence between linear analytical and nonlinear finite element methods. The reliability of these results is further strengthened by the comparison with Oppenheim's results for rectangular pulses.

An arch ring of non-uniform thickness subjected to rocking is employed next. This so-called ***'part-elliptical'*** arch is described with an elliptical (upper) and a circular (lower) curve, and is frequently encountered in long-span masonry bridges. The response of such a structure in comparison with the uniform circular arch is investigated.

- Based on the existing method of a variational formulation in literature (Alexakis & Makris, 2014), in the beginning their study calculates the hinge locations of a

continuous monolithic circular arch when subjected to a given level of acceleration $\ddot{x}_g$. What is new in this study is that the locations of the imminent hinges are calculated analytically through closed-form solutions. The results are in excellent agreement with those derived from the semi-analytical approach of previous study (Alexakis & Makris, 2014).

- Regarding the part-elliptical arch, (i) stability analysis and (ii) dynamic response analysis are engaged. Stability analysis involves both variational and Lagrangian formulation. In the context of a demand assessment, namely for a given slenderness, it is found that systematically higher acceleration levels are required to set a part-elliptical arch on rocking compared to those required for a circular one. This implies that an arch with increasing thickness from the key to the springers (as described with λ) performs enhanced resistance to hinge formation and rocking when subjected to ground horizontal excitation. Therefore, it has reasonably been adopted in the past as an improved profile in terms of seismic performance, for long-span masonry bridges. Moreover, when comparing two arches of the same slenderness t / R but of different angles of embrace β it is concluded that the one of larger β becomes a four-hinge mechanism for a higher horizontal acceleration εg.
- Dynamic response analysis is performed in the time domain through analytical and numerical methods. In the former, time-histories of the rocking response are computed from the analytical solution of the Lagrangian equation of motion. Idealised pulses are used as base excitation to represent conditions of near-source ground shaking. Once rocking occurs it turns out that the non-uniform profile impacts the response but not in a straightforward fashion. Evidently, the response is very sensitive to the excitation period unveiling the profoundly non-linear nature of the problem.
- Apart from the analytical treatment, two-dimensional numerical analysis with finite elements is performed. The results are presented comparatively with those of the analytical method for long-duration pulses. Both methods provide time-histories of the dynamic response which in general lines are in remarkable agreement. This is very important taking into account the essentially different assumptions adopted in two approaches: The analytical method considers a rigid, monolithic arch of zero tensile strength in which sliding at the joints is prevented. On the contrary, the numerical

model implies a stiff but not ideally rigid structure with a predefined hinge mechanism, where interfaces are reasonably rough allowing theoretically sliding.

The monolithic circular buttressed arch under seismic action is examined. Among the three possible failure mechanisms, the so-called Mechanism II (or mixed or semi-global) is studied. This mechanism is associated with the formation of three hinges in the arch and one hinge at the corner of the buttress. It develops under specific geometries and particularly when thick arches are supported by slender buttresses.

- A variational formulation utilising the principle of stationary potential energy as proposed by Alexakis & Makris (2014, 2017, 2018) is revisited for the four different buttress geometries. Some of the main conclusions are:

1. Increasing the buttress width ensures stability as it requires higher values of acceleration to transform the structure into a mechanism. For example, a 50% increase of the width leads to 50% higher values of critical accelerations. Generally, when the slenderness s increases, either by increasing the buttress width or by decreasing the height, the structure becomes more unstable as it entails lower values of acceleration to impose rocking.
2. Smaller values of embrace β have a favourable effect to the stability.
3. The case of a relative stocky buttress (b / R =0.75, H / R = 1) is a limit state where for larger buttresses the arch becomes relatively vulnerable and under a critical acceleration another mechanism is mobilised where all four ruptures occur at the arch.
4. Concerning the buttresses, Housner's finding (1963) is confirmed. According to that, between two equally slender structures but different in size the larger one is the more stable.
5. An important observation from Figure 5.7 where the locations of the imminent hinges are depicted, concerns the angles φ_i (i=1, 2, 3). It is found that they satisfy the relation $\varphi_1 + \varphi_3 = 2\varphi_2$ as it is described by equation (5.10). Expressing the angles φ as functions of the angles of each link (θ_i) (see equation 5.11), it leads to the critical mechanism that yields the minimum ground acceleration. This configuration consists of two equal links (with the same angle θ_i) and one larger and resembles the one that Oppenheim (1992) has considered as a *representative arch* in his study.

➢ A time history analysis at the buttressed arches consisting of individual voussoirs (with predefined hinge locations) is conducted. The nonlinear rocking behaviour of 3d buttressed arch models is highlighted with the aid of the explicit algorithm available in the FE code Abaqus. The seismic excitation is introduced in the horizontal direction along the base of the soil layer with trigonometric pulses of one cycle and Ricker wavelets. The sensitivity of the 3d model to the pulse characteristics is depicted in the overturning spectra of Figures 5.11, 5.12, 5.14 & 5.15. It is concluded that:

1. The structural system exhibits a significant resistance to low duration pulses. In this way, a Ricker wavelet of period T_E = 0.2 sec (case A) is practically impossible to overturn the illustrated buttressed arch (a_p = 3 g!!).
2. The dominant failure mechanism is Mechanism II (or semi-global)
3. The long duration Ricker wavelets have a detrimental effect on the stability of the buttressed arch. Specifically, for sufficiently large periods (T_E > 0.9 sec) the minimum acceleration gradually approaches very close to the pseudo-static value.
4. The one-sine pulse is the most detrimental in comparison with the Ricker wavelet, especially for low duration pulses. For moderate and long period pulses the effect of the type of motion is minimal. The beneficial effect of the Ricker pulses with respect to the one-sine pulses is attributed merely to the favorable asymmetry which offers an additional "safety net".
5. From the comparison of the different buttress geometries (Figure 5.10 & 5.12) it is inferred that even a small increase in the buttress width offers stability to the structure regardless the impulse type.

This chapter presents the overall response of an **embedded vaulted tunnel** into a stiff clay soil under vertical and lateral loading with the aim of identifying the developed physical and structural mechanisms affecting the static and seismic capacity of the structure. The pivot points of this chapter are:

(1) The assembly of an advanced finite-element model of the aforementioned structure.

(2) The step-by-step analysis of the construction sequence which allows a spherical observation of the soil-structure interaction.

(3) The two arching mechanisms developed to receive the applied loads by the structural arch and the soil arching.

(4) The contribution of the backfill soil as a cushion mechanism for the embedded structure.

(5) the accumulation of permanent displacements as well as at the maximum soil reactions that can develop in the structural elements.

(6) The crucial role of the structure geometry studying and analysing a vaulted structure with slightly enlarged buttresses.

(7) The seismic response of this category of structures (embedded arched structures) and their vulnerability to a variety of ground motions.

Regarding (1), an advanced finite-element modeling of the soil-structure system is developed, incorporating the construction sequence. Special attention has been given choosing the appropriate boundary conditions, the interface and the soil material modelling.

Regarding (2), when observing the structure's response during the construction sequence the following can be extracted:

- The prevailing initial conditions at the excavated trench are passive at the bottom whilst active at the surface.
- As the backfill height gradually increases, two different conditions of the earth pressures are established behind the structure: An active state behind the buttress accompanied with a passive state behind the arch.

- The deformed configurations of the structure enclose the ongoing developed structural mechanism of a vaulted tunnel through the whole procedure of its embankment.

Regarding (3), A fictitious arch is developed within soil medium to carry the overburden load, along with the structural arch. According to this 'soil arching' mechanism, stress paths are diverted within soil medium around the embedded vault. The remaining part

of the overburden load is sustained by the structural arch and transferred to the buttresses with a combined shear and vertical load. This severe shear force developed at the bottom of the arch is demonstrated as concentration of contact pressures in the profile of Figure 6.11e.

Regarding (4), backfill soil contributes as a cushion mechanism for the embedded structure: (i) it offers the horizontal reaction at the arch base to prevent arch from flattening upon the overburden load, (ii) by virtue of two-dimensional redundancy it receives directly a portion of the overburden load (soil arching).

Regarding (5), arches on enlarged buttresses are more safe and stiff structures. The applied loads aren't distributed in a vertical direction but they are obliquely directed outwards. This outward thrust is safely transferred downwards along the additional part. Evidently, part of the horizontal force needed to support the arch is now received by the buttresses as shear mechanism. In addition, the stiffen buttress offers enhanced capacity under moment loading due to the arch tendency to flatten.

Finally, regarding (6), the seismic response of such structures and their vulnerability to a variety of ground motions is investigated. In this perspective, idealised Ricker pulses are imposed to the base as input motion and the influence of their characteristics (a_p, T) are highlighted. For different periods T_E, different structural mechanisms are mobilised resulting in excessive horizontal earth reactions at different positions. At the excavation interface the earth pressures development is rather irrelevant to the pulse period, it depends yet on the pulse amplitude.

7.2 Epilogue-Recommendations for further research

The development of the current subject is of great interest and many topics could be further investigated.

- Regarding the circular and the part-elliptical arches, the development of the semi-analytical method could expand taking into consideration more complicated geometries, loading and boundary conditions. Regarding the finite element model, the analysis can be extended in a future study to address a monolithic, no-tension arch.

- Regarding the embedded structures, the arching mechanisms, both structural and soil, could be further investigated. Different soil properties for the soil backfill and the soil stratum could lead us to the better understanding of the soil-structure interaction. More advanced soil failure criterion could be applied. Moreover, the material decay should be taken into consideration in the FE analyses.

References

Abaqus (2008). "Theory and analysis user's manual", version 6.8-3. Providence, RI, USA: Dassault Systèmes Simulia Corp.

Alexakis H, Makris N (2013). "Structural stability and bearing capacity analysis of the tunnel-entrance to the stadium of ancient Nemea." *Int. J. Arch. Herit*. 7: 673–692.

Makris, N., and Alexakis, H. (2013). "The effect of stereotomy on the shape of the thrust-line and the minimum thickness of semicircular masonry arches." *Arch.Appl. Mech*, 83: 1511–1533.

Alexakis H., Makris N. (2013). "Minimum thickness of elliptical masonry arches." *Acta Mech* 224: 2977–2991.

Alexakis H, Makris N (2014). "Limit equilibrium analysis and the minimum thickness of circular masonry arches to withstand lateral inertial loading." *Arch Appl Mech*, 84: 757–772

Alexakis, H. and Makris, N (2017). "Hinging mechanisms of Masonry Single-Nave Barrel Vaults subjected to Lateral and Gravity Loads". J*ournal of Structural Engineering, ASCE*, ISSN, 0733–9445

Alexakis, H. and Makris, N (2018). "Minimum Horizontal Acceleration of the Single Nave Barrel Vault and the Rocking Frame." *International Journal of GeoEngineering Case Histories*, Vol.4, Issue 4, p.275

Alexakis, H. and Makris, N (2023). "Vector analysis and the stationary potential energy for assessing equilibrium of curved masonry structures." *Mathematics and Mechanics of solids*. 1-17.

Apostolou M (2011). "Soil–structure interaction under strong seismic moment: Material and geometric nonlinearity." Dissertation, National Technical University of Athens.

Baratta et al (2004). "Strength capacity of a No-Tension portal arch-frame under combined seismic and ash loads." *Journal of Volcanology and Geothermal Research*, v. 133, iss. 1-4 [SPECIAL ISSUE], p. 369-376.

Brandonisio G, Mele E, De Luca A. (2017). "Limit analysis of circular buttressed arches under horizontal loads." *Meccanica*; 52(11–12):2547–65.

Brandonisio G, Angelillo M, De Luca A. (2020). "Seismic capacity of buttressed masonry arches." *Engineering Structures* 215 110661.

Calderini C, Lagomarsino S (2014). "Seismic response of masonry arches reinforced by tie-rods: static tests on a scale model." *J Struct Eng* 141(5)

Cannizzaro F, Pantó B, Caddemi S, Caliò I. (2018). "A Discrete Macro-Element Method (DMEM) for the nonlinear structural assessment of masonry arches.'' *Engng Struct*; 168: 243-256

Cavalagli N, Gusella V, Severini L. (2017). "The safety of masonry arches with uncertain geometry." *Comput Struct*; 188: 17–31.

Clemente P (1998). "Introduction to dynamics of stone arches.'' *Earthq. Eng. Struct. Dyn.* 27: 513–522

Coisson R, Vernizzi G, Yang X (2009). "Mathieu functions and Numerical solutions of the Mathieu equation.'' In: *IEEE Proceedings of the International Workshop on Open Source Software for Scientific Computation*, pp. 3–10.

Coulomb C.A (1821). Theorie des machines simples

Couplet P (1729, 1730). De la poussée des voûtes, Histoire de l'Académie Royale des Sciences, pp. 79–117, 117–141. Académie royale des sciences, Paris

D' Agostino S & Bellomo (2001). M. Ponti in muratura e in calcestruzzo armato. Manuale di ingeneria Civile (Vol. II). Buologne: Zanichelli/ESAC.

De Lorenzis L, DeJong MJ, Ochsendorf (2007). ''Failure of masonry arches under impulse base motion.'' *Earthquake Engineering and Structural Dynamics* 36(14):2119–36.

De Luca et al (2004). ''A simplified procedure for assessing the seismic capacity of masonry arches.''

De Jong M, De Lorenzis L, Adams S, Ochsendorf J (2008). ''Rocking stability of masonry arches in seismic regions.'' *Earthq. Spectra* 24: 847–865

De Santis S, de Felice G. (2014). ''A fibre-based approach for the evaluation of the seismic capacity of masonry arches.'' *Earth Engng Struct Dyn*; 43: 1661-1681.

Dimitrakopoulos E, DeJong M. (2013). **"**Seismic overturning of rocking structures with external viscous dampers." *Comp Methods Earth Engng*; 30: 243–258.

Dimitri R, Tornabene F. (2015). "A parametric investigation of the seismic capacity from masonry arches and portals of different shapes." *Engng Failure Analysis*; 52: 1-34

Di Carlo F, Coccia S, Rinaldi Z. (2018). "Collapse load of a masonry arch after actual displacements of the supports." *Arch Appl Mech*; 88:1545–1558.

da Porto F, Tecchio G, Zampieri P, Modena C, Prota A. (2016). ''Simplified seismic assessment of railway masonry arch bridges by limit analysis.'' Struct Infrstruct Engng; 12:5, 567-591

Gaetani A, Lourenco P, Monti G, Moroni M. (2017). "Shaking table tests and numerical analyses on a scaled dry-joint arch undergoing windowed sine pulses." B Earth Engng; 15: 4939-4961.

Gerolymos N, Gazetas G, Tazoh T. (2005). "Static and Dynamic Response of Yielding Pile in Nonlinear soil." *Proceedings, 1st Greece-Japan Workshop: Seismic Design, Observation and Retrofit of Foundations*, Athens 2005

Gregory, D (1697). Catenaria. Phil.Trans, 19(231): 637-652

Heyman J (1966). The stone skeleton. International Journal of Solids and Structures 2: 249–279.

Heyman J (1969). "The safety of masonry arches." *Int. J. Mech. Sci*. 11: 363–385

Heyman J (1982). The Masonry Arch. Ellis Horwood, Chichester

Housner G. W (1963). "The behaviour of inverted pendulum structures during earthquakes." *Bull. Seismol. Soc. Amer*. 53: No. 2, 403-417.

Huerta S (2001) Mechanics of masonry vaults: the equilibrium approach. In: Historical Constructions. University of Minho, Guimaraes, pp 47–69

Hooke, R (1676). "A description of helioscopes and some other instruments." London: T.R for John Martyn

Ishibashi, I., and Zhang, X. (1993). "Unified dynamic shear moduli and damping ratios of sand and clay." *Soils Found*., 33(1), 18

Krarnovsky I.A (2011). "Theory of arched structures."

Kollár L, Ther T. (2019). "Numerical model and dynamic analysis of multi degree of freedom masonry arches." *Earth Engng Struct Dyn*; 48(7): 709-730.

Kooharian, A (1952). "Limit analysis of voussoir (segmental) and concrete arches." *Journal of the American Concrete Institure*, 24(4), 317-328.

Langer R (1934). "The solutions of the Mathieu equation with a complex variable and at least one parameter large." *Trans. Am. Math. Soc*. 36 (3): 637-695

La Hire, P. de (1695). "Traite de mecaniqueo: ou l on explique tout ce qui est necessaires dans la pratique the arts & les proprieties des corps pesants lesquelles ont un plus grand usage dans la physique." Paris: de l 'imprimerie Royale et se vend chez Jean Anisson

Lemaitre, J., and Chaboche, J. (1990). Mechanics of solid materials, Cambridge Univ. Press, Cambridge, UK

Leontari A, Apostolou M. (2018). "Linearised response of arched structures under pulse-type excitation." *Arch Appl Mech*; 88(7): 1121- 1137.

Leontari A, Apostolou M. (2021). "Stability and Rocking response of non-uniform masonry arches. The 'part-elliptical profile'." *Engineering Structures*, Volume 228, 11519

Makris N and Roussos Y (1998). "Rocking response and overturning of equipment under horizontal pulse-type motions" Rep. No. PEER- 98/05, *Pacific Earthquake Engrg. Res. Ctr*., University of California, Berkeley, Calif.

Makris, N., and Alexakis, H. (2015). "Limit equilibrium analysis of masonry buttresses and towers under lateral and gravity loads." Arch.Appl. Mech., 85(12), 1915–1940.

Marino M, Neri F., De Maria A, Antonio B. (2014). "Experimental data of friction coefficient for some types of masonry and its correlation with an index of quality masonry (Iqm)." 2nd European Conference on Earth Engng & Seism, Istanbul

Marcolongo, R (1937). Studi Vinciani, Memorie sulla geometria e la meccanica di Leonardo da Vinci. Napoli: S.I.E.M-Stabilimento Industrie Editoriali Meridionali

Milankovitch M. Beitrag (1904). zur theorie der druckkurven. Dissertation zur erlangung der Doktorwürde, K.K. Technische Hochschule. Vienna

Moseley, H (1843) "The mechanical principles of engineering and architecture." London Longman, Brown, Green and Longmans

Oppenheim I. J (1992) "The masonry arch as a four-link mechanism under base motion." *Earthquake Engineering and Structural Dynamics* 21: 1005–1017.

Oppenheim I. J (1996) "Earthquake analysis of masonry structures." *11th World Conference on Earthquake Engineering*, paper No. 543.

Ochsendorf J. Collapse of masonry structures PhD thesis (2002). Department of Engineering, University of Cambridge, Cambridge.

Ochsendorf (2004) "Collapse of masonry buttresses" J. Archit. Eng., 10(3), 88-97

Pulatsu B, Erdogmus E., Lourenco P. (2019). "Comparison of in-plane and out-of-plane failure modes of masonry arch bridges using discontinuum analysis." *Engng Struct*; 178: 24-36

Reccia E, Milani G, Checci A, Tralli A. (2014). "Full 3D homogenization approach to investigate the behavior of masonry arch bridges: The Venice trans-lagoon railway bridge." *Constr Build Mat*; 66: 567-586

Sawamura, Y., Ishihara, H., Otani, Y., Kishida, K., Kimura, M., (2019). "Deformation behavior and acting earth pressure of three-hinge precast arch culvert in construction process." *Underground Space*, vol. 4(3), pp. 251–260

Sandor G. N, Erdman A.G (1934). Advanced Mechanism Design: Analysis and Synthesis, Volume 2, 1984

Sarhosis V, De Santis S, de Felice G. (2016). "A review of experimental investigations and assessment methods for masonry arch bridges." *Struct Infr Engng*; 12(11): 1439-1464

Sarhosis V, Forgács T, Caddemi S, Lemos J. (2019). "A discrete approach for modelling backfill material in masonry arch bridges." *Comp Struct*; 224: 106108

Stockdale G, Milani G. (2019). **'**Diagram based assessment strategy for first-order analysis of masonry arches." *J Build Engng*; 22: 122–129.

Stockdale G, Sarhosis V., Milani G. (2020). "Seismic capacity and multi‐mechanism analysis for dry‐stack masonry arches subjected to hinge control." *Bull Earthq Engng*; 18: 673-724

Tasios T. (2010). "Seismic engineering of monuments, The first Prof. Nicholas Ambraseys distinguished lecture." *Bull Earthquake Eng*. 8:1231–1265

Tempesta G, Galassi S. (2019). "Safety evaluation of masonry arches. A numerical procedure based on the thrust line closest to the geometrical axis." *Int J Mech Sc*; 155: 206–221

Vucetic, M., and Dobry, R. (1991). "Effect of soil plasticity on cyclic response." *J. Geotech. Eng*., 117(1), 89–107

Zampieri P, Simoncello N, Pellegrino C. (2019). "Seismic capacity of masonry arches with irregular abutments and arch thickness." *Const Build Mat*; 201: 786-806

Ziegler, H. (1959). "A modification of Prager's hardening rule." *Quart.Appl. Math*., 17, 55–65.

Zhang J, Makris N (2001). "Rocking response of free-standing blocks under cycloidal pulses." *Journal of Engineering Mechanics*, ASCE 127(5): 473–483.

APPENDICES

Appendix A (Chapter 3)

A.1 Segment AB of the circular arch transformed into a four-link mechanism

For this single-degree-of-freedom system, the angle $\theta = \theta_{AB} = \theta_0$ is chosen arbitrarily and without violating the constraint, as the Lagrangian independent variable (coordinate). The arch segment under examination is portrayed in Figure A1.

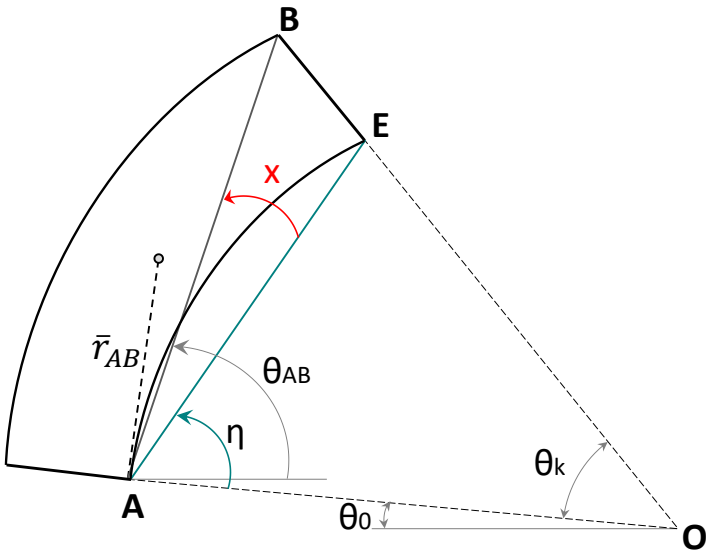

Figure A1 Geometric parameters of the arch segment AB under examination.

The relationships amongst the remaining angles will be defined with the aid of trigonometric identities. Firstly, the relationship between the angle *x* and the angle of the segment *AB* will be calculated. If the internal radius *a=OA* and the external one *b=OB*, from triangles and the law of sines in the triangle *OAB,* the following equation results:

$$\frac{\sin\theta_k}{AB} = \frac{\sin(\eta + x)}{OB} \tag{A.1}$$

In the triangle *AEB* the angle $\widehat{\mathrm{AEB}}$ is equal to $\pi - \eta$. From the law of sines it yields:

$$\frac{\sin(\pi - \eta)}{AB} = \frac{\sin(x)}{BE} \tag{A.2}$$

From the ratio of equations (A.1) and (A.2) the following equation is obtained:

$$\frac{\sin\theta_k}{\sin(\pi - \eta)} = \frac{BE}{OB}\,\frac{\sin(\eta + x)}{\sin(x)} = \frac{b - a}{b}\,\frac{\sin(\eta + x)}{\sin(x)} \tag{A.3}$$

Considering that:

$$\theta_k + 2\eta = \pi \rightarrow \theta_k = \pi - 2\eta \tag{A.4}$$

$$\sin\theta_k = \sin(\pi - 2\eta) = \sin(2\eta)\ \&\ \sin(\pi - \eta) = \sin(\eta) \tag{A.5}$$

The Eq. (A.3) becomes:

$$\frac{\sin(2\eta)}{\sin(\eta)} = \frac{b - a}{b}\,\frac{\sin(\eta + x)}{\sin(x)} \tag{A.6}$$

Expanding the numerators Eq. (A.6) is transformed to:

$$\frac{2\sin(\eta)\cos(\eta)}{\sin(\eta)} = \frac{b-a}{b}\,\frac{\sin(\eta)\cos(x)+\cos(\eta)\sin(x)}{\sin(x)} \tag{A.7}$$

Rearranging Eq. (A.7), it yields:

$$2\cos(\eta)\sin(x) = \frac{b-a}{b}\,\{\sin(\eta)\cos(x)+\cos(\eta)\sin(x)\} \tag{A.8}$$

The final expression is:

$$\tan x = \frac{b-a}{b+a}\tan\eta \tag{A.9}$$

Dividing the semicircle into *N* segments, the arch will consist of *N-1* segments. The angle of embrace in terms of *N* is expressed as:

$$\frac{(N-1)\pi}{N} \tag{A.10}$$

while the angle made with the horizontal line θ_0 is expressed as $\frac{\pi}{2N}$.

Therefore, the angle of embrace of the first segment is $\theta_k = \frac{k\pi}{N}$. Then, the angle η can be computed from the following relation:

$$2\eta + \theta_k = \pi \rightarrow \eta = \frac{\pi}{2}\left(1-\frac{k}{N}\right) \tag{A.11}$$

Specifically, in the case of the Oppenheim arch the latter is divided into (N-1) = 7 segments while the first link of the four-link mechanism consists of k=3 segments. The corresponding angles of interest are:

$$\frac{7\pi}{8} \rightarrow 157.5^0,\ \theta_k = \frac{3\pi}{8}\ \&\ \eta = \frac{5\pi}{16}$$

Because $b-a=t$ and $b+a=2R$ it follows:

$$\frac{b-a}{b+a}=\frac{t}{2R}=0.15\rightarrow x=\arctan\left(\frac{0.15}{2}\tan\left(\frac{5\pi}{16}\right)\right)\approx 0.1118 \quad \text{(A.12)}$$

and the angle of the first link is:

$$\theta_{AB}=x+\eta-\frac{\pi}{16}=0.8972^{\circ} \quad \text{(A.13)}$$

Thus, the angles of embrace of the three resulting segments of the four-link mechanism from left to right are $3\pi/8,\ 2\pi/8,\ 2\pi/8$ respectively.

The angle $\widehat{KAB}$ is denoted with ψ_{AB} as shown in Figure A1 and can be calculated through the relation:

$$KB^2=AK^2+AB^2-2AK\cdot AB\cdot\cos(\psi_{AB}) \quad \text{(A.14)}$$

which gives:

$$\cos(\psi_{AB})=\frac{KB^2-AK^2-AB^2}{2AK\cdot AB} \quad \text{(A.15)}$$

A2. Lagrange equation

Generally, the Lagrange equation of a mechanical system is $L=T-U$. Firstly, the kinetic energy of each part of the arch (Figure A2) should be expressed as a function of the derivative of the variable θ and the potential energy $U(\theta)$. The kinetic energy is given by the rotational speed of the center of mass and the part of the moment of inertia I_{AB} (Eq. (A16)).

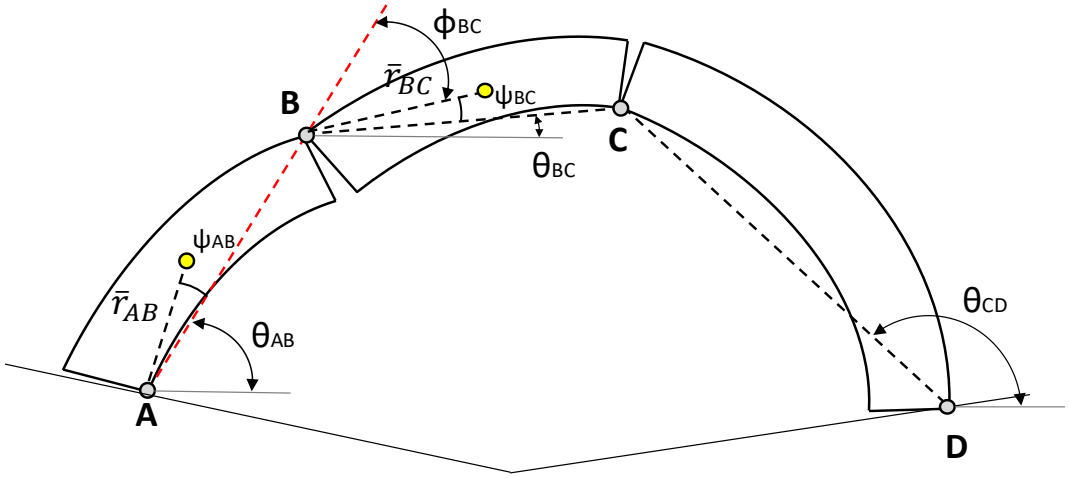

Figure A2 Rotations θ_{AB}, θ_{BC} and θ_{CD} of the three segments which are formed when the arch is transformed into a four-link mechanism.

$$T_1 = \frac{1}{2}\, m_{AB}(\bar{r}_{AB})^2 + \frac{1}{2}\, I_{AB}\dot{\theta}^2 = \frac{1}{2}\, m_{AB} v_{AB}^2 + \frac{1}{2}\, I_{AB}\dot{\theta}^2 \qquad \text{(A.16)}$$

where, the mass of the first beam is denoted with $\mathrm{m_{AB}}$ whilst the rotational speed as the angle changes is given by the formula:

$$v_{AB} = \bar{r}_{AB}\frac{d\theta}{dt} = \bar{r}_{AB}\,\dot{\theta} \qquad \text{(A.17)}$$

Similar notations hold for the other two beams.

The center of mass of the second beam rotates around the joint *B*, but *B* also moves with a rotational speed $\mathrm{v_B} = (\mathrm{AB})\frac{\mathrm{d}\theta}{\mathrm{dt}}$ perpendicular to the beam (*AB*), so the velocity of the center of mass $\bar{r}_{BC}$ is the vector sum $\vec{v}_2 = \vec{v}_B + \vec{v}_{BC}$. To find the kinetic energy, the square of the velocity measure $\mathrm{v_2^2}$ is calculated which is equal to the inner product $v_2^2 = \vec{v}_2 \,.\, \vec{v}_2 = v_B^2 + v_{BC}^2 + 2\vec{v}_B \cdot \vec{v}_{BC}$.

But the velocity $\vec{v}_B$ is perpendicular to beam *AB* and $\vec{v}_{BC}$ is perpendicular to *BC*, so they form the same angle as AB and $\bar{r}_{BC}$, i.e., equal to ϕ_{BC}. Therefore:

$$\vec{v}_B \cdot \vec{v}_{BC} = v_B v_{BC} \cos\phi_{BC} = v_B v_{BC} \cos(\theta_{AB} - \theta_{BC} - \psi_{BC}) \tag{A.18}$$

Thus, the kinetic energy for the second beam is:

$$\begin{aligned} T_2 = \frac{1}{2} m_{BC} v_2^2 + \frac{1}{2} I_{BC} \dot{\theta}_{BC}^2 \\ = \frac{1}{2} m_{BC} (v_B^2 + v_{BC}^2 + 2 v_B v_{BC} \cos(\theta - \theta_{BC} - \psi_{BC})) + \frac{1}{2} I_{BC} \dot{\theta}_{\mathrm{BC}}^2 \\ = \frac{1}{2} m_{BC} [\left(AB\dot{\theta}\right)^2 + \left(\bar{r}_{BC} \dot{\theta}_{\mathrm{BC}}\right)^2 + AB \bar{r}_{BC} \dot{\theta} \dot{\theta}_{\mathrm{BC}} \, cos(\theta - \theta_{BC} \\ - \psi_{BC}) + \frac{1}{2} I_{BC} \dot{\theta}_{\mathrm{BC}}^2 \end{aligned} \tag{A.19}$$

The case of the third beam is the same as the first one. Adding all three components, $T_{1,2,3}$, yields the formula of the kinetic energy implemented in the main text.

A.3 Derivatives of the angles

As it is already mentioned, the angle θ_{AB} has been chosen as the independent variable of the Lagrangian equation. The rotations θ_{BC}, θ_{CD} of the other two links (BC, CD) can be written as a function of $\theta = \theta(t)$. Therefore, $\theta_{BC} = \theta_{BC}\left(\theta(t)\right)$ and $\theta_{CD} = \theta_{CD}\left(\theta(t)\right)$. Their derivatives with respect to time are:

$$\frac{d\theta_{BC}}{dt} = \frac{d\theta_{BC}}{d\theta} \frac{d\theta}{dt} = \theta'_{BC} \dot{\theta} \tag{A.20}$$

and,

$$\frac{d\theta_{CD}}{dt} = \frac{d\theta_{CD}}{d\theta} \frac{d\theta}{dt} = \theta'_{CD} \dot{\theta} \tag{A.21}$$

The same procedure is followed to compute the second derivatives.

A.4 Moments of Inertia

If σ denotes the constant mass density, the arch mass is given by the double integral

$$M = \int\int dm = \sigma \int\int dr\,(r d\theta) = \int_a^b r\,dr \int_{\theta_1}^{\theta_2} d\phi = \sigma \frac{b^2 - a^2}{2} \phi_0 \tag{A.22}$$

where ϕ_0 is the angle of the arch segment apparently equal to $\theta_2 - \theta_1$. The center of mass can be calculated using a similar integral:

$$\vec{r}_{c.m} = \frac{1}{M} \int\int \vec{r}\,dm = \frac{\sigma}{M} \int\int \vec{r}\,dr\,(r d\phi) \tag{A.23}$$

Integration yields:

$$\vec{r}_{c.m} = \frac{4(b^3 - a^3)\sin\left(\frac{\varphi_0}{2}\right)}{3(b^2 - a^2)\varphi_0} \left\{ \cos\left(\frac{\varphi_0}{2} + \theta_1\right) \hat{\imath} + \sin\left(\frac{\varphi_0}{2} + \theta_1\right) \hat{\jmath} \right\} \tag{A.24}$$

$$r_{cm} = \frac{4(b^3 - a^3)\sin\left(\frac{\varphi_0}{2}\right)}{3(b^2 - a^2)\varphi_0} \tag{A.25}$$

Next, the distances to the centre-of-mass of links AB, BC, CD measured from hinges A, B, D respectively are calculated.

Hinge *A* in the figure is defined by the position vector

$$\vec{r}_A = a\cos\theta_1\,\hat{\imath} + a\sin\theta_1 \hat{\jmath} \tag{A.26}$$

Then, the distance of the center of mass $\vec{r}_{cm}$ from hinge *A* is:

$$d_A = |\vec{r}_{cm} - \vec{r}_A|$$
$$= \sqrt{a^2 - \frac{4(a^2+ba+b^2)[2(a^2+ba+b^2)(\cos(\varphi_0)-1)+3a(a+b)\varphi_0\sin(\varphi_0)]}{9(a+b)^2\varphi_0^2}} \quad \text{(A.27)}$$

Accordingly, from hinge B, defined by the vector:

$$\vec{r}_B = b\cos\phi_1\,\hat{\imath} + b\sin\phi_1\hat{\jmath} \quad \text{(A.28)}$$

the distance d_B is equals to:

$$d_B = \sqrt{b^2 - \frac{4(a^2+ba+b^2)[2(a^2+ba+b^2)(\cos(\varphi_0)-1)+3b(a+b)\varphi_0\sin(\varphi_0)]}{9(a+b)^2\varphi_0^2}} \quad \text{(A.29)}$$

A.5 The four-link mechanism as a trapezoid

For our calculations it is important to define the lengths of the links as well as all the involved angles.

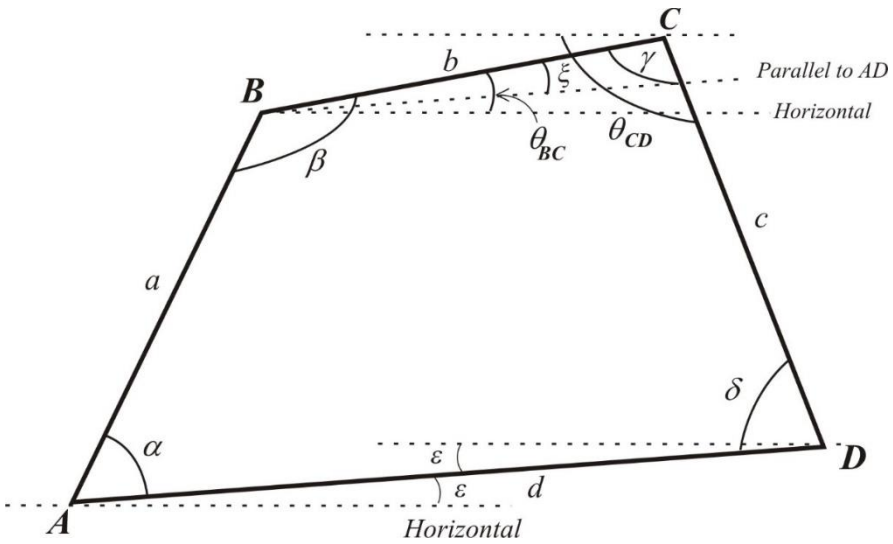

Figure A3 The three links AB, BC, CD and the line AD form a quadrilateral with angles α, β, γ, δ.

The length of the links AB, BC and CD is:

$$l^2 = a^2 + b^2 - 2ab\cos(\theta) \tag{A.30}$$

where θ is the angle of embrace of each arch segment.

The length of the horizontal line is

$$h = 2R\ sin\frac{\theta}{2}$$

AD in Figure A3 is given by the formula

$$AD^2 = t^2 + 4R(R+t)\sin^2\frac{\theta}{2} \tag{A.31}$$

where $t = b - a, R = (a+b)/2$.

Let 'α' the angle of the quadrilateral associated with the hinge *A*. Then, the angle between the horizontal line and the line segment *AD* is $\epsilon = \theta_{AB} - \alpha$. Its sine is given by the expression:

$$\sin\epsilon = \frac{t}{AD}\sin\left(\frac{\pi}{2} + \frac{\theta}{2}\right) \tag{A.32}$$

A.6 The rotations θ of each link

The angles, involved in the Lagrangian equation must be expressed in terms of the independent variable $\theta_{AB} = \theta$. It is useful first to mention the following relations of the angles α, β, γ, δ of the quadrilateral (see Figure A3).

$$\alpha + \beta = \pi + \xi, \qquad \alpha + \beta + \gamma + \delta = 2\,\pi \tag{A.33}$$

From Figure A3, the rotations of each link can be expressed in terms of the angle ε as follows:

$$\theta_{AB} = \alpha + \epsilon \quad \text{(A.34)}$$

$$\theta_{BC} = \xi + \epsilon \quad \text{(A.35)}$$

$$\theta_{CD} = \pi - \delta + \epsilon \quad \text{(A.36)}$$

From the triangles ABC and BAD involving the diagonals AC and BD, the following equations are derived:

$$AC^2 = a^2 + b^2 - 2ab\,cos(\beta) = c^2 + d^2 - 2cd\,cos(\delta) \quad \text{(A.37)}$$

$$BD^2 = a^2 + d^2 - 2ad\,cos(\alpha) = b^2 + c^2 - 2bc\,cos(\gamma) \quad \text{(A.38)}$$

From where the following relations between the angles yield:

$$cos(\beta) = \kappa + \lambda\,cos(\delta)\,, cos(\gamma) = \mu + \nu\,cos(\alpha) \quad \text{(A.39)}$$

where:

$$\kappa = \frac{a^2 + b^2 - c^2 - d^2}{2ab}, \lambda = \frac{cd}{ab}, \mu = \frac{b^2 + c^2 - a^2 - d^2}{2bc}, \nu = \frac{ad}{bc} \quad \text{(A.40)}$$

If the angles of Eq.A.39 are replaced by Eq.A.33, it yields:

$$cos(\alpha - \xi) = -\kappa - \lambda\,cos(\delta)\,, \qquad cos(\delta + \xi) = -\mu - \nu\,cos(\alpha) \quad \text{(A.41)}$$

Let, $\omega = \delta + \xi,\ \chi = \delta + \alpha \Rightarrow \chi - \omega = \alpha - \xi$.

Then, $cos(\omega) = -\mu - \nu\,cos(\alpha) \Rightarrow \omega = arccos(-\mu - \nu\,cos(\alpha))$.

Hence, ω is expressed in terms of the angle α and consequently the angle θ. Also, $cos(\omega - \chi) = cos(\alpha - \xi) = -\kappa - \lambda\,cos(\delta)$.

Plugging in $\delta = \chi - \alpha$ and expanding the cosines it results to:

$$P\,cos(\chi) + Q\,sin(\chi) = -\kappa \tag{A.42}$$

where $P = cos(\omega) + \lambda\,cos(\alpha)$, $Q = sin(\omega) + \lambda\,sin(\alpha)$.

If $tan(\psi) = \frac{Q}{P}$, then Eq.(A.42) becomes:

$$cos(\psi - \chi) = -\frac{\kappa}{(P^2 + Q^2)^{1/2}} = -\frac{\kappa}{\sqrt{1 + \lambda^2 + 2\lambda\,cos(\alpha - \omega)}} \tag{A.43}$$

In the following equations the various angles are expressed as a function of the angle $\alpha = \theta - \epsilon$:

$$\omega = \ arccos(-\mu - \nu\,cos(\alpha)) \tag{A.44}$$

$$\psi = \arctan\left(\frac{Q}{P}\right) = \arctan\left(\frac{sin(\omega) + \lambda\,sin(\alpha)}{cos(\omega) + \lambda\,cos(\alpha)}\right) \tag{A.45}$$

$$\psi - \chi = \arccos\left(\frac{-\kappa}{\sqrt{1 + \lambda^2 + 2\lambda\,cos(\alpha - \omega)}}\right) \tag{A.46}$$

Using previous identities, it is now straightforward to compute the rotations θ_{BC}, θ_{CD}.

The moments of inertia in the Lagrangian equation are calculated with respect to the center of mass from the general formula:

$$I_{cm} = \frac{4}{3}(a^3 - b^3)r_{cm}\sigma \sin\left(\frac{\varphi_0}{2}\right) - \frac{1}{4}(a^2 - b^2)(a^2 + b^2 + 2r_{cm}^2)\sigma\varphi_0 \tag{A.47}$$

The distances of the centers of mass of the three segments from the coordinate center are calculated next.

$$\begin{gathered}\vec{r}_{cm}(AB) = 7.01(-\hat{\imath} + \hat{\jmath}) \rightarrow r_{cm} = \sqrt{7.01^2 + 7.01^2} = 9.91 \\ r_{cm}(BC) = r_{cm}(CD) = 10.24\end{gathered} \tag{A.48}$$

Replacing Eq.(A.48) to Eq.(A.47) it yields:

$$I_{AB} = 151.874\sigma$$
$$I_{BC} = I_{CD} = 46.542\sigma \quad \text{(A.48)}$$

For the case of the Oppenheim arch:

$$AB \approx 11.70\, m, \;\; BC = CD \approx 8.09\, m$$

The line AD that closes the quadrilateral is not exactly parallel to the horizontal line (Figure A3). The length of the horizontal is:

$$h = 2R\, sin\left(\frac{\Theta}{2}\right) = 2\, sin\left(\frac{7\pi}{16}\right) \approx 19.62 \text{ meters} \quad \text{(A.49)}$$

where Θ is the angle of embrace of the arch (as opposed to the main text, here a different notation for the angle of embrace is chosen in order to avoid confusion with the angle β of the quadrilateral, introduced above). Then, the distance AD is given by

$$AD^2 = t^2 + 4R(R+t)\sin^2\frac{\Theta}{2} = 1 + 440\cos^2\left(\frac{\pi}{16}\right) => AD \approx 20.60 \text{ meters} \quad \text{(A.50)}$$

Replacing Eq.(A.50) to Eq.(A.32) it yields:

$$sin(\epsilon) = \frac{t}{AD} sin\left(\frac{\pi + \Theta}{2}\right) \approx 0.0095 => \epsilon \approx 0.54^0 \quad \text{(A.51)}$$

Appendix B (Chapter 4)

Algebraic manipulations to derive Eq. 4.28.

Potential Energy of the solid surface determined by the elliptical upper curve of the arch (ACD′), and the segments (OA), (OD′) as illustrated in Figure 4.4:

$$V_{el} = \int dV = g\rho \iint (r\sin\varphi) r dr d\varphi \qquad \text{B.1}$$
$$= \frac{(ab)^3}{3} g\rho \int_{\varphi_1}^{\varphi_2} \frac{\sin\varphi \, d\varphi}{\left(\sqrt{b^2 cos^2\varphi + a^2 sin^2\varphi}\right)^3}$$
$$= g\rho \frac{ab^3}{3}\left(\frac{1}{\sqrt{b^2 + a^2 tan^2\beta_0}} - \frac{1}{\sqrt{b^2 + a^2 tan^2(\pi - \beta_0)}}\right)$$

Potential Energy of the solid surface determined by the circular lower curve of the arch (A′C′D), and the segments (OA′), (OD) as illustrated in Figure 4.4:

$$V_{circ} = g\rho \int \sin\varphi \, d\varphi \int_0^c r^2 \, dr = g\rho \frac{\left(R - \frac{t}{2}\right)^3}{3} (\cos\varphi_1 - \cos\varphi_2) \qquad \text{B.2}$$
$$= g\rho \frac{c^3}{3}\left(cos^2\beta_0 - cos^2(\pi - \beta_0)\right)$$

The Potential Energy of the part-elliptical arch is derived by subtracting B.2 from B.1, namely:

$$V_{el} = g\rho \frac{ab^3}{3}\left(\frac{1}{\sqrt{b^2 + a^2 tan^2\beta_0}} - \frac{1}{\sqrt{b^2 + a^2 tan^2(\pi - \beta_0)}}\right)$$
$$- g\rho \frac{c^3}{3}\left(cos^2\beta_0 - cos^2(\pi - \beta_0)\right) \qquad \text{B.3}$$
$$= g\,\rho\,\frac{2\,R^3}{3}\left(\frac{(1 + r')^3}{\sqrt{1 - \varepsilon^2\,\cos^2\varphi_0}} - (1 - r')^3\right)\cos\varphi_0$$

Appendix C (Chapter 5)

In this appendix the centre of gravity and the weight of the first segment of Figure 5.4 are presented analytically (Eqs.5.1-5.3). It should be noted here that segment 1 consists of two areas, the arch portion and the buttress area which embodies two parallelepipeds and a little triangle at their intersection.

The coordinates of the centre of gravity (x_{arch}, y_{arch}) and the weight W_{arch} of the arch portion are:

$$x_{arch} = R(1 + \frac{r^2}{3}) \frac{\sin \varphi_1 - \sin \varphi_0}{\varphi_1 - \varphi_0} \quad \text{C.1}$$

$$y_{arch} = -R(1 + \frac{r^2}{3}) \frac{\cos \varphi_1 - \cos \varphi_0}{\varphi_1 - \varphi_0} \quad \text{C.2}$$

$$W_{arch} \to 2R^2 r(\varphi_1 - \varphi_0) \quad \text{C.3}$$

where $r = t/2R$.

The coordinates of the centre of gravity (x_{tr}, y_{tr}) and the weight W_{tr} of the arch portion are:

$$x_{tr} = R(1 + \frac{r}{3}) \cos \varphi_0 \quad \text{C.4}$$

$$y_{tr} = R(1 - \frac{r}{3}) \sin \varphi_0 \quad \text{C.5}$$

$$W_{tr} = 2R^2 r^2 \cos \varphi_0 \sin \varphi_0 \quad \text{C.6}$$

The coordinates of the centre of gravity (x_{P1}, y_{P1}) and the weight W_{P1} of the first parallelepiped are:

$$x_{\mathrm{P1}} = R(\cos \varphi_0 + s_{\mathrm{b}}) \quad \text{C.7}$$

$$y_{\mathrm{P1}} = R \sin \varphi_0 \quad \text{C.8}$$

$$W_{\mathrm{P1}} = 4R^2 r \sin \varphi_0 \, (s_{\mathrm{b}} - r \cos \varphi_0) \quad \text{C.9}$$

The coordinates of the centre of gravity (x_{P2}, y_{P2}) and the weight W_{P2} of the second parallelepiped are:

$$x_{\mathrm{P2}} = R((1-r)\cos\varphi_0 + s_{\mathrm{b}}) \tag{C.10}$$

$$y_{\mathrm{P1}} = R(\sin\varphi_0 - c_{\mathrm{h}}) \tag{C.11}$$

$$W_{\mathrm{P1}} = 4R^2 r \sin\varphi_0\,(s_{\mathrm{b}} - r\cos\varphi_0) \tag{C.12}$$

where $s_b = b / 2R$ and $c_h = h / 2R$.

Replacing Eqs.(C.1-C.12) to Eqs.(5.1-5.3) it yields:

$$x_1 W_1 = R^2(4c_{\mathrm{h}}s_{\mathrm{b}} - r^2\sin 2\varphi_0 - 2r\varphi_0 + 2r\varphi_1) \tag{C.13}$$

$$y_1 W_1 = \frac{2}{3}R^3(6c_{\mathrm{h}}{s_{\mathrm{b}}}^2 - 6c_{\mathrm{h}}(-1+r)s_{\mathrm{b}}\cos\varphi_0 - r(3+r^2)\sin\varphi_0 + (-3+r)r^2\cos{\varphi_0}^2\sin\varphi_0 + 3r\sin\varphi_1 + r^3\sin\varphi_1) \tag{C.14}$$

$$W_1 = -\frac{2}{3}R^3(r(3+r^2)\cos\varphi_1 + 6c_{\mathrm{h}}s_{\mathrm{b}}(c_{\mathrm{h}} - (1+r)\sin\varphi_0) + r\cos\varphi_0\,(-3 - r^2 + r(3+r)\sin{\varphi_0}^2)) \tag{C.15}$$